Title
The Structure of the Solar Wind in the Inner Heliosphere

Author
Lee, Christina On-Yee

Publication Date
2010

Peer reviewed|Thesis/dissertation

The Structure of the Solar Wind in the Inner Heliosphere

by

Christina On-Yee Lee

A dissertation submitted in partial satisfaction of the

requirements for the degree of

Doctor of Philosophy

in

Earth and Planetary Science

in the

Graduate Division

of the

University of California, Berkeley

Committee in charge:

Professor Imke de Pater, Chair

Dr. Janet G. Luhmann

Professor Raymond Jeanloz

Professor Robert P. Lin

Spring 2010

The Structure of the Solar Wind in the Inner Heliosphere

Abstract

The Structure of the Solar Wind in the Inner Heliosphere

by

Christina On-Yee Lee

Doctor of Philosophy in Earth and Planetary Science

University of California, Berkeley

Professor Imke de Pater, Chair

This dissertation is devoted to expanding our understanding of the solar wind structure in the inner heliosphere and variations therein with solar activity. Using spacecraft observations and numerical models, the origins of the large-scale structures and long-term trends of the solar wind are explored in order to gain insights on how our Sun determines the space environments of the terrestrial planets.

I use long term measurements of the solar wind density, velocity, interplanetary magnetic field, and particles, together with models based on solar magnetic field data, to generate time series of these properties that span one solar rotation ($\sim$27 days). From these time series, I assemble and obtain the synoptic overviews of the solar wind properties.

The resulting synoptic overviews show that the solar wind around Mercury, Venus, Earth, and Mars is a complex co-rotating structure with recurring features and occasional transients. During quiet solar conditions, the heliospheric current sheet, which separates the positive interplanetary magnetic field from the negative, usually has a remarkably steady two- or four-sector structure that persists for many solar rotations. Within the sector boundaries are the slow and fast speed solar wind streams that originate from the open coronal magnetic field sources that map to the ecliptic. At the sector boundaries, compressed high-density and the related high-dynamic pressure ridges form where streams from different coronal source regions interact. High fluxes of energetic particles also occur at the boundaries, and are seen most prominently during the quiet solar period. The existence of these recurring features depends on how long-lived are their source regions.

In the last decade, 3D numerical solar wind models have become more widely available. They provide important scientific tools for obtaining a more global view of the inner heliosphere and of the relationships between conditions at Mercury, Venus, Earth, and Mars. When I compare the model results with observations

for periods outside of solar wind disturbances, I find that the models do a good job of simulating at least the steady, large-scale, ambient solar wind structure. However, it remains a challenge to accurately model the solar wind during active solar conditions. During these times, solar transients such as coronal mass ejections travel through interplanetary space and disturb the ambient solar wind, producing a far less predictable and modelable space environment. However, such conditions may have the greatest impact on the planets - especially on their atmospheres and magnetospheres. I therefore also consider the next steps in modeling, toward including active conditions.

For the Team

Contents

List of Figures

Acknowledgements

With the completion of this dissertation, my 26-year career as a student has finally come to a happy end. My Ph.D. experience at UC Berkeley has been an incredible one, and I would like to thank many people for making this possible.

First I would like to thank my family for their generosity and their unconditional support for me to pursue a career in science. I am particularly grateful to my mom who always called to make sure I was eating and getting enough sleep. Simple things like this can easily be neglected so it's good to have someone to keep me "in-check". I am very grateful to my step-father who helped put me through college and got me around during my pre-license years. I miss him a lot and wished he was here to see me finish. I would also like to thank Don for his genuine interest in my research and progress through school. I hope he will continue to ask questions regarding my research and share with me his interest for the stars and planets. I am grateful for Jenn for her enthusiasm and support toward my pursuit for a higher education. I hope we will continue to inspire each other to seek and learn - there is so much out there in the universe! I am grateful for Jenny, Hugh, and their children for always providing good company and tasty meals during the holidays. The leftover food always made wonderful lunches and dinners for a starving student such as myself. I would also like to thank Michiel and Anique for their enthusiasm and energy whenever I see them. They do not know this, but they "infected me" with their passion for cooking and tasty foods, and for this I thank them. Last but not least, for many reasons I am very grateful for having Henk and Marijke in my life. Their deep understanding of my doctoral-related struggles has made me feel less crazy and not so alone.

Many wonderful friends provided tremendous support and kept me sane and positive-minded these past several years. Through some major arm-twisting at times, my friends made sure I came out of my work hole to enjoy a good meal or two, and have some fun every now and then. I thank them for this along with the years of adventures and laughter we shared together. I am particular grateful to Nicole Schlegel, Christopher Walker, Meg and Ryan Starr, Tony Gonsalves, Nicholas Matlis, Aarash Zarrabi, Estelle Cormier, Gwenael and Irma Fubiani, Jennifer Crane,

Adrianne Anderson, Mona Selim, Marine Champsaur, Jeff Graf, Kei and Chou-ka Nakumura, Tammy Parrish, Jim Heirbaut, Robbert van der Scheer, Ellen Hendriks, Mechiel and Tatiana Wilbrink, Martijn Heck, Erik Kieft, Erik Delsman, Saskia Geraedts, Cameron and Bryan Stone, Felix Sturm, Guillaume Plateau, Saskia van Manen, Vanessa Valdez, and Falk Meissner. All of you are awesome in so many ways! And to those who made road trips with me and Jeroen (you know who you are): I am thankful for these unforgettable times as they always re-energized me after many long months of hard work. "Work hard, play hard" as they say!

Without the Earth and Planetary Science department, my Ph.D. career would not have been possible. I am probably the first student in this department to study "space weather" but hopefully I will not be the last. I am very grateful for the breath of knowledge that I obtained in the topic of Earth science, thanks to the courses and department seminars as well as the teaching opportunities that were offered to me. I definitely have a greater appreciation and a deeper understanding of our planet and all the different processes that has occurred or is undergoing on the surface, in the atmosphere, and in its interior. I would particularly like to thank a number of professors in the department, including Michael Manga, Richard Allen, Don DePaolo, Roland Burgmann, and Raymond Jeanloz, for their inspiration and their enthusiasm in teaching. I would also like to thank the graduate student affair officer, Margie Winn, for always putting on a cheerful face while answering my gazillion random questions.

Through the EPS department, I met several classmates and together we formed the invaluable cohort group. Vicky Lee, Su-chin Chang, Sarah Godsey, and Nicole: these past several years you provided me the much needed support, words of encouragement, and hugs during tough times. Mostly importantly, you provided me a safe space to talk and to listen. I am very grateful for all of this and can not imagine what my Ph.D. experience would have been like without you.

I also owe a great deal to my friends and colleagues at the UC Berkeley Space Sciences Laboratory who have provided cheer, encouragement, and enjoyable discussions (scientific and non-scientific). I am especially grateful to Steve Ledvina, George Fisher, Dave Brain, Greg Delory, Brian Welsch, Loraine Lundquist, Rob Lillis, Jasper Halekas, Matt Fillingim, Tess McEnulty, Ben Lynch, Yan Li, and Dietmar Krauss-Varban. I also want to thank Dave and Greg for keeping me in the "Mars and Moon loops" (hopefully one of these days I can jump back into those research topics!) and Rob for getting us together for the occasional Friday Mars Beer. I am also grateful for the indispensable services provided by the SSL support staff, especially Trish Dobson, Brenda Williams, Zania Harris, Judy Williams,

Bruce Satow, Greg Paschall, and Robert Boyd. In addition, I would like to thank Edgar Jones, Antonio Castellanos, and Janet Cooks for always being so cheerful and taking an interest in my studies and my personal life.

I am grateful to my dissertation committee, including Robert Lin and Raymond Jeanloz, who provided support and many helpful comments. Several scientists also deserve special credit for their guidance, contributions to, and useful input on the research presented in this dissertation, including Nick Arge, Dusan Odstrcil, Pete Riley, Christopher Russell, Lan Jian, Glenn Mason, Ian Richardson, Todd Hoeksema, Xuepu Zhao, and Yang Liu.

My studies were supported financially by the U.S. government. I am grateful for three awards: the 2003 NASA Summer Space Grant, the 2005-2006 National Defense Science and Engineering Graduate fellowship funded by the Department of Defense, and the 2008 Space Scholars funding provided by the Air Force Research Laboratory. I also received support from the NSF/STC CISM project under agreement number ATM-010950. In general, I thank all the tax-paying Americans who made these programs possible.

Without the various scientific projects and research programs, all of which are supported by the U.S. government, a portion of my doctoral research would not possible. The majority of the spacecraft observations used in my dissertation were obtained from public online databases such as the NASA Goddard Space Flight Center Space Physics Data Facility, the ACE Science Center at the California Institute of Technology, and the STEREO data website at the University of California, Los Angeles Institute of Geophysics and Planetary Physics Space Science Center. Solar magnetogram data sets were used to drive the numerical model simulations presented in this dissertation, and the access to these data sets were made possible by the Mount Wilson Observatory, the Stanford Wilcox Solar Observatory and the National Solar Observatory. The numerical simulations presented in my studies were made possible by the NASA GSFC Community Coordinated Modeling Center, who provided access to the numerical models, and by the modelers, who spent many years developing the numerical codes. I am particularly grateful to Dusan, Nick, Pete, Anna Chuklaki, Peter MacNeice, Lutz Rattstatter and Michael Hesse, all who helped me countlessly and graciously with matters relating to the solar wind simulations.

Much is owed to Janet Luhmann and Imke de Pater, both who have been remarkable co-advisors and mentors to me. Both of them have always been very enthusiastic and supportive of my research endeavors. Because they are both aware of my interest for a broad range of scientific topics (how many times have they

heard me say "That is SO COOL!!"?), without their guidance I probably would have taken an additional 5 years to complete my dissertation. I have learned so much from them these past several years, each with her own way of thinking and solving problems. They answered my questions with patience, treated my work with respect, and gave generously their time, especially during the months leading up to the qualifying exam, which I will forever appreciate. Most importantly, they provided me the much-needed support and understanding as I struggled my way through scientific research and the peer-review publishing process.

Finally, my biggest thanks is given to my husband, Jeroen van Tilborg, who is a true partner, team player, and a cheerleader. He has truly suffered with me through every step of the process, including preparation for the qualifying exam, rejection from a peer-reviewed journal, and the entire dissertation writing process. I know it was not easy for him, and I thank him for helping me through the many periods of struggle. At the same time, it was not without effort that he made life very enjoyable by planning out many fun activities to do with me (too many to name!). I am extremely grateful for this, and his efforts to keep our lives as balanced as possible. Overall, I certainly could not have gotten through the entire Ph.D. process without his strength, energy, laughter, patience, and compassion. More importantly, I could not have come this far without his love and belief in me regardless of the outcome. For all of this and much more, I will never be able thank him enough.

[I would like to also give small thanks (or no thanks?) to the following sources of work-breaks and procrastination: Fringe, Big Bang Theory, Bones, 24, Lie to Me, Law & Order, Doctor Who, How I Met Your Mother, Family Guy, Simpsons, Burn Notice, Psych, Monk, Fox Soccer Channel, Turner Classic Movies, BBC America, Science Channel, PhD Comics, TPF, TFS, JustJared and in general the internet and television. Without you I could have probably finished sooner.]

Chapter 1

Introduction

1.1 Motivation for this dissertation research

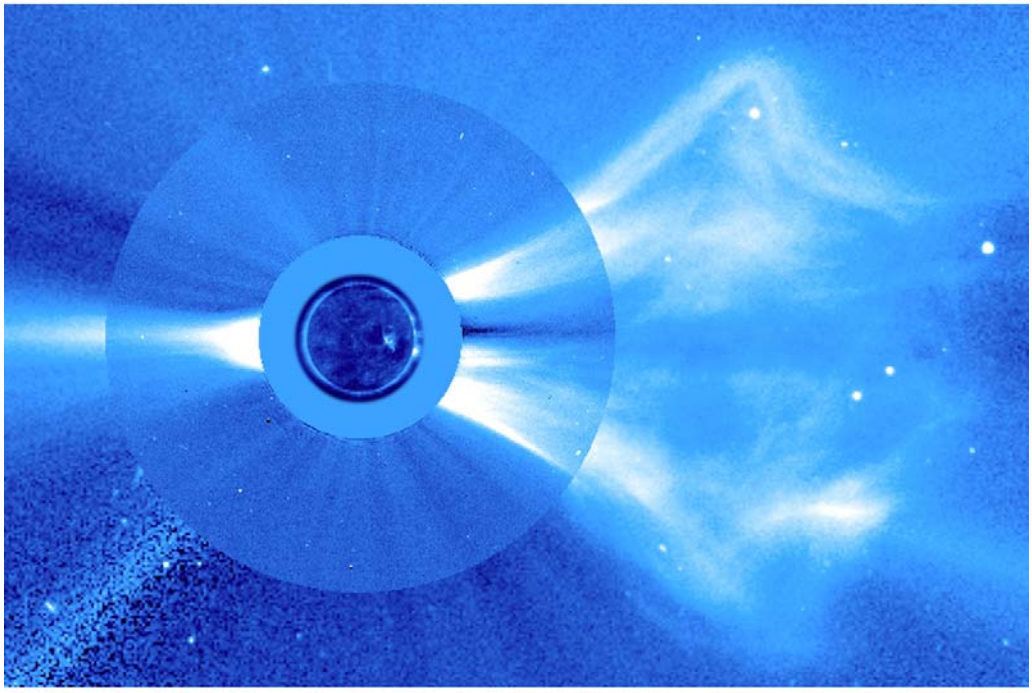

Figure 1.1: A composite image of the Sun taken by the NASA/ESA SOHO spacecraft (see http://sohowww.nascom.nasa.gov/gallery/bestofsoho.html). The extreme ultraviolet image shown on the center disk reveals the bright active regions on the Sun. The faint white light image shown on the larger disk is the atmosphere of the Sun. Shown on the right is a white-light image of a coronal mass ejection (CME).

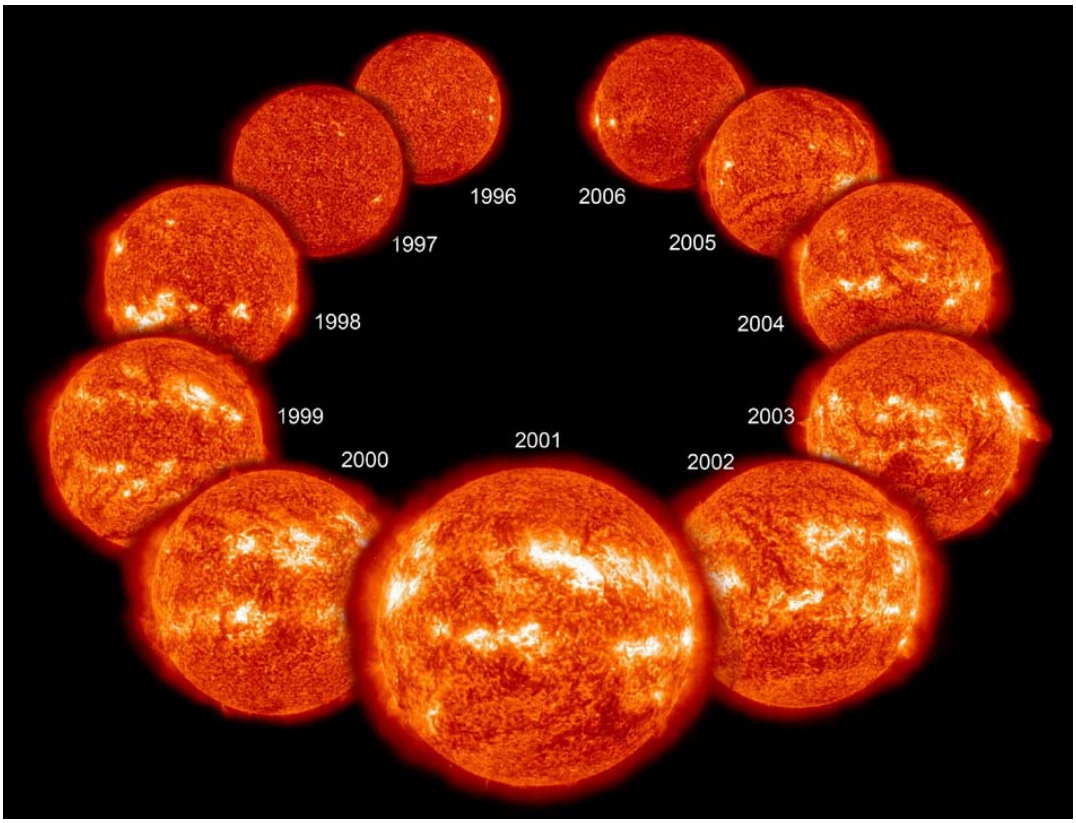

Figure 1.2: Images of the Sun from the SOHO Extreme ultraviolet Imaging Telescope (EIT) for each year of an entire solar cycle. Year 1996 occurred during solar minimum whereas year 2001 occurred during solar maximum followed by the commencement of the next solar minimum during year 2006. Images are taken at the 304 Angstrom wavelength.

The Sun, a star that formed over 4.5 billion years ago, is located at a distance of about 150 million kilometers (called 1 astronomical unit, or AU) from Earth. To the unaided eye, the Sun appears to be a calm and unchanging object in the sky. However, telescope images show that the Sun can be very dynamic (Figure 1.1), its behavior changing according to an 11-year cycle (Figure 1.2). Not only does the Sun provide the main source of heat and light for life on Earth, it also influences the geospace environment through its extensive atmosphere, the solar corona. From the solar surface, the million-degree solar corona expands in all directions into space, filling the solar system with a flow of hot plasma called the solar wind. The solar wind, threaded by the solar magnetic field lines, is composed mainly of an electrically neutral mixture of electrons and ions. With solar activity varying according to

the solar cycle, the solar wind conditions in space are constantly changing. When episodic events occur at the Sun (*e.g.,* Figure 1.1), the disturbances propagate through the solar wind and produce extreme conditions that affect the geospace environment.

The research presented in this dissertation is motivated by a growing interest and need to understand the "space weather" conditions at Earth. Our society's infrastructure has become highly vulnerable to major space environment disturbances that are triggered by solar activity, but we can potentially mitigate the harmful effects on our technological systems through space weather forecasting. Over the last decade, increasingly sophisticated numerical models of the solar wind have been developed and are constantly being tested. One good way to test the accuracy of the models is to run simulations of the solar wind conditions during the quiet, or "minimum", period of the solar cycle. Although in general the conditions are relatively predictable, reproducing the space-based observations can be quite challenging.

As part of an ongoing effort to expand our understanding of the geospace weather conditions, in this dissertation I focus on the characterization of the large-scale solar wind parameters with an emphasis on the time periods surrounding the previous and current solar cycle minimum phase (around years 1997 and 2010, respectively). I utilize long-term spacecraft measurements from near-Earth spacecraft to generate time series and synoptic overviews of various solar wind parameters and compare the results between the two minimum solar cycle periods. Such an extensive comparison is scientifically useful and insightful for understanding how our Sun is evolving over time for a given solar cycle phase.

The research presented in this dissertation will be useful in many ways. The results and analyses will assist numerical modelers to improve their space weather forecasting codes. As the next solar maximum approaches around 2013 (see prediction at http://www.swpc.noaa.gov/SolarCycle/), a scientific understanding of ground- and space-based data in combination with the models will provide an opportunity to realistically and reliably model and forecast the global solar wind and the disturbances that propagate through it. Recently, the twin-spacecraft Solar TErrestrial RElations Observatory (STEREO) mission launched into the 1 AU orbit around the Sun. As such, there is a unique opportunity to obtain multi-perspective observations of the solar wind conditions for a given event time. In the future, it would be interesting to compare the results presented in this dissertation with longer-term observations from STEREO. Moreover, as there are many other beacons in space en route or at other planetary locations (*e.g.,* Mercury MESSENGER, Venus Express, Mars Global Surveyor, Cassini at Saturn), there are opportunities

to extend our knowledge of the geospace environment to other locations. This is especially important if the current planetary spacecraft do not have onboard the instruments to measure certain solar wind parameters.

1.2 The Sun

1.2.1 Some general solar facts

Our Sun is a massive ball of gas that consists mainly of hydrogen (92.1%, by mass), helium (7.8%) and other elements (0.1%). Essentially, the Sun is held together and compressed under its own gravitational attraction. With a radius of about 700,000 kilometers (109 Earths can fit across) and mass of 2×10^{30} kilograms (333,000 Earth masses), the Sun is the largest object in the solar system. Putting

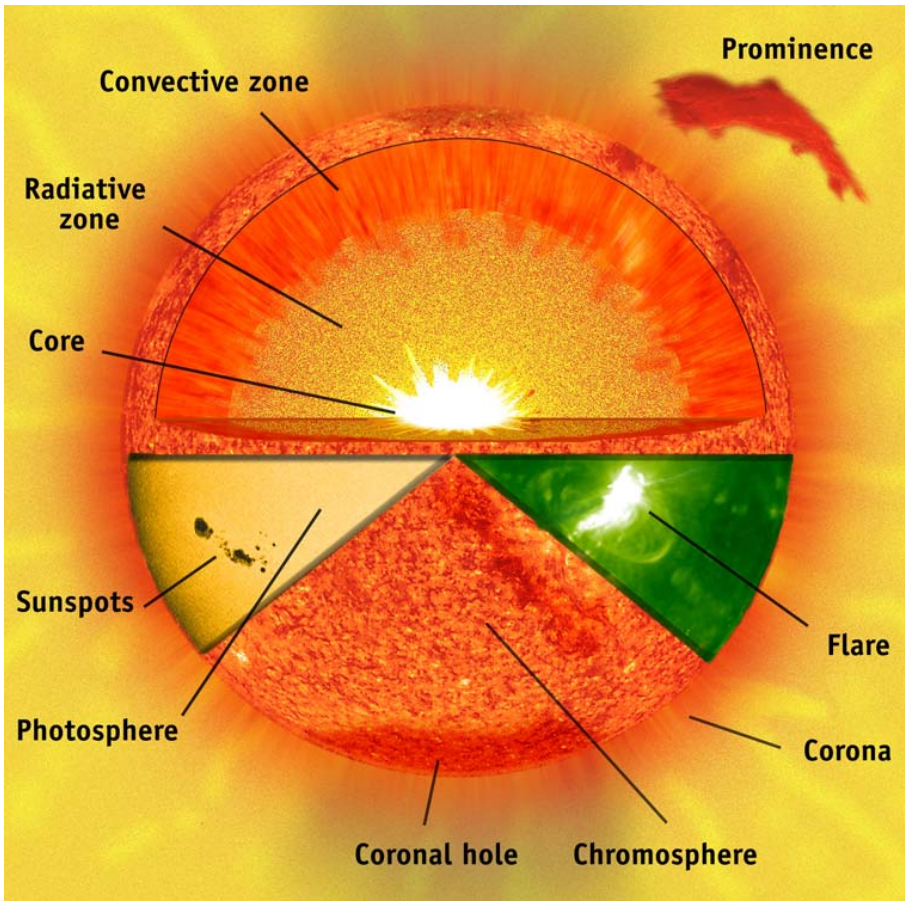

Figure 1.3: Cartoon illustration of the layers of the Sun.

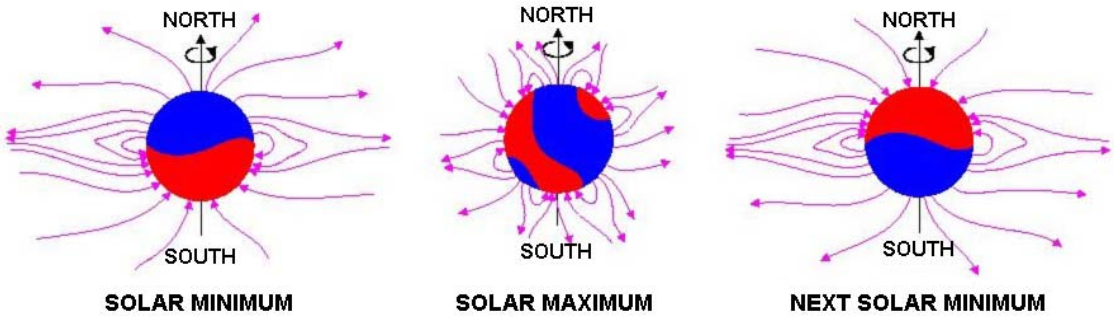

Figure 1.4: Cartoon illustrating the variations of the solar magnetic field polarity and structure during the solar cycle minimum and maximum phases. Image adapted from http://www.sp.ph.ic.ac.uk/ forsyth/reversal/.

its size in perspective, approximately 1.3 million Earths can fit into its volume.

In addition to having an active atmosphere, the Sun has many layers beneath (Figure 1.3) where different physical processes are important. Nuclear fusion of hydrogen atoms to create helium is occurring at the very hot (15,600,000° K) and dense (150 g cm^3, 13 times more dense than solid lead) inner core. The energy produced from such nuclear reactions is then transported outward from the core, which occupies about 25% of the solar radius, to the bottom of the radiative zone. It is at this layer that the energy propagates an additional 50% of the solar distance through a very slow and diffusive process. On average, it takes about 170,000 years for the nuclear energy to transport from the core to the top of the radiative zone. Above this lies the rotating convection zone, where turbulent, convective motions further transport the nuclear energy to reach the surface of the Sun. From here, it takes about 8 minutes for sunlight to travel to Earth at a distance of 1 AU.

The Sun is also a magnetically active star. Currently, it is widely believed that the Sun's magnetic field is generated by a magnetic dynamo, a mechanism through which a rotating, convecting, and electrically conducting fluid acts to maintain a magnetic field over a long period of time. In the case of the Sun, the "fluid" is the ionized gas. Because rotation and convection is required in dynamo theory, it is believed that the solar dynamo occurs between the radiative zone and the surface.

During solar minimum, the solar magnetic field configuration resembles that of an iron bar magnet, just like Earth's magnetic field and is called a magnetic "dipole" (see Figure 1.4, left). At the solar equator, the magnetic field lines are closed, forming loops. At the polar regions, the magnetic field lines are open due to

the outflowing solar wind pressure, and so one end of the field line does not connect back to the Sun.

1.2.2 The visible Sun

The solar surface, the photosphere, is the visible layer (Figures 1.3 and 1.5) that has an average temperature of about 5,700° K. The surface is actually a thin gaseous layer, about 500 kilometers thick. Many features can be seen on the photosphere, as shown in Figure 1.5. The lefthand panels are obtained in the wings

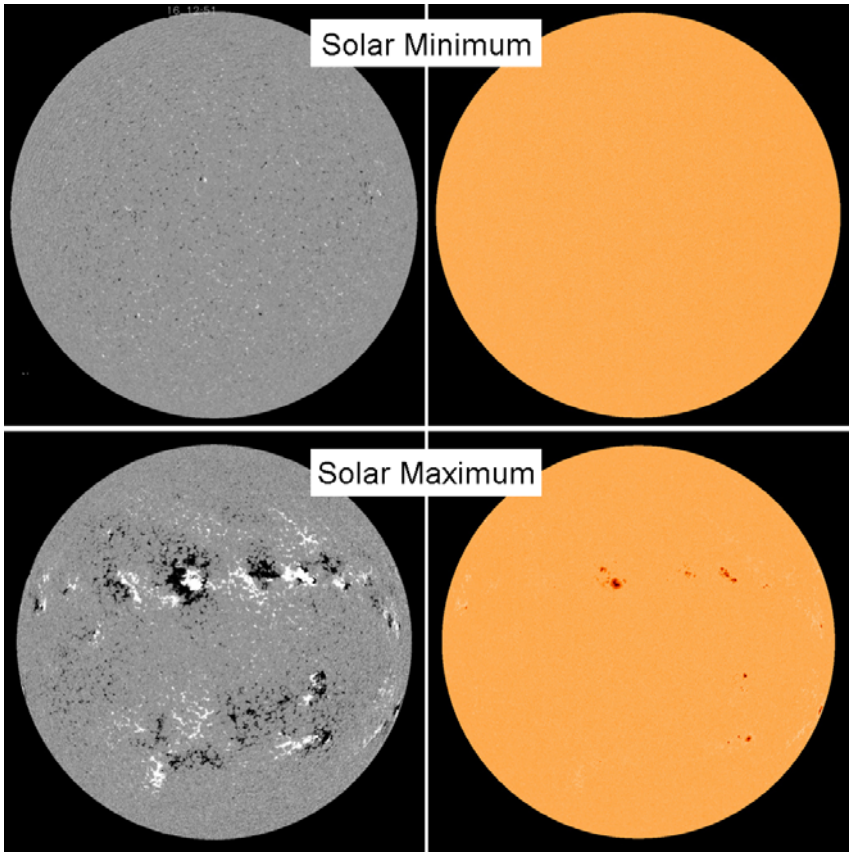

Figure 1.5: SOHO Michelson Doppler Imager (MDI) (left) magnetogram and (right) continuum image taken near the Ni I 6768 Angstrom wavelength. The magnetogram shows the magnetic fields in the solar photosphere, where the colors indicate the direction of the magnetic field polarity (white for outward, black for inward). The continuum image shows the Sun in the visible range of the spectrum. The top (bottom) row of images is taken during solar minimum (maximum).

of certain spectral lines that respond to magnetic fields, whereas the right panels are continuum images of the visible surface. On the left, the "magnetograms" show the locations of paired magnetic field regions (shown in black and white) at the surface. The black areas are regions where the magnetic polarity is directed inward toward the Sun, whereas the white areas are regions where the polarity is directed out toward the observer. These black and white areas usually appear in pairs. The coronal geometry above these fields can be thought of as half-loops of magnetic field lines protruding out of the solar surface.

The most intense magnetic regions have dark sunspots that appear on the photosphere, as shown in the continuum images on the right of Figure 1.5. These magnetically intense sunspots are cooler (about 3,700° K) than the adjacent areas and thus give off less light, appearing darker. As shown in Figure 1.5, not all regions with polarity features have corresponding dark sunspot features. Sunspots typically are visible for several days, although some very large ones have lasted for many weeks.

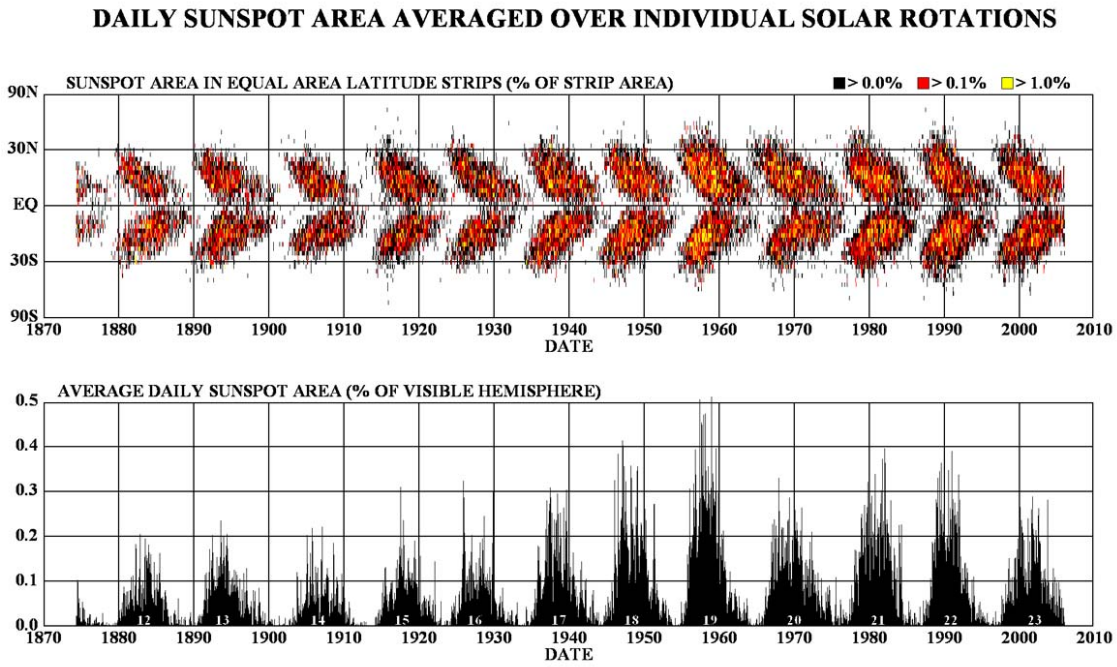

Figure 1.6: (top) Butterfly diagram of sunspots from years 1870 to 2010. (bottom) Average daily percent of sunspots areas seen on the visible solar disk. Public image from NASA.

The total number of sunspots appearing on the photosphere varies over an 11-year cycle (Figure 1.6). The surface is relatively spotless during solar minimum (see Figure 1.5, top row) in comparison to the solar maximum period (see Figure 1.5, bottom row). In addition, the latitudinal locations of the sunspots also vary, where the sunspots migrate from higher latitudinal regions during the rising phase of solar maximum, to the equatorial regions during the decline toward the minimum phase.

The movement of the sunspots across the face of the Sun lead to the deduction that the Sun rotated on its axis at a rate of about 27 days per rotation. Since the Sun is a ball of gas, it does not rotate rigidly like a solid mass. Instead, it undergoes a differential rotation, where different latitudinal bands rotate at different rates. Specifically, the equatorial band rotates faster (about 25 days per rotation) than the polar regions (about 36 days per rotation).

1.2.3 The solar atmosphere

The solar corona is also visible to the unaided eye but only during total solar eclipses when the Moon occults the Sun (Figure 1.7, left). During such times the gross coronal structures, such as the helmet streamers (Figure 1.7, right), can be seen. There are also routine spacecraft observations of the solar corona with telescopes and coronagraphs. A coronagraph instrument utilizes a small occulting

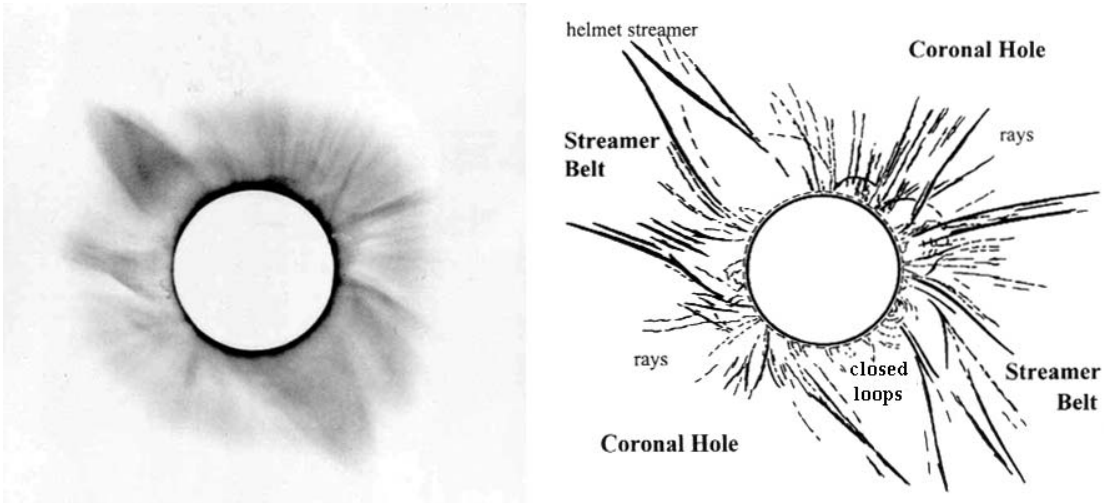

Figure 1.7: The coronal structure during the total solar eclipse of 11 July 1991. (left) Negative white light image adapted from Lang (1995). (right) Sketch of the coronal structure, from Kallenrode (2001).

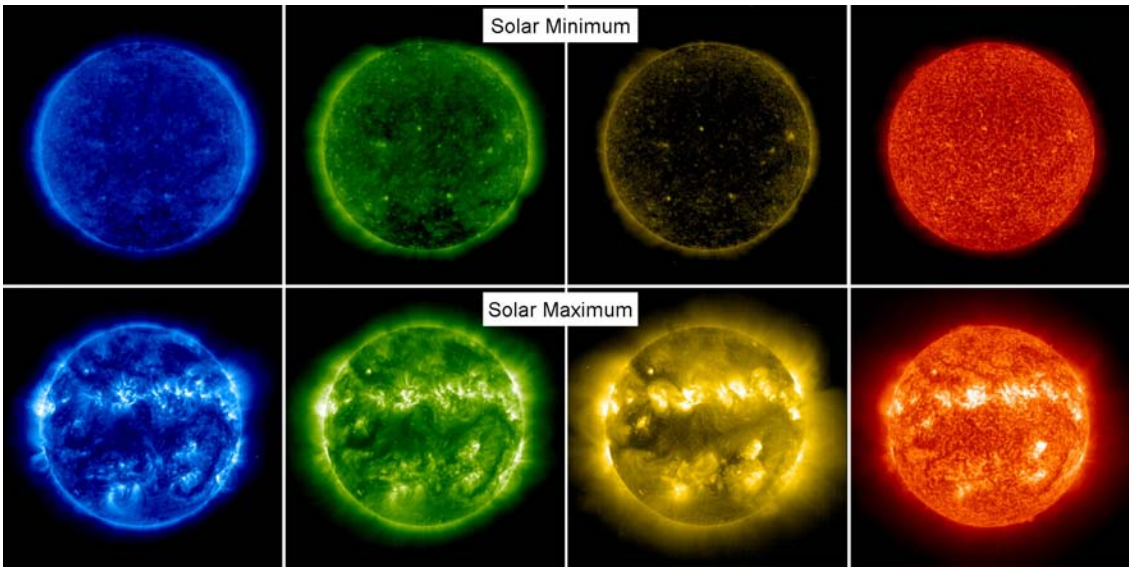

Figure 1.8: SOHO Extreme ultraviolet Imaging Telescope (EIT) images of the corona at wavelengths of 171, 195, 284, and 304 Angstroms (left to right). Each wavelength reveals the solar material at different temperatures (1 million, 1.5 million, 2 million, and 70,000 degrees), where the hotter (cooler) temperatures correspond to the higher (lower) height in the solar atmosphere.

disk to mask the solar disk and block off the photospheric light (see, *e.g.,* Figure 1.1). In general, the shapes of the coronal structures observed during the total eclipses will vary, depending on the solar cycle phase. For solar minimum observations, the coronal structures are typically more symmetrical (*e.g.,* Figure 1.7).

The hot plasma of the solar corona emits most of its energy in the extreme ultraviolet and X-ray wavelengths. Figure 1.8 shows images of the solar corona taken during the solar minimum and maximum phases. There is a noticeable difference in features during the two cycle periods of observations. During solar minimum (top row of images in Figure 1.8), the most prominent coronal features are dark regions called coronal holes. These are regions that contain cooler gas and hence appear dark. At solar minimum, the coronal holes are predominantly located in the polar regions of the Sun. Also seen are some small bright active regions (groups of sunspots on the photosphere). When the Sun is more active during solar maximum (bottom row of images in Figure 1.8), features such as polar plumes, magnetic coronal loops containing dense plasma with stronger emissions, and coronal holes can be seen. Overall, the solar corona is constantly changing.

1.3 The interplanetary medium

The solar corona is continuously expanding out to interplanetary space, filling it with a tenuous outflow of ionized plasma and magnetic field from the Sun. This solar wind outflow is a result of a large difference in the gas pressure between the solar corona and interplanetary space. Despite the huge gravitational pull of the Sun, the plasma expands outward due to the pressure difference, creating our interplanetary medium.

1.3.1 Solar Wind

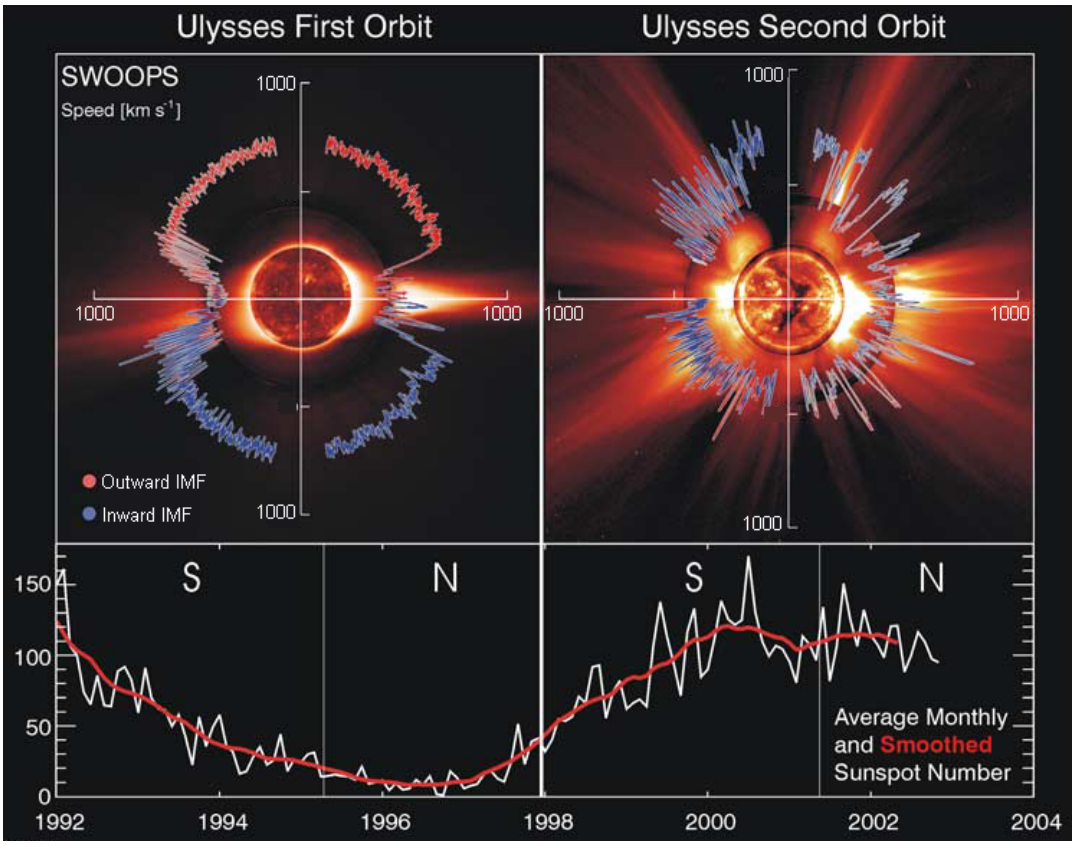

Figure 1.9: Solar wind speed as a function of solar latitude during (left) solar minimum and (right) solar maximum. The background images are composite images from EUV observations of the solar disk together with white light images of the solar corona. Bottom panel shows the monthly sunspot numbers to illustrate the solar cycle phases. Figure from McComas *et al.* (2003).

In the orbital plane of Earth (also called the ecliptic plane, tilted about 7° from the solar equatorial plane), the measured solar wind speed is typically around 450 km s^{-1}. This equates to a travel time of about 4 days for the solar wind to reach Earth. However, higher solar latitude measurements from the Ulysses spacecraft have shown that the solar wind is actually composed of both a slow and fast speed solar wind component (Figure 1.9). During solar minimum (see Figure 1.9, left), the fast solar wind streams flow out at a speed of about 800 km s^{-1} from the high solar latitude, polar coronal hole regions, whereas the slow speed component of about 450 km s^{-1} mainly flows from the low latitude, equatorial coronal hole regions. During solar maximum (Figure 1.9), the separation of the slow and fast speed solar wind regions is not as organized, where the fast speed streams can originate from lower solar latitude coronal hole regions in additional to the polar coronal holes.

The configuration of the solar wind in interplanetary space is that of a spiral (Figure 1.10). If we think of the solar wind as a succession of fluid parcels coming from a fixed source on the Sun (Figure 1.11), because the Sun is rotating the solar wind source essentially moves beneath the radially emitted parcels. The effect is that a given solar wind fluid parcel will trace out a spiral shape over time, also known as an Archimedean or Parker spiral. This effect is analogous to a stream of water coming out of a rotating sprinkler water hose. At 1 AU in the ecliptic plane, the spiral makes an angle of about 45° with respect to the Sun-to-Earth line for the solar wind speed of 450 km s^{-1}.

1.3.2 Interplanetary magnetic field

Frozen into the solar wind is the interplanetary magnetic field (IMF). As the solar wind streams radially outward from the magnetically open solar coronal hole regions, it carries with it the solar magnetic field lines. Thus, the spiral configuration (Figure 1.10) also describes the shape of the IMF structure in the interplanetary medium.

Typically during solar minimum, the majority of solar open field lines extend from the coronal holes that are located in the high solar latitude and polar regions (see an example illustration in Figure 1.4, left and rightmost panels). As the solar wind flow from the dark coronal hole regions and extends into interplanetary space, the field lines are redistributed to the lower solar latitudinal and equatorial regions (see, *e.g.,* Figure 1.12).

Near the solar equatorial region, field lines of opposite polarity are separated by a neutral zone (gray shaded area in Figure 1.12). This neutral zone extends outward into the interplanetary medium, forming what we call the heliospheric

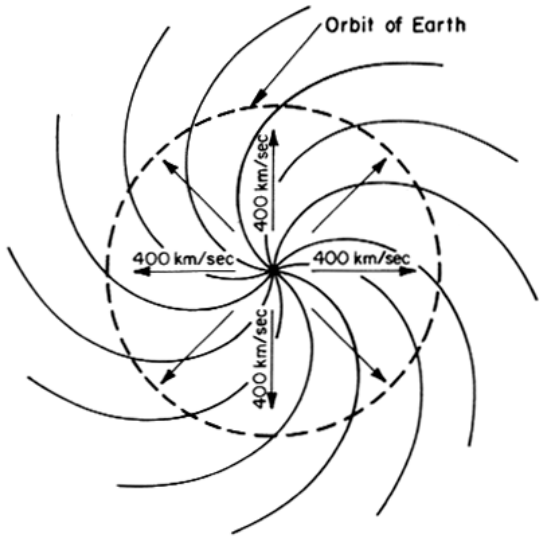

Figure 1.10: In the ecliptic plane, the radial flow of the solar wind with the frozen-in magnetic field together with the rotation of the Sun generates an Archimedean (or Parker) spiral configuration. Figure from Hundhausen (1995).

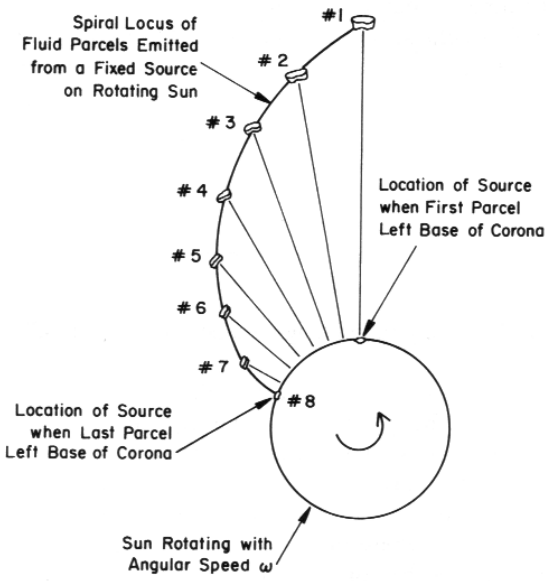

Figure 1.11: Illustration of solar wind parcels emitted at constant speed from a fixed source on a rotating Sun. The resulting shape is a spiral configuration shown in Figure 1.10. Figure from Hundhausen (1995).

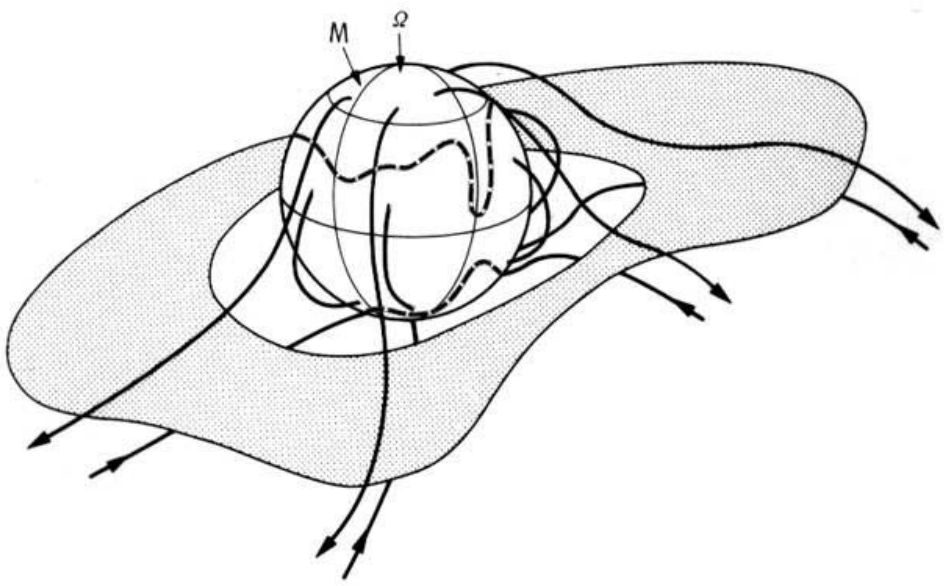

Figure 1.12: Illustration of the heliospheric current sheet (shaded in gray) for a steady period of the solar cycle. Fields of positive, outward-pointing (negative, inward-pointing) polarity are located in the northern (southern) solar hemisphere. Dashed lines illustrate the polar coronal holes and their extensions, where the open field lines originate. Figure from Smith, Tsurutani, and Rosenberg (1978).

current sheet (HCS). Essentially, the HCS is an extension of the solar equatorial region. During solar minimum when the magnetic dipole axis is nearly aligned with the solar rotation axis, an observer in the ecliptic plane (which is tilted about 7° from the solar equatorial plane) will alternately lie above and below the current sheet as the Sun rotates. As a result the observer will see a magnetic sector pattern of alternating polarities. During other solar cycle phases, particularly the declining phase, the dipole axis is tilted more substantially. As a result, the current sheet will be more warped, like a ballerina skirt, and the observer will see a more complicated magnetic sector pattern.

1.3.3 Solar wind interaction with Earth

The interaction of the solar wind with the Earth's dipole magnetic field creates a "cavity" in the solar wind called a magnetosphere (Figure 1.13). On the sunward side of Earth, the supersonic solar wind plasma encounters the geomagnetic field, causing the solar wind to slow down to subsonic speeds and flow around Earth. This

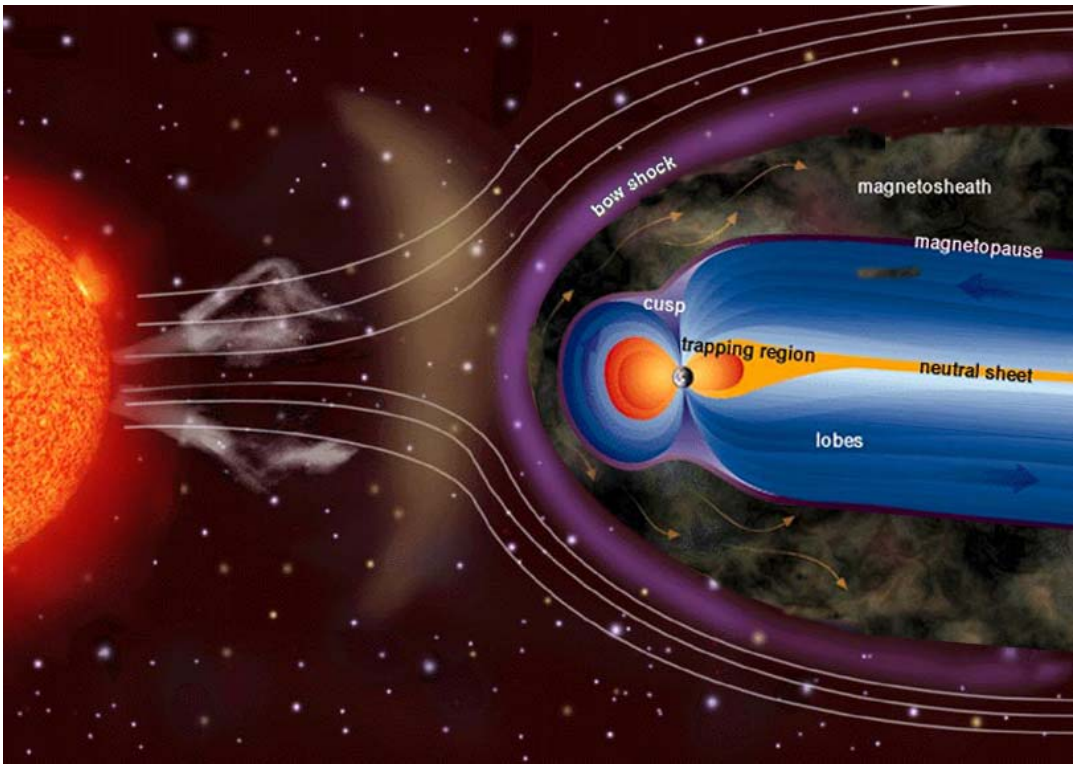

Figure 1.13: Illustration of the Sun-to-Earth solar wind interaction. Composite illustration adapted from figures courtesy of Windows to the Universe, http://www.windows2universe.org and NASA.

region includes the bow shock and magnetosheath and is similar to the structure that forms at the front of a boat as it speeds through the water. The location of the bow shock depends on the solar wind conditions. Under quiescent conditions, the location of the "nose" of the bow shock is typically around 14 earth-radii from the geocenter (1 earth radius is about 6,400 km). If the interplanetary conditions are disturbed, the magnetosphere becomes more compressed and pushes the bow shock nose closer to Earth. Behind the magnetosheath, the solar wind plasma and interplanetary field come in contact with the sunward dipole field of Earth, creating a boundary called the magnetopause. Since, the geomagnetic field is pointed northward here, if the interplanetary field is pointed southward the two fields connect. In such cases, the solar wind plasma can flow along the connected field lines and interact more strongly with Earth's atmosphere.

On the nightside of Earth's magnetosphere, the solar wind stretches the geomagnetic dipole field out to form the magnetotail. The opposite dipole field po-

larities form two lobes in this tail region, separated by a current sheet. It is not well-known how far the magnetotail extends, but spacecraft measurements have detected the tail at least 200 earth-radii downstream from Earth.

1.4 Space weather: far-reaching effects

The "weather" or conditions in the geospace environment can be quite important with far-reaching effects. During active solar conditions, coronal mass ejections (CMEs) propagate though the interplanetary medium (Figure 1.14) and dramatically change the solar wind properties by increasing the densities and magnetic field strengths, accelerating the flow velocities, and populating it with solar energetic particles. Near Earth, CMEs can produce strong interplanetary shock waves and southward interplanetary magnetic field, which in turn can produce strong ge-

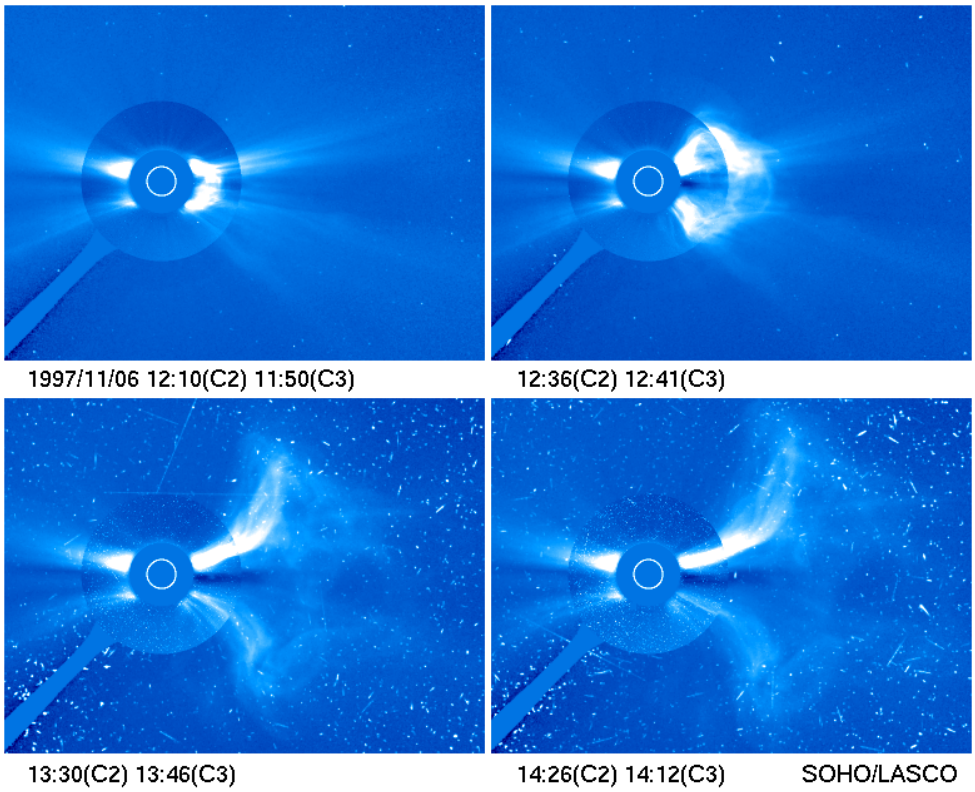

Figure 1.14: Time-lapsed photos showing the development of a CME and its space weather effects at the SOHO satellite in near-Earth space. Image courtesy of the SOHO/LASCO consortium.

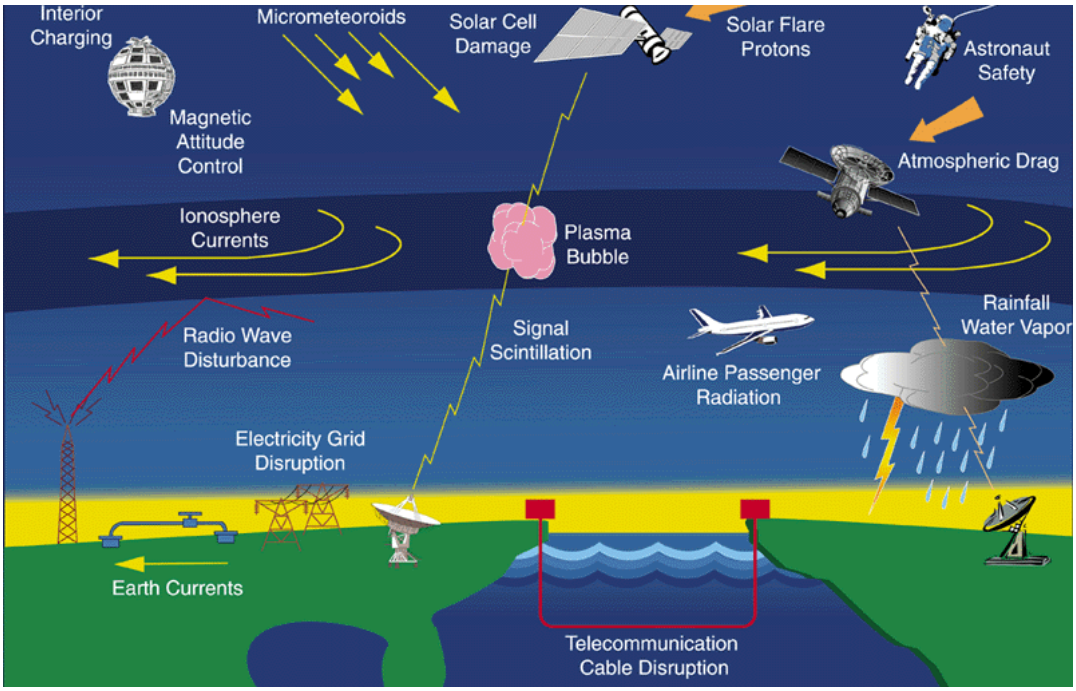

Figure 1.15: Space weather hazards: the effects of space weather extends from geostationary space to the ground. Figure from Baker (2000).

omagnetic storms that impact both space-based technology (*e.g.,* Figure 1.14) and ground-based systems (see Figure 1.15).

The concept of "space weather" can also be applied to other planetary locations, such as Mercury, Venus, and Mars. Various investigations are currently underway to understand the solar wind conditions at these locations.

1.5 Dissertation outline

With the exception of Chapter 4, the following chapters are a collection of papers that have been published in the journal *Solar Physics*. A brief summary of each chapter is presented below.

In Chapter 2 (see also Lee *et al.*, 2009a), I began to test two existing space weather models for quiet solar wind conditions. To investigate how well the models describe the solar wind structure from the Sun out to 1 AU, the model results were compared to solar wind measurements from the ACE spacecraft. The results showed that there was a good overall agreement between the observations and the model results for the general large-scale solar wind structures and trends, such as

the timing of the high density structures and the low- and high-speed solar wind streams, as well as the magnetic sector patterns.

In Chapter 3 (see also Lee *et al.*, 2009b), I investigated the solar wind conditions at 1 AU during the recent declining to minimum phase of the solar cycle (around year 2008). When I made a comparison to the conditions observed during a similar phase of the previous solar cycle minimum, I found that the overall values were significantly different in comparison. In particular, I found that the IMF values were lower during the recent minimum period. As such, I investigated whether the lower IMF values were a direct consequence of the lower solar polar fields that were observed at the same time.

In Chapter 4, I continued my investigation of the lower IMF by focusing on how the observed solar photospheric fields map into interplanetary space and control the IMF observed in near-Earth space. Using a potential field model of the solar corona to compute the coronal hole magnetic fields, I investigated how the strength of the photospheric field affects the interplanetary magnetic flux and in particular, how much the observed interplanetary fields of different cycle minima can be understood simply from differences in the areas of the coronal holes as opposed to differences in the surface fields within them. For the model boundary condition, I invoked a different (smaller) value than is typically used in the potential field model. This is in order to construct a consistent picture of the observed coronal holes and the near-Earth interplanetary field strength as well as polarity measurements for the near-minimum activity phases of current and previous solar cycles.

In Chapter 5 (see also Lee *et al.*, 2010), I changed my focus back to near-Earth observations of the interplanetary medium, including the low energy energetic particles that propagate in the solar wind. I particularly focus on the organization of energetic particles by the solar wind structure, namely the corotating interaction regions (CIRs) and the shocks that are driven by the episodic interplanetary coronal mass ejections. For this investigation I utilized data from a longer range of time, during the declining to minimum phase of the recent solar cycle (years 2003 to 2009). Because the CIR-associated particles are very prominent during the solar minimum, the long solar minimum period of this current cycle provided an opportunity to examine the overall organization of CIR energetic particles for a much longer period than during any other minimum since the dawn of the Space Age. I also contrasted the solar minimum observations with the declining phase when a number of solar energetic particle events occurred, producing a mixed energetic particle population. In addition, I compared the observations from this minimum period with those from the previous solar cycle (around 1994 to 1997).

Chapter 2

The Solar Wind at 1 AU During the Declining Phase of Solar Cycle 23: Comparison of 3D Numerical Model Results with Observation

Abstract

We present results of solar-wind parameters generated by 3D magnetohydrodynamic (MHD) models. The ENLIL (name for the Sumerian god of the Sun) inner-heliosphere solar-wind model together with the "MHD Around a Sphere" (MAS) or Wang-Sheeley-Arge (WSA) coronal models, describe the steady solar wind stream structure and its origins in the solar corona. The MAS/ENLIL and WSA/ENLIL models have been tuned to provide a simulation of plasma moments as well as interplanetary-magnetic field magnitude and polarity in the absence of disturbances from coronal transients. To investigate how well the models describe the ambient solar wind structure from the Sun out to 1 AU, the model results are compared to solar-wind measurements from the ACE spacecraft. We find that there is an overall agreement between the observations and the model results for the general large-scale solar-wind structures and trends, such as the timing of the high-density structures and the low- and high-speed winds, as well as the magnetic sector structures. The time period of our study is the declining phase of Solar Cycle 23 when the solar activity involves well-defined stream structure, which is ideal for testing a quasi-steady state solar wind model.

2.1 Introduction

Heliospheric space weather is a description of the conditions in interplanetary space caused by variations in solar activity. The solar wind, a magnetized plasma which continuously flows out from the solar corona at average speeds of ≈400 km s^{-1}, makes up the interplanetary medium through which plasma and magnetic

field disturbances triggered by solar activity can propagate. During quiet times, when there are no episodic disturbances known as coronal mass ejections (CMEs) that travel across interplanetary space and affect the solar wind properties, the variability is determined by the conditions in the quiet corona and by interactions between the solar-wind streams as they travel outward. Even for realistic long-term predictions of the episodic solar disturbances, it is necessary to understand the ambient solar-wind structure.

Numerical techniques are becoming more widely used to obtain realistic simulations of the physics of the heliosphere as well as for the development of prediction models. As a first step, models have been developed to simulate the solar wind in the inner heliosphere during quiet solar conditions. Wang and Sheeley (1990a; 1992) found an empirical relationship that predicts both the interplanetary magnetic field (IMF) polarity and the radial solar wind speed at 1 AU, the latter using an empirical relationship between the solar wind speed and the coronal flux tube expansion determined from a potential source surface model of the corona (Levine, Altschuler, and Harvey, 1977). One advantage of this semi-empirical model is its use of the photospheric magnetic field observations to obtain a detailed and realistic description of the open field regions in the corona from which the solar wind flows. Pizzo (1991) developed a 3D magnetohydrodynamic (MHD) model that generates a time-stationary large-scale structure of the inner heliosphere and incorporates an idealized tilted dipole geometry. The model was used to study the tilted-dipole corotating stream fronts near the heliographic equator. In a subsequent study, Pizzo (1994) investigated the deformation of the heliospheric current sheet (HCS) in this model due to the interactions of the global corotating stream flows. More recently, the Wang and Sheeley model was updated by Arge and Pizzo (2000) to include a simple 1D modified kinematic model of the solar wind propagation between the source surface at 2.5 $R_\odot$ (solar radii) and 1 AU that takes into account stream interactions and allows solar wind forecasts at the first Lagrange point (L_1, located $\approx$1.5 million km from the Earth roughly along the Sun–Earth line). Meanwhile, Usmanov *et al.* (2000) developed a 2D MHD quasi-steady state global axisymmetric solar wind model, again with a simplified coronal field, that included Alfvén waves to simulate a physics-based heating and acceleration of the solar wind flow. Later, Usmanov and Goldstein (2003) produced a 3D model that included a tilted dipole and the solar rotation, providing a self-consistent way to treat stream interactions. There are also numerical codes that simulate the solar wind through coupled MHD solar corona-heliosphere models (*e.g.,* Riley, Linker, and Mikic, 2001; Odstrcil, 2003). Typically, the coronal calculations are performed

starting at ≈1 $R_\odot$ (the coronal base) out to 20–30 $R_\odot$ beyond the critical point and the solution is used as the inner boundary condition of the heliospheric model. An important reason for having such two-component solar-wind codes is because the nature of the simulation regions are very different – the heliospheric code is better designed for supersonic and super-Alfvénic advection, whereas the coronal code is better designed for the lower corona.

With the increasing availability of regular magnetic field observations of the solar photosphere, a number of modelers have been utilizing such data as boundary conditions to produce global solar wind simulations. Usmanov (1993a; 1993b) presented the first studies that utilized full-rotation synoptic charts from Wilcox Solar Observatory (WSO) (Hoeksema and Scherrer, 1985) in a 3D solar wind model. They have since been followed by others, (*e.g.,* Mikic and Linker, 1995; Linker and Mikic, 1997; Riley, Linker, and Mikic, 2001; Roussev *et al.*, 2003; Odstrcil, 2003; Odstrcil, Pizzo, and Arge, 2005; Cohen *et al.*, 2007). These synoptic charts are magnetic maps of the whole Sun, in which the data are taken over one solar rotation as viewed from Earth (≈27.2753 days). By convention one solar rotation is also called one Carrington Rotation (CR), in which CR 1 started on 9 November 1853[1]. In addition to the availability of magnetic field observations of the solar surface, there are now many archived data sets that are generated from spacecraft observations of the solar wind near or at 1 AU. These data sets have been obtained over many CRs, making it possible to compare results with models for different solar activity conditions (*e.g.,* Cohen *et al.*, 2008). In particular, it is possible to compare observations of the quiet solar wind with numerical model results to test their performance in simulating the solar wind in the inner heliosphere. Such tests provide some measure of validation for the models for use at quiet times, as well as establishing their usefulness for describing the ambient conditions prior to disturbances.

The purpose of this paper is to present comparisons of several numerical solar wind model results with spacecraft observations to demonstrate the current state of the art. We focus on two models: *i*) the coronal part of the Wang-Sheeley-Arge model (Arge *et al.*, 2004) coupled to the ENLIL solar wind model (Odstrcil, 2003) (henceforth, WSA/ENLIL), and *ii*) the coronal part of the MHD-Around-A-Sphere (MAS) model (Riley, Linker, and Mikic, 2001) coupled to the ENLIL solar wind model (henceforth, MAS/ENLIL). We use these models to simulate the solar wind near the ecliptic plane at 1 AU and compare the results with observations made

[1]See http://alpo-astronomy.org/solar/rotn_nos.html for a full listing of CR numbers and their associated start and end dates.

by the *Advanced Composition Explorer* (ACE) spacecraft located at the L_1 point. One reason for testing these particular models is that they are publicly available for research and/or forecasting uses through the runs-on-request service at the Community Coordinated Modeling Center (CCMC), a multi-agency facility located at the NASA Goddard Space Flight Center. In Section 2 we briefly introduce the solar-wind models and the solar magnetograms that are used for their initial boundary conditions. In Section 3 we describe the results that are generated by the models. In Section 4 we compare these results with the ACE observations for the recent declining phase of Solar Cycle 23 (January 2003 to December 2005). In addition, we intercompare the results generated by the WSA/ENLIL and MAS/ENLIL models. In Section 5 we summarize the overall performance of the two models, providing some insight for future model users and the model developers. Since the model codes are constantly updated by the code developers, it should be understood that ENLIL version 2.3a, MAS version 2.3a, and WSA version 2.3a were used at CCMC in generating the results for this study.

2.2 Solar Wind Model

The coronal portion of the WSA model (*cf.* Arge *et al.*, 2004) simulates the solar magnetic field from the photosphere out to 21.5 $R_\odot$. The model utilizes the potential field source surface (PFSS) approximation for the coronal field (*cf.* Schatten, Wilcox, and Ness, 1969). This source surface is a hypothetical sphere centered around the Sun at 2.5 $R_\odot$, where the magnetic field lines of the corona are constrained to be radial to simulate the effect of the solar wind. The inner boundary of the model makes use of the line-of-sight magnetic field measurements of the solar photosphere, which utilize the spectral lines Fe I 525.0 nm for the WSO and Mount Wilson Observatory (MWO) or Fe 630.2 nm for the National Solar Observatory (NSO) (Henney, Keller, and Harvey, 2006; Ulrich *et al.*, 2002). These measurements are assembled into synoptic maps from daily full-disk magnetograms that are acquired over one CR. A spherical harmonic solution is computed for the potential magnetic field everywhere within 2.5 $R_\odot$ based on the map of radial fields as the inner boundary conditions (*cf.* Wang and Sheeley, 1992). In the region between the source surface to the outer boundary at 21.5 $R_\odot$, the Schatten current sheet model (Schatten, 1971) is incorporated to provide a more accurate magnetic field topology in the outer corona. To derive the solar wind flow speed at 21.5 $R_\odot$, the model utilizes an empirically-derived formula that relates the speed at the source surface to the relative expansion of the magnetic field from the photosphere to the source surface. This formula is an improvement on the original Wang and Shee-

ley formula (Wang and Sheeley, 1990a; 1990b) by including the minimum angular separation between an open field footpoint and the closest coronal hole boundary (or open field region) (*cf.* Arge *et al.*, 2004). The solar wind speed assigned at the 21.5 $R_\odot$ surface is then propagated radially outward using the ENLIL solar wind model described below. Note that we only use the coronal portion of the original WSA model (described in Arge *et al.*, 2004), whereas the WSA model at the Space Weather Prediction Center (SWPC) (http://www.swpc.noaa.gov/ws), for example, includes the 1D kinematic code that ballistically propagates the solar wind out to 1 AU. The solar coronal temperature T is chosen such that the total pressure is uniform on the outer coronal boundary, where the total pressure is the sum of the thermal pressure, $p = 2nkT$ (n is the proton number density, k is the Boltzmann constant) and magnetic pressure. For the WSA/ENLIL model the outer coronal boundary is 21.5 $R_\odot$. To derive the mass density, conservation of momentum flux is assumed.

The MAS coronal model is a 3D time-dependent MHD finite difference model that solves Maxwell's equations as well as the continuity, momentum and energy equations (*cf.* Riley, Linker, and Mikic, 2001). The MAS model analyzed here uses synoptic magnetograms from NSO as the input parameter to determine the radial component of the magnetic field. An ideal gas equation of state with a polytropic index of 1.05 approximates heat-conduction processes and thermal energy sources. The initial plasma and field parameters used to solve the MHD equations are determined from a potential field model and a Parker solar wind solution (Parker, 1958). The initial coronal solution is advanced in time until a steady-state solution is reached. The coronal component of MAS extends from the base of the solar corona at 1 $R_\odot$ to 30 $R_\odot$, where staggered nonuniform meshes are used in the radial and meridional directions and grid sizes range from 81 × 81 × 64 to 121 × 121 × 128 ($r \times \theta \times \phi$). Because the version of the MAS model at CCMC is the simple polytropic version where a simple energy equation is used, the highest speeds achieved are too low by a factor of two, and the contrast between low and high speeds are weaker compared with observations (Luhmann *et al.*, 2004). To correct for this, at 30 $R_\odot$, the speed is derived from an *ad hoc* description (Riley, Linker, and Mikic, 2001) for the photospheric sources within open field regions based on the following parameters: a nominal constant slow flow speed, a nominal constant fast flow speed, the minimum distance from an open-closed boundary, a nominal thickness of the slow flow band (≈0.1 radians, or ≈6°), and a nominal width of the region in which the flow speed is raised to match the coronal hole flow (≈0.05 radians, or ≈3°). Similar to the WSA coronal model, the density is derived by as-

suming conservation of momentum flux at the source surface and thermal pressure balance is assumed in deriving the solar coronal temperature.

The ENLIL solar wind code (*cf.* Odstrcil, 2003) is a time-dependent 3D numerical model for simulating the ambient solar-wind flow in the heliosphere. The solar coronal models provide the input boundary conditions (solar coronal temperature or plasma pressure, density, velocity, magnetic fields) to drive this model. Based on the MHD description, the model solves for plasma mass, momentum, energy density, and magnetic field. The ratio of specific heats is chosen to be 1.5 to describe a fully ionized solar wind plasma. The model uses a uniform mesh of $1280 \times 45 \times 180$ ($r \times \theta \times \phi$) grid points. To concentrate gridpoints in the low-latitude region of interest for the Earth, the spherical grid extends only to heliolatitude $\pm 45°$. The spacings in the radial, θ, and ϕ directions are 0.59 $R_\odot$, 2° and 2°, respectively. The inner radial boundary of the ENLIL model is at 21.5 or 30 $R_\odot$ depending on whether the WSA or MAS coronal models are used, respectively. These distances are beyond the fast-mode MHD critical point of the solar wind, where the solar material flows away from the Sun roughly along radial trajectories. Solar rotation is added at the ENLIL inner boundary by imparting a corotational magnetic-field component.

These coupled models are available at the CCMC website (http://ccmc.gsfc.nasa.gov). To execute runs of MAS/ENLIL or WSA/ENLIL, the user must specify the Carrington Rotation, solar coronal model (WSA or MAS), solar observatory, and maximum radial distance (out to 10 AU). From the output generated, the user can use an on-line graphics tool to produce various displays such as color contour plots, 1D line plots, *etc.*, based on the user-specified plot parameters. Alternatively, the user can opt to download the results in ASCII format and use their own graphics and analysis software. Note that the download of the ASCII data is not an option unless a special request is made to CCMC to provide the data.

2.2.1 Model Input Options

For the WSA and MAS coronal models that are available at CCMC, the photospheric field full-rotation synoptic magnetograms are obtained from either NSO/Kitt Peak or MWO (Henney, Keller, and Harvey, 2006; Ulrich *et al.*, 2002; Howard, 1976). An advantage to using the MWO measurements is that the magnetograms updates more than ten times per day (depending on observing conditions) versus NSO, which updates up to three times per day since late 2003 when the SOLIS magnetograph became operational; updates only occurred once during the pre-SOLIS period (Arge *et al.*, 2004). Another advantage to using magnetograms

from MWO is that there are fewer data gaps. Note that the CCMC/MAS model currently only uses magnetograms from NSO, whereas the CCMC/WSA model uses magnetograms from either observatory. Although it has not been implemented yet, CCMC plans to provide a version of the MAS coronal model that utilizes magnetograms from MWO. The synoptic maps are constructed from full-disk magnetograms acquired over one CR, which are in contrast to daily updated synoptic maps that do not have specific start and end dates (see Arge and Pizzo, 2000, for a discussion).

Throughout this study, we noticed that NSO had more unusable or absent magnetograms for a given CR than MWO and thus it was not possible to simulate the solar wind for a number of CRs at CCMC. Magnetograms from both NSO and MWO have corrections applied to the raw data, taking into account the spectral line saturation effects, magnetic zero-point instrumental offsets, polar fields, *etc.*, (*cf.* Arge *et al.*, 2002; Arge and Pizzo, 2000). Since the version of the MAS coronal model at CCMC only utilizes full Carrington maps created from NSO magnetograms, we will only show model results generated from the traditional NSO Carrington map option. Although not shown in this paper, the WSA/ENLIL model simulations generated from either the MWO or NSO magnetograms reveal very comparable solar-wind results for each CR, with little to negligible difference in some cases.

2.3 Data Description

We requested a uniform set of model runs from the CCMC website and downloaded the model results in ASCII format. Programs were written to further process the ASCII data (*e.g.* by coordinate transformation and averaging) and generate the figures shown throughout this paper. Since the model produces a quasi-steady solar-wind solution, there is no direct time information in the ASCII data sets. However the effective time can be determined from the solar longitude values. Since it takes 27.2753 days for the Sun to make one full solar rotation as viewed from the Earth, one day in a CR (24 hours) is equivalent to the Sun rotating ≈13.2°. Thus, the solar longitude information can be converted to time, where 360° solar longitude is equivalent to the beginning of day 1 of CR, down to 0° solar longitude which is roughly equivalent to the end of day 27 of CR. The time resolution of the model data is ≈218 minutes (3.6 hours), given by the ENLIL computational grid resolution in solar longitude which is 2°. In the present study, time series were generated for comparison with L_1 data sets such as ACE. Examples of a 1D line plot for CRs 2017 and 2018 are shown in Figure 2.1. In both CRs 2017 and 2018, there are two dynamic pressure peaks corresponding to the stream interaction regions surround-

ing the crossing of the HCS. During this quiet solar period, the solar wind had a well-defined two-stream, two-sector structure with a steep boundary gradient in magnetic field and velocity at the HCS crossings.

A different plot style is adopted for displaying solar wind parameters to get a better sense of the near-ecliptic structure over a large range of CRs for the present low solar activity period. The 1D time series are effectively stacked against each other (Figure 2.1, right) such that the x-axis displays the CR number (1999–2038), the y-axis displays the day of the CR (1 to 27), but here the color represents the magnitude of the solar-wind parameter of interest. In Figure 2.1, the red values represent the solar-wind high-dynamic pressure (peaks in the time series), whereas the blue values represent low dynamic pressure (troughs in the time series). Figures 2.2, 2.3, and 2.4 show plots for density, ρ, velocity, v, and dynamic pressure, $\frac{1}{2}\rho v^2$, respectively, for the ACE observations and models. The black areas in the plots represent data gaps in the ACE observations (top row). For the model results, CRs for which run simulations could not be executed due to unusable or absent magnetograms are represented by black strips. At the time, it was not possible to obtain model data from CCMC that are computed for Earth's location. Thus, for the purposes of our study the data sets for the model results were downloaded for a fixed radial distance of 1 AU and a fixed latitude of 0° (model solar equatorial

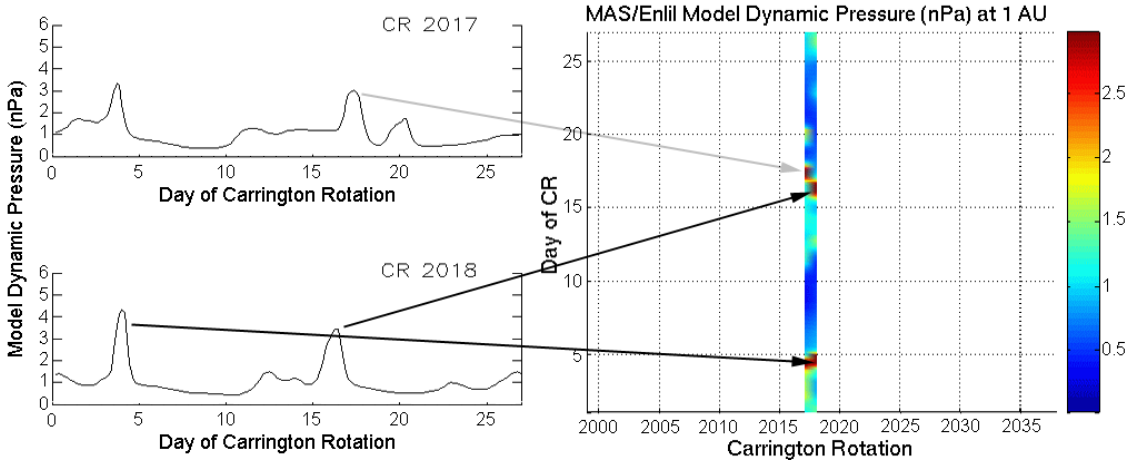

Figure 2.1: Shown are time series of dynamic pressure (left) modeled at 1 AU for CRs 2017 and 2018. The time series can be stacked against each other, where the magnitude of the dynamic pressure is now represented in color (above); highs = red, lows = blue. A time series organized by CR can be displayed in this fashion, forming a color contour plot of CR versus day of CR (day 1, day 2, . . . day 27).

plane, within 8° of the ecliptic plane).

2.4 Comparison with Observations at 1 AU

We compared the solar wind model results with observations from the Solar Wind Electron, Proton, and Alpha Monitor (SWEPAM) (McComas *et al.*, 1998) and magnetometer (MAG) (Smith *et al.*, 1998) instruments onboard the ACE spacecraft. Since its launch in 1997, the ACE spacecraft has resided at the L_1 point, measuring the solar wind continuously. The archived data sets can be acquired from the NASA Goddard Space Flight Center Space Physics Data Facility website (http://spdf.gsfc.nasa.gov/). For this study, we utilize the four-minute resolution solar-wind plasma data that are averaged from the Level 2 64-second resolution data, and the Level 2 IMF data with a resolution of four minutes.

As mentioned earlier, comparisons with measurements obtained during a quiet solar period of the solar cycle are appropriate because these are the most ideal conditions for testing a quasi-steady state solar wind model. The time period ranges from 24 January 2003 to 18 January 18 2006 (CR 1999 to 2038). During this declining period of Solar Cycle 23, the HCS had a remarkably steady two-sector structure for many CRs. This can be seen in the ACE observations (Figure 2.2a), where from CR 1999 to 2019 there are two persistent high-density structures that correspond to two-stream interaction regions. The two high-density structures show up in red and start roughly on days 7 and 20 of CR 1999. In the latter half of the time range, CR 2020 to 2038, the ACE observations show four high-density ridges per rotation starting roughly on days 3, 10, 17, and 27 of CR 2020. These correspond with the stream interaction regions of the four-sector HCS structures. Figures 2.2a and 2.3a show that whenever the densities are low, the velocities are high, as expected for approximate solar-wind momentum flux constancy. The solar-wind dynamic pressure is calculated from the solar wind density and velocity and is shown in Figure 2.4a. The number of high dynamic pressure ridges corresponds to the number of sector structures mentioned above.

Comparison of the model results with ACE measurements reveals that the WSA/ENLIL and MAS/ENLIL models simulate the general features of the large-scale solar wind structure. For example, Figures 2.2b and 2.2c show that the models reproduce the main density structures that were observed by ACE. In particular, the timing of the structures is similar to the observations to within a few days. The shapes of the structures are also approximately replicated. The magnitudes of the high density structures are also quite similar, although for some CRs the peak model values are higher than the ACE values. The models also simulate the high velocity

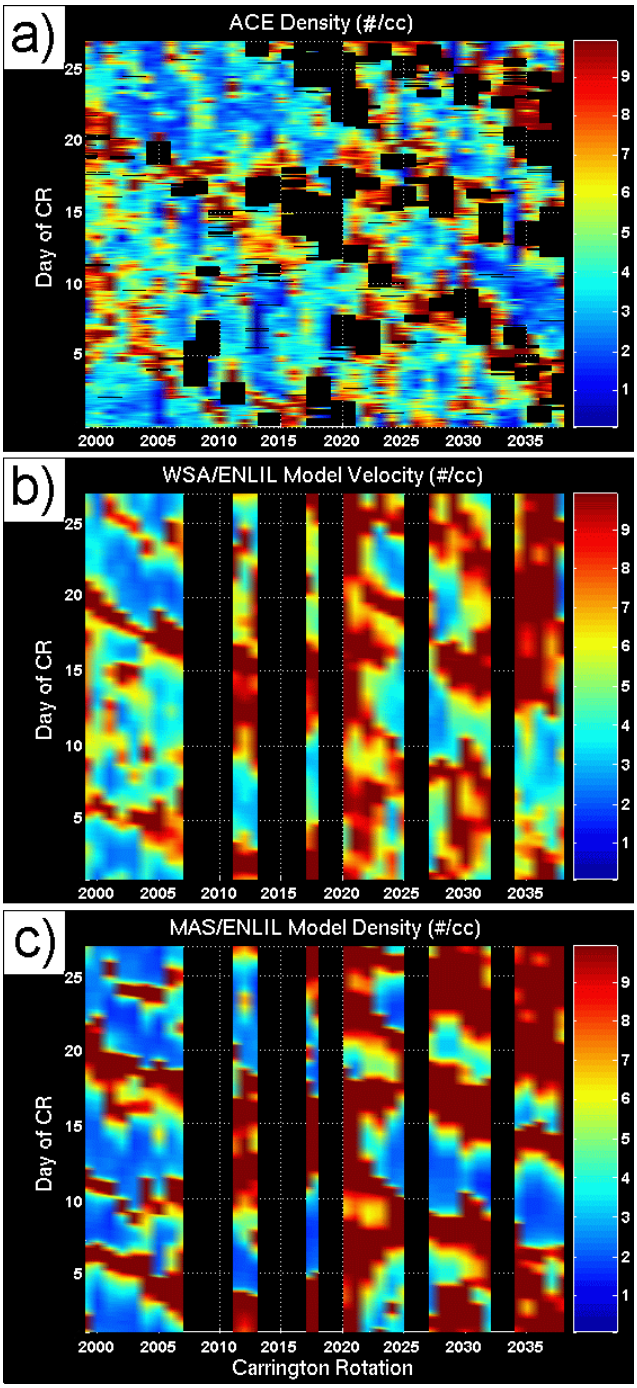

Figure 2.2: Comparison of (a) ACE observations with the (b) WSA/ENLIL and (c) MAS/ENLIL results for density. Synoptic maps were not available for CRs 2008, 2009, 2010, 2014, 2015, 2016, 2019, 2026, and 2033 (black data strips). Data dropouts appear in the ACE data whenever the values are exceptionally high.

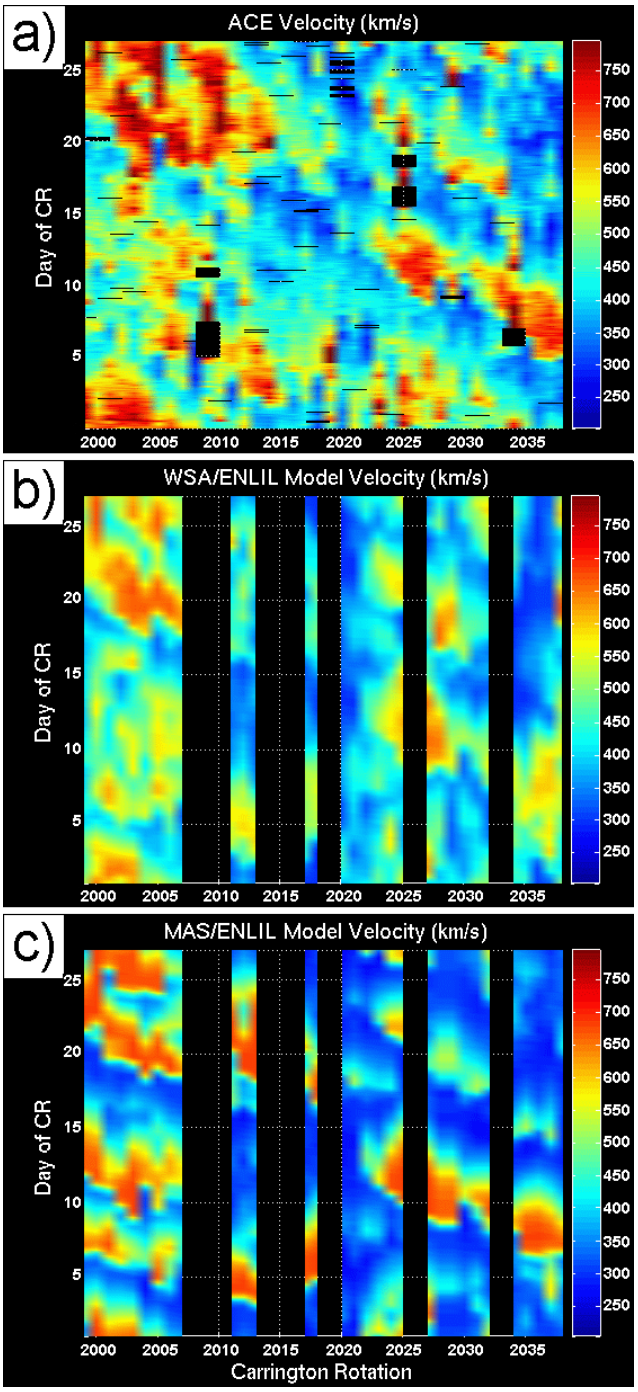

Figure 2.3: Comparison of (a) ACE observations with (b) WSA/ENLIL and (c) MAS/ENLIL model results for velocity. The observations reveal that where the densities are low (Figure 2.2a, blues) the velocities are high (a, reds). These high-velocity structures last for many CRs.

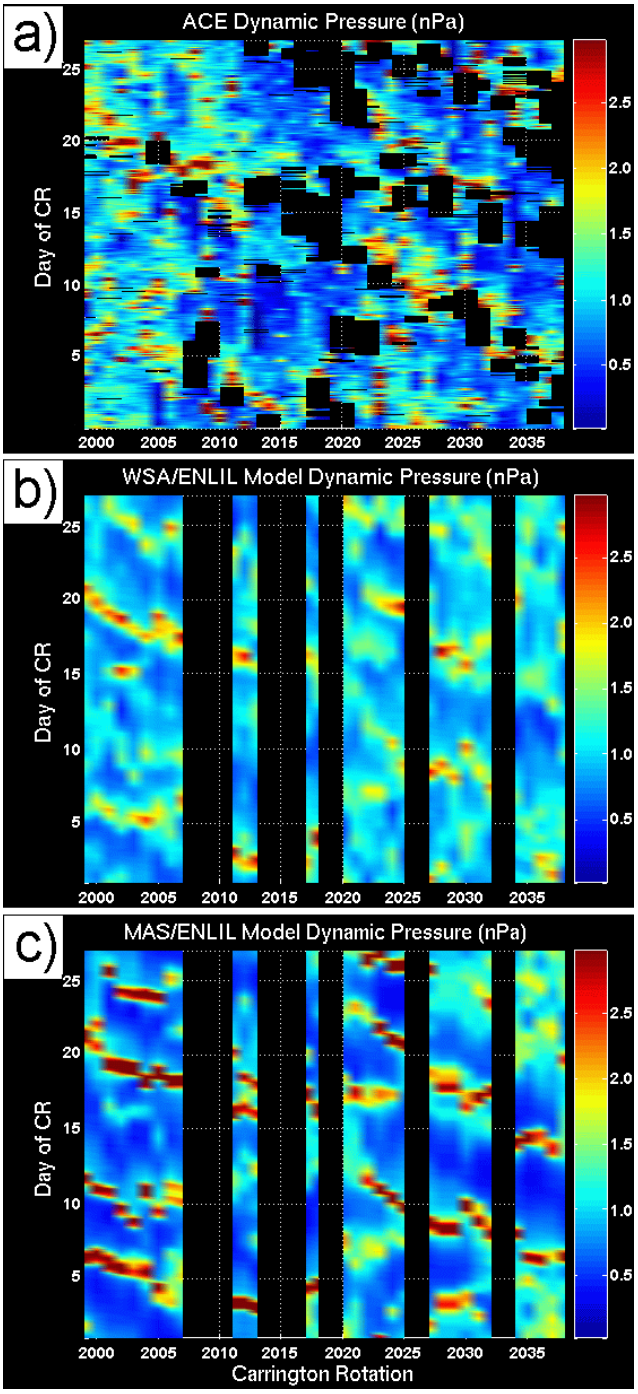

Figure 2.4: Comparison of (a) ACE observations with the (b) WSA/ENLIL and (c) MAS/ENLIL model results for dynamic pressure.

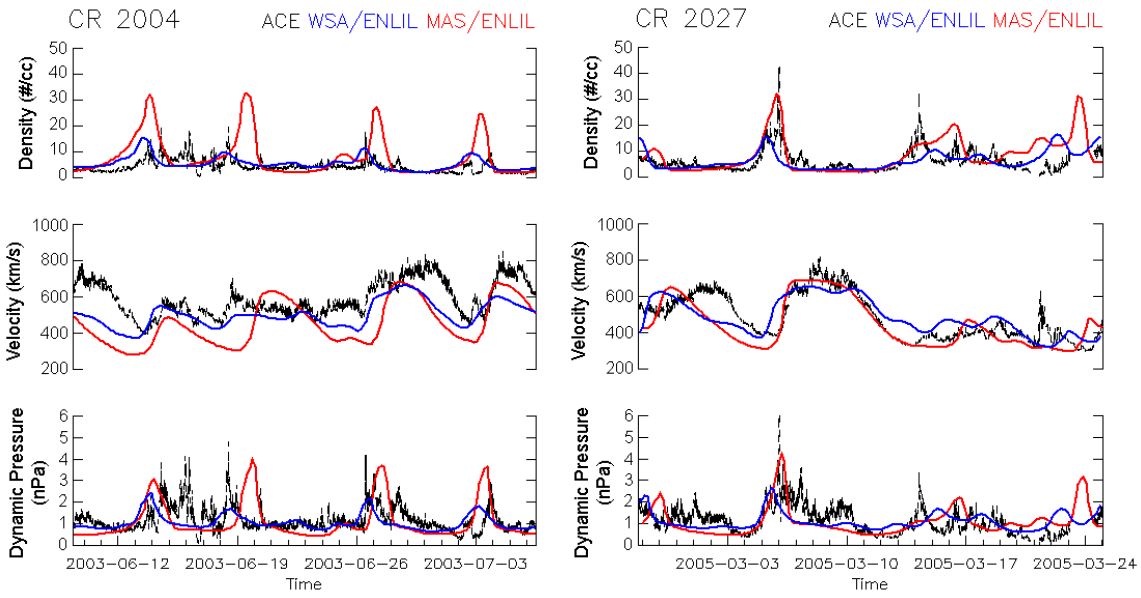

Figure 2.5: Time series for CRs 2004 (left) and 2027 (right) of ACE observations *versus* model results for density (top panels), velocity (center panels), and dynamic pressure (bottom panels). Shown in red are the MAS/ENLIL results, in blue the WSA/ENLIL results, and in black the ACE observations.

structures that were observed by ACE (compare Figures 2.3a with 2.3b and 2.3c). The overall shape of the high-velocity structures are replicated and the timing of the structures is good to within a few days in comparison with the observations. For dynamic pressure, the model results (Figures 2.4b and 2.4c) generally agree with the ACE observations (Figure 2.4a) in terms of the overall shape and timing of the high pressure ridges.

Figure 2.5 reveals some of the typical characteristics of the model performance, including the effective model "time" resolution imposed by the numerical grid for CRs 2004 and 2027. The top panels show the model densities for CR 2004 (Figure 2.5, left) where the MAS/ENLIL model results are overestimated by about 50–200%, as opposed to CR 2027 (Figure 2.5, right) where the densities are more comparable to the ACE observations. The opposite is true for the velocity results. The middle panels show that for CR 2004 the magnitudes of the model velocities are underestimated by a few tens of percent in comparison with the ACE values, whereas the values for CR 2027 are quite comparable. The bottom panels reveal the typical behavior of the model results for dynamic pressure, where the comparisons

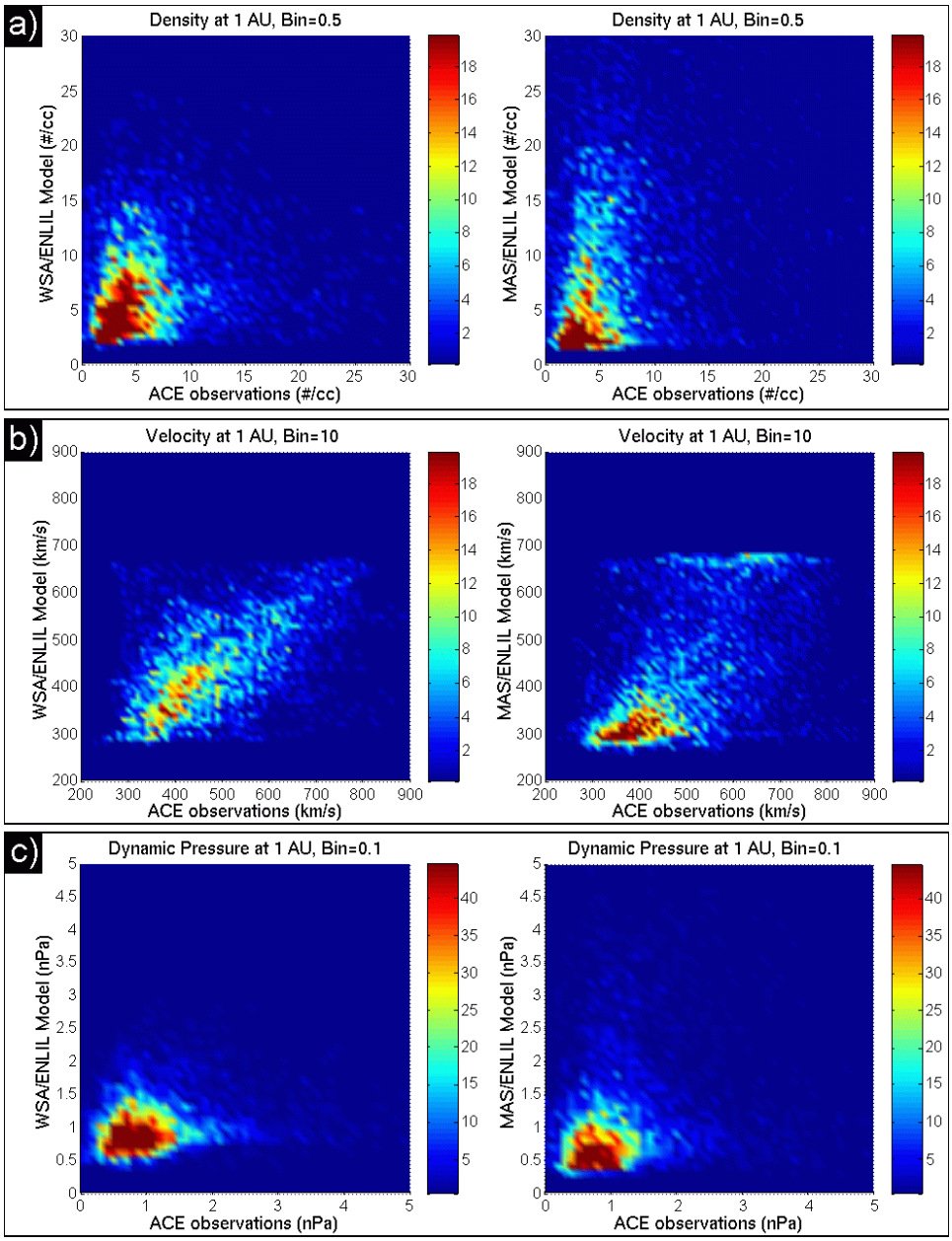

Figure 2.6: Distribution of occurrences of the ACE and model results for (a) density, (b) velocity, and (c) dynamic pressure. Color contours show statistics of the number of times a specific value is found in the models *versus* the ACE observations. The left column displays the results for ACE observations *versus* WSA/ENLIL results (x- and y-axes, respectively); the right column shows the results for ACE observations *versus* MAS/ENLIL results. The binning intervals are 0.5 cm^{-3}, 10 km s^{-1}, and 0.1 nPa for density, velocity, and dynamic pressure, respectively.

are generally comparable to the ACE observations.

To better evaluate how well the models compare to the observations, we produced contour diagrams where we plot the statistics of the model values versus the corresponding data, shown in Figure 2.6. For a perfect correlation, one expects a ridge with a straight spine along a slope corresponding to one. In constructing these contour plots, the ACE data have been averaged to the same time resolution as the CCMC simulation's effective time resolution (≈218 minutes). Figure 2.6a shows the contour plots for the occurrences of density values for the entire period analyzed. The maximum contours in the distribution of density values, shown in red, occur roughly within 10 cm^{-3} for both the WSA/ENLIL (Figure 2.6a, left) and MAS/ENLIL (Figure 2.6a, right) models *versus* ACE. The overall comparison of the velocity values between WSA/ENLIL and ACE is shown in Figure 2.6b (left). This distribution is almost 1:1, within the maximum contour. Note that the distribution is centralized around the average solar wind speed for both the model and the observations. For the MAS/ENLIL and ACE comparison (Figure 2.6b, right), the overall distribution looks less linear, where the distribution of occurrences is biased toward high values in the observations. Figure 2.6c shows that the dynamic pressure comparisons are the most similar for both models, where the maximum occurrence distributions of the dynamic pressure values are centralized around 0.4 nPa to 1.5 nPa.

As an illustration of the point-to-point model comparison with the observations, Figure 2.7 shows the observed densities compared to specific modeled values for the entire data set used here. For a computed range of 2–3 cm^{-3} (Figure 2.7a), there is a spread in the observed ACE values with a peak occurrence centered at the model range, implying that when the models compute these density values, ACE observes similar values most of the time. The spread of the values indicates that the models tend to underestimate the observed values more often than they overestimate them. For a computed range of 3–4 cm^{-3} (Figure 2.7b), the peak occurrence of the ACE values is less than the model range by ≈2 cm^{-3}, implying that the models overestimate the observed values most of the time. The amount of the overestimation by the models increases with density (see Figures 2.7c and 2.7d). When the models calculate densities of values greater than about 4 cm^{-3}, ACE observes lower values most of the time.

Figure 2.8a and 2.8b, which are similar to Figure 2.7 but for speeds, show that for the model ranges of 300–400 km s^{-1} and 400–500 km s^{-1} the peak occurrences of ACE observations have a very large amplitude and are centered around the respective model values. When the models give these velocity values, ACE observes

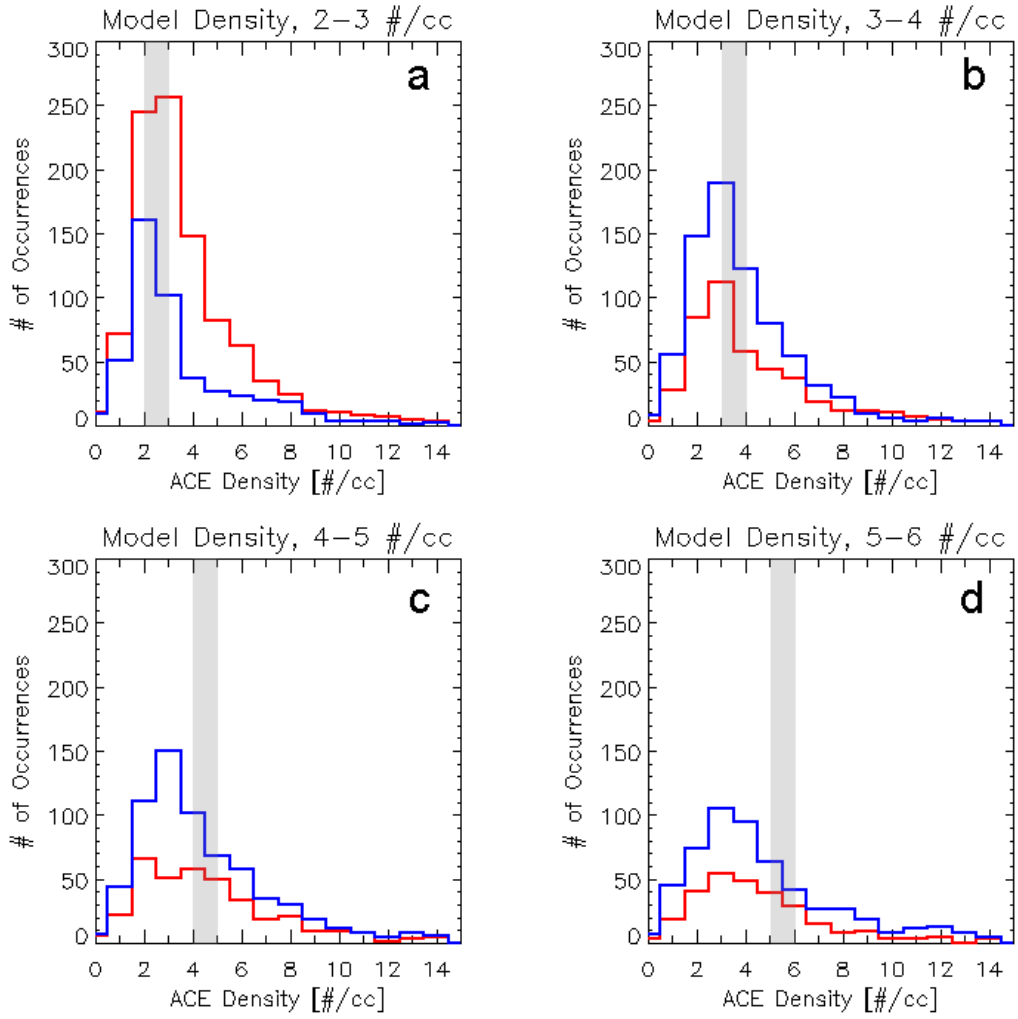

Figure 2.7: Histograms illustrating the accuracy of specific computed densities from the models compared to the observed values. The colors represent the ACE comparison with MAS/ENLIL density values (red) or from ACE comparison with WSA/ENLIL (blue), as shown in Figure 2.6a. Note that the gray bars indicate the model density range in question, where the width is one bin width. (a) For a computed range of 2–3 cm^{-3}, there is a spread in the ACE values with a peak occurrence distributed around the model range (indicated by the gray bar). (b) For a computed range of 3–4 cm^{-3}, the peak occurrence of the ACE values is systematically less than the model range by about 2 cm^{-3}. (c and d) As the computed densities increase, the amount of the density overestimation by the models increases, *i.e.*, the models often give densities of greater than $\approx$4 cm^{-3} than what ACE is observing.

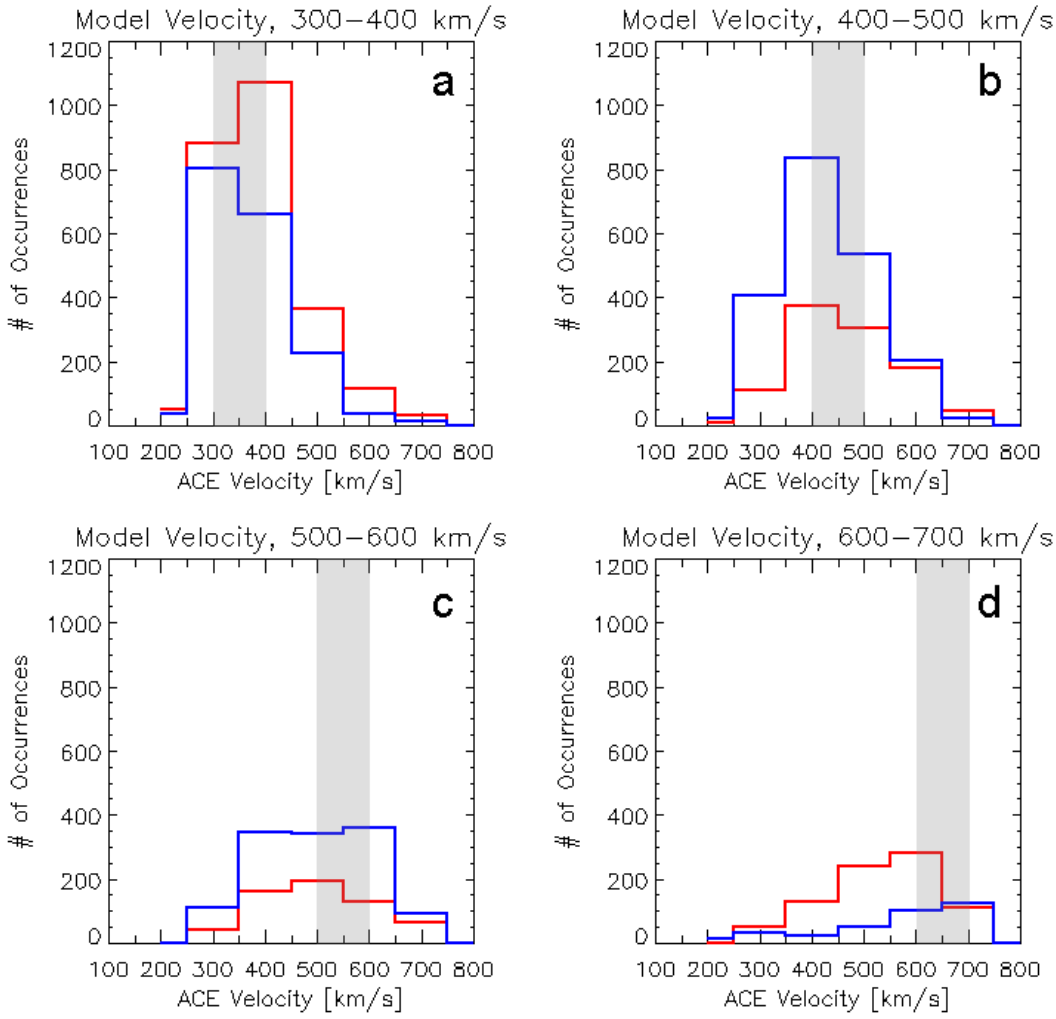

Figure 2.8: Similar to Figure 2.7, but for speeds. As before, red represents the MAS/ENLIL model results and blue for the WSA/ENLIL results. (a and b) For the computed ranges of 300–400 km s^{-1} and 400–500 km s^{-1}, the peak occurrences of the observed values are peaked around the respective model ranges, indicated by the gray bars. This implies that the models give velocities similar to what ACE observes, within $\approx \pm 100$ km s^{-1} most of the time. (c) For the computed range of 500–600 km s^{-1}, the observed distribution is relatively flat and broad, but the average value is roughly centered around values lower by $\approx$100 km s^{-1} than the model range. (d) At the largest model velocities shown, the observed speed distributions are much broader than in (a) and (b), but are centered around the model range.

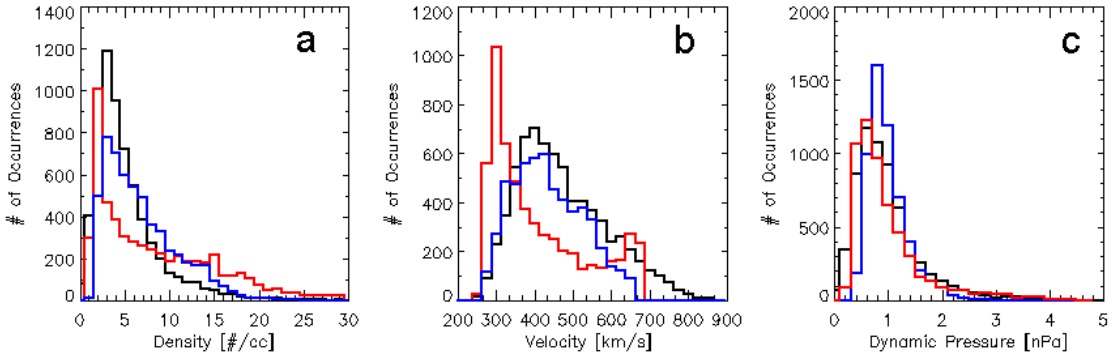

Figure 2.9: Histograms of the ACE and model results in Figure 2.6 for (a) density, (b) velocity, and (c) dynamic pressure. The ACE observations are shown in black, the MAS/ENLIL results in red, and the WSA/ENLIL results in blue.

similar velocities most of the time. This is not surprising because the models have generally been empirically tuned to reproduce commonly observed velocities. Figure 2.8c shows that for the computed higher speed range of 500–600 km s^{-1}, the amplitude of the peak occurrence is not as high, but the peak is centered around the model range. For the MAS/ENLIL-based comparison (shown in red) the peak distribution is not as high compared to the number of occurrences at the wings of the distribution, implying that a good amount of the time ACE is observing other values when the model computes values within 500–600 km s^{-1}. In addition, the width of the peak distribution for the WSA/ENLIL-comparison (shown in blue) is quite broad (three-bins-width across), implying that when the model gives these velocities, ACE observes values over a broad range, sometimes differing by 100s of km s^{-1}. Figure 2.8d shows that for the highest model velocities tested, the distributions of observations have a smaller amplitude peak than shown in Figures 2.8a and 2.8b, but it is centered around the model range.

Figure 2.9 shows another type of display illustrating the comparisons of model and observed values for the data shown in Figure 2.6. Figure 2.9a shows that the distribution of occurrences for density peaks around 4 cm^{-3} for the ACE observations (shown in black) and WSA/ENLIL model values (shown in blue), whereas the MAS/ENLIL model values (shown in red) have the maximum number of occurrences slightly less, around 2 cm^{-3}. Compared to the ACE and WSA/ENLIL results, the peak distribution is narrower for the MAS/ENLIL model results and has more occurrences above 15 cm^{-3}. Figure 2.9b shows the distribution of occurrences for velocity. For both the WSA/ENLIL model results and ACE observations,

the observed distribution is centered around the average solar wind speed. Notice that the WSA/ENLIL velocity values reach a maximum limit of roughly 675 km s^{-1}. This is due to an upper limit of velocity values imposed at the WSA/ENLIL model interface to avoid numerical problems that may arise from the model coupling. Figure 2.9b (red) shows that the MAS/ENLIL number distribution have two peaks instead of one. The primary distribution is centered around the velocity value of 300 km s^{-1}, whereas the secondary peak is centered around 675 km s^{-1}. The velocity values simulated by the MAS/ENLIL model approach a limit slightly higher than that for WSA/ENLIL (see also Figure 2.6b, right). Figure 2.9c shows that the dynamic pressure distributions are most similar in shape, as in Figure 2.6c. However, the peak values from the WSA/ENLIL results are higher by ≈30%. Note that a small contribution of high dynamic pressure values, 2 nPa to 4 nPa, can be seen in the model results and observations.

It is important to note that any transients from interplanetary CMEs (ICMEs) that may occur in this period of ACE observations have not been removed from the data. In general, the overestimations of the density values that we discussed earlier may be due to either an inadequate boundary condition on the density, or to the use of an approximate (polytropic) equation of state. Figures 2.6b and 2.9b show that the model velocity values often do not reach the highest velocity values observed by ACE, where the largest model velocity values do not exceed 700 km s^{-1}. In addition to what was stated earlier, the limit on the largest velocity values computed may also be due to the empirical formulae used in calculating the solar wind speed by the WSA and MAS coronal models, and/or partially due to the smoothing that occurs in the model, especially at the WSA/ENLIL and MAS/ENLIL interfaces. However, when we calculate the values for the solar-wind dynamic pressure, these systematic effects essentially cancel out and produce results that are generally comparable with the ACE observations (see Figure 2.5, bottom panels).

Figure 2.10 focuses on the comparison of the results between the WSA/ENLIL and MAS/ENLIL models. There are some subtle differences, caused by the differences between the WSA and MAS coronal models used for the inner boundary conditions of ENLIL. Figure 2.10 (top, left) shows that both models have the largest number of occurrences of density values that are ≤ 10 cm^{-3} (shown in red). However, for values ≥ 15 cm^{-3} the MAS/ENLIL results have more occurrences than WSA/ENLIL (shown in light blue). Figure 2.10 (middle, left) shows that these differences are more pronounced at the inner model boundary of 0.14 AU (≈30 $R_\odot$) than at 1 AU (see Figure 2.2). For the velocity values, Figure 2.10 (top, right) shows that the MAS/ENLIL velocities have more occurrences of low values (around

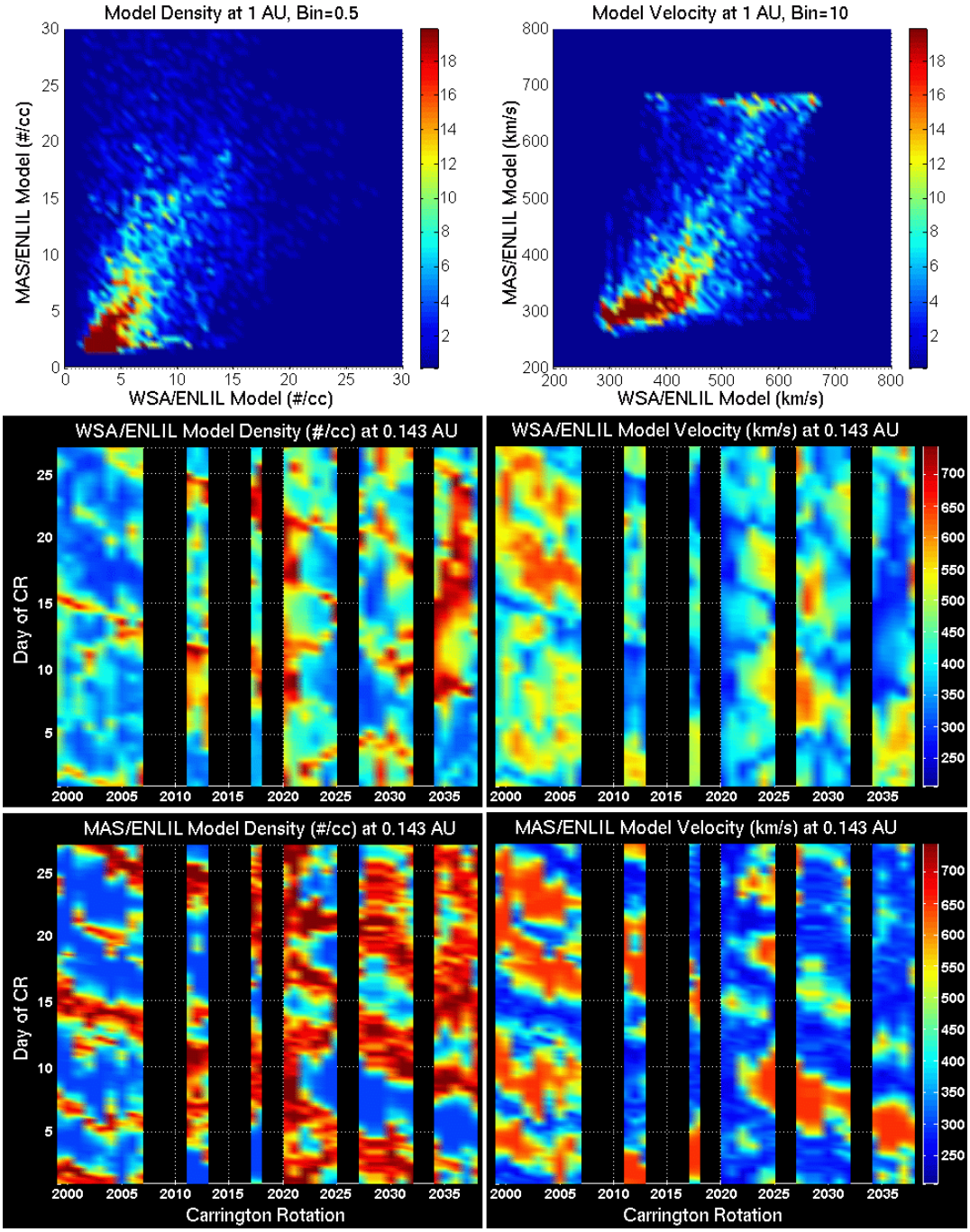

Figure 2.10: (top row) Distribution of the model density and velocity values at 1 AU. (middle, bottom rows) Model results in the format of Figure 2.2, but near the ENLIL inner boundary ($\sim$30 $R_\odot$, or 0.14 AU).

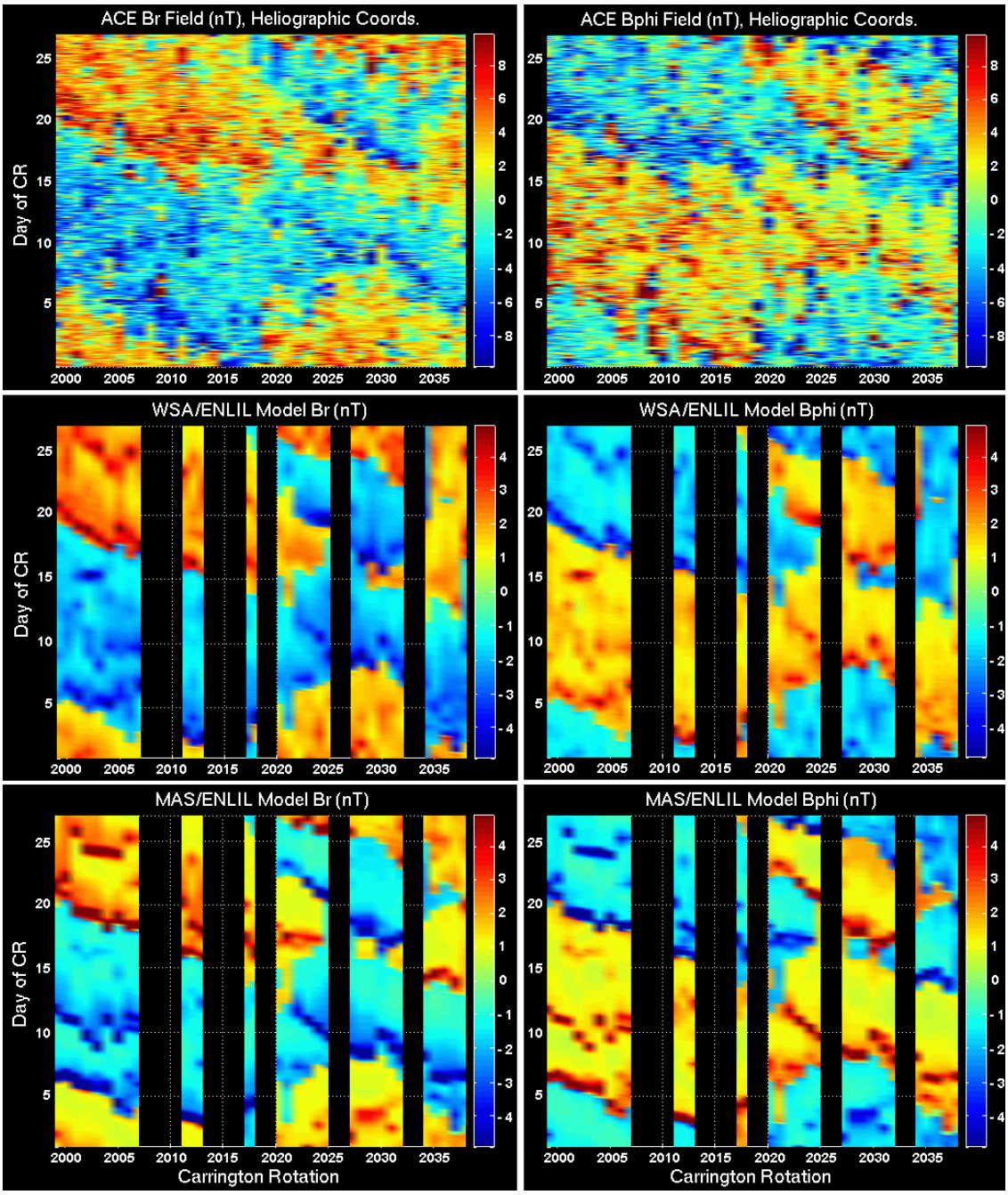

Figure 2.11: (left) Radial and (right) ϕ components of magnetic field at 1 AU in the model solar equatorial plane. The ACE magnetic field (top row) has been converted to the heliographic coordinate system of the ENLIL model. Note that the color scales shown for the WSA/ENLIL and MAS/ENLIL models (middle and bottom rows) are half as high as the ACE color scale.

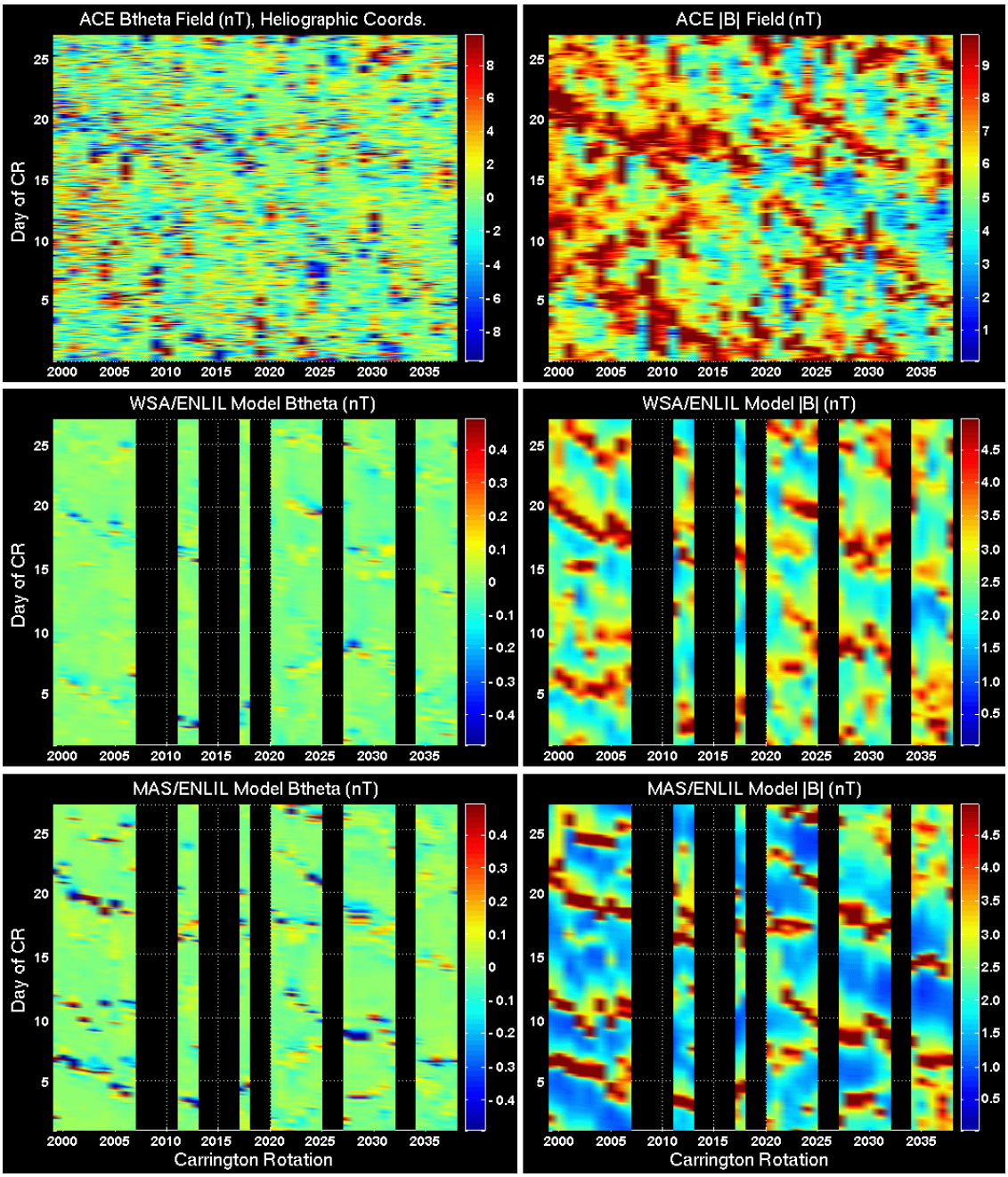

Figure 2.12: (left) θ component and (right) the total magnetic field at 1 AU. Shown are the ACE observations (top row) and the model results (middle and bottom rows). Note that the color range of the modeled theta component is less than the ACE color range by about one tenth, whereas for the total magnetic field the color range for the model figures is half as high.

300 km s^{-1}) and slightly larger occurrence of higher values (around 700 km s^{-1}), whereas the WSA/ENLIL results show more occurrences for the mid-range values (400–450 km s^{-1}). This can also be seen in Figure 2.10 (bottom, right) where the MAS/ENLIL results at 0.14 AU show the velocity occurring at values that are either high (red) or low (blue) but not as much in the middle range (cyan). Despite these subtle differences between the results generated from MAS/ENLIL and WSA/ENLIL, their overall comparisons with the ACE observations suggest they can be used for general analyses of solar wind origins and structure during the declining phase of the solar cycle.

Figure 2.11 shows the results for the modeled IMF for the radial and ϕ (East–West) components in comparison with the ACE observations. As mentioned in a previous section, the results are obtained at 0° latitude, the solar equatorial plane of the model. To make the comparison with the model results, the ACE magnetic-field data have been converted to the heliographic coordinate system of the ENLIL model. Referring to the ACE observations (Figure 2.11 top row), the positive (or negative) magnetic-field polarity is fairly uniform over many days in one CR before the field abruptly changes. Also, the two-sector structure that is seen at the beginning of this quiet solar period is stable over many rotations, until about CR 2020 when a four-sector structure is observed. This is also apparent in both the WSA/ENLIL and MAS/ENLIL model results. The models accurately generate the shapes and the number of the positive and negative sectors, and accurately reproduce the timing of when these structures occur, to within a few days of the observations. Note that the color scales shown for the model results differ from the ACE observations. The modeled magnetic field is underestimated by a factor of $\approx$2.

Figure 2.12 shows the results for the θ (North–South) component and the total magnetic field. Since the results shown are for the theta component of the magnetic field in the solar equatorial plane (Figure 2.12, left column), the values are mostly zero (green color). Occasionally, there are values of negative and positive magnetic field (blue and red, respectively) seen by ACE (Figure 2.12, top left). This occurs when the solar wind is deflected at the stream interaction regions (Gosling *et al.*, 1978; Gosling and Pizzo, 1999). Figure 2.13 shows a time series for CR 2013 (MAS/ENLIL), where the solar-wind deflection due to stream interactions (indicated by the arrows) is apparent in the velocity and magnetic fields components. Figure 2.12 shows that the models simulate these deflection features, but there are less of these features in comparison to the ACE observations. In addition, the overall magnitude of the modeled values are much more underestimated than ACE. For

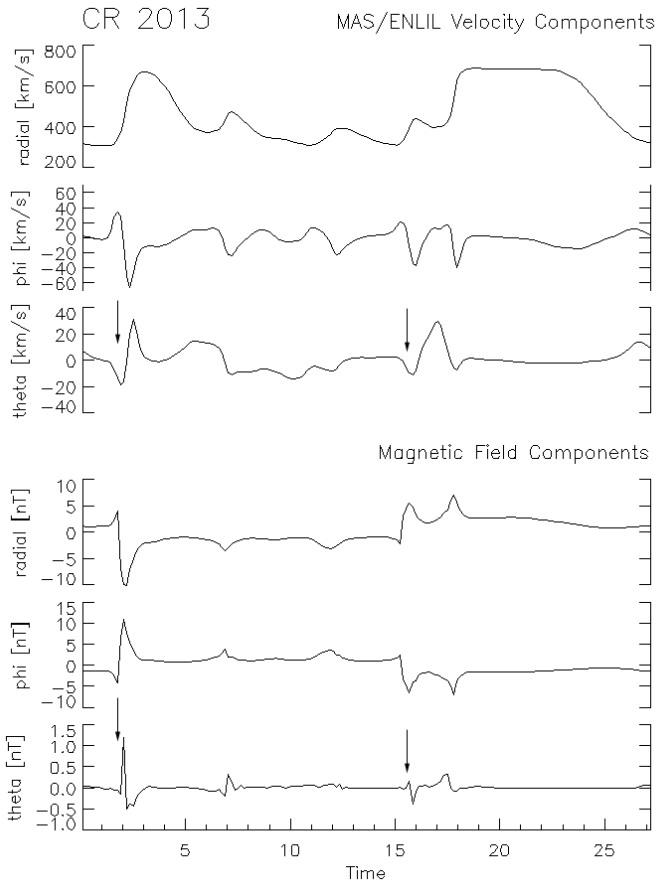

Figure 2.13: Deflection of the solar wind at stream interaction regions. Shown above is a time series plot for CR 2013 generated by the MAS/ENLIL model. The top (bottom) three panels show radial, ϕ, and θ component of solar wind velocity (magnetic field) components, respectively. The arrows indicate some of the deflection events for this particular Carrington Rotation.

the total magnetic field observed by ACE, Figure 2.12 (top right) reveals ridges of high magnetic fields (red) where the sector boundaries occur. The models reproduce these high field structures, where the timing and shape of the structures are comparable to those shown in the ACE results. However, the model values are underestimated compared to the observations, where the values are smaller by a factor of $\approx$2.

To better evaluate the comparison of the model values with those from the ACE observations, we plot the statistics similar to those shown in Figure 2.6. Figure 2.14a

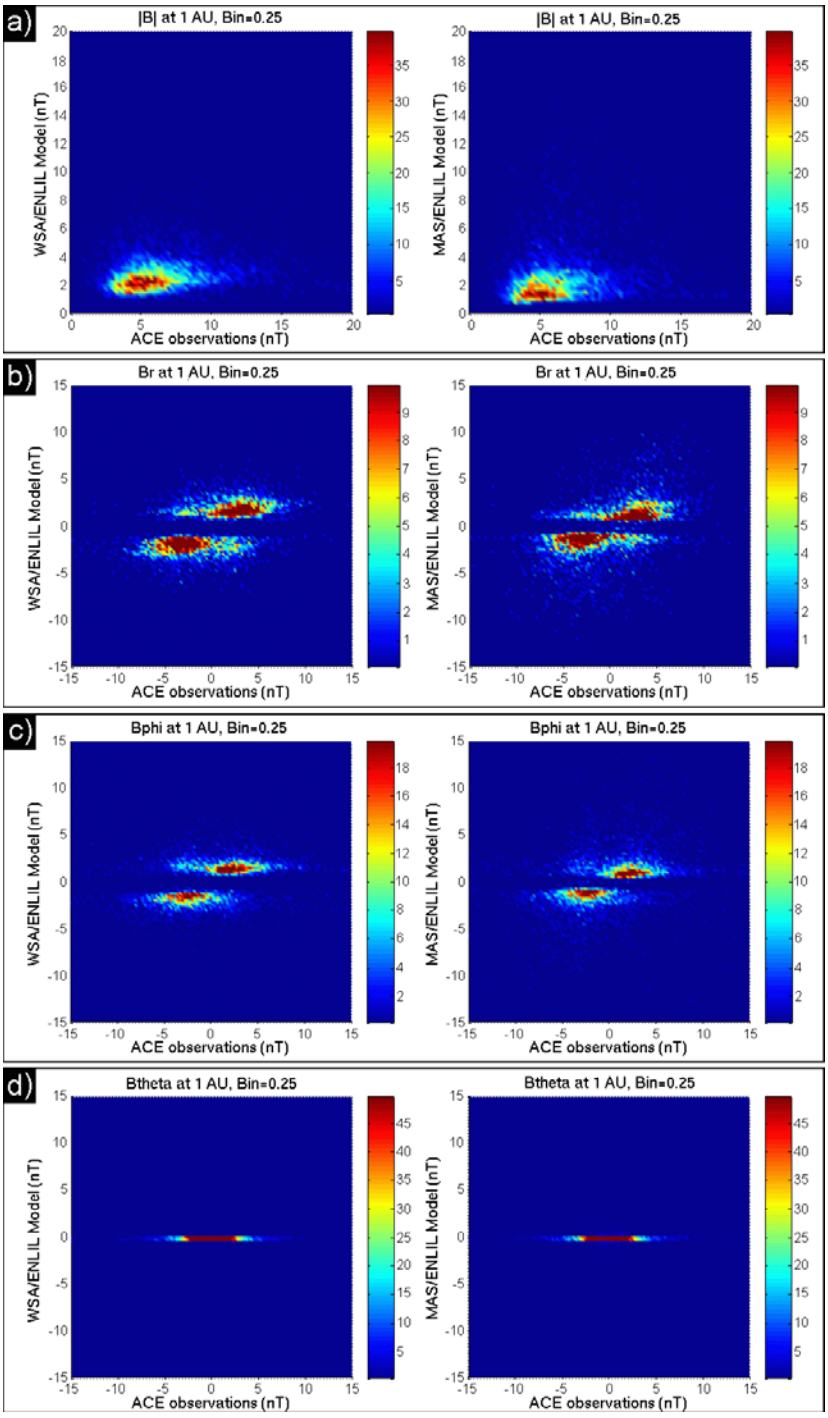

Figure 2.14: Color contours for (a) magnitude of the magnetic field, (b) radial B, (c) B_ϕ, and (d) B_θ components. The ACE data shown in Figures 2.11 and 2.12 have been averaged to the time resolution of the CCMC data (≈218 minutes). The binning interval is 0.25 nT.

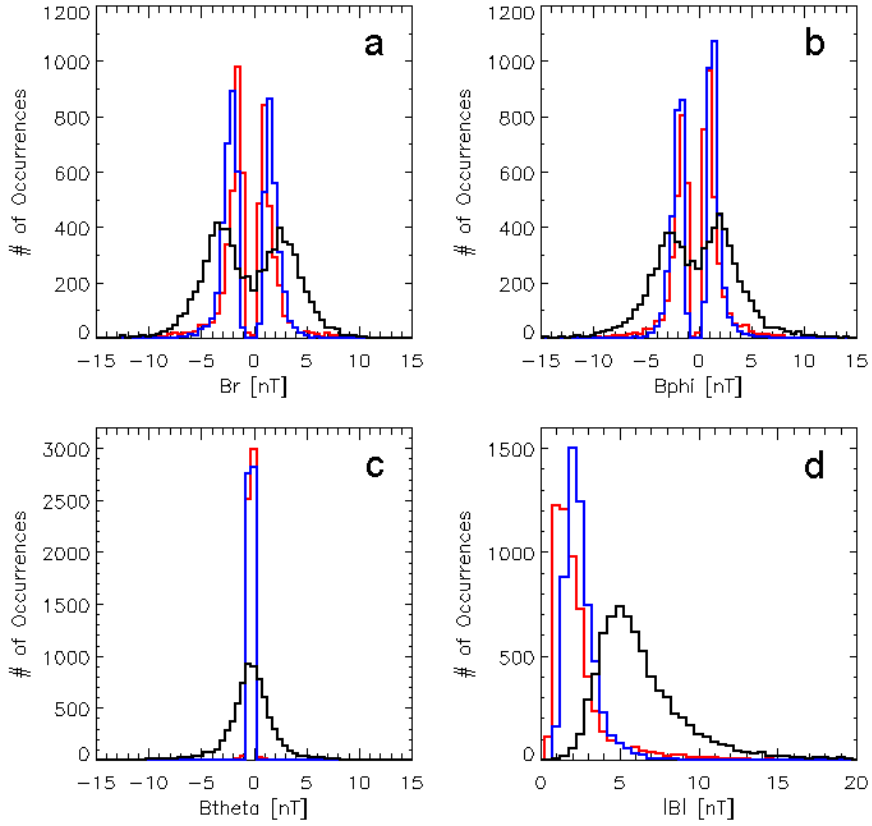

Figure 2.15: Histograms of the results shown in Figure 2.14 for (a) radial B, (b) B phi, (c) B theta, and (d) total magnetic field. The ACE observations are shown in black, the MAS/ENLIL results in red, and the WSA/ENLIL results in blue.

shows that the maximum contour in the distribution for the total magnetic field occurs roughly around 5 nT for the ACE observations, where the main distribution ranges from roughly 3 nT to 10 nT. The maximum contour for the model values occur at lower values, around 2 nT (1 nT) for the WSA/ENLIL (MAS/ENLIL) model, and the main distribution ranges from roughly 1 nT to 5 nT for both models. Figures 2.14b and 2.14c show that the maximum contours in the distribution of the radial and ϕ components of the magnetic field values for the ACE observations are centered around ± 4 nT, where the main distribution resides within ± 10 nT. For the same magnetic field components, both models produce values that are lower than the observations, where the maximum contours in the distribution are centered around ± 2 nT and the range of the main distribution are $\pm(1$ to 5) nT. Figure 2.14d shows the contours in the distribution of values for the theta component. The main

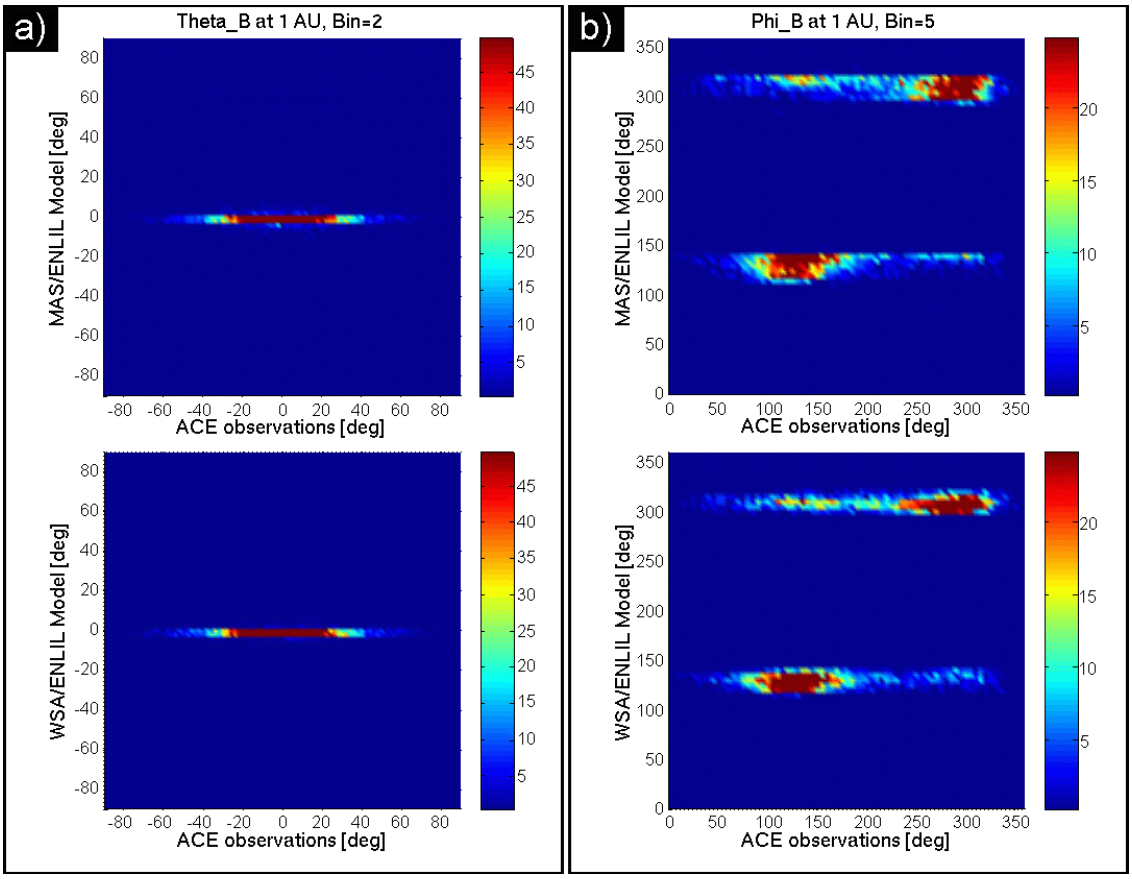

Figure 2.16: Color contour plots for (a) θ_B and (b) ϕ_B, the angles of the IMF relative to the Sun-Earth line observed in the solar ecliptic plane at 1 AU. (a) For the IMF component perpendicular to the solar ecliptic plane, θ_B, the peak of the distribution for both the observation and the models is centered around 0°. (b) For the Archimede's spiral direction of the IMF, ϕ_B, the peak of the distribution is centered around 135° (315°) for the IMF direction toward (away from) the Sun. Since the ACE data includes observations from active solar periods, there are θ_B and ϕ_B values that extend beyond the aforementioned central values for the maximum distributions.

distribution for the ACE observations are within ±10 nT, where the maximum contour is within ±5 nT. The distribution of the model values are significantly lower, where the range of values are within ±0.5 nT.

Figure 2.15 shows the distribution of occurrences for the magnetic-field results, similar to the results shown in Figure 2.9. Figures 2.15a and 2.15b show that for

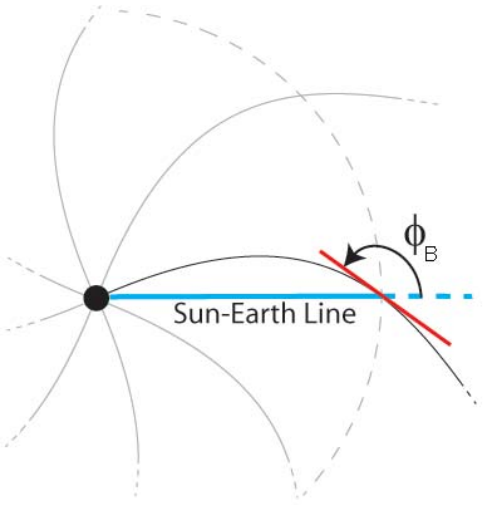

Figure 2.17: Illustration of how ϕ_B is defined in Figure 2.16, where the Sun–Earth line is 0°.

both the ACE radial and phi components of the magnetic field results (shown in black), respectively, a double-peak number distribution centered around ±4 nT can be seen. The majority of the observed values ranges from 0 nT to ±10 nT. The WSA/ENLIL (blue) and MAS/ENLIL (red) model values also have double-peak distributions, but compared to the observations the maxima are centered at lower values, around ±(1 to 2) nT, and the overall distributions have a narrower range of values, from ±(1 to 5) nT. For the θ component of the magnetic field, Figure 2.15c shows a single-peak distribution centered at 0 nT for the ACE values, where the range of the distribution is within ±5 nT for a large majority of the values. The peak number distribution for the model values are also centered at 0 nT, but the distribution is much narrower, ranging within ±0.5 nT. For the total magnetic field, Figure 2.15d shows the peak distribution for ACE is centered around 5 nT, where the majority of values range from 1 nT to 15 nT. For the models results, the peak distributions are centered at a lower value of around 2 nT and the ranges for the majority of the distribution are from (1 to 7) nT and (0.5 to 10) nT, respectively.

Figure 2.16 shows the angles of the IMF, θ_B and ϕ_B, relative to the Sun-Earth line observed in the solar ecliptic plane at 1 AU. The maximum contour in the distribution for θ_B, the IMF component perpendicular to the solar ecliptic plane, is centered around 0° for both the observations and the model results, as shown in Figure 2.16a. For the Archimedes spiral direction of the IMF, Phi_B, the peak

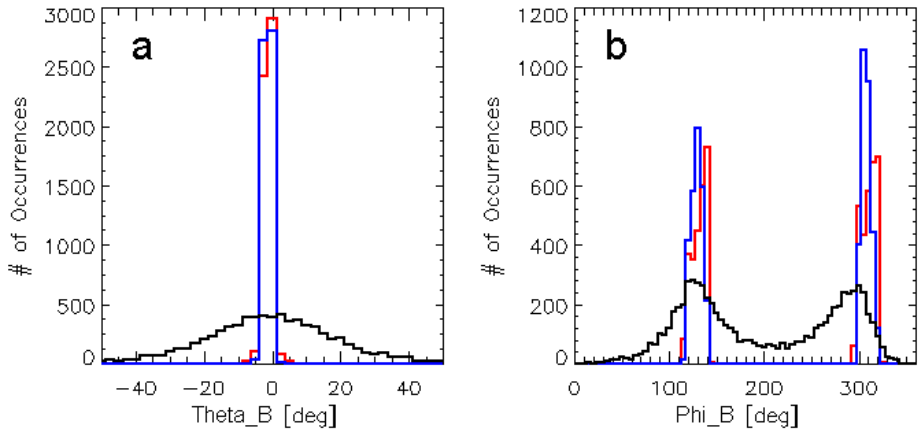

Figure 2.18: Histograms of the results shown in Figure 2.16 for (a) θ_B and (b) ϕ_B. The ACE observations are shown in black, MAS/ENLIL results in red, and WSA/ENLIL results in blue.

of the distribution is centered around 135° (315°) for the IMF direction toward (away from) the Sun, as shown in Figure 2.16b. These directions correspond to the nominal toward and away IMF along the 45° Parker Spiral field in the coordinate system used. An illustration to show how we define ϕ_B is provided in Figure 2.17. Since the ACE data include observations from active solar periods, there are θ_B and ϕ_B values that extend beyond the central values for the peak of the respective distributions. Figure 2.18 shows the distributions of occurrences for these results. Transient disturbances in the solar wind contribute to the wings of the observed distributions.

2.5 Summary and Discussion

The abundance of near-Earth spacecraft observations of the solar wind provides an opportunity to compare 3D numerical model results with the data and test their performance in simulating the ambient structure. In this study, we presented the model results for solar wind density, velocity and dynamic pressure, as well as the IMF components. The model results are generated by the MAS/ENLIL and WSA/ENLIL MHD models, both of which are available at the CCMC website for runs-on-request simulations. We compared the model results with the ACE SWEPAM and MAG observations for the declining phase of Solar Cycle 23, from CRs 1999 to 2038 (24 January 2003 to 18 January 2006). The results show that

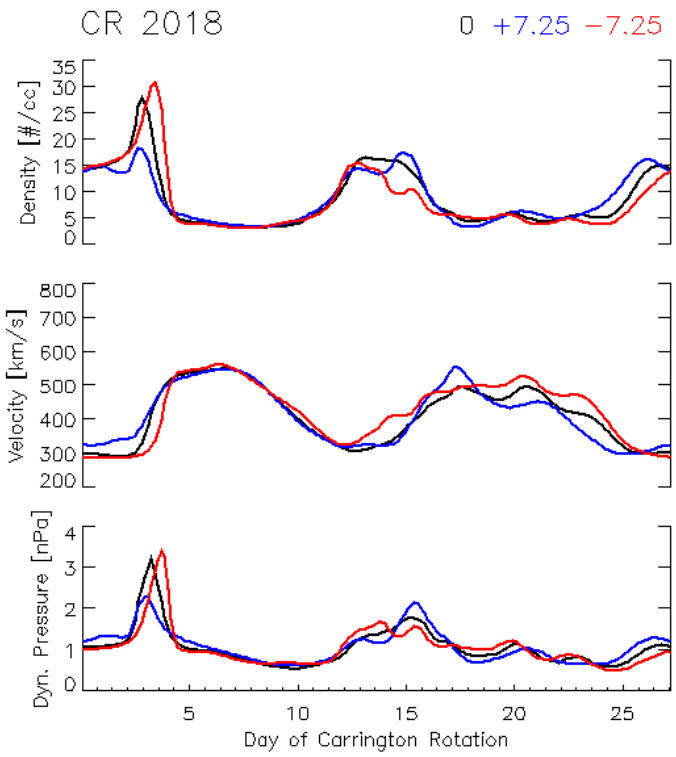

Figure 2.19: WSA/ENLIL model results for CR 2018 at different latitudes: (red) -7.25°, (black) 0°, and (blue) +7.25°, where the model solar equator is at 0°. The results show the typical range of values generated for the same CR but at the different latitudes. Although the magnitudes of the parameters typically vary within a few percent (sometimes up to a few tens percent), the overall shape and trend are very comparable.

there is a good agreement between the observations and the model results for the general large-scale solar wind structures.

At the time of the study, the option was not available at CCMC to obtain results calculated at Earth's location. The latitude of Earth with respect to the solar equatorial plane (0° latitude) resides within ±7.25° latitude, changing by 2.164° within one CR. Figure 2.19 illustrates the typical range of solar wind parameter values calculated for CR 2018 at ±7.25° and 0° latitudes. The magnitudes of the values do not necessarily differ by much, typically within a few percent as shown. For other CRs the differences can be as much as a few tens percent, but the major trends remain very comparable.

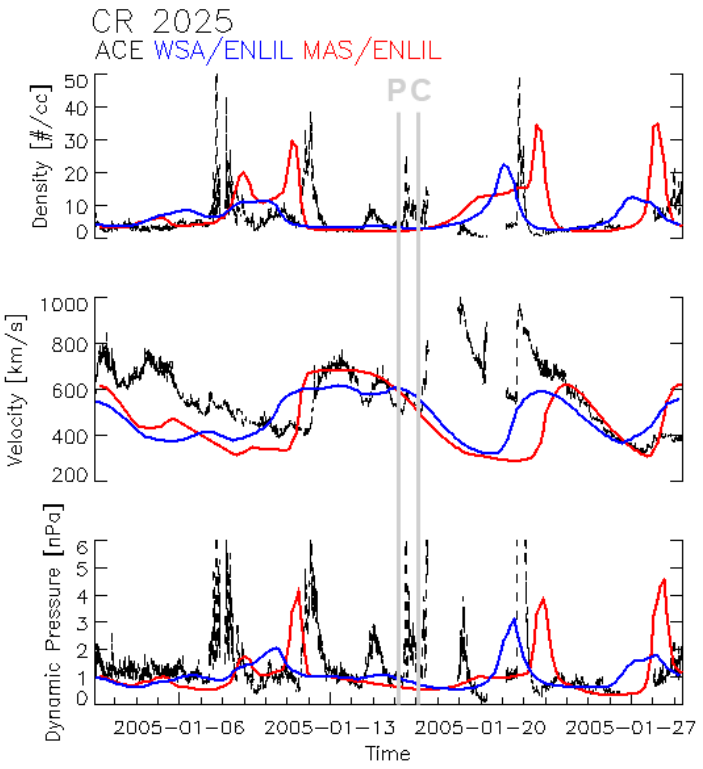

Figure 2.20: A series of very strong proton events and their associated CME events during CR 2025. The vertical gray solid lines mark one of proton (P) and CME events (C). As reported by the NOAA Space Environment Services Center (http://umbra.nascom.nasa.gov/SEP/seps.html), the >10 MeV proton event began on 16 January 2005 at 02:10 UT (marked by P) following a X2.6 flare event that occurred late on the 15th. The peak flux following this flare occurred on the 16th at 18:40 UT, in which the peak signature can be seen from the ACE densities (top panel). In comparison, the model densities are noticeably flat during this time. According to the CME list provided by LASCO at NRL (Large Angle and Spectrometric Coronagraph Experiment at the Naval Research Laboratory, see http://lasco-www.nrl.navy.mil/index.php?p=content/cmelist), four very large halo CME events occurred on 15 January 2005 at 06:30 UT and 23:06 UT, 17 January 2005 at 09:30 UT, and 20 January 20 2005 at 06:54 UT. The ACE spacecraft measured their speeds (marked by C, middle panel) a few days after the onset of the events while the model velocities do not provide any indications of these events.

Based on the results presented, the WSA/ENLIL and MAS/ENLIL models can be used as tools to analyze, and to some extent forecast, the solar wind structure for quiet solar periods and prior to solar wind disturbances. It is important to note that any disturbances triggered by ICMEs during our period of interest have not been removed from the data and will thus influence the comparison with the models results. As such, we find that the models did not capture a number of the density or velocity peaks that were probably caused by solar activity. For example, the models did not simulate the density peaks between 15 to 18 January 2005 of CR 2025 (Figure 2.20). These peak densities were produced by a CME and/or shock associated with active region (AR) 10720. For the same solar storm, the models also did not simulate the high velocities observed by ACE that resulted from the halo CME events that began on 15 January 2005. It remains a challenge to model the heliosphere for active solar conditions, but there are ongoing efforts within the modeling community to develop and test numerical codes that will model heliospheric disturbances caused by solar transients. In particular, the cone model of CMEs, developed by Zhao, Plunkett, and Liu (2002) to explain coronagraph signatures of halo CMEs geometrically, is used to initiate disturbances in the solar wind simulation described here (*e.g.,* Odstrcil, Riley, and Zhao, 2004; Odstrcil, Pizzo, and Arge, 2005).

These models can be used to infer the solar wind sources. We examine the coronal sources of the solar wind for our period of study using the WSA coronal model. Figure 2.21 generated at CCMC shows examples of the calculated open coronal field footpoints or coronal holes and the related photospheric field data for CRs 2013 and 2027 during the two- and four-sector HCS period, respectively. The top panel shows the calculated global coronal field polarity at 21.5 $R_{\odot}$, the second panel shows the observed radial photospheric field from NSO, the third panel shows the predicted solar wind speed at 21.5 $R_{\odot}$, based on the empirical formula discussed in Section 2, and the bottom panel shows the predicted foot points of the open field lines at the photosphere (i.e., the coronal holes). For CRs that occur during the two-sector period of the HCS, the open sources on the corona typically originate from the low- and mid-latitude regions (less than $\approx 50^{\circ}$), shown in Figure 2.21 (left). For the four-sector period, the open sources predominantly come from both low- and mid-latitudes regions, but they also occasionally come from the edges of the polar coronal holes, shown in Figure 2.21 (right). For both cases, the low-latitude sources are often well-isolated. Overall, what we find is consistent with the observations of Luhmann *et al.* (2002) for the declining phase of the solar cycle, in which the sources of the solar wind in the heliosphere include contributions from polar regions

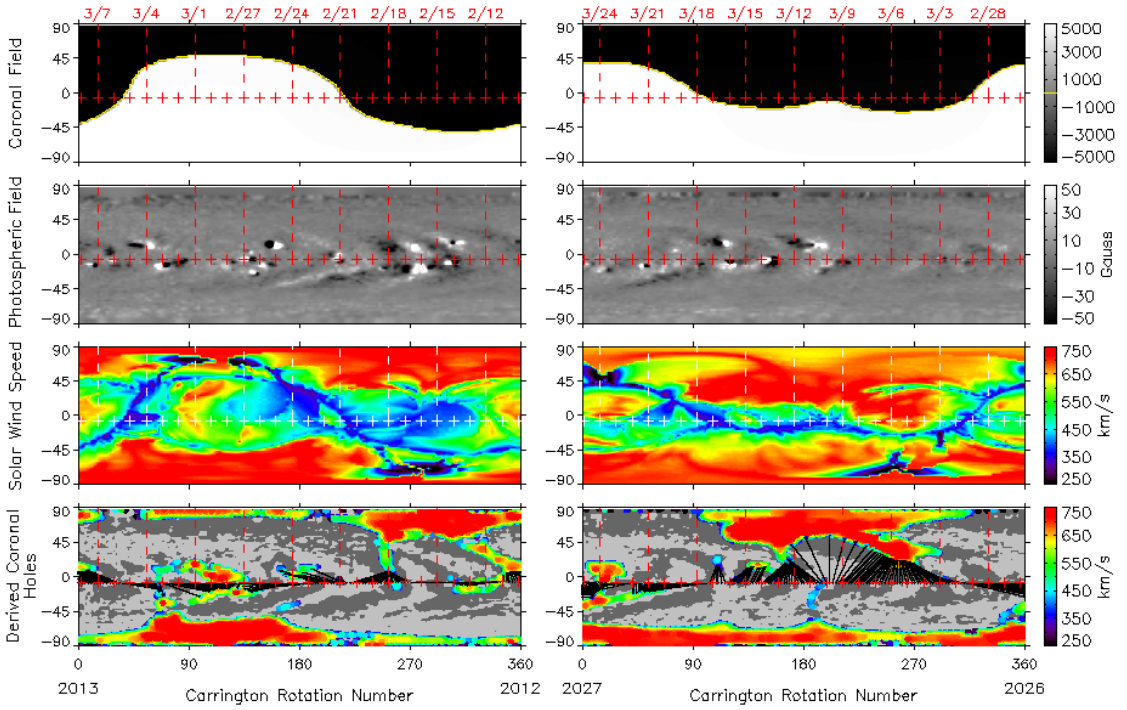

Figure 2.21: The coronal sources for CRs 2013 (left) and 2027 (right) using the WSA coronal model at CCMC: (top panels) The calculated global coronal field polarity at 21.5 $R_\odot$, where the yellow solid line indicates the current sheet. (second panels) The observed radial photospheric field from NSO. (third panels) The predicted solar-wind speed at 21.5 $R_\odot$. (bottom panels) The calculated footpoints (colored dots) of the open field lines at the photosphere (*i.e.*, coronal holes). The different colors indicate the solar wind speed (at $21R_\odot$) associated with the flux tubes, whereas the solid black lines connect between the outer coronal boundary at 21.5 $R_\odot$ and the source regions of the solar wind at the photosphere. For all panels, the + symbol indicate the daily position of the sub-Earth point on the Sun, which varies between $\pm 7.25°$ in solar latitude due to the inclination of solar rotation axis with respect to the ecliptic plane. Note that the newest (oldest) data are located on the left side (right side).

as well as from the more active low-to-mid-latitude regions. Although the results shown for the calculated coronal holes are generated by the WSA coronal model, they can be generalized to the MAS coronal model since Riley *et al.* (2006) showed that the MAS and PFSS models generate very similar results.

In the meantime, guided by comparison studies such as those presented in

this paper, numerical modelers can make improvements to their models. As stated previously, model velocity values from both MAS/ENLIL and WSA/ENLIL were often underestimated compared to ACE, which may be due to the empirical formulae used in calculating the solar wind speeds. Currently, improvements are being made to the formula in the WSA-coronal model (Arge *et al.*, 2004) by McGregor *et al.* (2006). For the model densities, the values are often overestimated either due to inadequate coronal model (MAS, WSA) boundary conditions on the density or to the use of an approximate (polytropic) equation of state. Improvements to the MAS coronal model to address these issues are underway (J. Linker, personal communication, 2006). Modelers are also working to improve the model magnetic field values, which were underestimated by a factor of ≈2. One way to do so is using magnetograms from different observatories that can be reliably inter-calibrated such that there is a higher level of confidence in their absolute field strengths rather than their relative values. Also, having a better sense for the polar field strengths relative to the equatorial values can help to improve the model magnetic field values. In addition, using time-dependent boundary conditions such that even for the ambient solution, time-varying magnetograms would be supplied to the model, would improve the model field values. Plans to improve the ENLIL solar-wind model are underway as well. Moreover, CCMC will provide model results computed at Earth's location such that direct comparisons can be made using near-Earth spacecraft data such as ACE.

To provide additional feedback to the modelers, we will conduct similar studies using multipoint spacecraft observations from both ACE and the recently launched *Solar TERrEstrial Observatory* (STEREO) (Kaiser, 2005) twin spacecraft. The relevant data sets from this mission will become openly available on the World Wide Web later in 2008. In addition, we will also test the models for their performance in simulating the solar wind at radial distances other than 1 AU. Spacecraft observations from missions such as the historical Helios 1 and 2 mission (Kunow *et al.*, 1977; Mariani *et al.*, 1978; Burlaga *et al.*, 1978), which observed the solar-wind structure at radial distances of 0.3 AU to 1 AU, and the *Pioneer Venus Orbiter* (Colin, 1980) can provide data sets for studying the ability of the model to describe the solar wind at the orbits of Mercury and Venus. More recent observations from the Mercury MESSENGER mission (Solomon *et al.*, 2001) can also be utilized once they become available. Finally, we note that our studies are complementary to other ongoing efforts of the Center for Integrated Space Weather Modeling (CISM) group (Luhmann *et al.*, 2004) to formally validate these models (Owens *et al.*, 2008) and assess their predictive capabilities.

Chapter 3

Effects of the Weak Polar Fields of Solar Cycle 23: Investigation Using OMNI for the STEREO Mission Period

Abstract

The current solar cycle minimum seems to have unusual properties that appear to be related to weak solar polar magnetic fields. We investigate signatures of this unusual polar field in the ecliptic near–Earth interplanetary magnetic field (IMF) for the STEREO period of observations. Using the multi-source 1 AU data set called OMNI, we find that for the current solar cycle declining phase to minimum period the peak of the distribution for the values of the ecliptic IMF magnitude is lower compared to a similar phase of the previous solar cycle. We investigate the sources of these weak fields. Our results suggest that they are related to the solar wind stream structure, which is enhanced by the weak polar fields. The direct role of the solar field is therefore complicated by this effect, which redistributes the solar magnetic flux at 1 AU nonuniformly at low–to–mid heliolatitudes.

3.1 Introduction

The recent Solar Cycle 23 deep solar minimum period appears to be unlike previous ones since the dawn of the Space Age. The Sun, which has been spotless for over 200 days in the year 2008, has weaker polar magnetic fields. The solar polar field values observed using ground–based magnetographs are half their previous solar minimum values (see Figure 3.1). This results in changes in the interplanetary medium. Measurements from the Ulysses spacecraft (Balogh *et al.*, 1992; Bame *et al.*, 1992) fast–latitude scans reveal that the average radial magnetic field values observed during the current minimum period are only about two–thirds of their values measured during the previous minimum period (Smith and Balogh, 2008). The related Ulysses plasma measurements reveal that the solar wind emanating

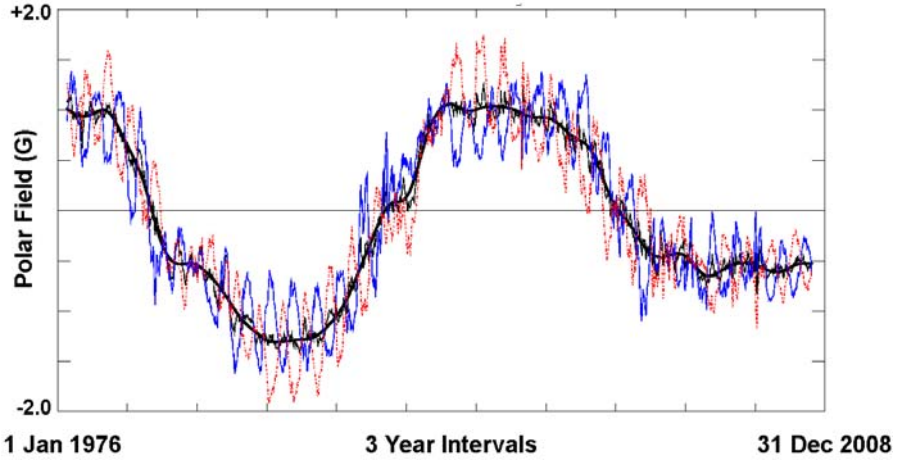

Figure 3.1: Solar polar field strength *versus* time. The figure is adapted from the original that is shown at the Stanford Wilcox Observatory website (http://wso.stanford.edu/gifs/Polar.gif). Blue (red) line represents the field strength observed in the north (south), the thin (thick) black line represents the average (smoothed average). Note that the calibration of the y-axis is not very reliable since the measurements are obtained from the poleward bins of the magnetograph (see Svalgaard, Duvall, and Scherrer, 1978, for a discussion). Nevertheless, the overall trend is shown very well.

from the large polar coronal holes is slightly slower, significantly less dense and cooler, with less mass and momentum flux than previous solar minimum values (McComas *et al.*, 2008; Issautier *et al.*, 2008).

In this study we examine the near–ecliptic solar wind and IMF at 1 AU for differences, if any, that exist as a direct result of the weaker solar polar fields of this cycle. We now know much more about the solar wind in terms of its different source regions. In particular, 3D models based on synoptic maps of the solar magnetic fields (*e.g.,* Riley, Linker, and Mikic, 2001; Arge and Pizzo, 2000) have allowed us to realistically map those sources into interplanetary space for solar minimum conditions. Previous model results have shown us that the ecliptic solar wind has a complicated mixture of open field source regions consisting of polar coronal holes, low latitude coronal holes, and polar coronal hole extensions (*e.g.,* Luhmann *et al.*, 2002). Luhmann *et al.* (2009) discuss the way in which weaker polar fields can lead to more prominent low–to–mid latitude coronal holes and therefore stronger high speed wind streams. The results presented in this study are of particular interest for terrestrial space weather as well as the interpretation of observations from the

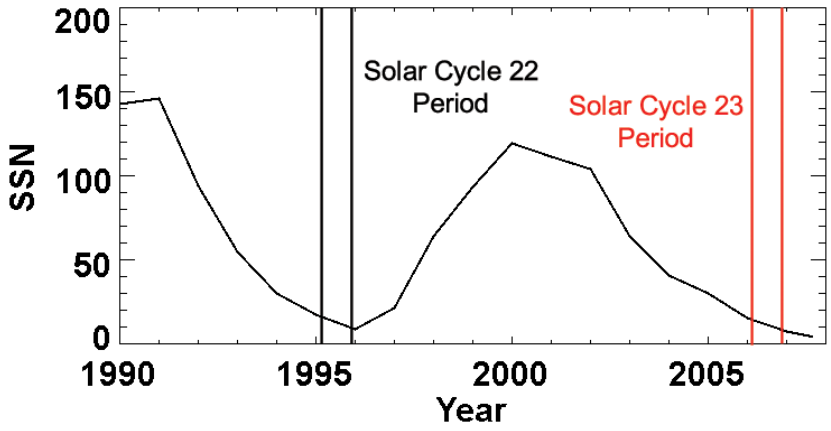

Figure 3.2: Sunspot number (SSN) for the periods of interest. The black bars indicate the period in SC 22 for 23 February to November 22 1995. The red bars indicate the period in SC 23 for 4 February to 4 November 2007.

Solar TERrEstrial Observatory (STEREO) mission (*cf.* Kaiser 2005).

The focus of our study is on the STEREO mission period. However, we use the OMNI solar wind plasma and magnetic field data to compare with a similar phase of the previous solar cycle. The OMNI hourly resolution data sets, obtained from the NASA Goddard Space Flight Center OMNIWeb website (http://omniweb.gsfc.nasa.gov/), have been normalized to 1 AU and have been transformed to the RTN (radial, tangential, and normal) coordinate system. The period of observations analyzed corresponds to the heliocentric phase of the STEREO twin spacecraft.

At the time of this study, the available STEREO data ranged from 14 February to 31 October 2007 for STEREO–A and from 1 March to 31 October 2007 for STEREO–B. These time periods fall within ten Carrington Rotations (CRs), 2053 – 2062 (4 February 2007 to 4 November 2007) of the Solar Cycle 23 (hereafter, SC 23) late declining to solar minimum phase. We thus select the OMNI data for this time range as well as from the previous cycle, SC 22 (CRs 1893 – 1902, 23 February to 22 November 1995), when the solar cycle phase is similar and the data coverage is comparable (see Figure 5.14).

3.2 Observations: IMF at 1 AU

Figure 3.3a shows a histogram of density observed at 1 AU during SC 22 (black) and 23 (red). These histograms have been normalized by the total number of measurements so that they are directly comparable. The peak occurrence for the SC 22

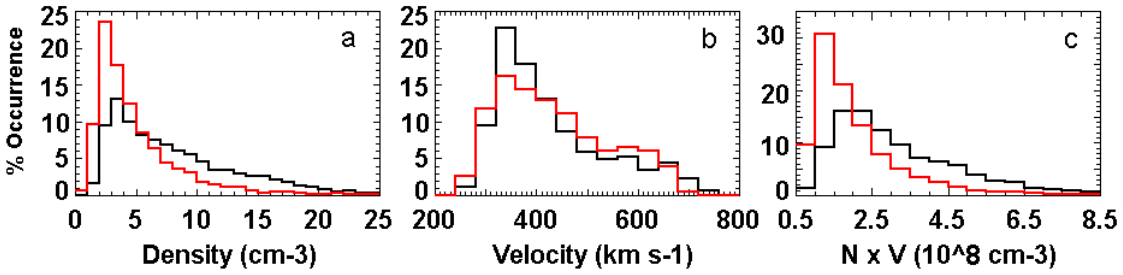

Figure 3.3: Histogram of occurrence at 1 AU for a solar minimum period spanning ten Carrington Rotations (see text for specific CR ranges). The colors represent data from SC 23 (red) and SC 22 (black). Shown are histograms for (a) density, (b) velocity, and (c) momentum flux, N×V.

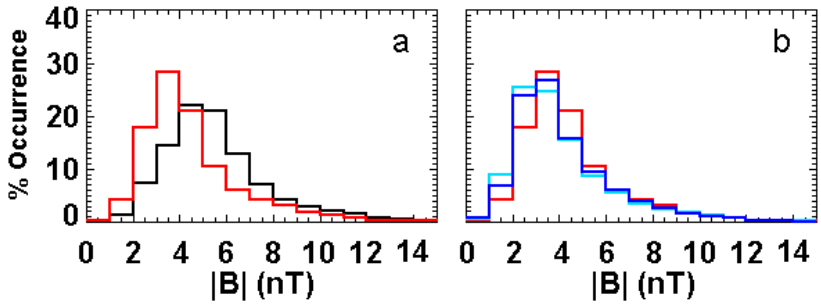

Figure 3.4: (a) Histogram of occurrence for the magnetic field magnitude observed over ten CRs during SC 22 (black) and 23 (red). (b) Similar histogram is shown for STEREO–A (dark blue) and STEREO–B (light blue) observations overplotted with SC 23 (red).

period is centered at 3.5 cm^{-3}. For the SC 23 period, the distribution is noticeably shifted toward lower values by about 30%, with the peak of the distribution centered at 2.5 cm^{-3}. The overall density distribution for the SC 23 period is narrower and has a percent occurrence that is much larger for values below 5 cm^{-3}. Notice that above 6 cm^{-3}, the SC 22 distribution has a larger percent occurrence.

Figure 3.3b shows a similar histogram but for velocity. Both the SC 22 and 23 velocity distributions have peak values occurring around 340 km s^{-1}. Notice that for SC 22 the percent occurrence of this peak distribution is 40% greater than that for SC 23. For both periods a high–speed tail distribution can be seen centered near 580 km s^{-1}, although the percent occurrence is slightly larger for SC 23. Figure 3.3c shows the momentum flux (N×V) for the two solar cycle periods.

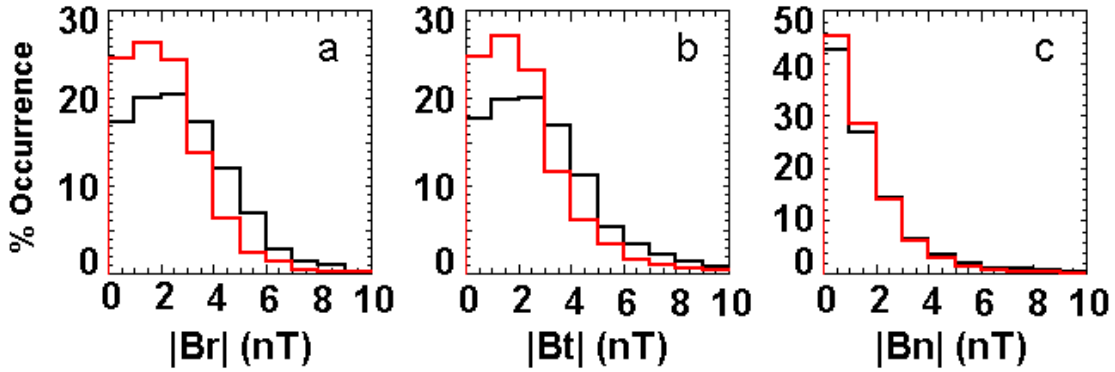

Figure 3.5: Histogram of occurrence for the absolute values of the (a) radial (R), (b) tangential (T), and (c) normal (N) magnetic field components observed over ten CRs during SC 22 (black) and 23 (red).

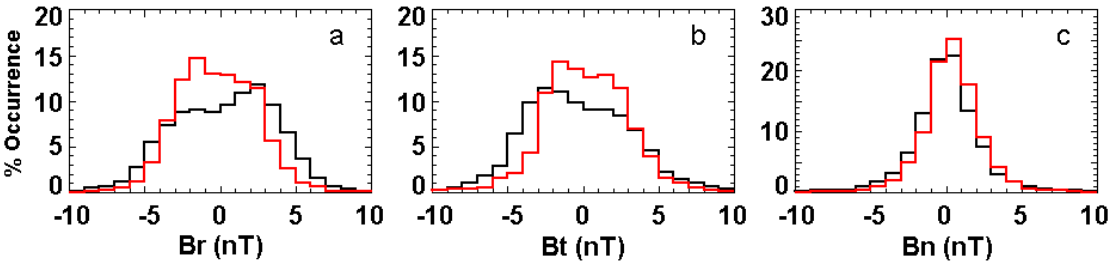

Figure 3.6: Histogram of occurrence for the (a) radial (R), (b) tangential (T), and (c) normal (N) magnetic field components observed over ten CRs during SC 22 (black) and 23 (red).

For SC 23, the peak occurrence occurs around 1.25 $cm^{-2}s^{-1}$, which is about 38% less than the peak value for the SC 22 period (2 $cm^{-2}s^{-1}$). Note that the decrease in the momentum flux during SC 23 is controlled by the density (see Figure 3.3a). This lower momentum flux is consistent with recent findings by McComas *et al.* (2008) using Ulysses data from high heliolatitudes, although as will be discussed below, the source(s) differ.

Figure 3.4a shows a histogram of the magnetic field magnitude. There is an overall shift toward lower values in the distribution of the field magnitude during SC 23 in comparison with SC 22. The peak of the distribution for the SC 23 period is centered at 3.5 nT, which is 30% less than 5 nT, the approximate central value for the peak of the SC 22 distribution. Figure 3.4b shows a comparison of the OMNI SC 23 observations with the 10–minute resolution STEREO–A and

–B magnetometer data (Acuña *et al.*, 2008) obtained from the STEREO *in situ* data website (http://www-ssc.igpp.ucla.edu/ssc/stereo) hosted by the Institute of Geophysics and Planetary Physics at the University of California, Los Angeles (*e.g.,* Luhmann *et al.*, 2008). The STEREO observations exhibit the same lower field distribution as the OMNI data.

To illustrate how the individual IMF components are contributing to the overall lower field magnitude during this current solar minimum period, we plot histograms of the standard RTN components. Figure 3.5a shows the histogram for the absolute values of the radial field. The SC 23 distribution is shifted toward lower field values, with the peak occurrence centered at 1.5 nT. The SC 22 distribution is slightly broader and has the peak occurrence centered at 2.5 nT. For the SC 23 period, radial field values that are $\leq$ 3 nT occur more often, by $\approx$25%, than during the SC 22 period. Figure 3.5b shows a similar histogram, but for the absolute values of the tangential field. The features shown are very similar to what was described previously for the radial fields in Figure 3.5a. Figure 3.5c shows the histogram for the absolute values of the normal field. In this case, the distributions for SC 22 and 23 share a similar trend and overlap with one another.

Figure 3.6 shows histograms of the same data as in Figure 3.5 but with sign information preserved. The asymmetry around zero of the radial (Figure 3.6a) and tangential (Figure 3.6b) components for the SC 23 period is an indication of the recently observed unbalanced ecliptic plane magnetic field polarity. Such unbalanced field polarities are observed quite commonly (*e.g.,* Hiltula and Mursula, 2006) and can be envisioned as a signature of greater heliospheric divergence of a particular sign of the coronal open fields. Figure 3.6a shows that the asymmetry in the distribution of the radial field values switched between SC 22 and 23. When the fields switched polarity between the two solar cycles, the heliospheric current sheet maintained its southward cone–shape, that is, the solar ballerina remained 'bashful' (see Hiltula and Mursula, 2006, for a discussion).

3.3 Association of low IMF with the stream structure

Since stream structures are prominent during the solar minimum phase, we investigate how they differ during the two solar minimum periods described in this paper, and consider the role(s) of their solar sources. Figure 3.7 shows the time series for velocity, density, and field magnitude observed during the SC 23 period. One can see that the high–speed streams (top panel) and their related high–density ridges (middle panel) are common and well–formed for this period. The red data points are data that have been filtered for field magnitudes $\leq$ 4 nT (bottom panel).

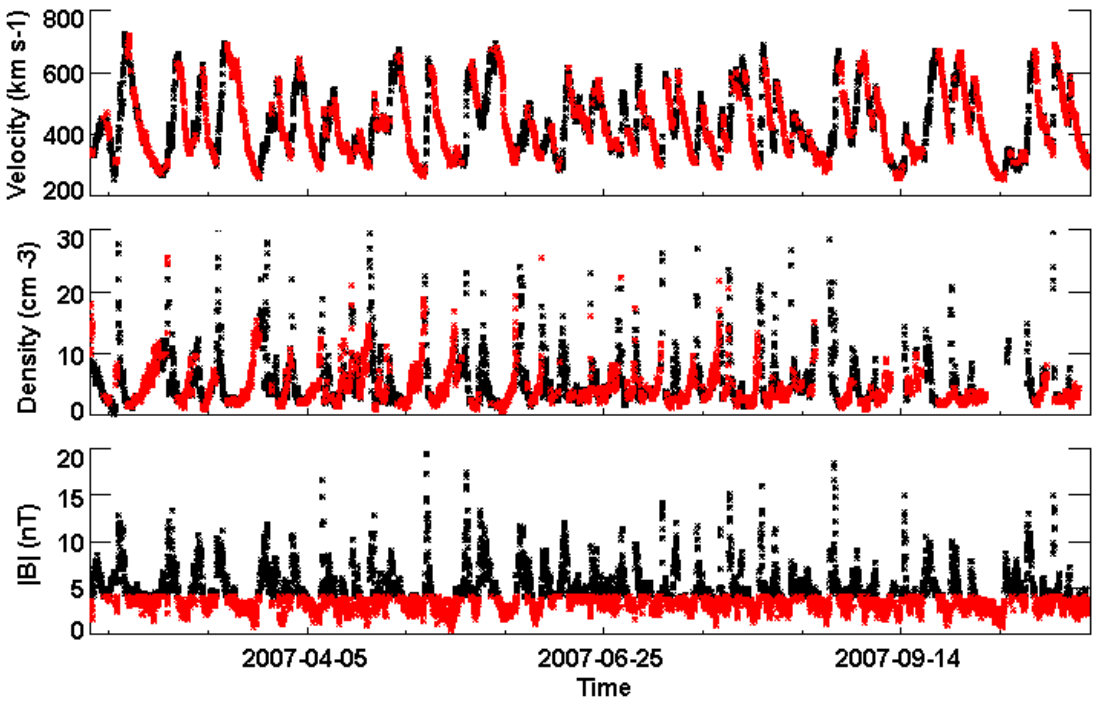

Figure 3.7: (top to bottom) Time series of the velocity, density, and field magnitude for the Solar Cycle 23 time period shown in Figures 3.3 and 3.4. The red values are data filtered for field magnitude values that are $\leq$ 4 nT.

The filtered data periods are then plotted over the entire data set including the density and velocity data. There is a clear association of the low field magnitudes with the trailing part of the high–speed streams, where the rarefaction regions occur behind the related compression ridges. The association with the rise of the high–density ridges is also very pronounced.

Figure 3.8 shows a similar set of time series for the SC 22 period. In comparison with the SC 23 period shown in Figure 3.7, the top panel of Figure 3.8 shows that there are generally fewer high–speed streams during SC 22. As before, the red dots correspond to data that have been filtered for field magnitudes $\leq$ 4 nT. The association of field magnitudes that are $\leq$ 4 nT with the trailing part of the high–speed streams is not as clean when compared to the current cycle (Figure 3.7, top panel). However, if we include data filtered for field magnitudes between 4 nT and 5 nT (shown in blue), the quality of the association is similar to what is shown for SC 23.

To examine in more detail the correlation between the velocity structures and

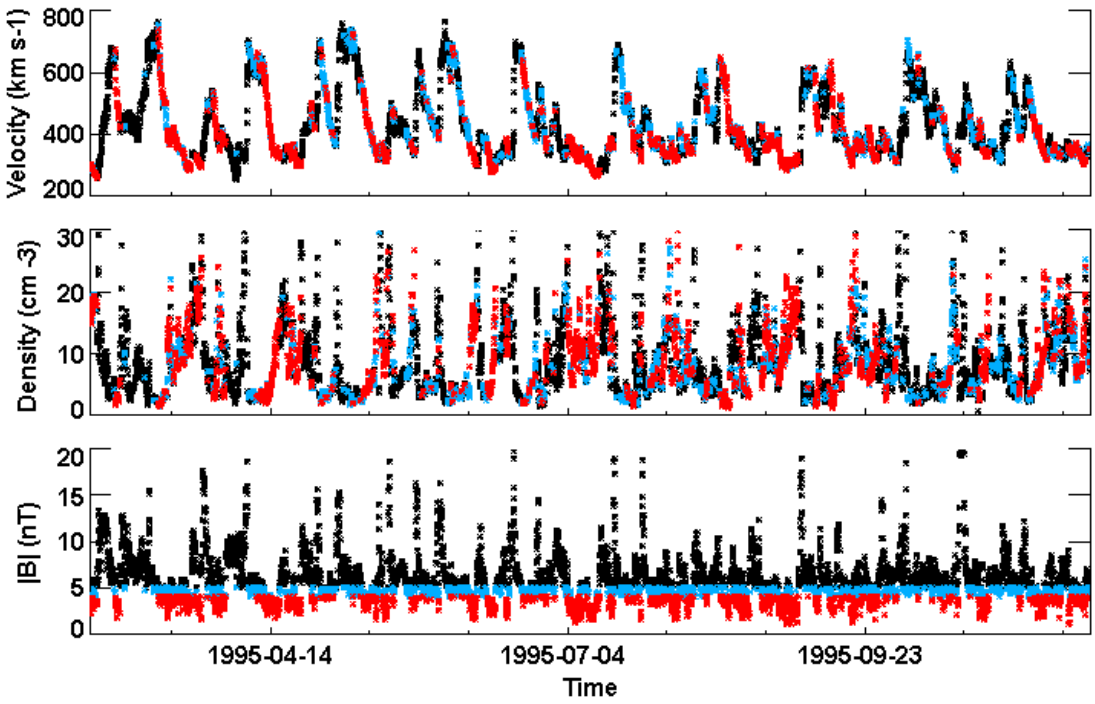

Figure 3.8: (top to bottom) Time series of the velocity, density, and field magnitude for the Solar Cycle 22 time period shown in Figures 3.3 and 3.4. The blue (red) values are data filtered for field magnitude values that are between 4 to 5 nT (≤ 4 nT).

the field magnitudes observed at 1 AU over the SC 22 and 23 periods, we plot time series that are organized by Carrington Rotation and effectively stack them against each other to produce color contour plots, as shown in Figures 3.9 and 3.10. The x-axis displays the day of the CR (0 to 27), the y-axis displays the CR number (1893 – 1902 for SC 22 or 2053 – 2062 for SC 23), and the color represents the magnitude of the solar wind velocity (top panels) or total magnetic field (bottom panels). The black areas in the plots represent data gaps in the observations.

Figure 3.9 (top panel) shows the high– (red, orange) and low–speed (cyan, blue) stream structures, which were very prominent during the SC 23 period. For each Carrington Rotation, there were typically two high–speed and corresponding low–speed streams. The bottom panel shows that the ridges of high magnetic field magnitudes (red) occur during the rise of the high–speed streams (top panel, regions where the colors abruptly transition from blue to red). In contrast, the ridges of low field magnitudes (blue) occur during the trailing part of the high–speed streams

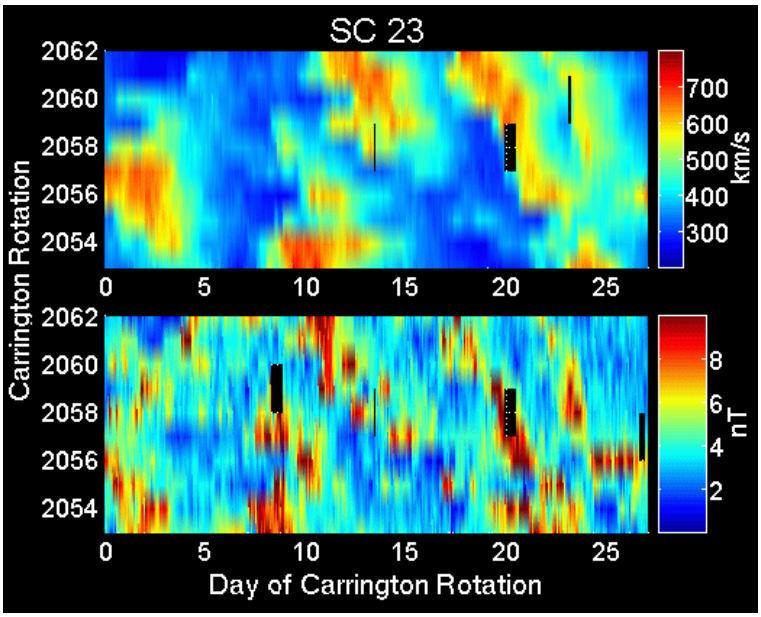

Figure 3.9: Color contour plot for the SC 23 time period. Shown are contours for (top panel) velocity (km s^{-1}) and (bottom panel) magnetic field magnitude (nT).

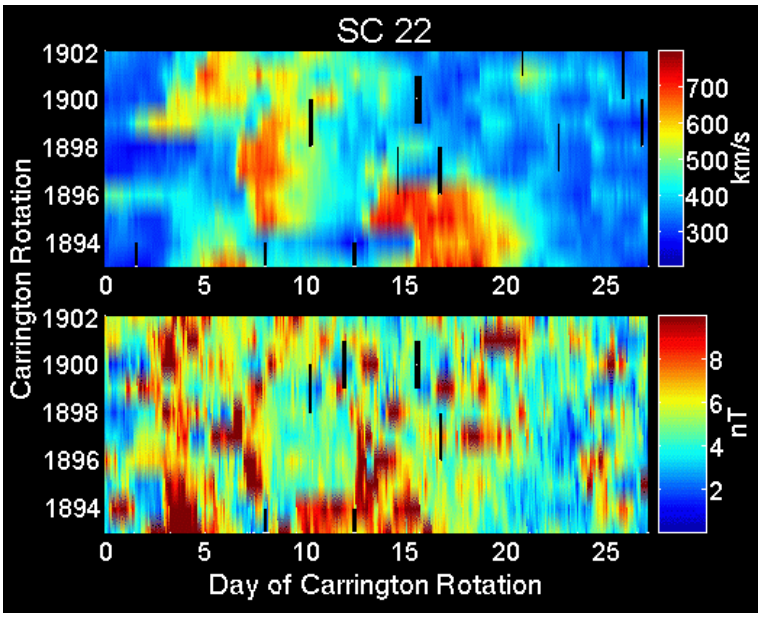

Figure 3.10: Color contour plot for the SC 22 time period. Shown are contours for (top panel) velocity (km s^{-1}) and (bottom panel) magnetic field magnitude (nT).

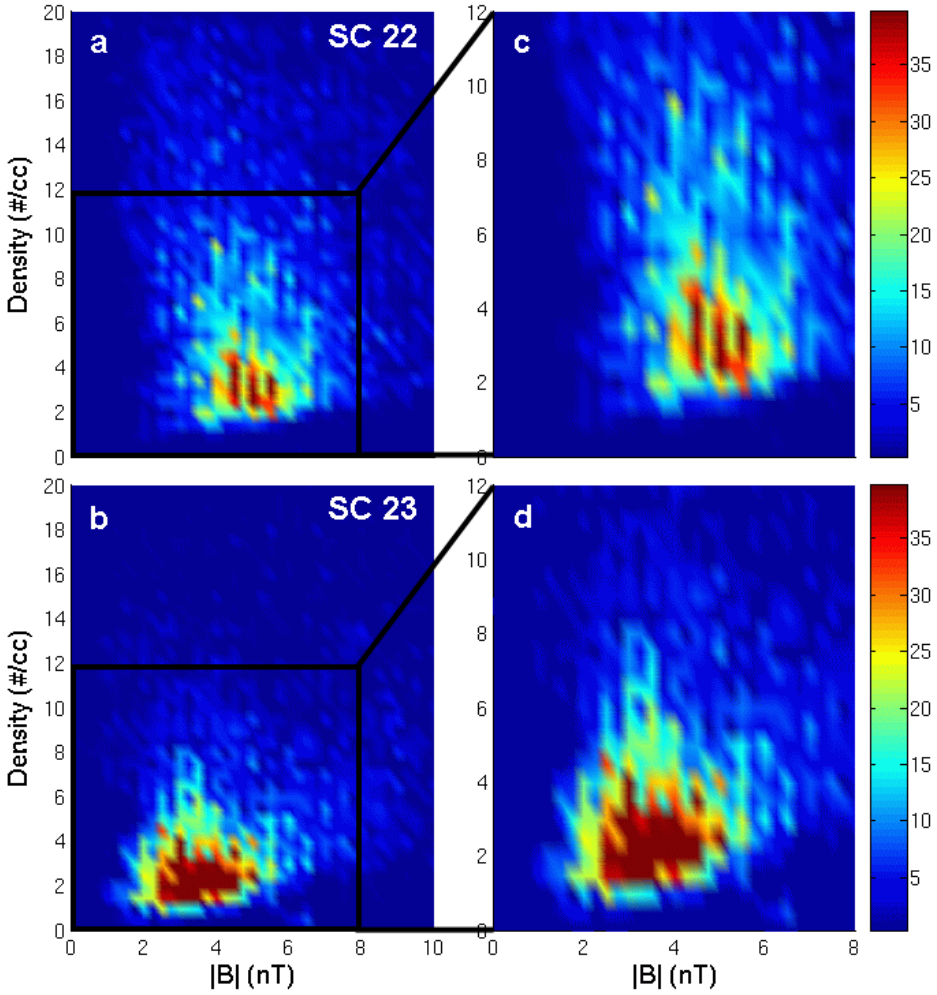

Figure 3.11: Color contour plot of the magnetic field magnitude *versus* density, for (a) SC 22, (b) SC 23, (c) zoomed–in version of (a), and (d) zoomed–in version of (b).

(top panel, regions where the colors slowly transition from yellow to green to blue).

Figure 3.10 shows similar color contour plots, but for the SC 22 period. Although there are high– and low–speed stream structures during this time period (see top panel), the high–speed streams are not as abundant and well–organized as those observed during the SC 23 period. Also, the contrast between the high– and low–speed stream structures (red to blue) is not as great. For example, the high–speed structure observed during CR 1896 on days 7 to 9 has a very gradual declining portion that lasts several days, where the speeds decrease from ≈550 km

s^{-1} (yellow–green) to ≈400 km s^{-1} (cyan) before the next high–speed stream structure commences on days 13 to 18. In contrast, the trailing part of the high–speed streams observed in the SC 23 period shows a more abrupt decline. The speeds go from ≈550 km s^{-1} (yellow–green) to ≈400 km s^{-1} in a day or so, followed by a sharp transition to speeds below 350 km s^{-1} (blue), which lasts for several days before the next high–speed stream onset. Figure 3.10 (bottom panel) shows the magnetic field magnitude observed at this time. Notice that during SC 22 the field magnitudes have more mid–range (green to yellow) and high (red) field values and fewer low field values (blue) when compared to the current cycle. In addition, the ridges of high magnetic field magnitudes (red) do not necessarily occur during the onset of the high–speed streams, nor do the low field values always occur during the trailing part of the high–speed streams. We note that some solar transient events occurred during the time periods presented. The number of interplanetary coronal mass ejections (ICMEs) observed during the SC 22 period is eight compared to two during the SC 23 time period (see Jian *et al.* 2006b, and http://www-ssc.igpp.ucla.edu/forms/stereo/stereo_level_3.html). This may in part explain the less organized nature of the SC 22 period.

We also examine the correlation between the observed densities and field magnitudes. Figure 3.11 shows color contours of the statistics of the magnetic field magnitudes *versus* density. The maximum values in the distribution are shown in red. For the SC 22 distribution, Figure 3.11a shows that the maximum occurrence ranges between field magnitudes of around 4 – 6 nT and density values of around 2 – 6 cm^{-3}. For the SC 23 distribution (Figure 3.11b), the maximum occurrence distribution is shifted toward lower values in field magnitude and broader in range, from approximately 2 to 5.5 nT. The density distribution is shifted toward lower values as well (about 1.5 – 6 cm^{-3}). Overall, the recent SC 23 period exhibits both lower field magnitudes and densities, consistent with the conclusions derived from Figures 3.5 through 3.10.

3.4 Origin of the low IMF

To determine the nature of the differences in the present cycle interplanetary fields and their possible relationship to the weak solar polar fields mentioned in the introduction, it is necessary to consider their origins. Although we do not show this, from the computed source surface coronal field maps available at the Wilcox Solar Observatory (WSO) (http://wso.stanford.edu/synsourcel.html) the neutral line of the heliospheric current sheet (HCS) is seen to be more warped during CRs 2053 – 2062 in SC 23 in comparison with CRs 1893 – 1902 in SC 22. If the slow wind

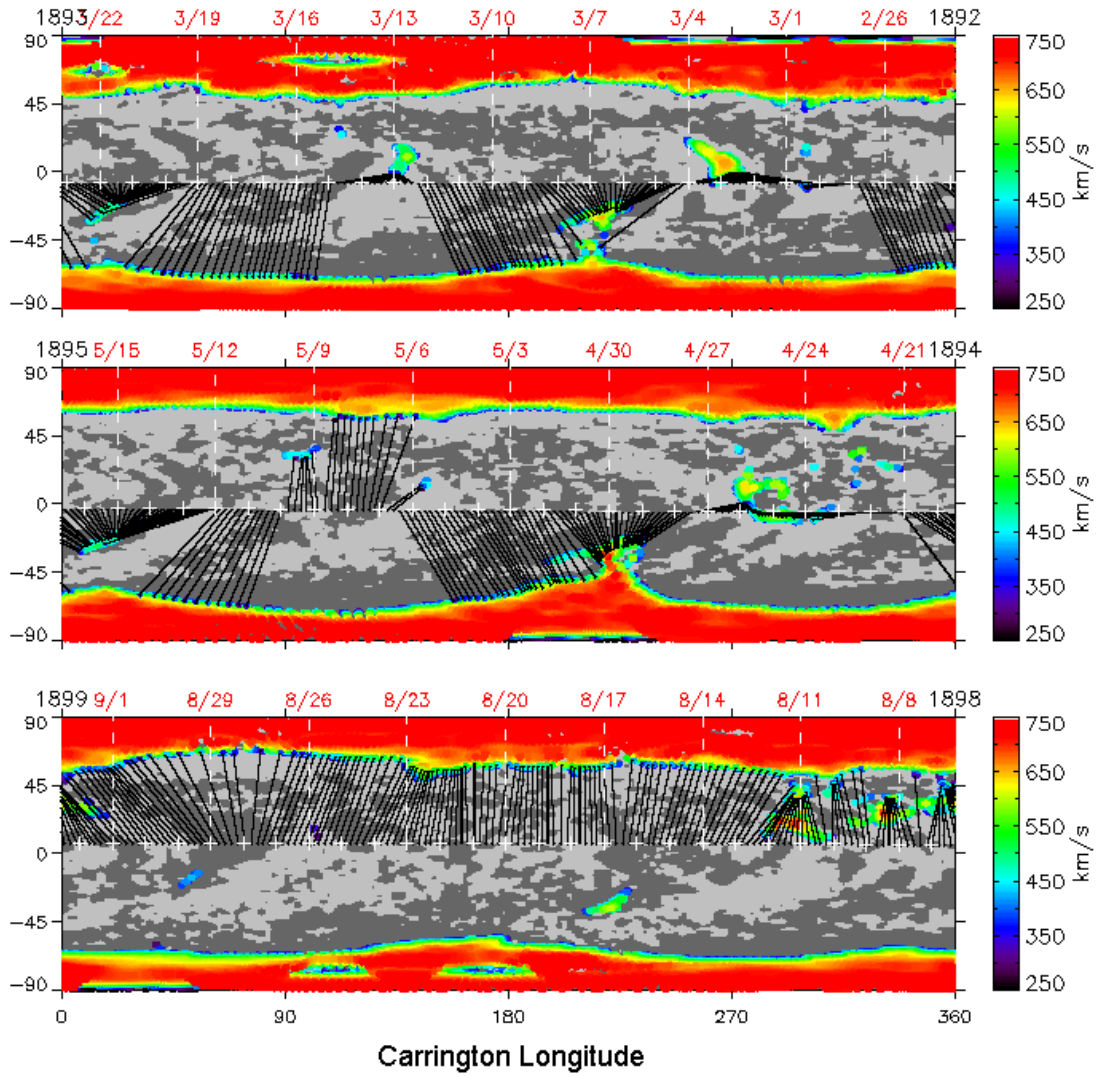

Figure 3.12: The derived coronal sources for CRs 1893 (top), 1895 (middle), and 1899 (bottom) using the WSA coronal model. The calculated footpoints (colored dots) of the open field lines at the photosphere are shown. The different colors indicate the solar wind speed (at $21R_{\odot}$) associated with the flux tubes, whereas the solid black lines connect the outer coronal boundary at 21.5 $R_{\odot}$ and the source regions of the solar wind at the photosphere. The + symbol indicates the daily position of the sub-Earth point on the Sun, which varies between $\pm 7.25°$ in solar latitude due to the inclination of solar rotation axis with respect to the ecliptic plane. Note that the newest (oldest) data are located on the left side (right side).

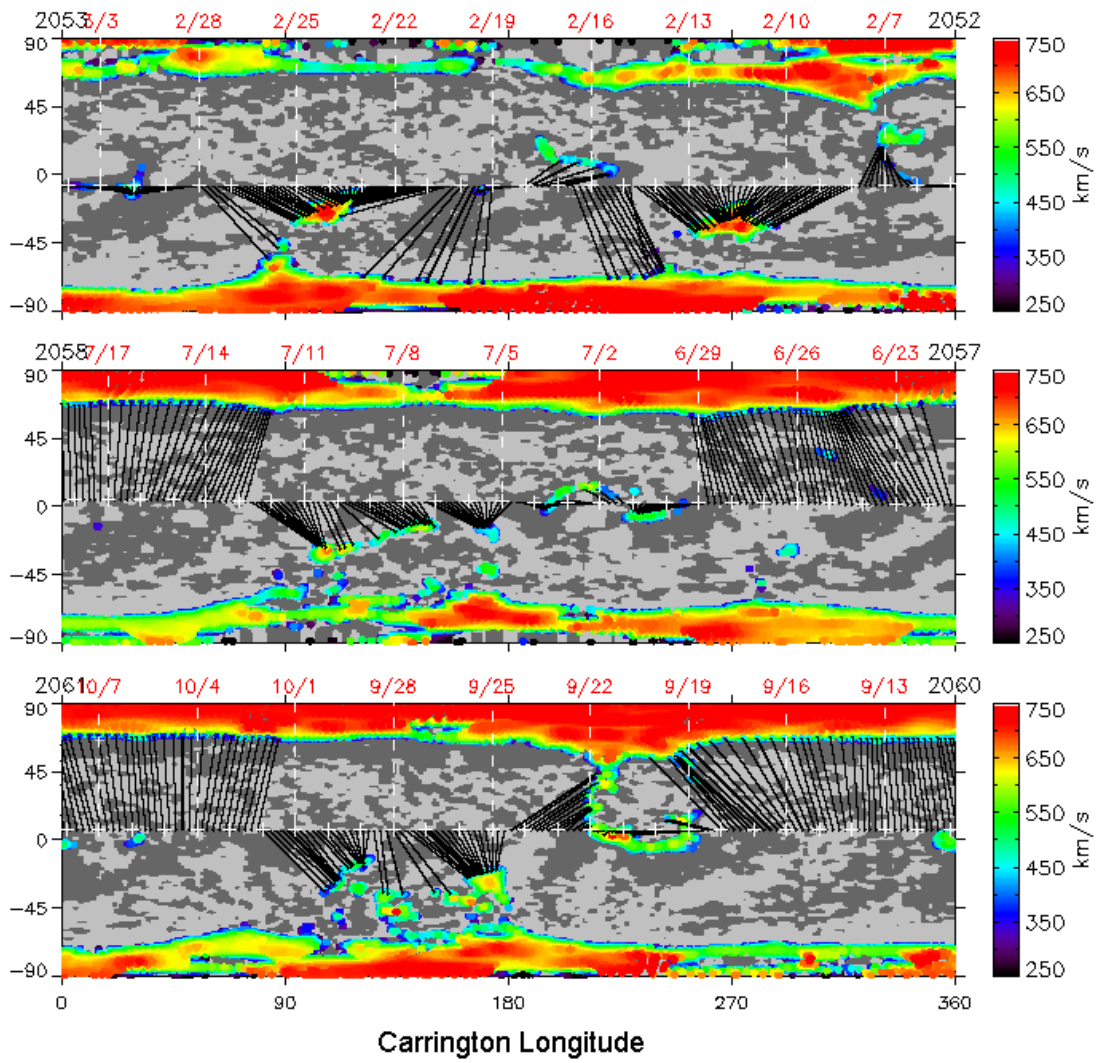

Figure 3.13: The derived coronal sources for CRs 2053 (top), 2058 (middle), and 2061 (bottom) using the WSA coronal model.

belt roughly follows the neutral line, the inference is that the stream structure should be more pronounced for the solar cycle minimum in SC 23, which we do observe, as shown in Figure 3.7 (top panel). The greater warping should maximize the interaction between the high– and low–speed streams. In comparison, when the heliospheric current sheet is flat and near equatorial, as it is during the previous solar minimum, the stream interactions are less well–formed and the ecliptic intersection of them shows less contrast. In particular, the formation of rarefactions in the

ecliptic is expected to be weaker as suggested by the results of Riley and Gosling (2007).

The sources of the high–speed streams are also different for these two near-solar minimum periods. Using the Wang–Sheeley–Arge (WSA) semi–empirical solar wind model (Arge *et al.*, 2004), we locate the sources of the high–speed streams observed at 1 AU. Standard plots used to map the solar wind sources with the WSA model are shown in Figures 3.12 and 3.13 for several Carrington Rotations from the periods under study. Here, the colored regions are the predicted foot points of the open field lines at the photosphere, *i.e.*, the coronal holes, where the colors indicate the solar wind speed at 21.5 $R_{\odot}$ arising from a particular open field region, while the black lines indicate where the open regions are magnetically connected to the ecliptic plane. Figure 3.12 suggests that for the time period in SC 22, the sources of the ecliptic solar wind streams are mostly polar coronal hole edges and extensions. In contrast, Figure 3.13 shows that for SC 23, most of the high–speed streams originate from isolated open field sources located in the low– and mid–latitude regions. It seems that there were very few comparable low– and mid–latitude holes supplying the high–speed wind during the SC 22 period. Extreme-ultraviolet (EUV) images from the SOlar and Heliospheric Observatory (SOHO) Extreme ultraviolet Imaging Telescope (EIT) (Delaboudiniere *et al.*, 1995) and STEREO Sun Earth Connection Coronal and Heliospheric Investigation (SECCHI) Extreme UltraViolet Imager (EUVI) (Howard *et al.*, 2002) confirm this difference.

To investigate the shapes and heliospheric extent of the high–speed stream sources, we consider the global outward mapping of the various coronal holes that are supplying the solar wind during the SC 22 and 23 periods. We use the potential field source surface (PFSS) approximation of the coronal field (*cf.* Schatten, Wilcox, and Ness, 1969) in the same manner as Zhao and Webb (2003) to map each derived open field region from the photosphere out to the source surface at 2.5 $R_{\odot}$ (solar radii). Magnetograms from the Stanford Wilcox Solar Observatory (WSO) are used as input to the PFSS model.

Figure 3.14 (top panel) shows the open and closed field regions below 1.25 $R_{\odot}$ for CR 1898 during the SC 22 period. The solid black curve marks the magnetic neutral line, whereas the color dotted areas and the blue–red field lines indicate the open and closed field regions, respectively. Six regions of open field lines can be seen for CR 1898, as shown in different colors. Three regions are polar coronal hole (PCH) extensions, two are polar coronal holes, and one is an isolated low–to–mid latitude coronal hole. The second panel shows the various photospheric sources mapped to the source surface. Note that the colors correspond to the colored

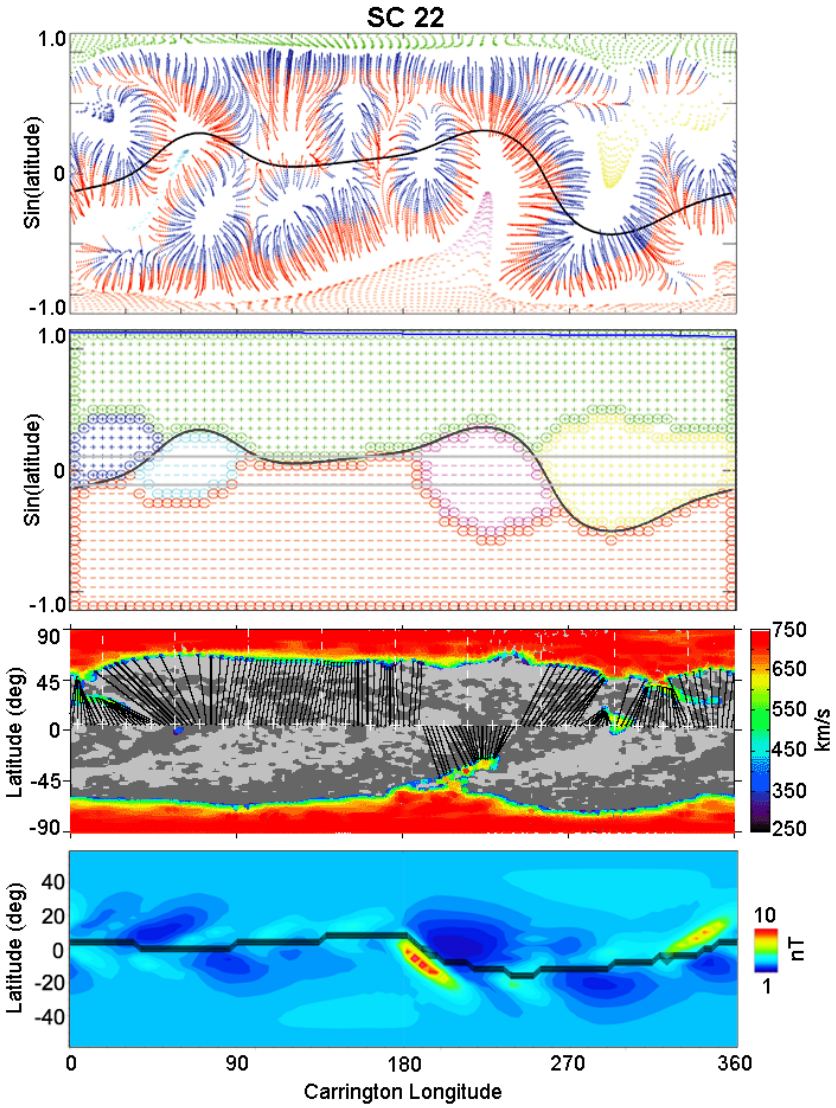

Figure 3.14: Global outward mapping of coronal holes supplying the solar wind for CR 1898 during the SC 22 period. (top panel) The open (color dotted areas) and closed (areas with blue–red field lines) field regions below 1.25 $R_{\odot}$ are shown. (second panel) The photospheric sources mapped out to the source surface at 2.5 $R_{\odot}$. The two solid gray bars mark the ecliptic plane location (between $\pm$ 7.25° latitudes). The thick blue curve near the top of the panel marks the projected Ulysses trajectory. (third panel) The WSA model predictions of the coronal hole areas and the solar wind speeds arising from them. (bottom panel) The magnetic field magnitude at 1 AU modeled by the coupled MAS/ENLIL solar wind model. The black curve seen throughout is the magnetic neutral line.

regions shown in the top panel. The magnetic polarities of the open field regions are indicated by the plus and minus symbols for open field pointing away from and toward the Sun, respectively. For CR 1898, the four isolated and PCH extensions of open field regions map out to a moderate latitude range at the source surface. Dominating the source surface map are open fields extending from within the PCH regions. The latitudinal extent of these open fields is wide, where some of the open fields map down to latitudes over a broad longitude range within the ecliptic plane (between $\pm$ 7.25° latitudes) as indicated by the two solid gray bars. Other Carrington Rotations from the SC 22 period of our study also show similar features, where the open fields from the PCHs have very wide latitudinal extents at the source surface and the isolated and PCH–extension regions of open fields have a moderate–to–narrow latitudinal range. This is consistent with the Ulysses results of McComas *et al.* (2008), where they showed that the band of solar wind variability was narrow and confined to low latitudes during this period. The solid blue curve near the top of this second panel marks the projected Ulysses trajectory for this Carrington Rotation period (data from http://cohoweb.gsfc.nasa.gov/helios/heli.html).

The third panel of Figure 3.14, similar to Figures 3.12 and 3.13, shows the WSA model predictions of the coronal hole areas and the solar wind speeds arising from them. The crosses mark the daily position of the sub–Earth point on the Sun, providing information about where the solar wind observed at Earth is coming from on the Sun. For CR 1898, the majority of the medium– to high– speed winds in the ecliptic are coming from the PCH edges and extensions. One thing to note is that there are subtle differences between the top and third panels with regard to the open field areas, in terms of shapes, locations, *etc.* This is due to the fact that the PFSS model here uses magnetograms from WSO whereas the WSA model uses magnetograms from the National Solar Observatory (NSO) (Henney, Keller, and Harvey, 2006) and a coupled coronal model consisting of the PFSS and Schatten current sheet model (Schatten, 1971). However these differences do not affect the basic information obtained from these source mappings.

The bottom panel of Figure 3.14 shows the mapping of the magnetic field magnitude at 1 AU based on the open field regions shown for CR 1898. The results are generated by the coupled coronal MHD–Around–a–Sphere (MAS) model (Riley, Linker, and Mikic, 2001), together with the ENLIL solar wind model (Odstrcil, 2003) (henceforth MAS/ENLIL). The coupled–model uses NSO magnetograms and is publicly available through the runs–on–request service at the Community Coordinated Modeling Center (CCMC) (http://ccmc.gsfc.nasa.gov). The colors shown are the field magnitude values in the units of nanoTesla, though it should be men-

tioned that the MAS/ENLIL solar wind model values tend to be underestimated by a factor of ≈2 compared to observations (see Lee *et al.*, 2009a, for a discussion). The regions of low field magnitudes (patches of dark blue) are confined to a narrow latitudinal range and usually coincide with the rarefaction regions in the trailing parts of the high speed streams (*e.g.,* Figures 3.7 and 3.8), which in this case are confined to fairly low latitudes.

Figure 3.15 shows similar plots to Figure 3.14 but for CR 2060 during the SC 23 period. The top panel shows six isolated low–to–mid latitude coronal holes that map out to a much wider range of latitudes at the source surface (second panel) than for the SC 22 period shown previously. In addition, the open field regions from the PCH regions do not have as large a latitudinal extent over a broad range of longitudes in contrast to Figure 3.14 (second panel) which is representative of the SC 22 period. Other Carrington Rotations from the SC 23 period also show the low–to–mid latitude coronal holes mapping out to a much wider latitude range over a broad range of longitudes at the source surface. This is consistent with the Ulysses results of McComas *et al.* (2008), who also showed that the band of solar wind variability has a larger latitudinal extent for this period compared with the previous SC 22 period. The implication is that Ulysses would have spent more time during the SC 23 period in the solar wind emanating from the low–to–mid latitude sources than in the previous period. The solid blue curve shown in the second panel marks the Ulysses trajectory for this Carrington period, showing that Ulysses was crossing the ecliptic plane during this time. The third panel shows the WSA predictions of the coronal holes and the speeds arising from them. In the ecliptic plane, most of the high–speed winds were coming from these low–to–mid latitude sources of open fields, in contrast to the previous period where the majority of the high–speed winds came from the PCH edges. The bottom panel shows the MAS/ENLIL model results for the field magnitude at 1 AU. Regions with low field magnitude values are more abundant during this period, and have a broader latitudinal range compared with the previous period.

The evolution of stream interactions and their related rarefactions may contribute to the weaker fields that are observed during this current minimum period. We investigate how the depth of the rarefactions, and thus the associated field magnitudes, depend on the low– and high–speed contrasts of the solar wind streams. Figures 3.16 and 3.17 illustrate the basic dynamical features of corotating compression and rarefaction regions in the equatorial plane (*e.g.,* Pizzo, 1982; Riley, Linker, and Mikic, 2001). These numerical results are from the MAS coronal–solar wind model and were used by Riley and Gosling (2007) to study the origins of radial

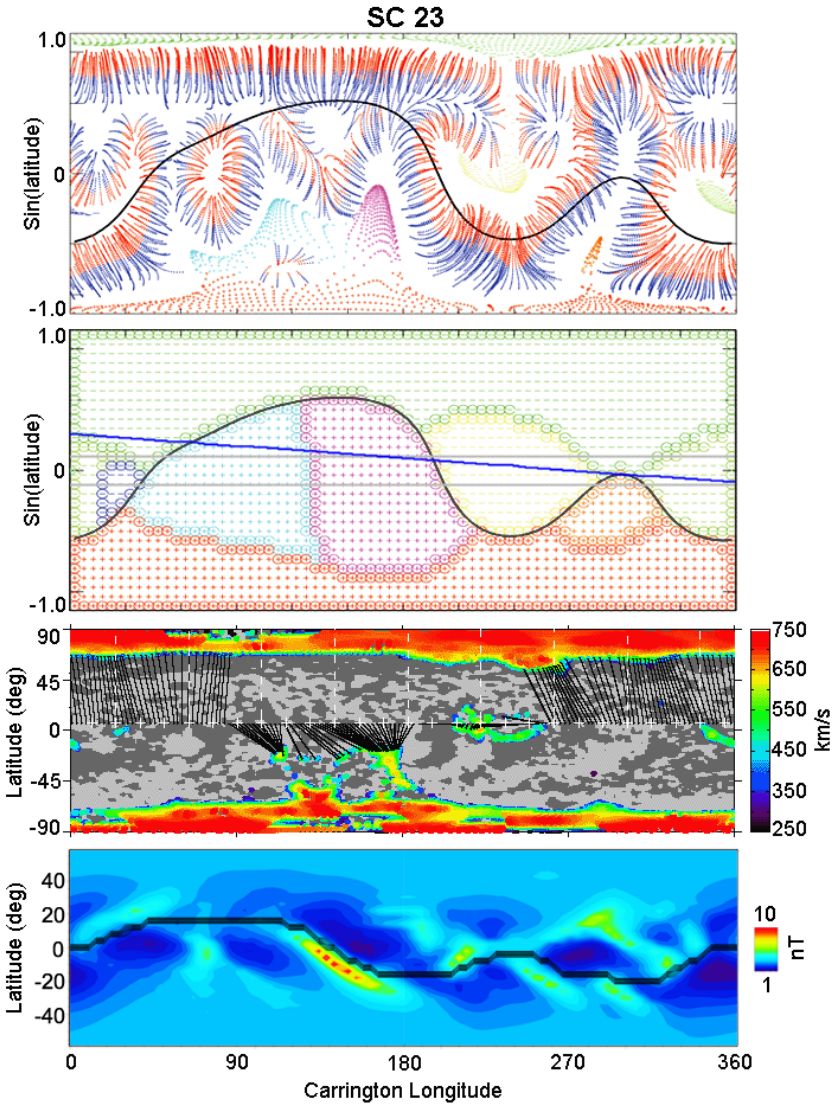

Figure 3.15: Global outward mapping of coronal holes supplying the solar wind for CR 2060 during the SC 23 period. (top panel) The open (color dotted areas) and closed (areas with blue–red field lines) field regions below 1.25 $R_{\odot}$. (second panel) The photospheric sources mapped out to the source surface at 2.5 $R_{\odot}$. The two solid gray bars mark the ecliptic plane location (between $\pm$ 7.25° latitudes). The thick blue curve marks the projected Ulysses trajectory. (third panel) The WSA model predictions of the coronal hole areas and the solar wind speeds arising from them. (bottom panel) The magnetic field magnitude at 1 AU modeled by the coupled MAS/ENLIL solar wind model. The black curve seen throughout is the magnetic neutral line.

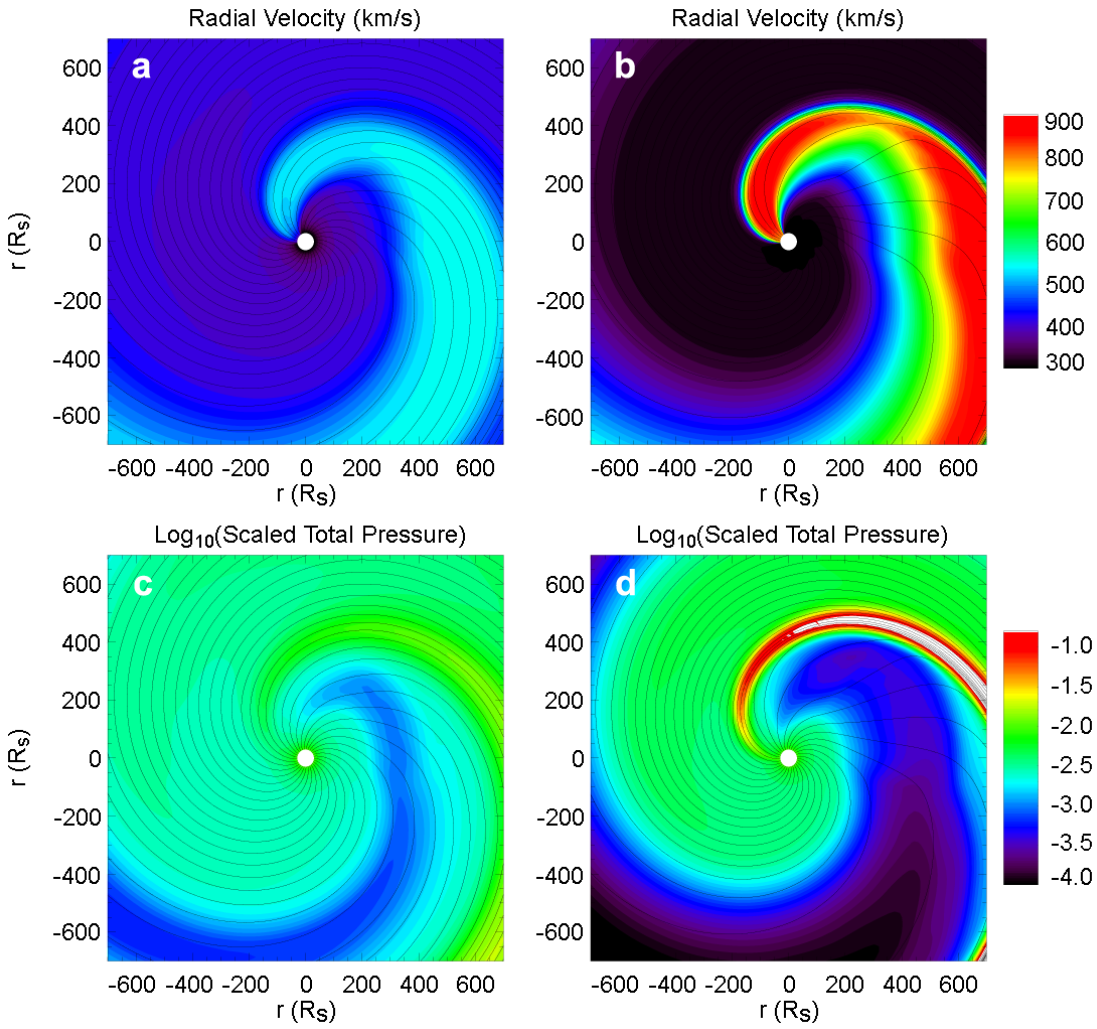

Figure 3.16: Numerical results generated by the MAS coronal–solar wind model in the equatorial plane for (a, b) radial velocity and (c, d) total pressure (magnetic and thermal, scaled for the adiabatic, spherical expansion of the solar wind). The initial conditions for the simulations consisted of a 300 km s^{-1} low–speed stream throughout, with a single, high–speed stream of either 400 km s^{-1} (a, c) or 800 km s^{-1} (b, d). The x- and y-axes are given in solar radii, where ~ 214 R_S is equivalent to 1 AU.

heliospheric fields in high–speed stream rarefaction regions. The initial conditions for the simulations consisted of a 300 km s^{-1} slow–speed stream throughout, with a single, high–speed stream of either 400 km s^{-1} (Figure 3.16a) or 800 km s^{-1} (Fig-

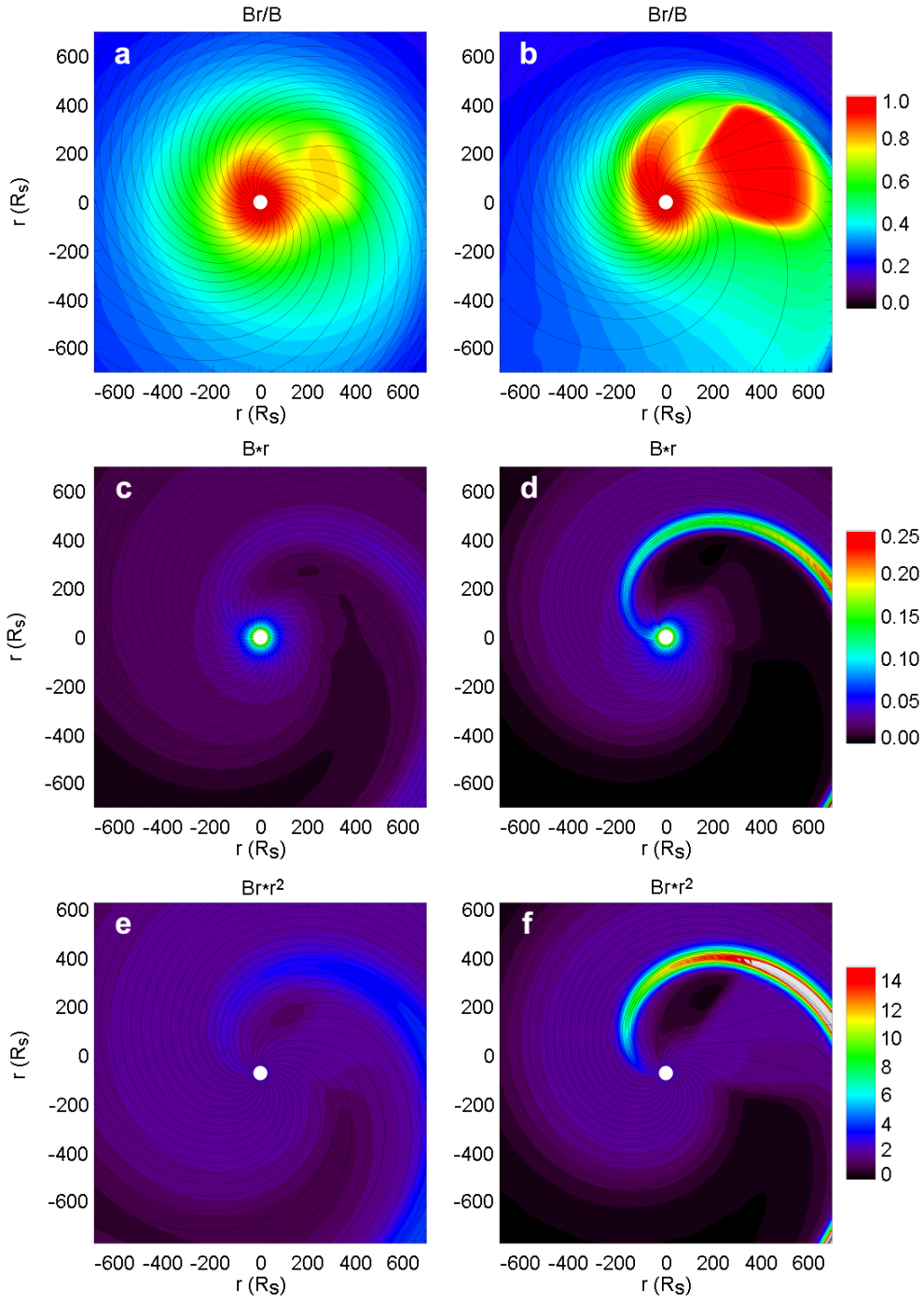

Figure 3.17: Numerical results for (a, b) B_r/B, (c, d) magnetic field magnitude scaled by r, and (e, f) radial magnetic field scaled by r^2.

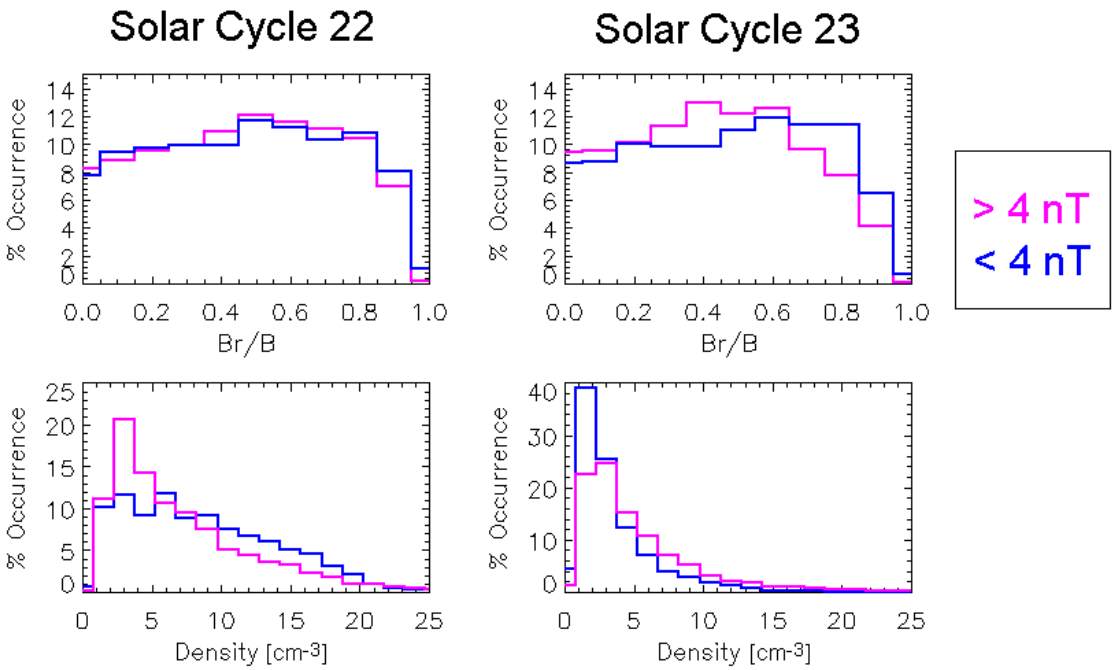

Figure 3.18: Histogram of occurrence at 1 AU for (top row) the ratio B_r/B and (bottom row) density. Data from the SC 22 (23) period is shown on the left (right). The colors shown are for data that have been filtered for when the field magnitude is less than 4 nT (blue) and greater than 4 nT (magenta).

ure 3.16b) from a coronal hole centered on the equator. At the boundary where the high–speed wind overtakes the slow–speed wind, a compression region forms where the pressure is higher and the field lines are closer together. For the slow–speed contrast case (Figure 3.16c), the compression region is much weaker, *i.e.,* less pressure, less compressed fields, compared to that for the high–speed contrast case (Figure 3.16d). Behind the compression region in both cases, a rarefaction region forms where the high–speed wind outruns the slow–speed wind behind it. However, for the high–speed contrast case, the rarefaction region has a much larger radial extent and is more rarefied. In addition, the ratio B_r/B is larger, where the near–radial fields occupy a broader region in radial distance and longitude (compare Figure 3.17b with 3.17a). Figures 3.17c to 3.17f show the details of the magnetic field magnitude and radial field (scaled by r and r^2, respectively). For the high–speed contrast case (Figures 3.17d and 3.17f), the magnetic field is noticeably lower behind the compression regions. These model results suggest that since the speed

contrasts are significantly higher during the SC 23 period (see discussion for Figures 3.7 and 3.9), there will be deeper rarefaction regions and thus lower magnetic fields in those regions.

The MAS model result shown in Figure 3.17b demonstrates that streams with high–speed contrasts have stronger near–radial field regions. Since it is known that during periods of near–radial fields, the field magnitudes and the densities are lower (Neugebauer, Goldstein, and Goldstein, 1997), we investigate the contribution of near–radial fields to the weaker fields observed this solar cycle period. Figure 3.18 shows histograms of the OMNI data for the ratio B_r/B (top row) and density (bottom row). The colors shown are for data that have been filtered for when the field magnitude is less than 4 nT (blue) and greater than 4 nT (magenta). During the SC 23 period (right column), there was an overall higher fraction of the field magnitude that was more radial during the times of low field (less than 4 nT). For these low field periods, the fraction of low densities was also much higher. This was not the case for the SC 22 period, as shown in Figure 3.18 (left column). These OMNI results are consistent with the MAS model results shown in Figures 3.16 and 3.17 in that the SC 23 conditions, with stronger ecliptic sources of high–speed streams, seem to produce greater rarefactions with the associated more–radial fields.

3.5 Summary and Discussion

We investigated signatures of the unusually weak polar field in the ecliptic near–Earth IMF for the STEREO period of observations, and compared the results with observations for a similar period from the previous solar cycle. Using the 1 AU OMNI data, for the SC 23 period we found the following for the peak of the distribution of values: both the ecliptic IMF magnitude and density were 30% lower, the momentum flux was 38% lower, and the velocity remained unchanged. This is consistent with the Ulysses off–ecliptic observations reported by McComas *et al.* (2008) and Smith and Balogh (2008). We showed that these weaker fields were clearly associated with the declining portions of the high–speed streams where the rarefaction regions occur.

Results from the WSA semi–empirical solar wind model showed that sources of the high–speed streams were different for the SC 23 period than for the previous solar cycle, where the coronal holes were more isolated and resided in the low–to–mid latitude regions. The global modeling results from the PFSS model of the coronal open field regions suggested that these isolated low–to–mid latitude holes mapped out to a much greater latitudinal area of the heliosphere for SC 23, and dominated the ecliptic plane. The MAS/ENLIL global modeling results for 1 AU showed that

the regions of low field magnitude also have a broader longitudinal range and were more abundant during SC 23. Results from the MAS MHD coronal–solar wind model illustrated how the evolution of the stream interactions can contribute to weaker fields and suggested that if the speed contrasts were higher during the SC 23 period, there would be deeper rarefaction regions and thus lower magnetic fields in those regions.

Based on the Ulysses observations reported by Smith and Balogh (2008), the weaker ecliptic fields may also be due to less open solar flux. However, since the ecliptic observations and model results shown in this study indicate that the low–to–mid latitude flux is not only from the polar regions (also see Luhmann *et al.*, 2009, for a discussion) and is moreover latitudinally redistributed by stream interactions, the interpretation is complicated. Future modeling of both the Ulysses and ecliptic IMF data together (P. Riley, private communication 2008) may shed more light on the origins of the weaker ecliptic IMF of this solar cycle period. In the meantime, caution must be exercised in evaluating these weaker ecliptic fields.

Chapter 4

Possible Influence of the Source Surface Changes on the Interplanetary Magnetic Field Magnitude

Abstract

The Solar Cycle 23 minimum period has been characterized by significantly lower solar and interplanetary field strengths, leading to periods of unprecedented conditions for planet-solar wind interactions. This provides an ideal time to investigate how the observed solar fields control the observed interplanetary fields. Using the Potential Field Source Surface (PFSS) model of the coronal magnetic field to compute the coronal hole/open fields, we investigate how the strength of the photospheric field affects the interplanetary magnetic flux and in particular, how much the observed interplanetary fields of different cycle minima can be understood simply from differences in the areas of the coronal holes as opposed to differences in the surface fields within them. Although the source surface value of 2.5 $R_{\odot}$ is typically used in the potential field applications, earlier studies have shown that using smaller source surface heights generates results that better match observations during periods of low solar activity. Thus, in this study we take a somewhat different approach of invoking smaller source surface radii in the PFSS model to construct a consistent picture of the observed coronal holes and the near-Earth interplanetary field strength as well as polarity measurements for the near-minimum activity phases of cycles 23 and 22. We find the values of $\sim$1.9 $R_{\odot}$ and $\sim$1.8 $R_{\odot}$ for the cycles 22 and 23 minimum periods, respectively, produce the best results. This solar cycle difference in the source surface height, is also expected from coronal magnetohydrodynamic modeling, given the weaker solar fields of the recent cycle. The larger coronal holes obtained for the smaller source surface radius of Cycle 23 somewhat offsets the interplanetary consequences of the lower magnetic fields at their photospheric footpoints. Current users of PFSS models are advised to use these smaller values for their source surface heights as long as the solar activity is

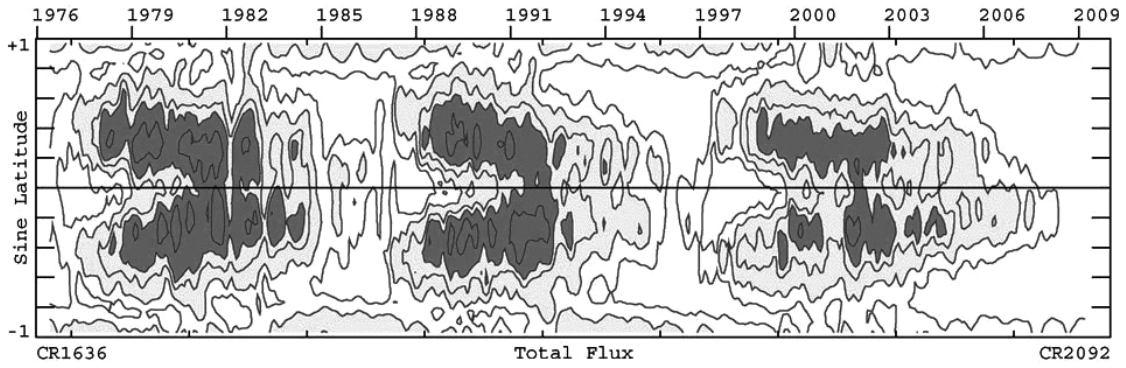

Figure 4.1: Observed total photospheric magnetic flux (longitudinally averaged) for the last three solar cycles. The contour levels are for magnetic field values of 50, 100, 200, 300, 500, and 1000 uT (100 uT = 1 Gauss), where the two strongest contours are shaded in dark gray and the two weakest contours are shown in white. The density and color of the contours suggests a weaker overall solar surface field this cycle compared to the previous ones. Image credit: Stanford University Wilcox Solar Observatory.

low. Similarly, the source surface radius should probably be treated as an additional variable parameter in flux transport studies of multiple solar cycles.

4.1 Introduction

The Solar Cycle 23 (SC 23) deep solar minimum period is unlike the corresponding phases of the previous two solar cycles. Ground-based magnetograph observations from the Wilcox Solar Observatory (WSO) shown in Figure 4.1 reveal that the solar fields have been reduced over the entire surface of the Sun, while the polar field values are about half those observed during the previous minimum period (Hoeksema, 2010). These weaker solar fields resulted in changes in the bulk properties of the interplanetary medium. In-ecliptic, near-Earth observations during the declining-to-minimum phase of SC 23 showed that the interplanetary magnetic field (IMF) strength (Figure 4.2) and solar wind density were ∼30% lower, whereas the momentum flux was ∼38% lower but the solar wind speeds remain unchanged (Lee *et al.*, 2009b). The *Ulysses* (Balogh *et al.*, 1992; Bame *et al.*, 1992) off-ecliptic observations for the same solar cycle period revealed similar changes in the heliospheric medium, including a reduction of the radial magnetic field by ∼64%, dynamic pressure by ∼22%, and thermal pressure by ∼25% (Smith and Balogh, 2008; McComas

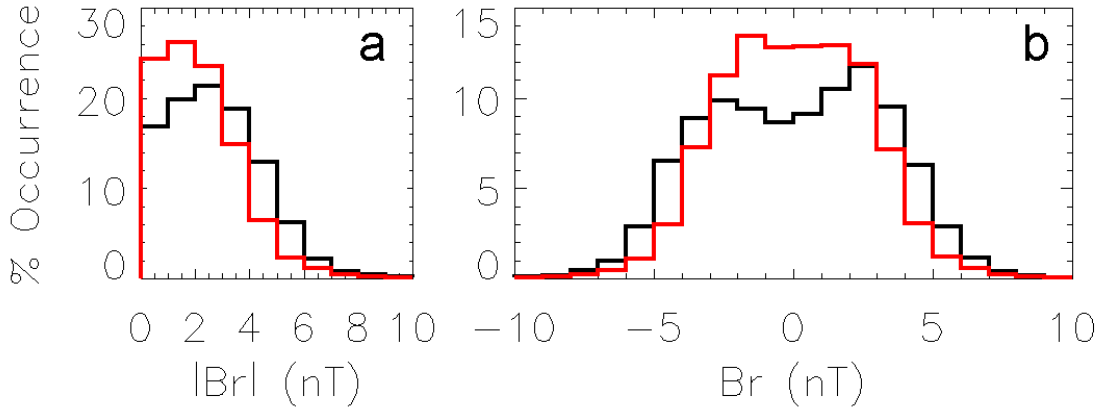

Figure 4.2: Histogram of occurrence for the (a) unsigned and (b) signed radial magnetic field observed near Earth during the SC 22 (black) and 23 (red) minimum periods.

et al., 2008).

The weaker solar field and IMF of this current minimum period makes it an ideal time to understand how the solar field maps into interplanetary space to control the observed IMF. In the past, different methods have been used to compute the IMF strength from the photospheric field (*e.g.,* Levine *et al.*, 1977; Zhao and Hoeksema, 1995; Wang, Robbrecht, and Sheeley, 2009, and references therein). In this study, we take a somewhat different approach to compare the computed IMF strength with observations by considering different source surface heights in the well-known Potential Field Source Surface (PFSS) model of the coronal magnetic field (Schatten, Wilcox, and Ness, 1969; Altschuler and Newkirk, 1969). Our goal is to build a coherent picture of the coronal holes and their footpoint fields as well as the interplanetary field and polarity measurements for the two most recent solar minima. In particular, our goal is to investigate 1) how the strength of the photospheric field modifies the magnetic flux coming from the Sun, and 2) how much of the recent weak IMF can be understood simply from changes in the coronal holes.

The PFSS model, which has been widely used for decades to study interplanetary fields and photospheric sources of the solar wind, provides a snapshot of the open coronal field regions. Because the model is based on photospheric magnetic field synoptic maps that are assembled from full-disk magnetograms obtained over a solar rotation, it can capture many details of the global field geometry, especially when the Sun is in the quiet phases of its activity cycle (*e.g.,* Levine *et al.*, 1977). The outer boundary of the PFSS model is usually a spherical source surface of ~ 1.5

to 3.5 solar radii ($R_\odot$) located at a constant height above the inner boundary at the photosphere. At the source surface, the field is radial. It is assumed that between the photosphere and the source surface the coronal fields are current-free. Even with the current-free and spherical source surface assumptions, the PFSS model can generate solutions that closely match those generated by the physics-based magnetohydrodynamic (MHD) models for cases when time-dependent phenomena are negligible during both the solar minimum and maximum periods (Riley *et al.*, 2006).

Recently, Wang, Robbrecht, and Sheeley (2009) used the PFSS model with a fixed source surface height of 2.5 $R_\odot$ together with a current sheet correction and synoptic map evolution model to analyze how the weak IMF can result from a reduction in flux emergence rates together with adjusted flux redistribution parameters. They concluded that slightly faster meridional flows would be sufficient to produce the observed weaker IMF from the observed rate of flux emergence in active regions. On the other hand, Levine (1982), Levine, Altschuler, and Harvey (1977), and Hoeksema, Wilcox, and Scherrer (1983) discuss the possible influence of different source surface heights on the mapping of the solar magnetic field into the interplanetary medium. Although the source surface value of 2.5 $R_\odot$ is typically used in PFSS applications, the value which has been tuned to match the IMF polarity pattern (see Hoeksema, Wilcox, and Scherrer, 1983), Schatten, Wilcox, and Ness (1969), Levine (1982), and Levine, Altschuler, and Harvey (1977) found that using smaller source surface heights generated PFSS results that better matched observations of open magnetic fields during periods of low solar activity. A reduction in the source surface height for this minimum period would be consistent with the coronal MHD simulations of Steinolfson, Suess, and Wu (1982), which showed the expected relationship between photospheric field strength and streamer belt height (see Figure 11 in their study).

Our analysis represents an exploration of the assumptions of Schatten, Wilcox, and Ness (1969), Levine *et al.* (1977), and Levine (1982), that the source surface height should be treated as a parameter in PFSS modeling. The theoretical implication is that the strength of the IMF should be influenced by the radial extent of the closed field regions in the corona as indicated in the MHD models. Our study is also complementary to the study by Wang, Robbrecht, and Sheeley (2009) in that it calls attention to another parameter to be considered in such studies. Last but not least, our study seeks to explain why this past cycle's solar minimum interplanetary field has assumed its particular magnitude.

4.2 Approach

Over the years, the PFSS model has been refined by Hoeksema (1984) and Wang and Sheeley (1992), and its strengths and weaknesses have been explored in studies such as those by Riley *et al.* (2006). We use the version of the PFSS model that has been documented in a previous report by Luhmann *et al.* (2002), which is currently available for running at the Community Coordinate Modeling Center (CCMC, http://ccmc.gsfc.nasa.gov). As Riley *et al.* (2006) demonstrated, the PFSS model is especially applicable during the solar minimum period in the sense that it describes the open field coronal holes on the photosphere and is consistent with effective the spherical source surface shape found in the corresponding MHD solutions. We use the spherical harmonic coefficients derived from the Mount Wilson Observatory (MWO) synoptic photospheric field maps, which are processed in the manner described by Arge and Pizzo (2000). Twenty orders of spherical harmonic coefficients are sufficient to capture the bulk of the important photospheric

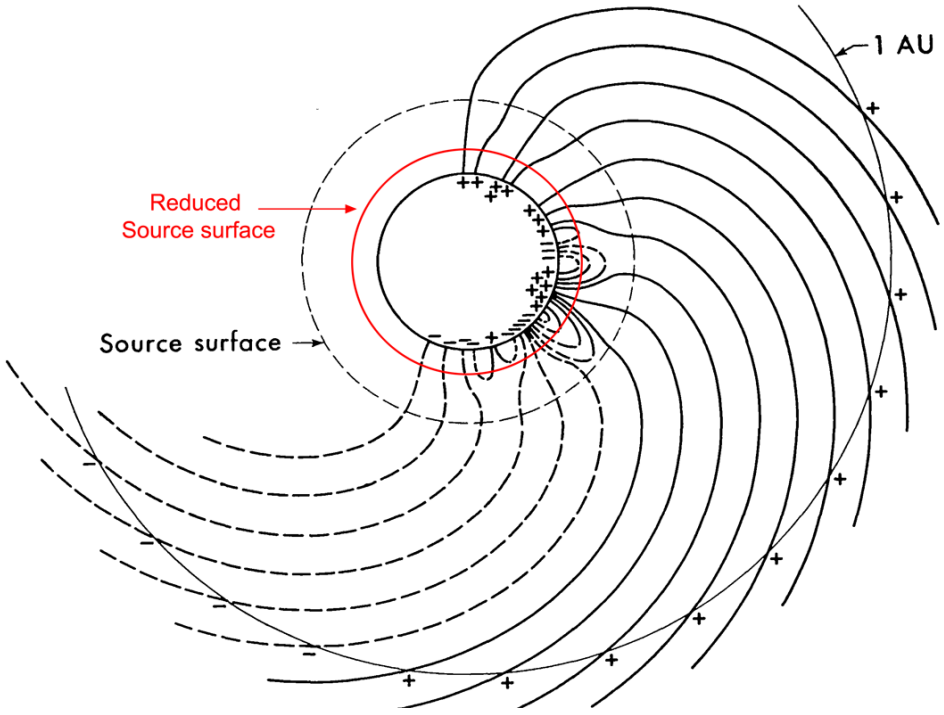

Figure 4.3: Cartoon to illustrate that a smaller source surface will encompass more open field lines and enlarge the coronal hole areas from which the open fields emanate. Figure adapted from Schatten, Wilcox, and Ness (1969).

features and their coronal effects for our solar minimum study period.

In this study we utilize the source surface height as a means of controlling the amount of solar photospheric flux that maps into the interplanetary medium. As illustrated in Figure 4.3, by reducing the source surface height in the PFSS model, more of the flux extends into the interplanetary medium as more coronal field structures become open (*i.e.* the source surface will intersect more field lines) and the photospheric areas from which the open structures emanate become larger. The implication is that what is observed in interplanetary space is a consequence of the photospheric field strength, the distribution of the magnetic flux, and the height where the last closed photospheric field lines, and thus the source surface height, occurs.

A few assumptions are made in using the PFSS model to characterize the amount of open flux in the heliosphere for the SC 22 and 23 minimum periods. It is implicitly assumed that all the open (interplanetary) magnetic flux comes from the coronal hole footpoints identified by the PFSS model. We also assume there is no significant heliospheric flux contribution by interplanetary coronal mass ejections, which is reasonable given that our period of study is the solar cycle minimum. To relate the computed open flux at the Sun to the observed radial IMF at 1 AU, we assume that the IMF magnitude is independent of heliographic latitude (see Balogh *et al.*, 1995) and thus varies in proportion to the amount of open flux (*e.g.,* Smith and Balogh, 2008).

The canonical value of 2.5 $R_{\odot}$ that is commonly used for the source surface in PFSS modeling is based on earlier works by Hoeksema, Wilcox, and Scherrer (1982; 1983) and Hoeksema and Scherrer (1986), although values between 1.5 $R_{\odot}$ and 3.5 $R_{\odot}$ have been discussed in studies by Levine *et al.* (1977), Schatten, Wilcox, and Ness (1969), and Altschuler and Newkirk (1969). It was the 2.5 $R_{\odot}$ value that gave the best overall agreement between the PFSS-inferred IMF polarities with those observed at Earth (Hoeksema, Wilcox, and Scherrer, 1983; Hoeksema, 1984). The smaller source surface values generally have been derived from soft x-ray images of coronal holes to better match the open flux geometry (see Levine *et al.*, 1977).

Our goal is to find a consistent picture based on PFSS modeling that describes both the solar sources and the interplanetary fields for this solar minimum period, and to investigate what differences, if any, exist compared to the previous minimum. More specifically, we try to develop a consistent picture of the sizes and shapes of the coronal holes seen in EUV images taken by EIT on the *Solar and Heliospheric Observatory* (SOHO, Delaboudiniere *et al.*, 1995) and EUVI *Solar TErrestrial RElations Observatory* (STEREO, Kaiser, 2005) Sun Earth Connection Coronal and

Heliospheric Investigation (SECCHI, Howard *et al.*, 2002) and the inferred IMF magnitude and polarity computed from the photospheric magnetic fields that map to the source surface.

Our study proceeds as follows: In section 3 we investigate the computed coronal hole footpoints for source surface values of 1.5, 1.8, and 2.5 $R_{\odot}$, which bracket the values generally used for PFSS modeling of the solar minimum period. We also show results of the PFSS calculations for the fraction of the open coronal areas and magnetic flux for the current and previous minimum periods, the values of which depend on the source surface height. In addition, we calculate the IMF values inferred from the PFSS results and compare them with those observed at Earth at 1 astronomical unit (AU). For the in-situ data, we use the OMNI data set available at http://omniweb.gsfc.nasa.gov/. Our comparison shows that the source surface height that produces the best values depends on the minimum period in question. We use the in-situ measurements at 1 AU to infer the best overall source surface value that gives the observed IMF magnitudes and polarities. In section 4 we discuss our results and draw some conclusions about matters such as the relationship between the solar field and interplanetary field.

4.3 PFSS Model Results vs. Observations

The bottom panels of Figures 4.4 and 4.5 show the comparison of extreme ultraviolet (EUV) synoptic maps from SOHO EIT and STEREO/SECCHI EUVI for Carrington Rotations (CRs) 1914 and 2060, respectively. These rotations were chosen as representatives from the previous and current solar minimum periods. The top three panels progressing downward are the PFSS model open field footpoint regions for the three source surface radii of 1.5, 1.8, and 2.5 $R_{\odot}$. The colors identify the radial field polarity in the open field or coronal hole areas (red for negative inward and blue for positive outward fields), for the three selected source surface radii. A qualitative comparison between the observations in the EUV maps and the different source surface maps suggests that the 2.5 $R_{\odot}$ source surface results are missing part of or entire coronal holes in both Carrington rotation examples, where the yellow circled areas in the EUV images show several clear omissions found in the 2.5 $R_{\odot}$ mapping (third panels from top in Figures 4.4 and 4.5).

The mapping results from both Carrington rotation examples suggest that a smaller source surface may be required to better approximate the observed open field regions. The comparison with the EUV maps shows that the 1.5 and 1.8 $R_{\odot}$ source surface results capture the coronal hole features that are omitted by the 2.5 $R_{\odot}$ results. However, we also note that the qualitative comparison shows that the

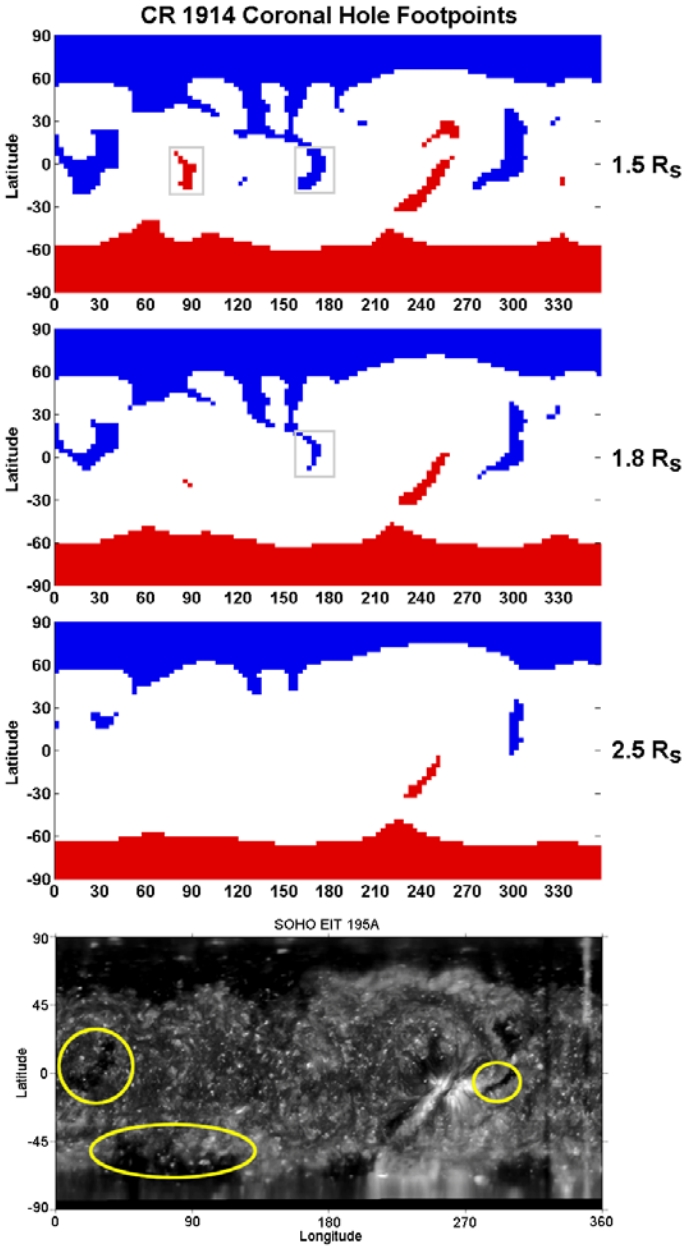

Figure 4.4: Comparison of PFSS results with 195 $\mathring{A}$ EUV map for CR 1914 (18 September to 15 October 1996) of cycle 22. The PFSS results are based on the 1.5, 1.8, and 2.5 $R_\odot$ source surface heights. The yellow circles mark the gross coronal hole features that are largely missing from the 2.5 $R_\odot$ mapping results. The gray rectangles mark the gross features that appear in the mapping results but not in the EUV image. The red (blue) denote the negative inward (positive outward) field.

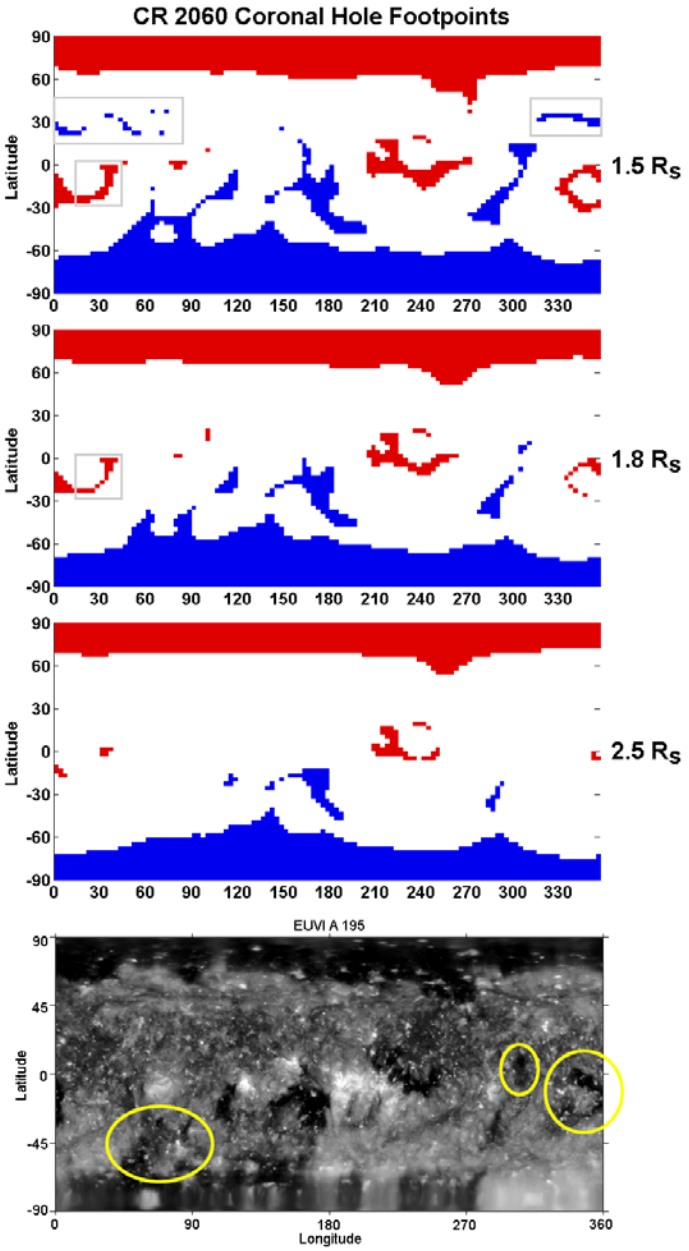

Figure 4.5: As for Figure 4.4 but for CR 2060 (14 August 2007 to 10 September 2007) of cycle 23.

smaller source surface results, especially those derived from using 1.5 $R_\odot$, produce coronal hole features (marked by gray rectangles) that are not observed. Out of these three source surface cases, the 1.8 $R_\odot$ source surface value appears to be a

good compromise for capturing the coronal hole features that are observed in both Carrington rotation cases. This radius is the better option for analyzing the possible implications for the interplanetary field and understanding how the photospheric field is related to it, at least at quiet times of the solar cycle.

One additional point to note here are the differences in the coronal holes for the current and previous minimum periods, which have been reported in recent studies. For the SC 23 minimum period, the solar corona exhibited larger, long-lived, low-to-mid latitude coronal holes (Lee *et al.*, 2009b; Luhmann *et al.*, 2009; Abramenko *et al.*, 2009), although the polar coronal hole areas were smaller in the north and the south (Kirk *et al.*, 2009). Moreover, Wang, Robbrecht, and Sheeley (2009) demonstrated that a larger fraction of flux is coming out of low-to-mid latitude coronal holes for the SC 23 minimum period than for SC 22. Thus photospheric fields not in the polar regions are especially important contributors to the interplanetary flux for the recent minimum.

In Figure 4.6a we show information about the total solar magnetic flux coming out of the photosphere as a function of time, as estimated from the twenty-order spherical harmonic coefficients derived from the MWO synoptic maps. Each point in this plot represents one Carrington Rotation. Between the solar minimum and maximum periods, there is change by a factor of ten or more in the total photospheric flux. The figure highlights the small difference between the two cycle minimum periods shown in the gray shaded regions (the selection based on comparable sunspot numbers), taking into account that the SC 23 minimum period is longer. Within the shaded bands, the average photospheric field for SC 23 is 0.35 μT compared with 0.384 μT for SC 22. If the summed coronal hole areas in the Carrington maps are the same, we would expect the IMF field to be different by their ratio of $\sim 8\%$. However, as shown in Figure 4.2 and also as reported in previous studies (*e.g.,* Lee *et al.*, 2009b), the difference in the average IMF values from both minima is about 30%.

The fraction of the photosphere within coronal hole areas for each Carrington Rotation is shown in Figure 4.6b. The values are computed from the three source surface radii (red for 1.5 $R_\odot$, blue for 1.8 $R_\odot$, and black for 2.5 $R_\odot$) for the entire period from the SC 22 declining phase to the SC 23 minimum period (CRs 1864 to 2086). However, while we show them for completeness, we do not expect the solar maximum results (unshaded section in the center of the plot) with PFSS to be as accurate and do not discuss them here (see Riley *et al.*, 2006, for such a discussion). As expected from PFSS modeling, the fractional areas of the coronal holes become larger as we decrease the source surface radius. During the solar minimum periods

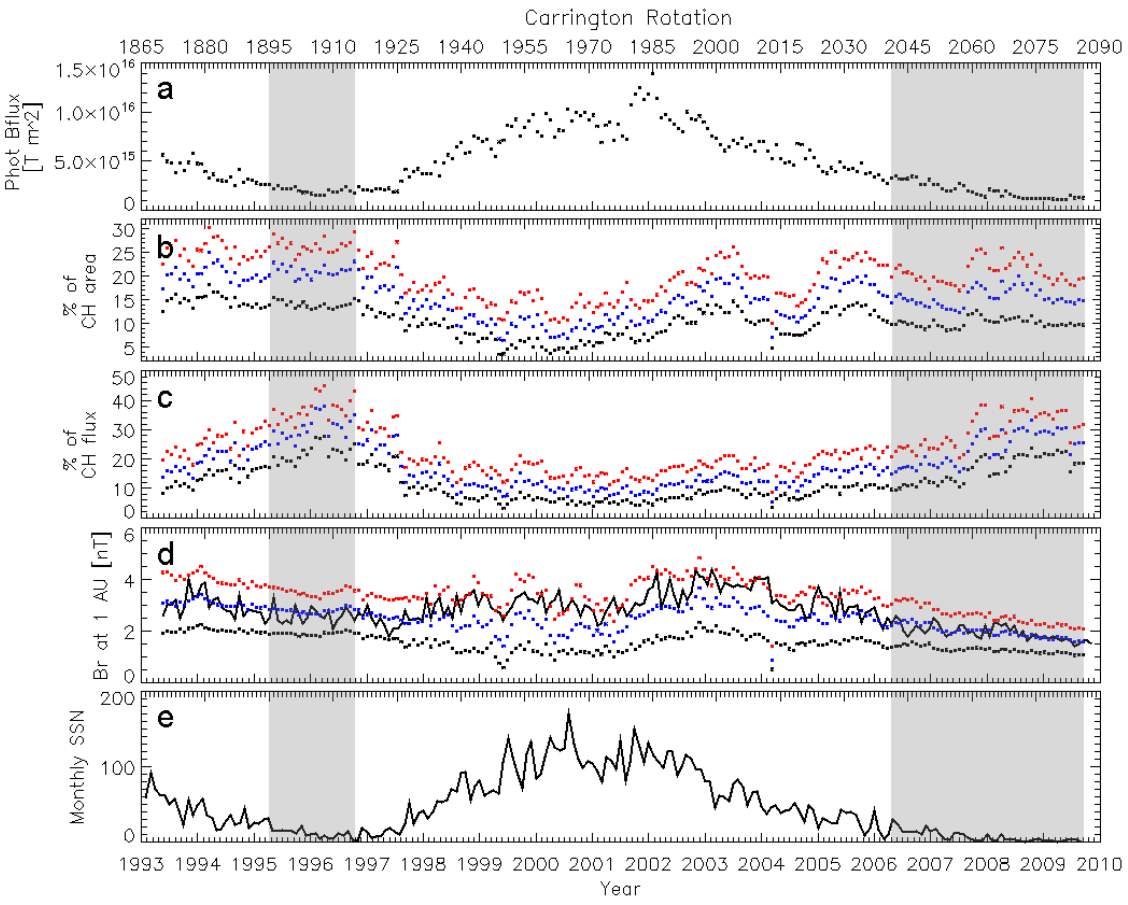

Figure 4.6: (a) Total flux emanating from the photosphere, (b) fraction of open coronal hole areas, (c) fraction of photospheric flux that maps to the source surface, (d) PFSS-inferred IMF at 1 AU versus Carrington Rotation-averaged OMNI observations (solid black line), and (e) monthly sunspot numbers. The colors shown represent the different source surface heights utilized in the calculations: 1.5 (red), 1.8 (blue), and 2.5 (black) $R_{\odot}$.

(gray shaded regions), for a given source surface value the fraction of open areas is smaller for the SC 23 minimum compared to SC 22. The difference is about 21%, 26%, and 27% for source surface values of 1.5 $R_{\odot}$, 1.8 $R_{\odot}$, and 2.5 $R_{\odot}$, respectively. This is in spite of that fact that Abramenko *et al.* (2009) and Wang, Robbrecht, and Sheeley (2009) found the fractional coronal hole areas are larger for the low-to-mid latitude regions for the SC 23 minimum period.

We show in Figure 4.6c the fraction of the photospheric flux that maps into

interplanetary space according to the PFSS model with the three source surface radii. For this analysis, we assume that all the heliospheric open flux originates in the coronal hole open field footpoints identified in the PFSS model. For a given source surface radius, the fraction mapped out has decreased for the SC 23 minimum period in comparison to the previous one. Specifically, the flux decreased by about 19%, 23%, and 25% for source surface radii of 1.5 $R_\odot$, 1.8 $R_\odot$, and 2.5$R_\odot$, respectively, during the current minimum period. So although this current minimum period has weaker globally integrated photospheric fields by about 8%, the general behavior of the open and closed photospheric fields and the fractional mapping of the photospheric fields into the heliosphere is quite different according to the PFSS modeling. We now ask the question of whether the production of the measured interplanetary field strength, which is less for SC 23 by about 30%, is determined in part by the source surface height itself.

In Figure 4.6d we use the OMNI data to compare with the PFSS-inferred radial IMF at 1 AU. The latter is calculated from the global source surface or open field flux under the assumption that radial IMF is independent of the heliographic latitude and varies in proportion to the (computed) open flux at the Sun (*e.g.,* see Smith and Balogh, 2008). The OMNI data (solid black line) for both minimum periods seems to be approximately described by the PFSS model when we use the source surface value of 1.8 $R_\odot$ (blue), although there is a slight suggestion of a larger source surface for the SC 22 minimum period. We note that OMNI data have been averaged over one Carrington Rotation in order to directly compare with the PFSS-inferred IMF values shown. Figure 4.7 further demonstrates that the 1.8 $R_\odot$ radius does the best of the three source surface radii in describing the IMF radial components at 1 AU in the solar minimum periods of this study. The histograms for the OMNI IMF (top panel) are similar to those shown earlier in Figure 4.2 but the data have been averaged over one Carrington Rotation. Following the same color scheme, the red (black) histograms are generated from data for the SC 23 (22) minimum period.

The small differences in the PFSS-inferred values for the two periods and the observations can be better understood from Figure 4.8. This figure shows the 1 AU IMF values predicted for each source surface radius for the data from each minimum period (dots connected by curves) compared to the average measured fields from the OMNI data (black for SC 22, red for SC 23). From power law fits to the data, the best source surface value for each minimum period are shown by the vertical dashed lines. The average in-situ IMF values from SCs 22 and 23 (2.6 nT and 1.9 nT, respectively) are shown as green horizontal bars. From the black and red

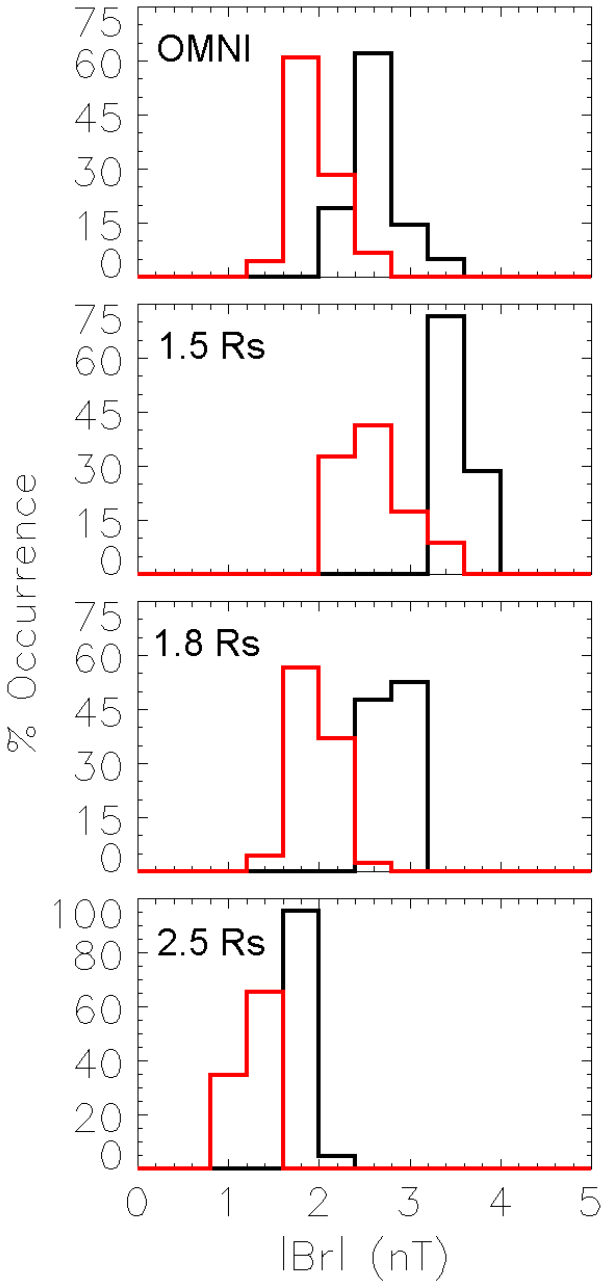

Figure 4.7: Histogram of occurrence for the Carrington Rotation-averaged OMNI radial field at 1 AU and the PFSS-inferred results using the 1.5, 1.8, and 2.5 $R_{\odot}$ source surface values. The red (black) data shown are for the SC 23 (22) minimum period.

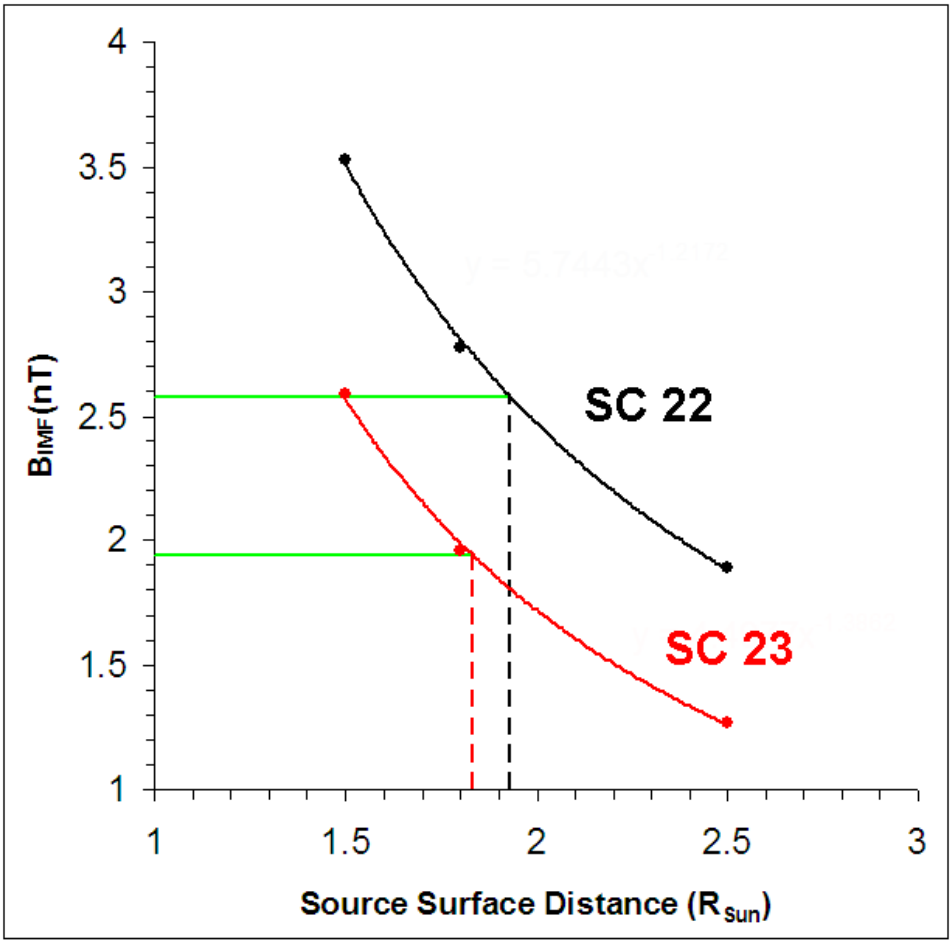

Figure 4.8: Best overall source surface values for SC 23 (red) or 22 (black) inferred from the median OMNI IMF values (green) from each respective solar minimum period. We obtain 1.93 and 1.83 $R_\odot$ for SCs 22 and 23, respectively, from power law fits to the data as shown.

dashed vertical lines, we obtain the best source surface radii of 1.93 $R_\odot$ and 1.83 $R_\odot$ for SCs 22 and 23, respectively. From the difference in the source surface heights required to obtain the observed IMF values, it is evident that a small change in the source surface value could explain the significant difference in the observed IMF. This method provides a more accurate way of understanding the interplanetary field strength than simply looking at the ratio of the photospheric fields without considering the coronal hole geometry and its outward mapping.

In addition to investigating the IMF strengths, we make a qualitative compar-

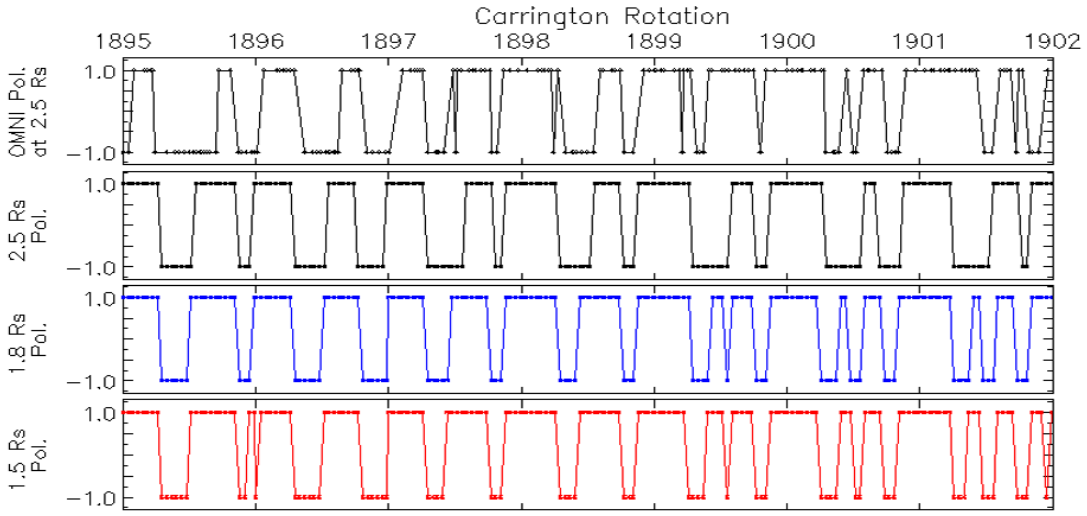

Figure 4.9: Daily-averaged OMNI polarity data and PFSS results for a selection of Carrington Rotations from the SC 22 minimum period. Each set of time series show (top) OMNI results projected back to 2.5 $R_\odot$ (black), together with the PFSS-derived polarities from source surface radius of (second) 2.5 $R_\odot$ in black, (third) 1.8 $R_\odot$ in blue, and (bottom) 1.5 $R_\odot$ in red.

ison of the PFSS-derived polarities with observations. Figures 4.9 and 4.11 show the polarity time series for a selection of Carrington Rotations from SCs 22 and 23, respectively. In each figure, we use the daily-averaged OMNI data which have been shifted backwards in time (a variable time shift based on the observed solar wind speed for each data element) such that the polarity values represent those at a distance of 2.5 $R_\odot$. We also use PFSS results of a similar time resolution as the OMNI data. For each set of Carrington groups shown in Figures 4.9 and 4.11, the OMNI data is shown in black in the top panel, and in the bottom three panels we show the PFSS results for 2.5 $R_\odot$, 1.8 $R_\odot$, and 1.5 $R_\odot$ (black, blue, and red, respectively). Overall the PFSS-derived polarities are quite comparable to the observations, although the timing of the sector boundary crossings sometimes differ.

If we compare amongst the three sets of PFSS results, we see that the predicted sector boundary crossings have different degrees of agreement. Panel a in Figures 4.10 and 4.12 shows the number of sector crossings for the same selection of Carrington Rotations shown in Figures 4.9 and 4.11. At times, the predicted number of crossings (2.5 $R_\odot$ in black, 1.8 $R_\odot$ in blue, and 1.5 $R_\odot$ in red) are in agreement with the observations (gray). However, the agreement does not occur for all three sets of PFSS results for a given Carrington Rotation. For example,

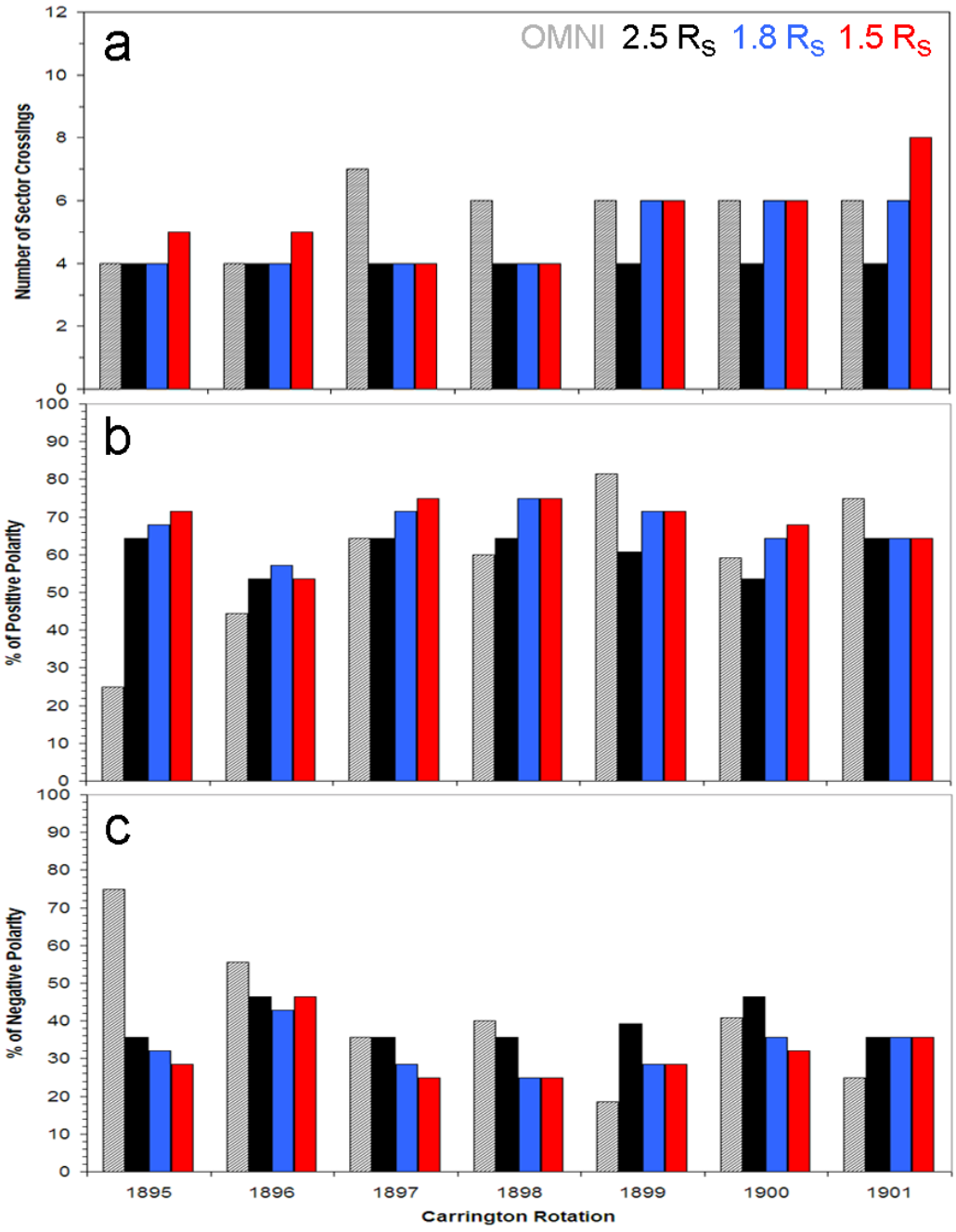

Figure 4.10: Statistics for Figure 4.9 showing (a) number of sector boundary crossings, (b) percent of positive polarity, and (c) negative polarity values for the daily-averaged OMNI data (gray) and the PFSS-derived polarities (2.5 $R_\odot$ in black, 1.8 $R_\odot$ in blue, and 1.5 $R_\odot$ in red).

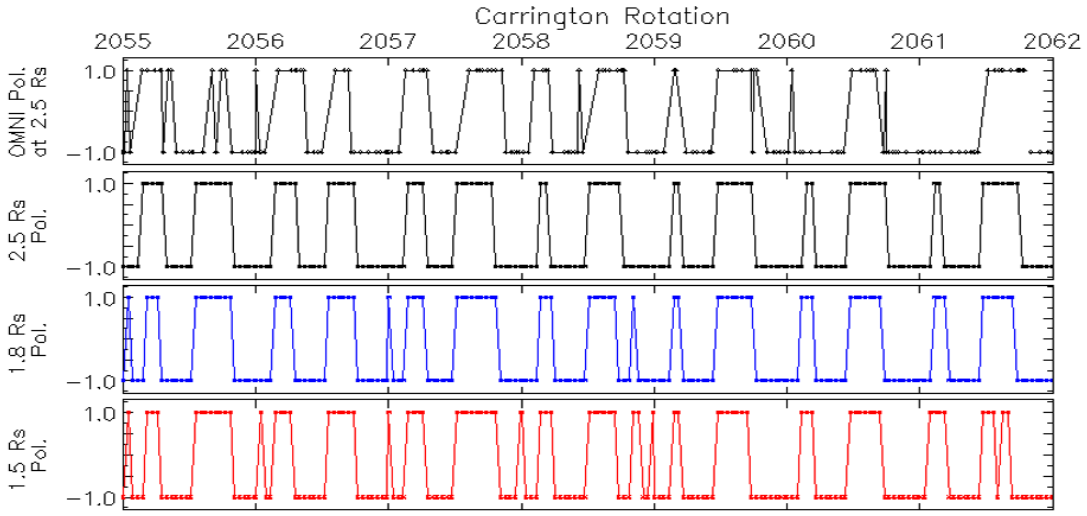

Figure 4.11: Daily-averaged OMNI polarity data and PFSS results for a selection of Carrington Rotations from the SC 23 minimum period. Each set of time series show (top) OMNI results projected back to 2.5 $R_\odot$ (black), together with the PFSS-derived polarities from source surface radius of (second) 2.5 $R_\odot$ in black, (third) 1.8 $R_\odot$ in blue, and (bottom) 1.5 $R_\odot$ in red.

during CRs 1895 and 1896 the 1.8 $R_\odot$ and 2.5 $R_\odot$ results are in agreement with the observations, but the 1.5 $R_\odot$ results predicted more crossings than observed. In another example, during CRs 1899 and 1900 the 1.5 $R_\odot$ and 1.8 $R_\odot$ results predicted the same number of crossings as the observations while the 2.5 $R_\odot$ results predicted fewer crossings. There are also times when only one out of the three sets of PFSS results are in agreement with the observations for a given Carrington Rotation (*e.g.,* CRs 1901, 2057, and 2058). In addition, there are times when all three sets of PFSS results predict too few or too many crossings (*e.g.,* CRs 1897, 1898, 2055, 2056, 2059, 2060, and 2061). Overall, the smaller PFSS source surface value of 1.8 $R_\odot$ seem to predict more often the observed crossings for the SC 22 minimum period. However, there does appear to be a particular source surface value that produces a majority agreement with observations for the SC 23 minimum period.

We show in panels b and c in Figures 4.10 and 4.12 the percent of positive and negative magnetic field polarity values, respectively. The percentage of predicted positive (or negative) polarity values is often within 20% of the observed values for both minimum periods. In general, there does not appear to be any one particular source surface value that always or most often produces the observed percentages, although there are few times when there is a match with the observations, such

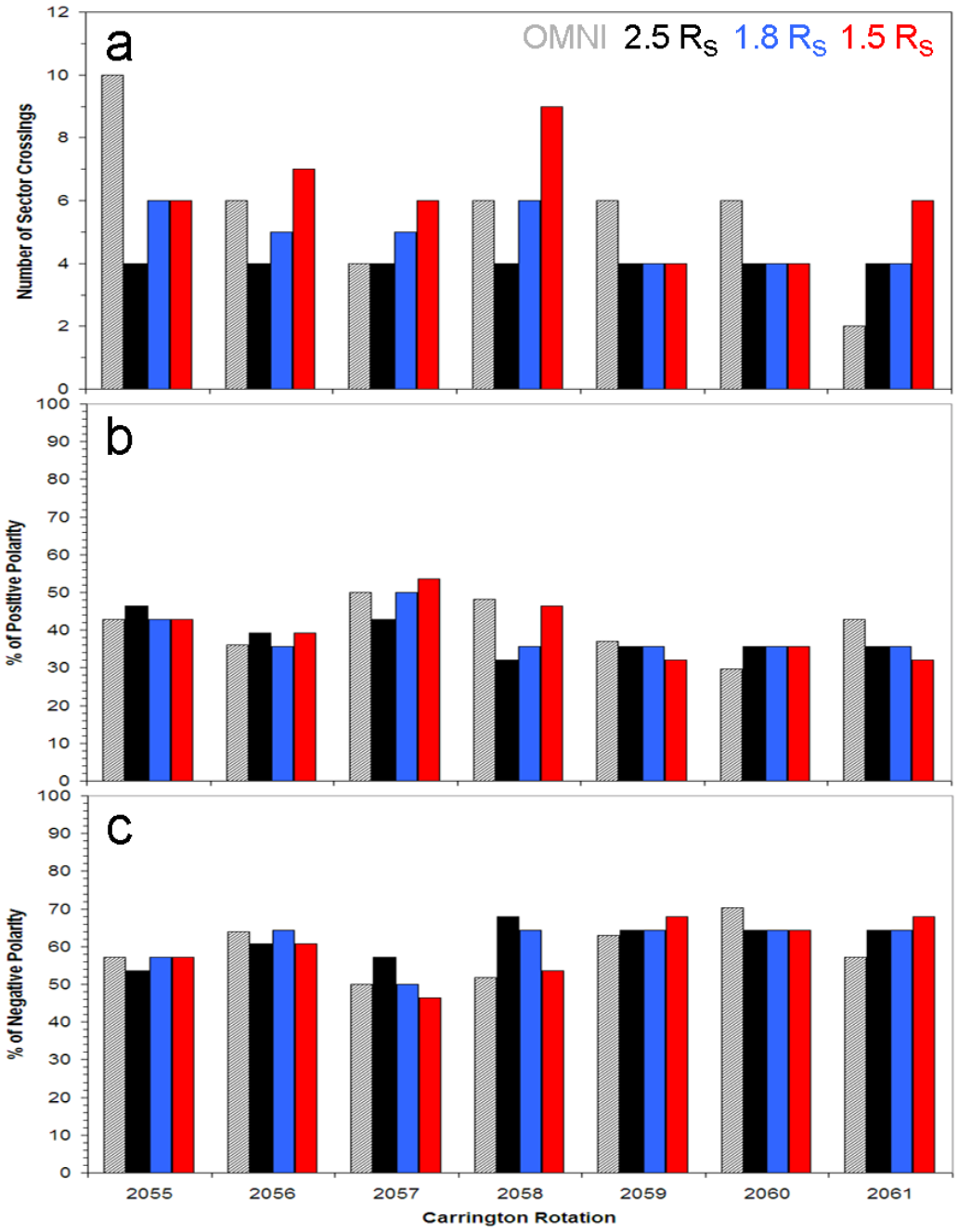

Figure 4.12: Statistics for Figure 4.11 showing (a) number of sector boundary crossings, (b) percent of positive polarity, and (c) negative polarity values for the daily-averaged OMNI data (gray) and the PFSS-derived polarities (2.5 $R_\odot$ in black, 1.8 $R_\odot$ in blue, and 1.5 $R_\odot$ in red).

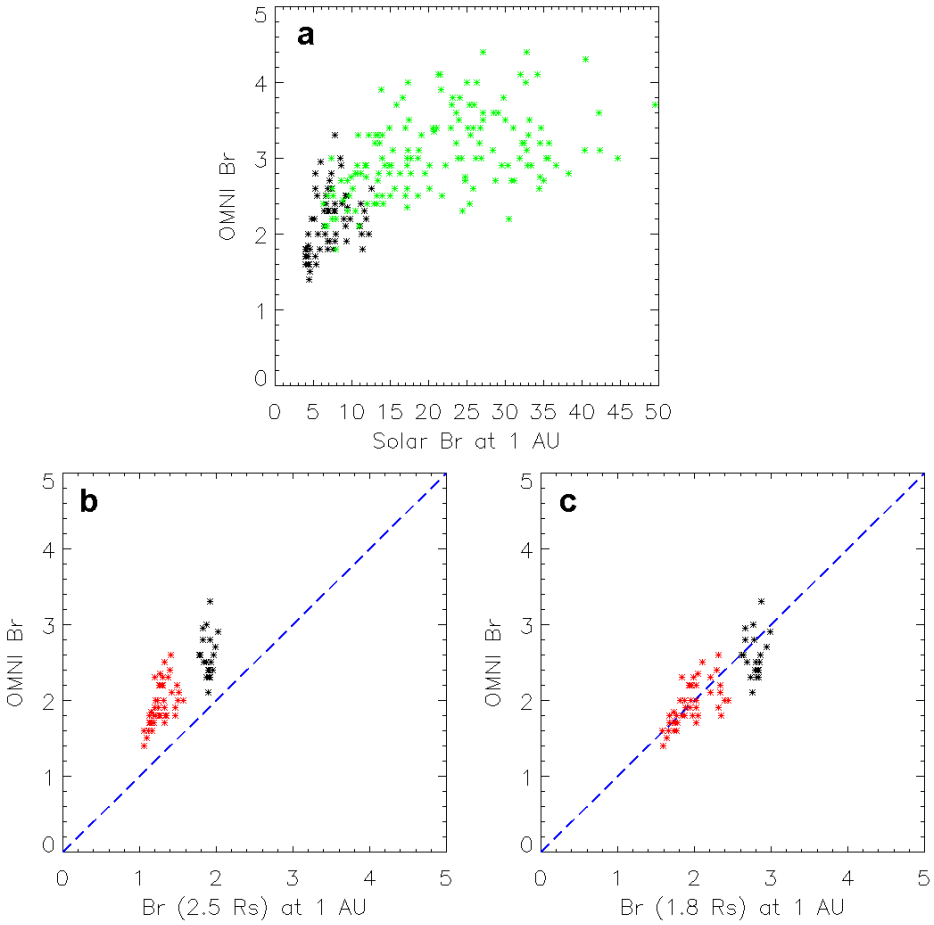

Figure 4.13: Correlation of the IMF values from observations and PFSS-derived results. (a) In-situ IMF with the PFSS-calculated photospheric fields projected to 1 AU for CRs 1865 to 2086. The black color marks the solar minimum period data shown in the shaded regions in Figure 4.6d whereas the green color marks data outside this period. (b) In-situ IMF with the PFSS-inferred IMF using the 2.5 $R_\odot$ source surface radius. Here we only show the data for the SC 22 and 23 minimum periods, color coded in red and black, respectively. (c) The same but for the 1.8 $R_\odot$ source surface radius. Values shown are in nanoTesla units.

as during CR 1897 in Figure 4.10b (2.5 $R_\odot$ matches) and CRs 2055 to 2057 in Figure 4.12b (1.5 and/or 1.8 $R_\odot$ matches). As a side note, the unbalanced field polarities in the PFSS-derived values can be observed for both minimum periods, which is consistent with the in-ecliptic 1 AU observations (see Figure 4.2b). Such

unbalanced fields are commonly observed (*e.g.,* Hiltula and Mursula, 2006) and can be envisioned as a signature of the greater divergence of a particular sign of the open coronal fields (Lee *et al.*, 2009b).

The analyses of the IMF magnitudes and polarities described above suggest that the 1.8 $R_{\odot}$ source surface radius is the most appropriate value to use in PFSS model applications in this current solar minimum period for this comparison. To further illustrate this, we correlate our PFSS results with the individual Carrington Rotation-averaged IMF observations shown in Figure 4.13. In panel a, we compare the interplanetary field observed at 1 AU with those derived from the total solar photospheric flux for the entire period shown in Figure 4.6d (CRs 1865 to 2086). For the IMF calculated from the total photospheric flux, we utilize flux conservation and determine the IMF values for a sphere with a radius of 1 AU. The green dots indicate the data in the unshaded portion in the top panel of Figure 4.6d, which is largely the solar maximum period, while the black dots mark the data from the minimum periods. Figures 4.13b and 4.13c illustrate the departure from proportionality if we simply assumed a direct relationship between the observed solar magnetic field and the measured IMF, not taking into account the areas and the locations of the coronal holes. In panel b we plot values for only the minimum periods (red for SC 23, black for SC 22) as shown by the shaded regions in Figure 4.6d using the OMNI data set and the PFSS-derived results based on the commonly used source surface radius of 2.5 $R_{\odot}$. Overall, the correlation with the observed IMF is not centered on the slope 1 line (blue dashed line). However, the correlation with the PFSS-derived values based on the source surface radius of 1.8 $R_{\odot}$, shown in panel c, is much closer to 1:1. The spread in the IMF values in the y-direction for the SC 22 minimum period is modestly larger ($\sim$ 11%) in comparison to the spread in the values for the SC 23 period ($\sim$ 8%).

4.4 Conclusions

Overall, using a smaller source surface value seems to make a significant difference in the prediction of the IMF strength from the PFSS model for both minimum periods, where a slightly larger value for the previous minimum period may be better, as suggested in Figure 4.8. A smaller source surface height for this current minimum period compared to the previous one is consistent with the MHD equations for the location of the cusp point of the coronal streamer, as discussed in the study by Pneuman and Kopp (1971). If the cusp location is used as a proxy for the source surface height, Eq. (1) from that study suggests that the weaker solar fields will produce cusp points that are closer to the solar surface, *e.g.*, the source surface

height will be lower. Such results (also Steinolfson, Suess, and Wu, 1982) suggest that the coronal pressure is not strongly dependent on the photospheric field in the largest–scale loops and open field regions, but that instead, the photospheric field strength and distribution control the solar wind fluxes by determining the source regions (location and area).

There are several conclusions from this study of potential practical use:

1) Several factors must be considered when inferring the interplanetary field strength from photospheric field strength, including the locations of the open fields (polar latitudes versus low-to-mid latitudes) and the sizes of the open field areas. Thus, in any PFSS modeling application that presumes one source surface height without some careful consideration of the mapping details, the results should be viewed with some caution.

2) As Figure 4.8 illustrates, a small change in source surface height can explain an inherent discrepancy between modeled and observed IMF values. Simply taking changes of the photospheric fields as a measure of the change in the IMF (as in panel a of Figure 4.13) is inadvisable. Future PFSS modeling efforts (*e.g.,* that of Wang, Robbrecht, and Sheeley, 2009) should probably treat the source surface height as another parameter, especially when trying to predict long term trends.

3) In a previous study, Lee *et al.* (2009a) found that the numerical model-generated values for the magnetic components of the total field were often underestimated by a factor of 2. It is possible that the boundary conditions, such as the source surface height of $2.5R_{\odot}$, used to drive the coronal component of the coupled corona-solar wind models could contribute to the underestimation of the magnetic field values. This will need to be tested in the near future by the model developers, possibly by using the smaller source surface values derived from this study in future model calculations and comparing the values with observations.

Chapter 5

Organization of Energetic Particles by the Solar Wind Structure During the Declining to Minimum Phase of Solar Cycle 23

Abstract

We investigate the organization of the low energy energetic particles ($\leq$ 1 MeV) by solar wind structures, in particular corotating interaction regions (CIRs) and shocks driven by interplanetary coronal mass ejections, during the declining to minimum phase of Solar Cycle 23 from Carrington Rotation 1999 to 2088 (January 2003 to October 2009). Because CIR-associated particles are very prominent during the solar minimum, the unusually long solar minimum period of this current cycle provides an opportunity to examine the overall organization of CIR energetic particles for a much longer period than during any other minimum since the dawn of the Space Age. We find that the particle enhancements associated with CIRs this minimum period recurred for many solar rotations, up to 30 at times, due to several high–speed solar wind streams that persisted. However, very few significant CIR-related energetic particle enhancements were observed toward the end of our study period, reflecting the overall weak high–speed streams that occurred at this time. We also contrast the solar minimum observations with the declining phase when a number of solar energetic particle events occurred, producing a mixed particle population. In addition, we compare the observations from this minimum period with those from the previous solar cycle. One of the main differences we find is the shorter recurrence rate of the high–speed solar wind streams ($\sim$ 10 solar rotations) and the related CIR energetic particle enhancements for the Solar Cycle 22 minimum period. Overall our study provides insight into the coexistence of different populations of energetic particles, as well as an overview of the large-scale organization of the energetic particle populations approaching the beginning of Solar Cycle 24.

5.1 Introduction

Using data accumulated over the declining to minimum phase of Solar Cycle 23 (hereafter SC 23), we investigate the organization by the solar wind structure of the energetic ions (0.3 to 0.7 MeV) and electrons (0.05 to 0.1 MeV) from different particle populations. In particular, we focus on the energetic particles that are associated with corotating interaction regions (CIRs) and those associated with solar events. Depending on the phase of the solar cycle, these two populations of energetic particles can mix with each other at times. The heliospheric distribution of the energetic particles and its dependence on the solar cycle phase is of interest since it tells us about the big picture of particle acceleration in the vicinity of the Sun-like stars.

Figure 5.1 (top) illustrates a stream structure that corotates in the solar equatorial plane in the inner heliosphere. A CIR forms where a high–speed stream originating in a coronal hole runs into the slower speed stream that precedes it. In the declining speed region of the high–speed stream, a rarefaction region forms. As the coronal holes that give rise to the high–speed streams may persist for several solar rotations, the streams may be observed to recur one or more times at intervals of the solar rotation period ($\sim$27 days as viewed from the Earth). Such recurring streams are very prominent during both the declining phase and the minimum period of the solar cycle (Richardson, 2004).

Shocks associated with CIRs can accelerate solar wind particles and produce energetic particles. Typically, these shocks form beyond Earth at 1 astronomical unit (AU) and accelerate energetic particles that stream into the inner heliosphere (*e.g.,* Barnes and Simpson, 1976; van Hollebeke *et al.*, 1978). However, CIR shocks can also form at and within 1 AU (Gosling and Pizzo, 1999; Forsyth and Marsch, 1999; Schwenn, 1990), and energetic particles associated with such CIRs may also be locally accelerated even in the absence of shocks. A typical intensity–time profile of CIR particles observed at 1 AU is shown in Figure 5.1 (bottom panel). In this example, each shaded area in the profile indicate particle increases due to CIRs that appeared on four successive 27-day solar rotations. The figure shows that CIR-related particles are found in the high–speed stream, consistent with the particles being accelerated at the reverse shock and streaming to 1 AU inside the high–speed stream.

Figure 5.1 (bottom panel) also shows that between the successive CIR–related particle events, there are particle increases related to solar events, as shown in the unshaded portions. Solar activity such as impulsive flares and coronal mass ejections can accelerate particles and produce a particle population called solar

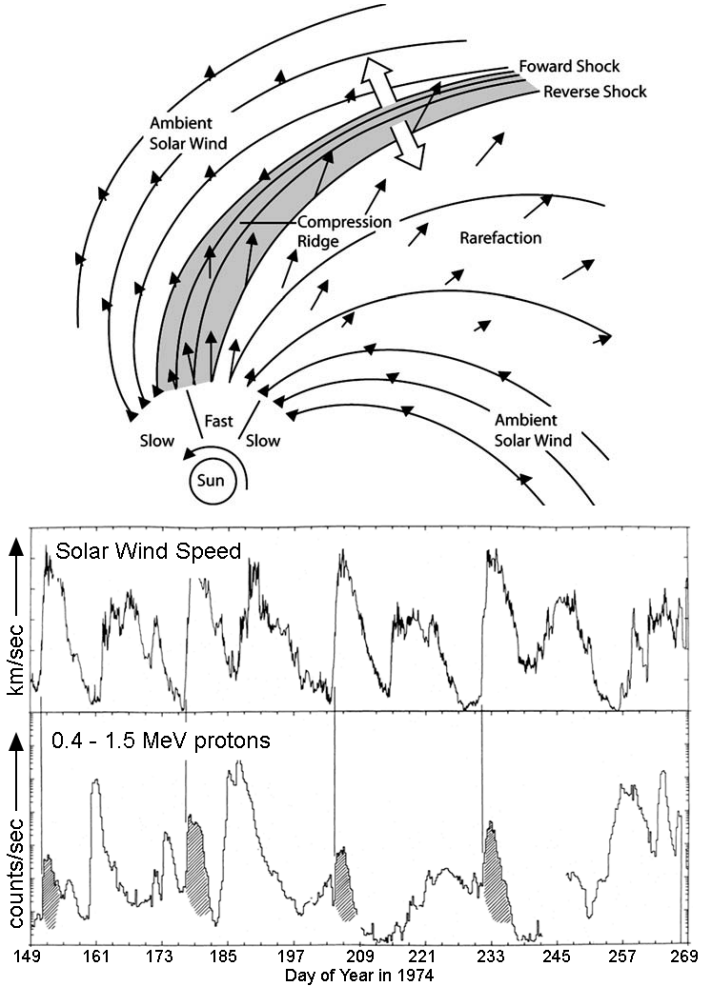

Figure 5.1: (top) Illustration of a 2D stream structure in the solar equatorial plane of the inner heliosphere (adapted from Pizzo, 1978; Jian *et al.*, 2006). (bottom) Solar wind speed and energetic proton intensity observed by the IMP–8 spacecraft (adapted from Mason and Sanderson, 1999; Scholer *et al.*, 1979). The shaded profiles indicate events associated with corotating high–speed streams whereas the unshaded profiles are related to solar events.

energetic particles (SEPs). At the Sun, impulsive flares locally accelerate particles to higher energies. Such flare-accelerated SEPs can have very prompt signatures in the intensity–time profiles observed at 1 AU, as shown in Figure 5.2. These SEP intensities rise abruptly before settling back to the ambient level a couple of days later.

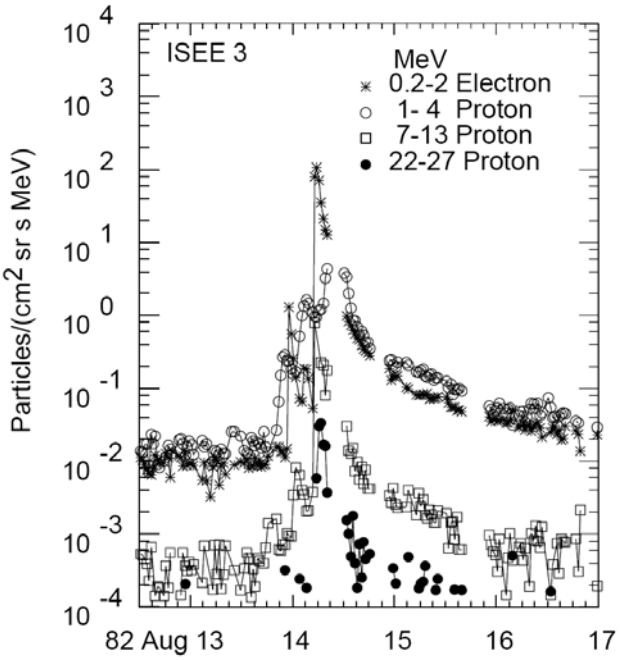

Figure 5.2: Intensity–time profiles of energetic electrons (0.2 to 2 MeV) and protons (1 to 4 MeV, 7 to 13 MeV, and 22 to 27 MeV) associated with solar flare events, as measured by ISEE-3. Figure adapted from Reames (1999).

Interplanetary coronal mass ejections (ICMEs) produce SEPs that have highly variable intensity–time profiles that are different from the flare-related particle signatures. ICMEs may extend in solar longitude from ∼50° (full-width) to 100° (full-width) for more energetic events, their associated shock front can be even broader (Wimmer-Schweingruber *et al.*, 2006, and references therein). Thus, as Figure 5.3 shows, the observed SEP intensity–time profiles will differ for the same CME event depending on where the observer is longitudinally connected to the CME shock, as discussed by Cane, Reames, and von Rosenvinge (1988), Reames (1999), and Cane and Lario (2006). It is the ICME shock that accelerates the particles magnetically connected with it, energizing the particles to intensity levels that can be greater than those related to CIR or impulsive flare events.

Solar events can occasionally occur during solar minimum and more frequently during the declining phase of the solar cycle. When solar events do occur during the minimum period, they can produce a SEP population that is mixed in with the CIR particle population such that the intensity–time profiles for this situation could be a combination of those that were shown in Figures 5.1 to 5.3. During such mixed

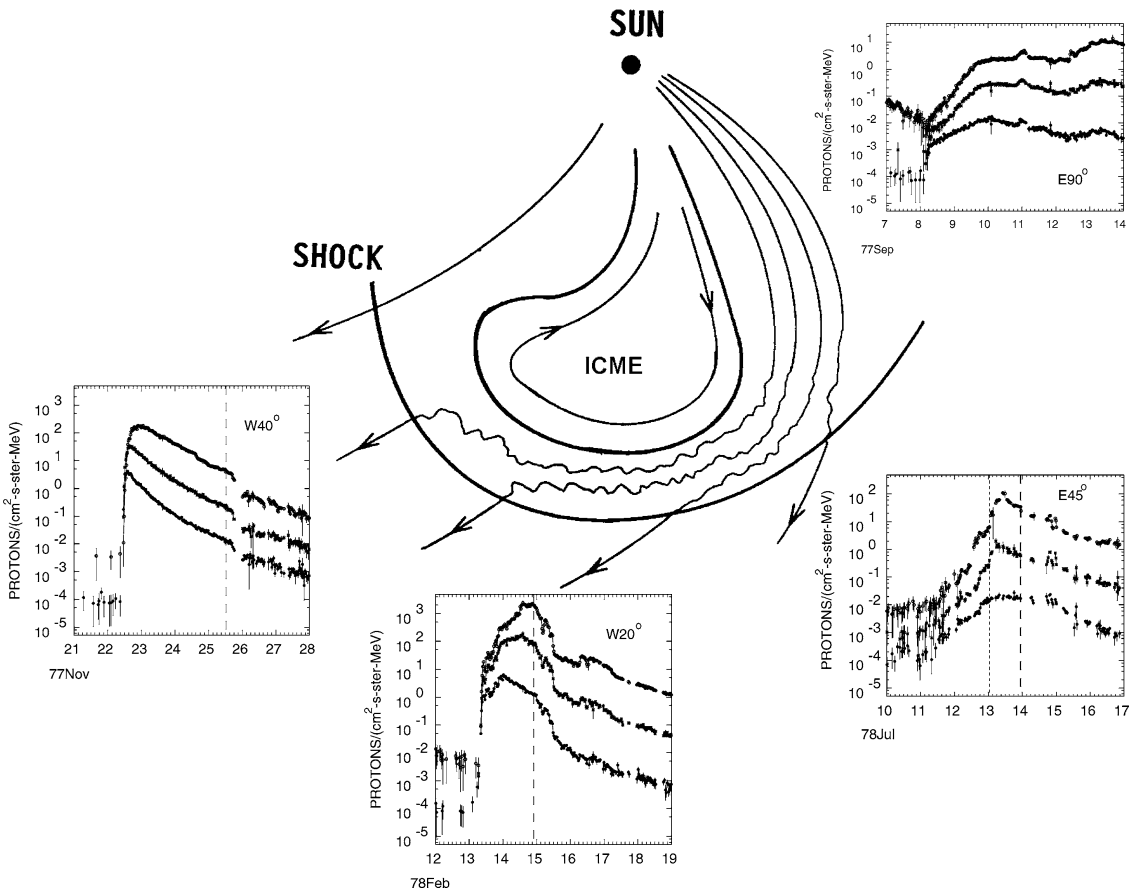

Figure 5.3: A cartoon illustration of a CME and its related shock. Also shown are time–intensity profiles for protons of ∼5, ∼15, and ∼30 MeV, as observed by the IMP-8 spacecraft. The profiles differ in shape for a given CME event depending on where the observer is located in solar longitude with respect to the CME ejecta and its related shock front. Dashed lines denote the times of the shock passages. Figure from Cane and Lario (2006).

event periods, the use of particle composition information can help to distinguish the different sources of the energetic particles. For example, the ^{3}He isotope, which is rare in the solar wind, is a very good indicator for impulsive events since they are the only known source (Desai *et al.*, 2006a; Mewaldt *et al.*, 2007).

With the extended solar minimum period of SC 23, there is an opportunity for us to examine the overall organization of the near–ecliptic energetic particles at 1 AU for a much longer solar minimum period than is typical. From this study, we wish to understand how the CIR particle characteristics such as intensity and

recurrence depend on the solar wind structure, especially the steepness and strength of their associated stream interactions, and whether the presence of SEPs affect the CIR events, such as increasing their intensities.

Our study is motivated by that of Sanderson *et al.* (1998) which used Wind spacecraft data (Ogilvie and Desch, 1997) to examine how the current sheet and compression regions controlled the observed CIR–related particle intensities at 1 AU during the solar minimum period between Solar Cycles 22 (hereafter SC 22) and 23. Their main conclusions were that the tilt and warp of the heliospheric current sheet plays an important role in determining the shape and pattern of high–speed solar wind streams and compression regions, all of which influence the intensities and occurrences of the energetic particles. Simply stated, the CIR particle events are organized by the structure of the solar wind streams. However, it is unclear whether variations in CIR particle event intensities are solely due to the characteristics of the solar wind stream interaction regions.

We will focus on the declining–to–minimum phase of SC 23, specifically, the > 6.5 year period from 23 January 2003 to 13 October 2009 (Carrington Rotations 1999 to 2088). We use particle data from the Electron, Proton, and Alpha Monitor (EPAM, Gold *et al.*, 1998) and the Ultra-Low Energy Isotope Spectrometer (ULEIS, Mason *et al.*, 1998) onboard the *Advanced Composition Explorer* (ACE) spacecraft located in orbit about the sunward Lagrangian point (L_1). We obtain the Level-2 hourly averaged EPAM data from the ACE Science Center (http://www.srl.caltech.edu/ACE/ASC/) and the ULEIS Level-2 hourly data from the NASA Goddard Space Flight Center Space Physics Data Facility (http://spdf.gsfc.nasa.gov/). For the plasma and magnetic field measurements we use the hourly OMNI data sets obtainable from http://omniweb.gsfc.nasa.gov/.

In Section 2 we discuss the global characteristics and recurrent features that are observed in the solar wind structure at 1 AU for our period of interest. In Section 3 we investigate the organization of the energetic particles and how they relate to the solar wind structure. In Section 4 we evaluate the types of particle events that occurred and how they may be related to the particle intensities observed. In Section 5 we compare some of the results for this minimum period with those from SC 22. Finally in Section 6 we summarize our results.

5.2 Solar wind structure

Figures 5.4 to 5.7 summarize the primary data during our period of study in a standard time series format. These include the key parameters for a study of solar wind structure relationships to the energetic particle characteristics. The

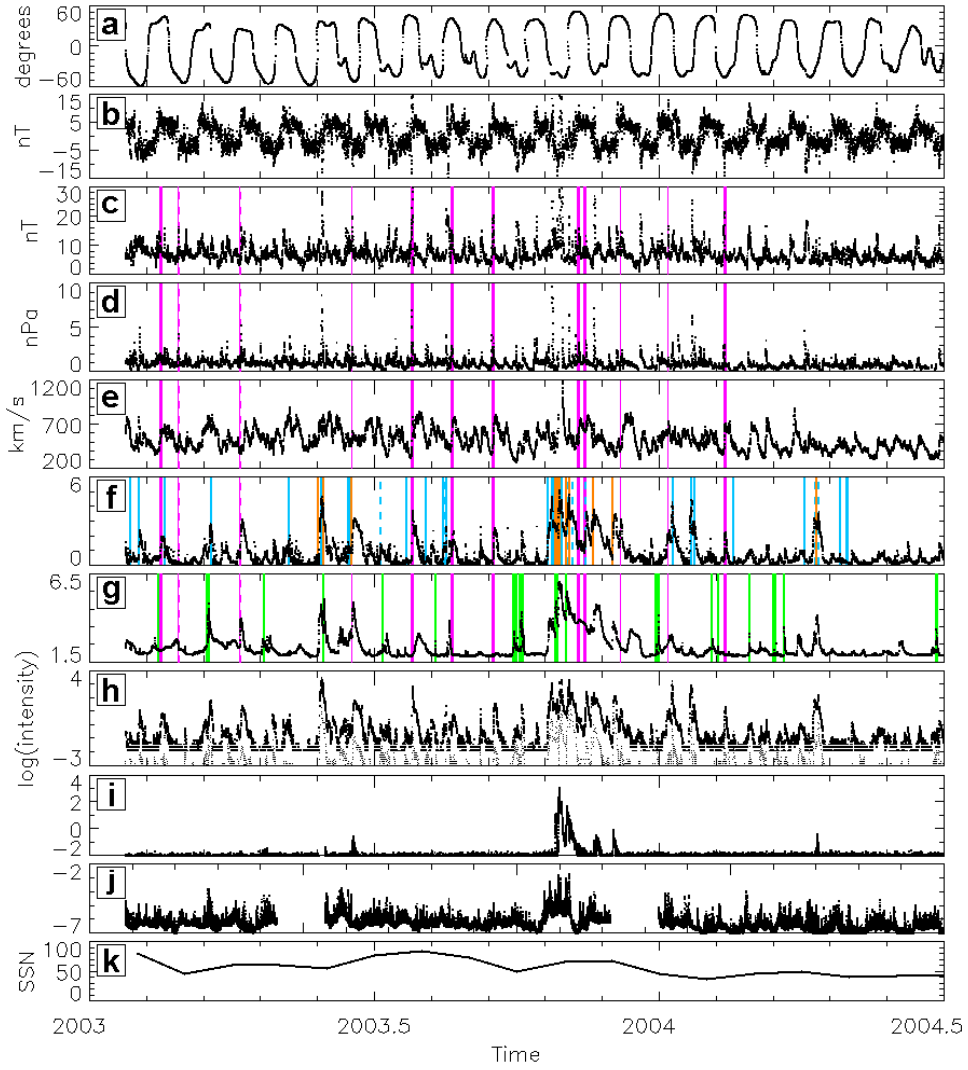

Figure 5.4: Time series from 2003 to 2004.5 of the (a) calculated distance of the HCS neutral line from the solar equator, (b) radial magnetic field, (c) total magnetic field, (d) dynamic pressure, (e) velocity, (f) EPAM 0.31 to 0.58 MeV energetic ions, (g) EPAM 0.053 to 0.103 MeV energetic electrons, (h) ULEIS 0.32 to 0.453 MeV n^{-1} ^{4}He (thick black) and ULEIS 0.32 to 0.64 MeV n^{-1} Fe (thin black) ions, (i) GOES–10 15 to 40 MeV protons, (j) GOES–10 1–8 Å X–ray flux data, and (k) monthly sunspot numbers. Color bars denote start times of various events that are discussed in Section 5.4: thin (thick) magenta for SIR (CIR) events, cyan for CME events, orange for SEP particle events, and green for beamed–electron events. The related shock event times are plotted as dashed bars using the same color scheme. We use hourly averaged data for (b) to (h) and 5-minute averaged data for (i, j).

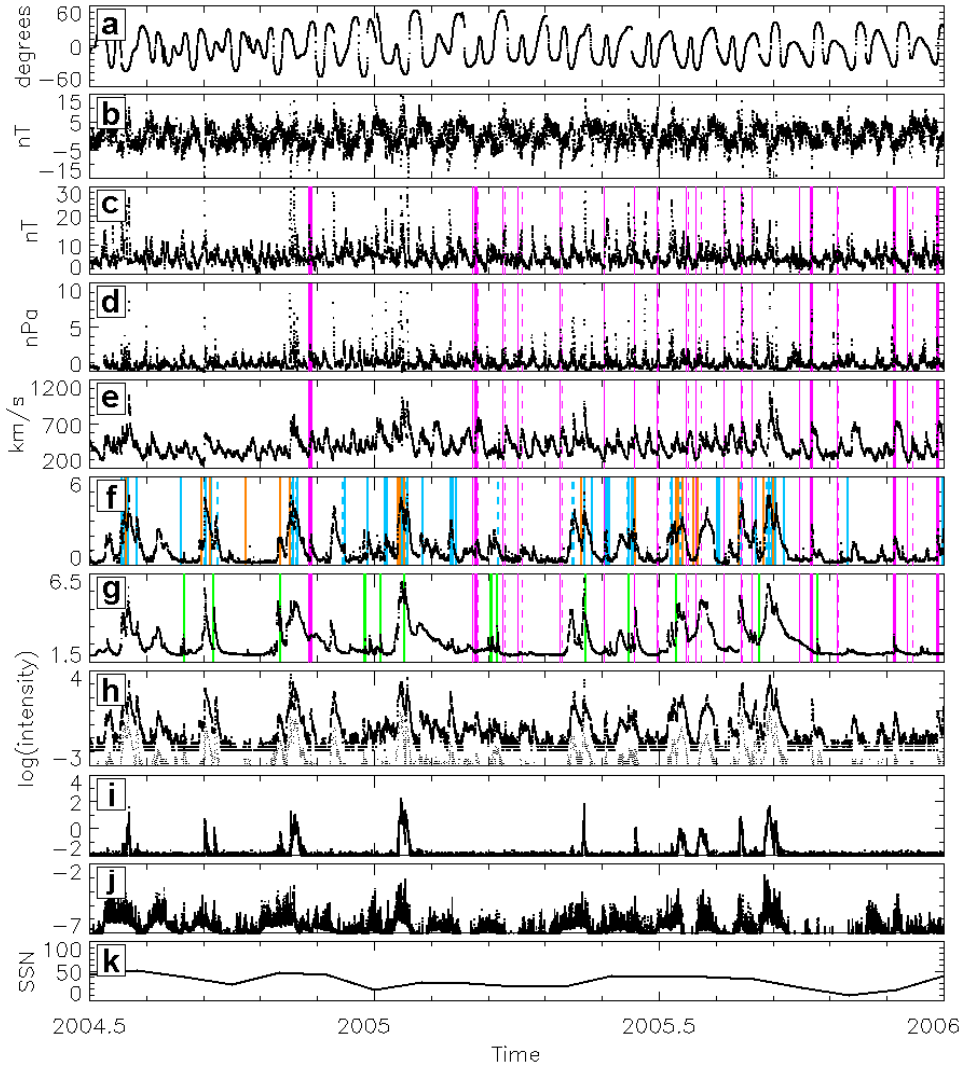

Figure 5.5: As for Figure 5.4 but from 2004.5 to 2006.

top panel (a) shows the approximate heliolatitude of the ecliptic plane from the heliospheric current sheet (HCS), calculated from the photospheric field synoptic map-based Potential Field Source Surface models of the coronal magnetic field (Schatten, Wilcox, and Ness, 1969; Altschuler and Newkirk, 1969). The progression from Figures 5.4 through 5.7 illustrates the simple dipolar (or two sector per solar rotation) structure of the HCS in the early part of the study interval, compared to the gentler, more quadrupolar warp observed in the later parts. The flattening of the warp during the last three years is notable and is expected during the descent

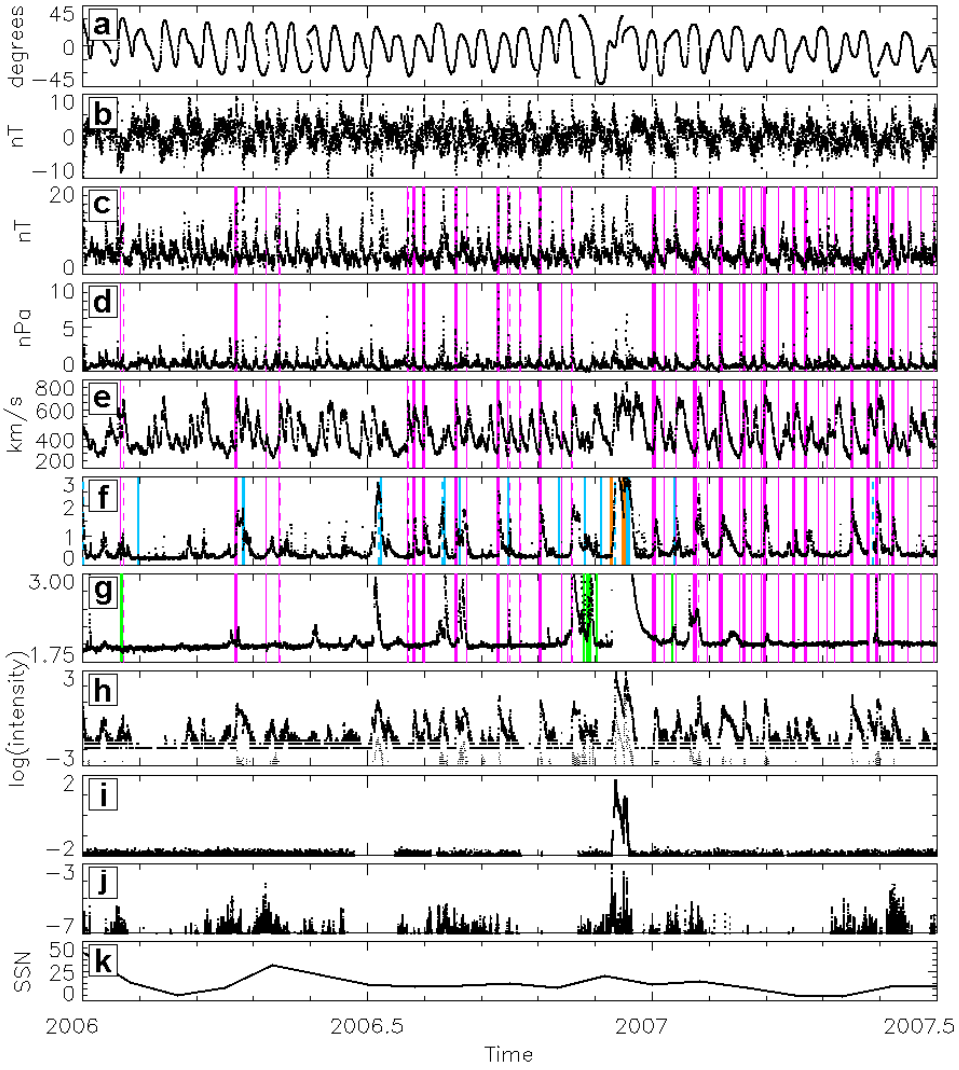

Figure 5.6: As for Figure 5.4 but from 2006 to 2007.5.

into a solar minimum period. The OMNI radial and total magnetic fields (panels b and c) indicate the interplanetary field polarity and strength at 1 AU, respectively. These are followed by the solar wind dynamic pressures and velocities (panels d and e). The next four panels contain samples of energetic particle measurements from the ACE (panels f to h) and GOES (panel i) spacecraft, providing an overview of the ion and electron populations at energies > 100 keV. The last two panels (j and k) provide the GOES X–ray flux and the monthly sunspot numbers for context.

To get a better sense of the recurring features of the solar wind structure over

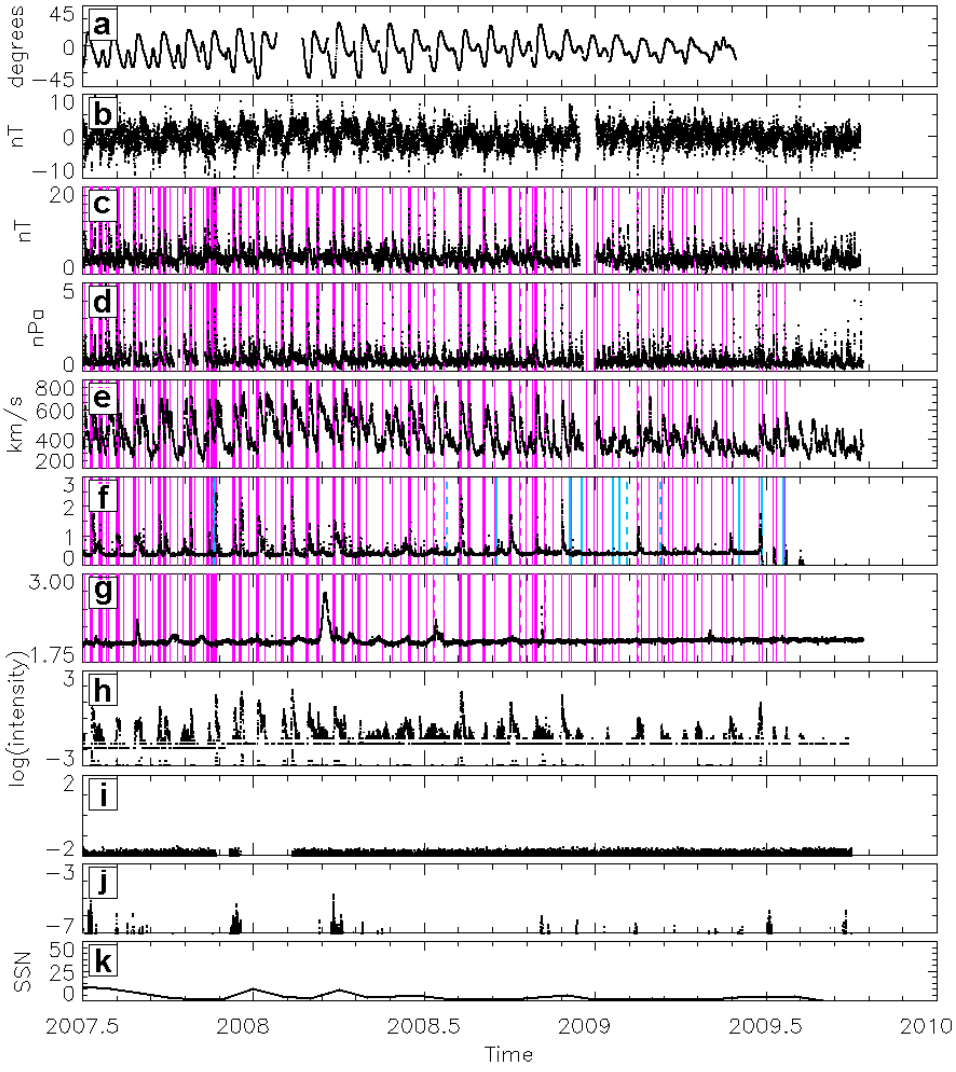

Figure 5.7: As for Figure 5.4 but from 2007.5 to 2010.

a large range of solar rotations (*e.g.*, one Carrington Rotation, which takes 27.2753 days as viewed from Earth), we adopt a different plot style to display the parameters shown in Figures 5.4 to 5.7. Figure 5.8 shows the color contour of the data, where the x-axis displays the Carrington Rotation (CR) number (1999 to 2088) with the corresponding rotation commencement date indicated every 10 rotations, the y-axis displays the time in days since the beginning of the CR (1 to 27.3), and the color represents the value of the parameter. Similar types of plots were used in Sanderson *et al.* (1998) and also by Lee *et al.* (2009b) to analyze the solar

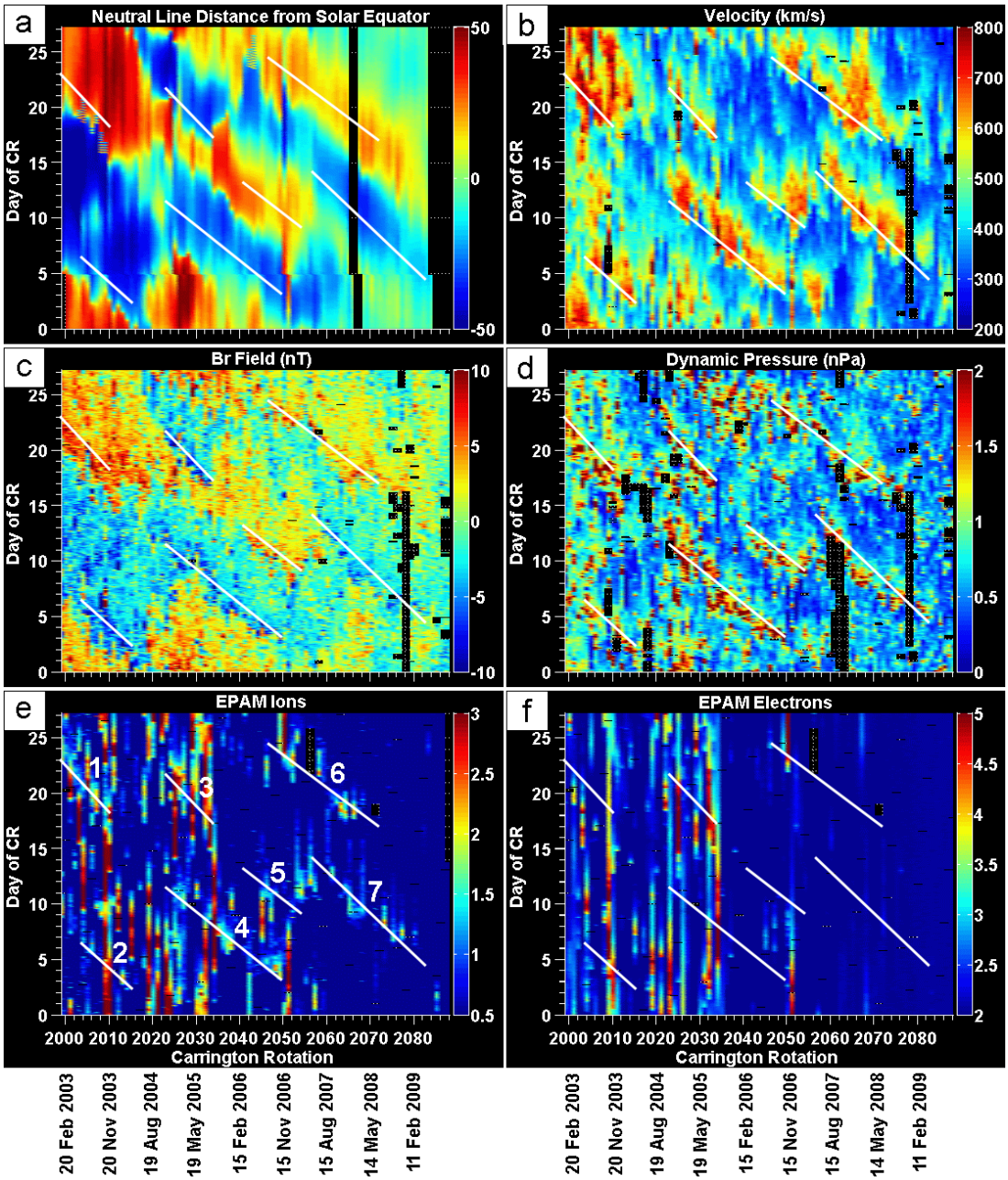

Figure 5.8: Shown are 1 AU color contour plots from CRs 1999 to 2088 for (a) the calculated distance (degrees) of the HCS neutral line from the solar equator, (b) velocity (km s^{-1}), (c) radial magnetic field (nT), (d) dynamic pressure (nPa), (e) EPAM 0.31 to 0.58 MeV energetic ions, and (f) EPAM 0.053 to 0.103 MeV n^{-1} electrons. White slanted lines and the number 1 to 7 mark the locations of features discussed in the text. Black gaps shown throughout are bad or missing data.

wind and interplanetary field structure over the previous solar cycle. This format brings out recurrent versus nonrecurrent behavior and also allows relationships to be visualized. Both the time series and color contour plots will be used concurrently in the discussion below to describe the features of solar wind structure.

We begin by investigating the structure of the HCS at 1 AU. Figure 5.8a shows the color contour of the heliographic position of the solar neutral line at 1 AU for our period of study. The distance of the neutral line from the solar heliographic equator was calculated for a radial distance of 2.5 $R_{\odot}$ from the potential field source surface coefficients (C.N. Arge, private communication, 2009) derived from synoptic maps constructed from archived Mount Wilson Observatory magnetograph images. The results were linearly time–shifted by five days, the time for the solar wind to reach 1 AU at an average speed of $\sim$345 km s^{-1}, to allow cross-comparison with the solar wind and energetic particle observations at 1 AU. Note that we do not take into account the $\pm 7^{\circ}$ excursion of Earth in heliolatitude.

During our period of study, the HCS transitioned from a steep, two–sector structure (deep reds and blues in Figure 5.8a) to a flatter, four–sector structure (yellows and greens). From CRs 1999 to 2018 (*i.e.* declining phase), the HCS was substantially tilted and often inclined at $\geq 40^{\circ}$ (see Figure 5.4a). The HCS maintained its steepness when it transitioned to a four–sector structure around CR 2018 (around 2004.5 in Figure 5.4a). However, after the transition the inclination angles fluctuated for a number of solar rotations (*e.g.*, from CRs 2018 to 2032) before returning to a relatively steady maximum inclination angle of around $\pm 30^{\circ}$ (see Figure 5.5a). The HCS gradually decreased in steepness during solar minimum, but it became very warped. Around CR 2056 until the end of the interval shown in Figure 5.8a, one of the northern folds in the HCS flattened out (green) so that the HCS is north of the equator for about one quarter of a rotation, and near or south of the equator for about three quarters of a rotation. This warping, which gave the ecliptic field a notable unbalanced polarity distribution, can also be seen in the time series after 2007.3 (Figures 5.6a and 5.7a).

As expected, the pattern of the magnetic sectors is similar to that in the HCS (compare Figures 5.8c with 5.8a). During our study interval, the solar magnetic field was directed inward at the solar north pole and outward at the solar south pole. Consistent with this, the interplanetary magnetic field (IMF) at Earth is generally directed away from the Sun (radial field is positive) when the HCS is displaced to the north, and toward the Sun (radial field is negative) when the HCS is displaced to the south. The timing of the observed magnetic sector and the calculated HCS sector boundaries are also noticeably similar, particularly during the periods between CRs

1999 to 2018 as well as CR 2060 to the end of interval. Thus in general, our manual time–shifting by five days of the calculated HCS structure at 2.5 $R_\odot$ to 1 AU is a good approximation.

Throughout our study interval, regions of compressed fields can be seen at the leading edges of the magnetic field sectors (either in red for away or deep blue for toward the Sun, Figure 5.8c). From 2003 to 2006 during the declining phase, the time series (Figures 5.4c and 5.5c) show the peak total magnetic field strength often reached or exceeded 20 nT. Afterward, during the approach to the solar minimum period, the peak total field strength was mostly below 20 nT (Figures 5.6c and 5.7c). We note that during the extended minimum period, the peak total field strengths were < 10 nT, whereas the radial field strengths were ± 5 nT or less (see Figure 5.7c, 2009.2 to 2009.5 and 2009.7 to 2009.8).

Field values of $\geq$30 nT due to shocks and ICMEs following solar events were also observed during the declining phase. Panels f to i in Figures 5.4 to 5.7 show the < 1 MeV n^{-1} energetic ion and electron intensities as well as the $\geq$15 MeV n^{-1} protons. A number of major solar particle events can be identified in both the high and low energy data, the last series of events being in December 2006. Also, panel j in Figures 5.4 to 5.7 shows the 1–8 Å X–ray flux data, which identifies solar flare events. (We will discuss in greater detail the solar events and the energetic particles in the forthcoming sections.)

A striking feature is the many recurring fast solar wind streams shown in Figure 5.8b. Using slanted white lines we manually mark the approximate locations of their leading edges, which roughly coincide with the stream interfaces as defined in the superposed epoch analysis by Gosling *et al.* (1978). Some recurrent streams spanned over 20 solar rotations, where one such sequence of streams occurred between Days 3 to 15 during CRs 2024 and 2050. This particular sequence originated from the northern solar hemisphere as indicated by the HCS and magnetic sector plots (Figures 5.8a and 5.8c), where the lines from Figure 5.8b are repeated to guide the eye. In general, the observed high–speed streams were located within the sector structure. The time series of the solar wind speed (Figures 5.4e to 5.6e) show that during the declining phase when the HCS was highly inclined, the velocity structure consisted of alternating periods of slow and fast solar wind, with maximum speeds ranging from $\sim$600 km s^{-1} to over 900 km s^{-1}. The unsteadiness and fluctuations in the solar wind speeds are sometimes due to ICMEs, especially in the first third period of our study interval. During the minimum solar period that followed, the stream structure was generally weaker, such as during 2009 to 2009.8 in Figure 5.7e (or CRs 2080 to 2088 in Figure 5.8c), though the speeds still exceeded $\sim$500 km

s^{-1} on occasion. We note that the lowest stream maximum speeds observed were ~350 km s^{-1} (see Figure 5.7e during 2009.4 to 2009.5, or Figure 5.8b during CRs 2082 to 2086).

Figure 5.8d shows that our period of study is also dominated by the high pressure ridges (red) associated with CIRs at the leading edges of the recurring streams, as marked by the slanted white lines from Figure 5.8b. It is known that the high–speed streams driving the CIRs typically occur following the magnetic sector boundaries (Crooker and Gosling, 1999; Gosling *et al.*, 1978). A comparison of Figure 5.8d with 5.8c does indeed show that the high pressure ridges occur behind these boundaries. Similar to the high–speed streams, the pressure ridges appeared much weaker during the solar minimum period (*e.g.*, 2009.4 to 2009.5 in Figure 5.7d, or CRs 2082 to 2086 in Figure 5.8d).

The notable slanted patterns in the color contour plots in Figure 5.8 indicate that the recurring features of the solar wind parameters appear earlier with each passing Carrington Rotation. For the high–speed streams, this implies that the coronal hole sources producing them have a rotation period less than the 27.3-day Carrington Rotation. Because the Sun rotates differentially, the location of the source region will determine the periodicity for the high–speed streams produced. It might be more appropriate to use the 27-day Bartels length, *e.g.*, Sanderson *et al.* (1998). Over 20 rotations, the additional 0.3 day per rotation on a Carrington Rotation scale amounts to 6 days, which is close to the slope of the recurrent features observed in Figure 5.8. However, to be consistent with prior studies (*e.g.*, Lee *et al.*, 2009a,b), we use the 27.3-day Carrington Rotation length, which represents a mid–latitude (or average) value and is readily associated with solar observations.

5.3 Organization of energetic particles

In Figure 5.8e, the intensities of the 0.31 to 0.58 MeV energetic ion population (mainly protons) as measured by the ACE EPAM instrument are shown. For this figure, the log of intensity is shown on the color scale. From the comparison with the slanted white lines, which as previously mentioned approximately indicate the leading edges of the solar wind streams, we identify the stream-associated recurrent particle enhancements indicated by the following groups of features: Days 18 to 23 of CRs 1999 to 2010 (hereafter called Feature 1), Days 2 to 7 of CRs 2004 to 2016 (hereafter called Feature 2), Days 17 to 22 of CRs 2022 to 2034 (hereafter called Feature 3), Days 3 to 12 of CRs 2022 to 2050 (hereafter called Feature 4), Days 10 to 13 of CRs 2040 to 2054 (hereafter called Feature 5), Days 17 to 25 of CRs 2040 to 2072 (hereafter called Feature 6), and Days 5 to 15 of CRs 2056 to 2084 (hereafter

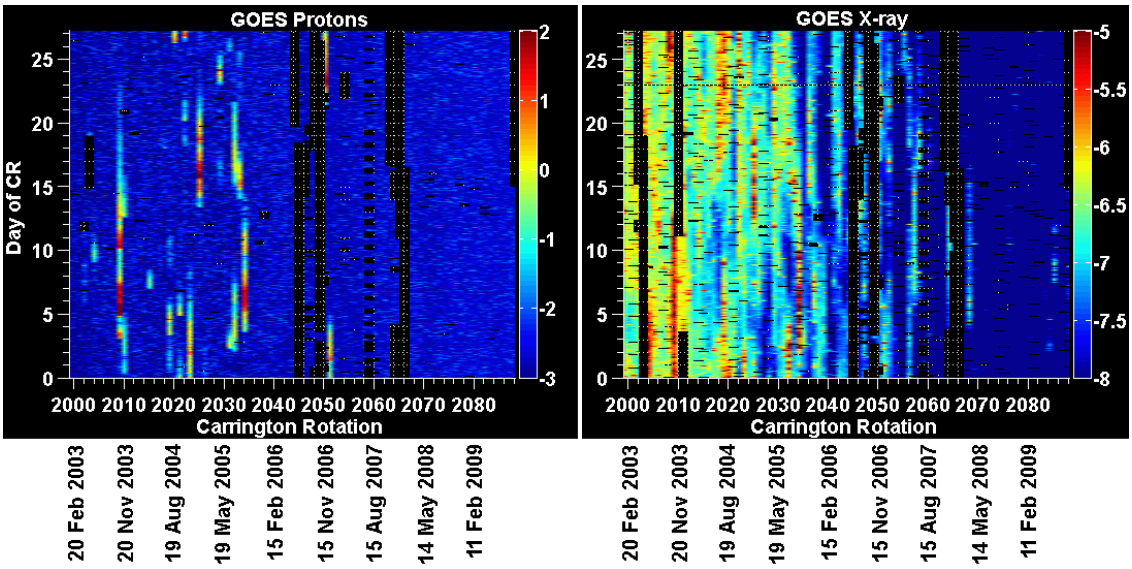

Figure 5.9: Color contour plots of the GOES–10 (left) 15 to 40 MeV energetic protons and (right) 1–8 Å X–ray flux. We use the 5-minute resolution data set, where the black areas denote sections of bad data and the color scale is log of intensity.

called Feature 7). Note that these recurring features together extend essentially throughout the whole period of our study, where Features 1 to 5 occur during the declining phase and Features 6 and 7 occur during the minimum period of the solar cycle. The time series of the same data set are also shown in panel f of Figures 5.4 to 5.7.

The recurrent ion particle enhancements (labeled 1 to 7 in Figure 5.8e) are co-located with the compression regions where the dynamic pressure values are high (Figure 5.8d) and located behind the magnetic sector boundaries (Figure 5.8c). When comparing the overall intensities of these recurrent particle enhancements, Feature 7 has the weakest intensities in comparison with Features 1 through 6. The weak signatures of the Feature 7 intensities can also be seen in Figure 5.6f and 5.7f, after 2007.3. It is at this time that one of the northern folds of the four–sector HCS structure flattened out (Figure 5.8a). In addition, no significant recurrent ion particle enhancements were observed after CR 2080, when the recurrent solar wind streams were very weak (see Figure 5.8b).

During the declining phase, the association between the Features 1 to 5 recurrent ion intensities and the observed high pressure ridges is obscured by signatures related to solar activity. From 2003 to 2007 (panel f in Figures 5.4 to 5.6), there

were periods of high intensity values that were well-above the background values. In Figure 5.8e, these solar event-related intensities appear as vertical features, particularly during CRs 1999 to ∼2052. Similar vertical features can also be seen when we plot the synoptic views for the GOES–10 (Aschwanden, 1994) 15 to 40 MeV energetic protons and 1–8 Å X–ray data in Figure 5.9. Such vertical features result from events that are extended in time but usually limited to one Carrington Rotation (the exception being long-lived active regions that may produce multiple events during a sequence of rotations). From the energetic proton plot (left), the changeover from the SEP-dominated to the CIR-dominated epoch can be clearly seen as a transition from vertical to slanted patterns. In addition, the majority of the impulsive flare events ceased shortly after CR 2058 (∼2007.5 in Figure 5.7) as shown in the X–ray data (right), although some weaker events occasionally occurred during the minimum period.

Figure 5.8f shows the contour plot of intensities for the 0.053 to 0.103 MeV energetic electrons, where periods of high intensities (vertical features) related to solar activity can be seen. It is noticeable that the electron enhancements due to the stream structures are not very prominent in these plots. Although we do see some weak enhancements near the slanted white lines that indicate the leading edges of the solar wind streams, these electron enhancements do not recur in a series like those for the energetic ions, especially after CR 2052 when the solar activity had subsided and the recurring streams were most prominent. This is further illustrated in Figures 5.6g and 5.7g, where we plot the energetic electron time series for 2006 to the end of our study interval and overlay colored bars to mark various particle event periods (to be discussed in greater detail in the next section). Here, the thin magenta bars mark the stream interaction region (SIR) events (streams that do not occur for more than one solar rotation, as defined by Jian *et al.* (2006a)) and the thick magenta bars mark the CIR events. From 2007 to 2008.5, for example, the recurrent ion enhancements (panel f) that are co-located with the magnetic compression regions and high–speed streams (panels c and e, respectively), are not observed in general for the energetic electrons.

Since the first half of our study period was dominated by signatures due to solar events, we examine the intensities for specific ion species that are associated with such activity. It is known that Fe ions are good indicators of impulsive solar flare and ICME events, where impulsive flare events are Fe-rich and ICME events are Fe-poor (at energies of 0.5 to 10 MeV n^{-1}) (Cane *et al.*, 2006; Mewaldt *et al.*, 2007). Panel h in Figures 5.4 to 5.7 shows the times series for the ULEIS 0.32 to 0.64 MeV n^{-1} Fe ion intensities (thin black line). Although the overall intensity values

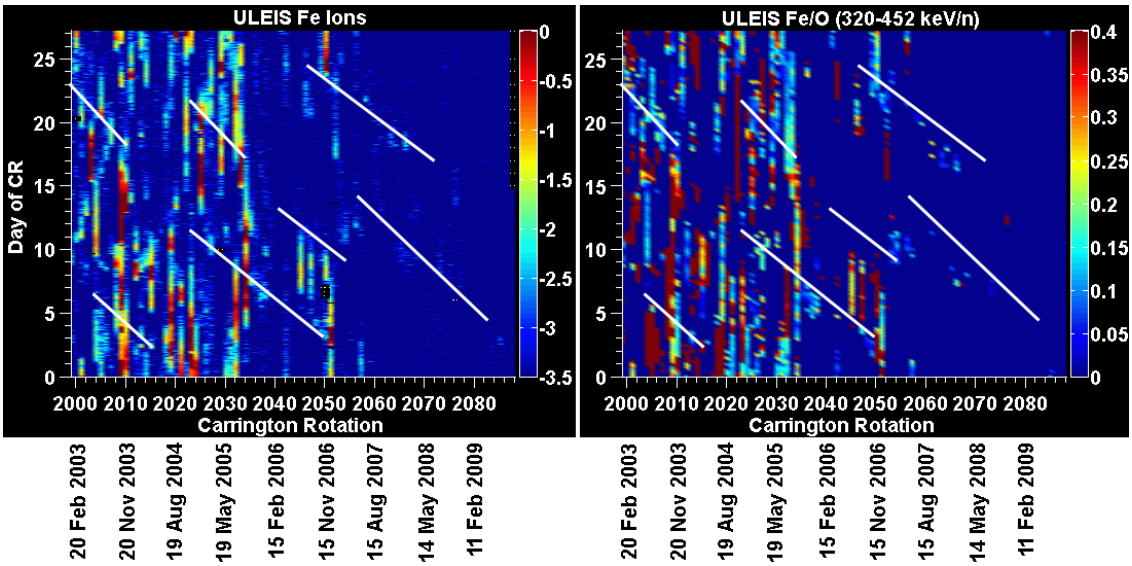

Figure 5.10: (left) ULEIS 0.32 to 0.64 MeV n^{-1} Fe ions and (right) ULEIS 6-hour resolution data for 0.32 to 0.452 MeV n^{-1} Fe/O. The slanted white lines mark the locations of the leading edges of the recurring solar wind streams discussed in the text.

are less than those for the energetic ions of similar energies (compare with panel f in Figures 5.4 to 5.7), we do see periods of high intensities related to solar particle events. These periods also appear as vertical features in the Fe color contour plot (Figure 5.10, left), from CRs 1999 to 2052.

It should be noted that signatures of Fe can also be present during intense CIR events (*e.g.*, Mason *et al.*, 2008), and so the use of the Fe intensity is not necessarily a clean discriminator for solar activity-related material. The recurrent Fe ion intensities (*e.g.,* Features 1 to 7) are observed (Figure 5.10, left), but their signatures are very weak in comparison with those for the EPAM ions (compare with Figure 5.8e, or compare panels f and h in Figures 5.4 to 5.7). To further distinguish between CIR-related and SEP-related Fe signatures, we plot Fe/O in Figure 5.10 (right) using the ULEIS 0.32 to 0.452 MeV n^{-1} Fe and O 6-hour resolution data set. The relative abundance of Fe in CIR events is less than in SEP events, where the CIR average of Fe/O is $\sim 0.088 \pm 0.007$ (Mason *et al.*, 2008) and the SEP average is $\sim 0.404 \pm 0.047$ (Desai *et al.*, 2006b). The CIR-related Fe signatures for values of Fe/O ~ 0.1 are shown in light blue. These CIR-related signatures are located throughout our period of study, including at the locations of the Features 1 to 7 intensities as marked by the slanted white lines. The SEP-related Fe signatures are

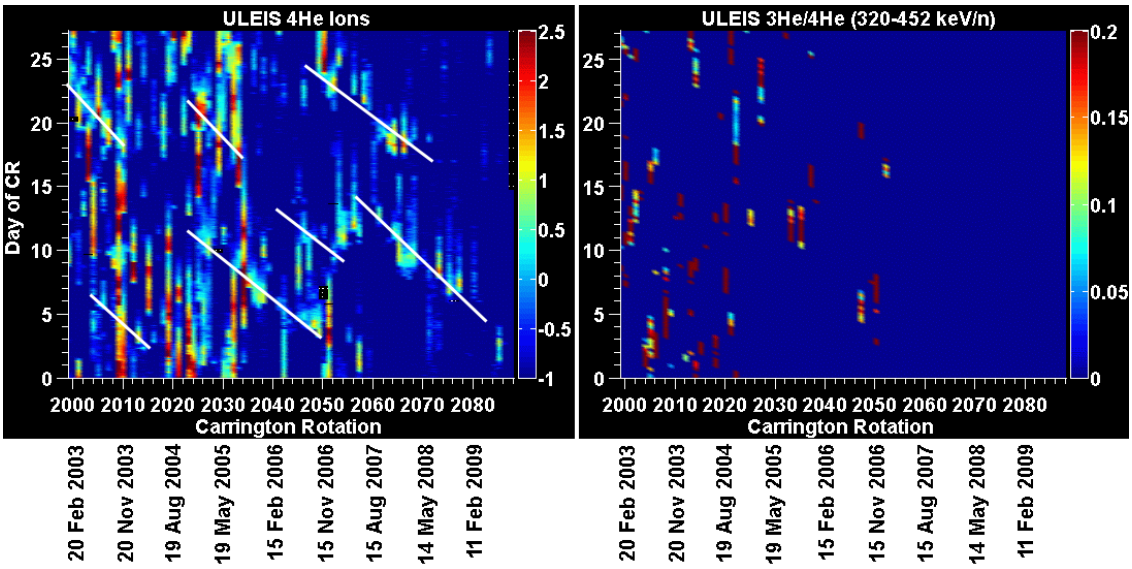

Figure 5.11: (left) ULEIS 0.32 to 0.453 MeV n^{-1} ^{4}He ions and (right) ULEIS 6-hour resolution data for 0.32 to 0.452 MeV n^{-1} ^{3}He/^{4}He. The slanted white lines mark the locations of the leading edges of the recurring solar wind streams discussed in the text.

shown in red for Fe/O $\sim$ 0.4. Figure 5.10 (right) clearly shows the decline of the Fe-enriched events as solar minimum was approached, after CR 2052. Many of the Fe/O values of $\sim$0.4 coincide with the vertical patterns of high Fe intensities seen in Figure 5.10 (left).

The rare ^{3}He isotope is also a very good indicator for impulsive events since they are the only known source (Desai *et al.*, 2006a; Mewaldt *et al.*, 2007). In this study, however, we do not show the ^{3}He intensities since most of the data are mixed in with spill-over from ^{4}He. Instead, we show the ULEIS 0.32 to 0.453 MeV n^{-1} ^{4}He intensities (Figure 5.11, left) and the ^{3}He/^{4}He values calculated from the ULEIS 0.32 to 0.452 MeV n^{-1} ^{3}He and ^{4}He 6-hour resolution data set (Figure 5.11, right). For the ^{3}He/^{4}He values, we removed the ^{4}He spill-over in the ^{3}He data by omitting values of ^{3}He/^{4}He $< 5\%$. From Figure 5.11 (left), the recurrent features are observed for ^{4}He. Although the intensities are relatively weaker than the EPAM energetic ions, the details of the signatures are very similar to those shown for the EPAM ions (compare panel h, thick black series, with f in Figures 5.4 to 5.7). The most prominent events in Figure 5.11 (right) are the ^{3}He-rich events that occurred between major SEP events. The decline in the ^{3}He-rich events as the solar cycle progressed toward the minimum phase can be clearly seen, although we note that

[3]He-rich events during quiet conditions have been reported by Mason *et al.* (2009b) but they do not appear in Figure 5.11 (right) because of low statistics.

5.4 Particle events

In Figure 5.12 we further examine the various particle events that contribute to the observed energetic ion enhancements shown in Figure 5.8e and repeated in 5.12a. For each type of particle event, we overplot symbols in panels b though e that indicate the reported event onset times on top of the energetic ion color contour plot. We note that the juxtaposition of a particular intensity structure and a particle event does not necessarily mean that the structure is associated with the source of the event particles. Similarly, the detection of an energetic particle event without an apparent intensity feature association does not mean there is none, as a connection to the event may be remote, via magnetic field lines connecting to the observer. For example, a CIR could pass by at the time of a SEP event from the far west in solar longitude, which has no associated structures in near-Earth space at 1 AU. Nevertheless, such plots can call attention to the complications of particle-feature and event associations and also illustrate that they are often ambiguous.

In Figure 5.12b we overplot circles on top of the ion color contour plot to identify events due to SIR events, and asterisks to mark the times of the related SIR shock events. We use the 'SIR Start UT' and 'Shock UT' event times based on ACE and Wind spacecraft observations from published lists by Jian *et al.* (2006a; 2008). The listed events are a mixture of both SIR and CIR events; if an SIR recurred on two or more solar rotations, it was also considered a CIR. The event list extends to late-July 2009 (CR 2085). A majority of SIRs and their related shocks occur at or near the Features 4 to 7 recurrent ion intensities that are correlated with the high dynamic pressure ridges. There is a noticeable event gap between CRs 2010 and 2020, probably when the HCS was slowly transitioning from a two– to four–sector structure. It is at this time, also, that there is a lack of strong and continuous high–speed solar wind streams (see Figure 5.8b). We also note the SIR events occurring after CR 2080 do not have noticeable corresponding particle enhancements in Feature 7.

In Figure 5.12c we plot near–Earth ICMEs and their related shocks, shown as circles and asterisks, respectively. The observed particle intensities that occurred around the same time are not necessarily caused by them, but are often related. The event times for the ICMEs are based on the plasma and magnetic field observations by ACE and Wind, and are obtained from a list compiled by I.G. Richardson and

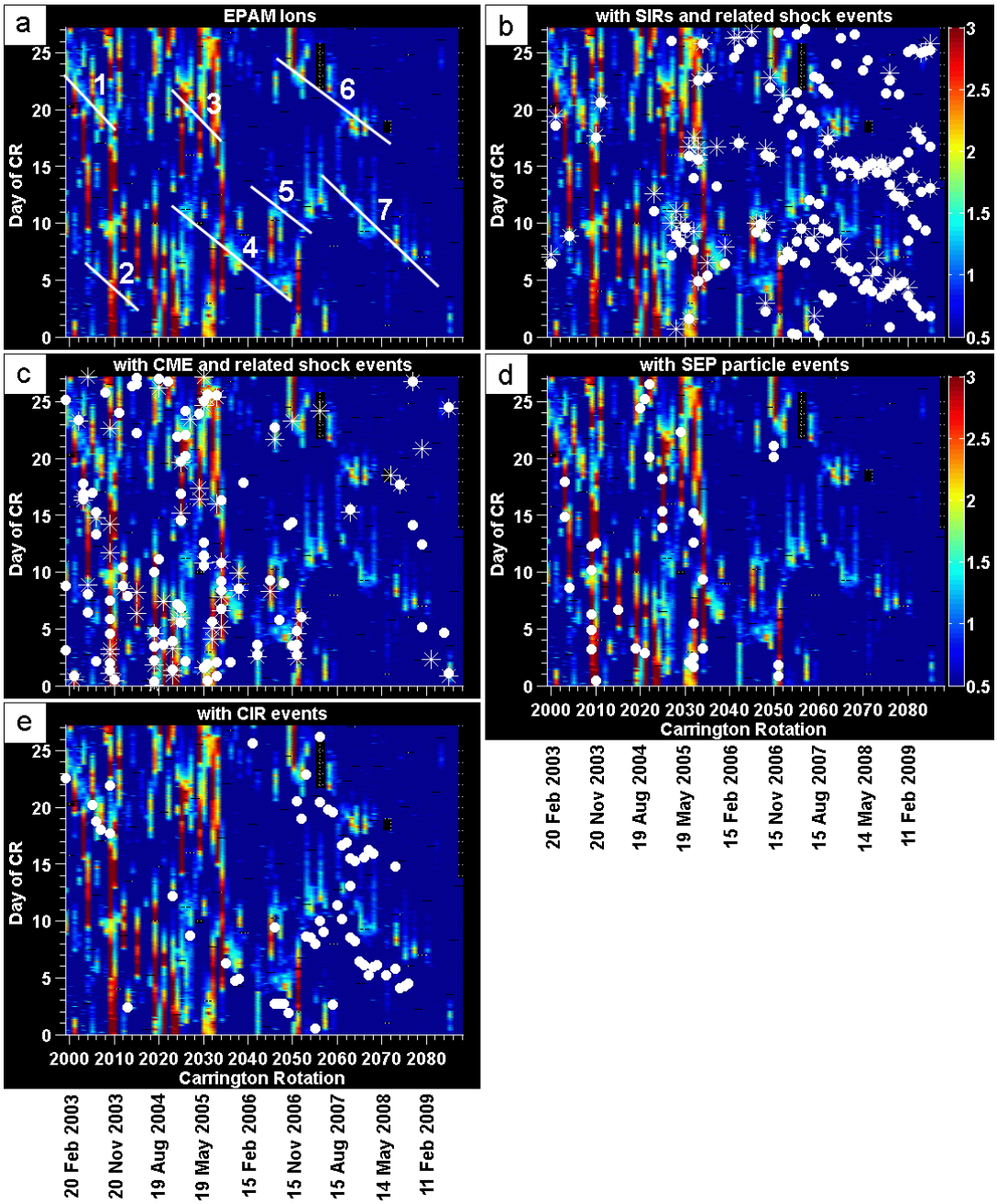

Figure 5.12: ACE EPAM 0.31 to 0.58 MeV ion intensities overplotted with (b) SIR events (circles) and their related shocks (asterisks), (c) CME events (circles) and their related shocks (asterisks), (d) SEP particle events, and (e) CIR-related particle events. The slanted white lines mark the locations of the leading edges of the recurring solar wind streams discussed in the text.

H.V. Cane that is available on the internet (http://www.ssg.sr.unh.edu/mag/ace/ACElists/ICMEtable.html; see also Cane and Richardson, 2003). We use the 'ICME plasma/field' start times from this list, which ends around late-July 2009 (CR 2085). For the ICME–related shocks observed by ACE and Wind, we use the shock start times from published event lists by Jian *et al.* (2006b; 2008). The list of shock events is also provided up to late-July 2009 (CR 2085). Figure 5.12c shows that the ICME events and their related shocks are concentrated roughly around CRs 1999 to 2052, during the active solar period, with a few sporadic events afterward. The ICME and related shock events correlate most with the vertical patterns of high ion intensities and not the Features 1 to 5 recurrent intensities that are related to the solar wind dynamic pressure, as expected. Because we only use the start times of the ICME events provided in the event lists mentioned, information regarding the durations of enhanced particle activity is not included.

Figure 5.12d shows SEP events that are either accelerated at the associated flare site or by the passage of a CME-driven shock obtained from a published list by Cane *et al.* (2006) for > 25 MeV proton events extending through the end of year 2005 (CR 2038). Four additional events for year 2006 are included as well. The SEP event start times are based on the GOES soft X–ray maximum intensity or the start of the type III bursts if the flare was behind the solar limb. The events shown occur mostly during the declining phase of our study and overlap mainly with the vertical pattern of high ion intensities.

Figure 5.12e shows energetic particle (heavy ion) events related to CIRs. The start times are based on the event lists provided by Mason *et al.* (2008; 2009a), where the events are observed by ULEIS through the end of 2008 October (middle of CR 2076). As expected, the CIR events plot along the contours of high ion intensities that are correlated with the high dynamic pressure ridges (e.g., Features 1 to 7 intensities). There is also a noticeable event gap between CRs 2010 and 2020, as shown earlier for the SIR events in Figure 5.12b.

In Figure 5.13 we examine events for the energetic electron particles. We repeat the contour plot of the energetic electrons (Figure 5.8f) with the Features 1 to 7 labeled on the left panel, and in the right panel we overplot the impulsive beamlike near–relativistic electron events (circles) observed by ACE EPAM near 1 AU. These events are associated with solar flare events observed between W30° and W80°, where W60° is the ideal average magnetic connection longitude to Earth. The list, extending to the beginning of year 2007 (CR 2052), is a continuation of the original list published by Haggerty and Roelof (2002) and can be found at http://www.srl.caltech.edu/ACE/ASC/DATA/level3/index.html. Although it

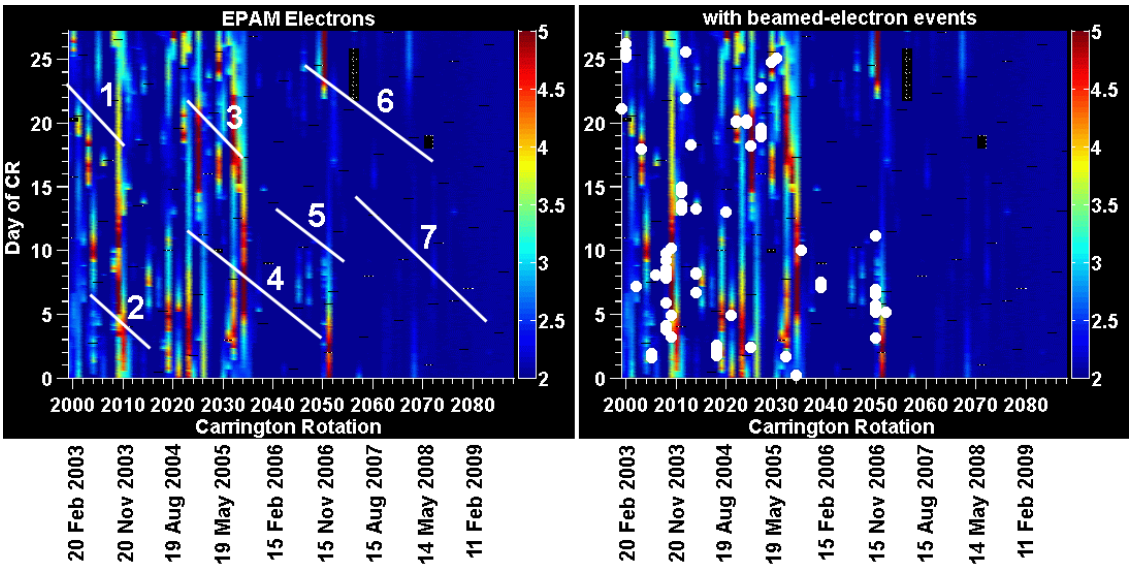

Figure 5.13: (left) ACE EPAM 0.053 to 0.103 MeV electron intensities overplotted with (right) beamed–electron events. The slanted white lines mark the locations of the leading edges of the recurring solar wind streams discussed in the text.

was reported by Haggerty and Roelof (2002) that these particular electrons are accelerated by CME–driven shocks, their recent study of the entire SC 23 period indicate that the electrons are a mixture of shock and flare accelerated electrons (Haggerty and Roelof, 2009). Figure 5.13 (right) shows that the electron events overlap with many of the vertical features (high intensities) due to solar activity, where the frequency of the reported electron events declined as expected as solar minimum was approached.

5.4.1 Mixed event periods

During the declining phase, the CIR particle population is mixed in with the population of energetic particles that are related to solar activity. We thus take a closer look at the energetic ion and electron particle enhancements that occurred at this time and revisit Figures 5.4 and 5.5. These figures are divided into two time intervals: 2003 to 2004.5 and 2004.5 to 2006, respectively. The solid color bars are plotted to represent the following particle events: thin magenta for SIR and thick magenta for CIR events, cyan for CME events, orange for SEP particle events, and green for beamed–electron events. The related shock event times are plotted as dashed bars using the same color scheme.

Panels f and g in Figures 5.4 and 5.5 show on several occasions the energetic particle enhancements that occurred during or around the times of both stream and solar-related event periods. One such example is the occurrences of two near–Earth ICME events on 15 and 16 June 2003 and one SIR event on 18 June 2003 (event times based on an online list by I.G. Richardson and H.V. Cane and a published list by Jian *et al.*, 2006a, respectively). Shortly after these events, comparable enhancements in the energetic ion (panel f) and electron (panel g) intensities were observed. In another example, shortly after 2004.0, one stream event occurred (6 January 2004) followed by a near–Earth ICME event (9 January 2004). The related energetic ion and electron enhancements can be seen, though the electron enhancement is relatively weak. In this particular example, the rise of the ion intensity commenced with the passage of the stream followed by a strong and relatively sharp peak that occurred with the passage of the ICME disturbance. Other mixed event-periods were also observed throughout 2005, especially the period between 2005.4 and 2005.7. During the minimum period, particularly after 2007 (Figures 5.6 and 5.7), the stream events dominated with a few solar events occurring sporadically (*e.g.*, Bucik *et al.*, 2009). It is not clear from these new displays (*e.g.*, Figure 5.12) that the intensities of the ICME shock-related events are affected by the presence of pre-existing SIR/CIR or ICME particle populations. The issue of seed populations is thus not further resolved by this study.

5.5 Comparison with the Solar Cycle 22 Minimum Period

To compare some of our results with those reported by Sanderson *et al.* (1998), we focus on the portion of the solar cycle where the sunspot numbers (SSN) are comparable. The period studied by Sanderson *et al.* (1998) began around November 1994 (approach of Solar Cycle 22 to 23 minimum period) and had SSN $\sim$45. Hence, in this section we narrow our study interval and begin our comparison on January 2006 (between CRs 2038 and 2039 in Figure 5.8) when the SSN was comparable (Figure 5.14b). It is clear from Figure 5.14 that the period with SSN $\leq$45 following SC 23 is already longer than during the previous minimum period even though the rising phase of SC 24 has yet to commence by the end of our study period. To compare our results with those from the previous minimum period, we refer to Plates 1 to 3 in Sanderson *et al.* (1998).

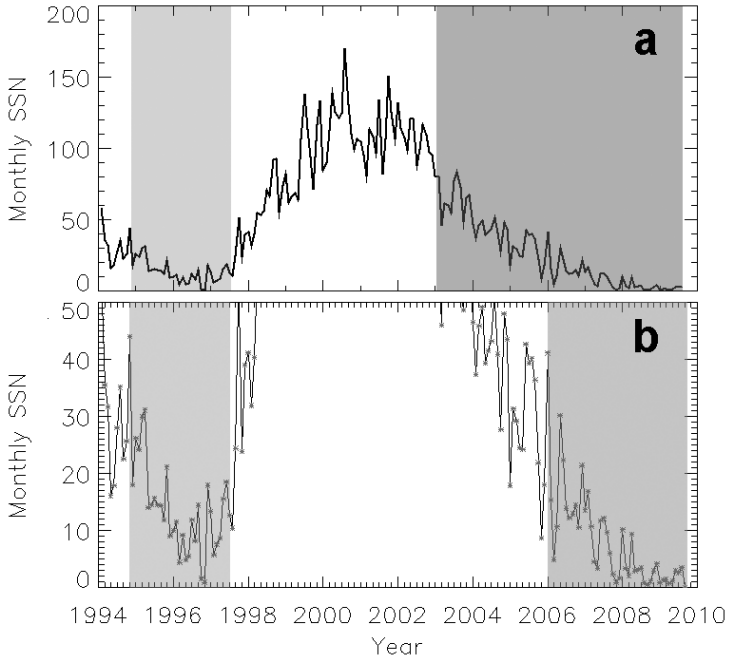

Figure 5.14: (a) Monthly sunspot number (SSN) for the periods of interest. The light gray shaded area indicates the period of study by Sanderson *et al.* (1998), beginning around November 1994. The dark gray shaded area indicates the period of this study. (b) Zoomed-in plot indicating comparable minimum period of this study with that of Sanderson *et al.* (1998).

5.5.1 Solar wind structure

For both minimum periods, the sector pattern, which followed closely the shape of the neutral line, had already transitioned from a steeper, two–sector structure to a flatter, four–sector structure. The HCS has maintained a four–sector pattern for the entire SC 23 minimum period thus far, although during the bottom of the minimum (2008 to late 2009, CRs 2064 to 2084) some warping occurred such that the HCS was north about one quarter of a solar rotation and near or south of the equator for about three quarters of a solar rotation. A similar warping also occurred during the bottom of the SC 22 minimum period but for a much shorter time interval [January to June 1996, CRs 1905 to 1909; see panels c and d of Plate 1 in Sanderson *et al.* (1998)]. Moreover, when we compare inclination angles, the HCS had a maximum tilt of $\sim 45^\circ$ during the SC 23 minimum period (see Figures 5.6a and 5.7a) in comparison to a maximum tilt of $\sim 30^\circ$ during the SC 22 minimum period (see panel c of Plate 1 in Sanderson *et al.*, 1998).

The pattern of the high–speed streams also followed the pattern of the sectors, as expected, during both minimum periods. For the SC 23 minimum, there were were several high–speed solar wind streams that were very long–lived (*e.g.* the streams that occurred during CRs 2022 to 2050 at Days 3 to 12 and also CRs 2056 to 2084 at Days 5 to 15 in Figure 5.8b). These recurring streams spanned over many solar rotations, up to $\sim$ 30 at times, whereas during SC 22 the recurring streams spanning $\sim$ 10 solar rotations were not quite as long-lived (see panel d of Plate 3 in Sanderson *et al.*, 1998). We note that the slopes of the recurrent features seen throughout this study (*e.g.*, Figure 5.8) are not observed in Plate 3 of Sanderson *et al.* (1998) since they use the 27-day Bartel rotation scale instead of the 27.3-day Carrington rotation scale.

Typically during the minimum phase of the solar cycle, the polar coronal holes and their extensions would supply the high–speed streams observed in the ecliptic (see Luhmann *et al.*, 2002, for a discussion). However, in a study by Lee *et al.* (2009b) where they were investigating the sources of the weaker ecliptic IMF, they found that for SC 23 there were many prominent low–to–mid latitude coronal holes that were supplying the high–speed streams observed at 1 AU. In contrast, the polar coronal holes and their extensions mostly supplied the high–speed streams during the SC 22 period. Luhmann *et al.* (2009) proposed that the weaker solar fields that occurred during the SC 23 minimum period led to more prominent low latitude coronal holes and therefore stronger high–speed streams.

A comparison was made in Lee *et al.* (2009b) for the distribution of the solar wind speeds and magnetic field strengths observed during the SC 22 and 23 minimum periods. Overall, the speed distribution for both minimum periods was comparable. In addition, the high–speed streams were reported to be well-formed for both periods, though for the SC 22 minimum there were fewer high–speed streams observed. For the interplanetary field strength, the values were reported to be $\sim$30% lower for the cycle 23 minimum period, which is also consistent with the Ulysses off–ecliptic observations reported by Smith and Balogh (2008).

5.5.2 Energetic particle enhancements

The energetic ion enhancements observed by ACE during the recent solar minimum period followed the pattern of both dynamic pressure and magnetic field enhancements associated with the stream interaction regions (*e.g.*, Features 4 to 7 in Figure 5.8e). This was also the case for enhancements of similar energies observed by Wind during the previous solar minimum (see panel e of Plate 3 in Sanderson *et al.*, 1998). For both cases, the recurrence of the ion enhancements occurred on the

time scales of the recurring high–speed streams observed during the respective minimum periods. The electron enhancements associated with the compression regions were also observed during both minimum periods (similar energy ranges), although they did not always occur when the ion enhancements were observed nor did they recur with the high–speed streams (see Figures 5.4 and 5.7). When the electron intensities were observed, they were often weaker than the ion enhancements (for SC 22 compare red time series in panels a and b of Plate 2 in Sanderson *et al.*, 1998; for SC 23 compare panels f and g in Figures 5.6 and 5.7 of this study).

Solar activity occurred sporadically for both solar minimum periods and produced particle enhancements for both the energetic ions and electrons. At times, these solar events commenced at or around the times of the streaming events, thus producing mixed signature profiles in the particle intensities. Both solar minimum periods have similar energetic particle event characteristics, with the differences only determined by the different solar wind structures and ICME event rates.

5.6 Conclusions

The unusually long solar minimum period of SC 23 has provided an opportunity to examine the large–scale organization of the energetic particles in the context of the ambient solar wind structure at 1 AU. We made an analysis of the SC 23 declining to minimum period, similar to the study by Sanderson *et al.* (1998) who conducted a global study using Wind observations of the association of energetic particles with CIRs for the minimum period of Solar Cycle 22. Their observations showed that the proton intensities followed a pattern of the solar wind compression regions, suggesting that the particle events are organized by the corotating structure of the solar wind streams. For our study, we utilized the in-situ OMNI solar wind plasma and magnetic field as well as the ACE particle data sets, spanning > 6.5 years of observations from CRs 1999 to 2088 (January 2003 to October 2009) that includes the declining phase and the minimum period.

During the declining phase, we find that the HCS was inclined and warped, forming a two–sector interplanetary magnetic field structure at Earth. During the approach to solar minimum, the HCS maintained a relatively steep inclination and the IMF transitioned to a four–sector pattern. The HCS became less steep during solar minimum, but some warps were observed.

Also, throughout our period of study there were several steady, high–speed solar wind streams and corresponding high dynamic pressure ridges. Some of these streams recurred for many solar rotations, at times up to 30 rotations, indicating the coronal sources producing these streams were quite long–lived. In particular,

these long–lived streams occurred during the period when the HCS was a four–sector structure. As solar minimum progressed, the high–speed streams and corresponding high pressure ridges became much weaker.

We find that the recurring energetic particle enhancements were associated with the long–lived high solar wind pressure regions. The CIR-related particles were observed throughout our period of study, but during the declining phase there were also many solar events that occurred. Using various solar event lists that have been published or made available online, we plotted the start times of these events on top of the particle intensity plots in an attempt to distinguish some of the sources that may have produced the various particle signatures. We find that some of the observed particle events during the present solar minimum may be related to ICME or flare events (or both). As the decline in solar activity progressed, the observed particle signatures due to CIR events became dominant. However, very few significant recurrent energetic particle enhancements were observed between CRs 2080 and 2088, which is consistent with the overall weak high–speed streams observed during this time and also with the presence of several still-active regions from cycle 23. As we approach Solar Cycle 24, we expect to see an ongoing presence of CIR-related energetic particle intensities and a more frequent occurrence of the SEP event-related enhancements. The details of the evolution of energetic particle event types should depend on both the solar wind structure and active region behavior during the new rising phase, along the lines of the overall picture described in this study.

Chapter 6

Conclusion and Future Work

6.1 Summary

In this dissertation, my goal was to broaden our scientific knowledge of the large-scale solar wind structure at 1 AU, including its variations with solar activity and its origins at the Sun. Moreover, with a growing interest and need to forecast the "space weather" at Earth I also wanted to test the capabilities of existing 3D numerical models in simulating the solar wind conditions. In order to make realistic long-term predictions of the episodic solar disturbances, I found it necessary to first understand the ambient solar wind structure and test the current models for quiet solar conditions. As such, I focused on the declining phase and minimum period of the solar cycle, particularly cycles 22 and 23. Compared to the previous minimum period, the deep solar minimum of Solar Cycle 23 provided a unique opportunity to study the solar wind for a much longer period of time since the dawn of the Space Age. I used long-term solar wind measurements from the near-Earth ACE spacecraft (data also included in the OMNI data set provided by NASA) as well as ground-based magnetic field observations of the Sun. In addition, I utilized a number of models to infer the coronal sources of the observed solar wind and interplanetary magnetic field (IMF).

My research progressed from obtaining a macroscopic overview of the solar wind structure at 1 AU to understanding the details at the Sun to explain the near-Earth observations. In Chapter 2, I evaluated the performances of two coupled solar corona-solar wind models by comparing their results with spacecraft observations of the large-scale solar wind structures. In Chapter 3, I examined the differences in the solar wind and IMF observed during cycles 22 and 23 and investigated the role of the solar wind streams in creating these differences. I extended this investigation in Chapter 4 by examining how the changes in the coronal hole areas and their locations at the Sun controlled the interplanetary field magnitudes observed at 1

AU. Finally in Chapter 5, I returned to the large-scale solar wind structure and examined how the energetic particles are organized during cycle 23 and whether there are noticeable differences in comparison to the previous minimum period.

6.2 Major contributions

Throughout the course of my research analyses, I have made new and interesting discoveries about the solar wind conditions as observed in the geospace environment. In particular, the recent solar cycle exhibited an unusually long phase of declining solar activity accompanied by a decrease in the solar surface field to values lower than the two previous solar cycle minima. Below is a list of the major contributions of this dissertation which investigated the interplanetary consequences:

The solar wind and interplanetary magnetic field:

- For the minimum period of Solar Cycle 23, the peak distribution of values for the ecliptic interplanetary magnetic field and density were about 30% lower while the momentum flux was 38% lower, in comparison to the previous cycle's minimum period. This confirms observations made at higher solar latitudes by the Ulysses spacecraft and shows the result applies to the entire inner heliosphere.

- The sources supplying the ecliptic solar wind streams observed during cycle 23 minimum period are mainly from coronal holes located in the low-to-mid solar latitude regions. For the cycle 22 minimum period, the sources of the solar wind came mainly from the polar coronal holes and their extensions.

- There were more recurrent, longer-lasting high-speed solar wind streams during the cycle 23 minimum period than the previous minimum. Some streams lasted for more than 30 solar rotations (1 solar rotation is $\sim$27 days), indicating that the coronal hole sources producing them were quite long-lived at Sun. In contrast, the cycle 22 minimum had streams that recurred for no more than 10 solar rotations.

- The lower interplanetary field strength observed during the cycle 23 minimum resulted in part from changes in the coronal holes, such as the locations of these open field regions (polar latitudes *versus* low-to-mid latitudes) and the sizes of the open field areas.

- The solar wind streams could also play a somewhat significant role in producing the observed weaker ecliptic interplanetary fields. If the contrast between the low and high-speed streams was larger for the cycle 23 minimum period, there would be deeper rarefaction regions and thus lower magnetic fields in those regions. But my analysis of solar wind sources back at the Sun proved that the weaker solar field for the cycle 23 minimum played a role as well.

- Particle enhancements observed during the cycle 23 minimum for low-energy (≤ 1 MeV) ions followed the patterns of both dynamic pressure and magnetic field enhancements associated with the solar wind stream interactions. Since some of the solar wind streams recurred on time scales of 30 solar rotations, the recurrence of the ion enhancements occurred on a similar time scale.

- The heliospheric current maintained a four–sector pattern during the cycle 23 minimum. However, some warping occurred such that the current sheet was north of the solar equator for about one quarter of a solar rotation and near or south of the solar equator for about three quarters of a solar rotation.

- The heliospheric current sheet was much more tilted with respect to the solar equator during the cycle 23 minimum. It was often inclined at more than 40°, with a maximum tilt of 45°. During the previous minimum period, the maximum tilt angle was about 30°.

Modeling:

- The standard source surface height of $2.5R_{\odot}$ in the potential coronal magnetic field model may no longer be the best value to use in representing the interplanetary field strengths during Solar Cycles 22 and 23 (particularly during their minimum activity periods). Using a smaller source surface value of $1.8R_{\odot}$ seem to better reproduce the interplanetary field for both minimum periods, with a slightly larger value for cycle 22.

- In modeling the solar wind at 1 AU during the declining phase of cycle 23, the 3D magnetohydrodynamic (MHD) WSA/ENLIL and MAS/ENLIL coupled solar corona-solar wind models did an overall good job in simulating the general large-scale solar wind structures and trends.

- On the few occasions when coronal mass ejections trigger disturbances in the solar wind at 1 AU, the models did not capture the high solar wind speeds or densities that were observed.

- The model-generated velocities were often underestimated by a few tens of percent in comparison to the near-Earth observations. This may be due to the empirical formulae used in calculating the solar wind speeds.
- The model-generated densities were often overestimated by about 50–200% in comparison to the near-Earth observations. This may be due to inadequate coronal model boundary conditions on the density or to the use of an approximate equation of state.
- The model-generated values for the magnetic components of the total interplanetary field were often smaller by a factor of 2 in comparison to the near-Earth observations. Possible factors that may cause this include inaccuracies in the observations-derived synoptic photospheric field maps that are used as boundary conditions for the models.

6.3 Implications for space weather forecasting

During the previous solar maximum (around 2001), some solar storms caused by coronal mass ejections created some damaging effects in near-Earth space and also at the ground-level. For example, during the 2003 Halloween solar storms many near-Earth satellites experienced power failure while others went into safe mode or experienced saturation with onboard sensors (Webb and Allen, 2004). Ground-based systems were also affected: in Wisconsin and New York, increased current levels were detected in transmission lines (Webb and Allen, 2004).

With the approach of the next solar maximum, there is a potential to mitigate the harmful space weather effects imposed on our technological systems. The development of state-of-the-art space weather forecasting models and their overall success in describing the quiet solar wind to first order has resulted in the related runs-on-request service at the NASA Community Coordinate Modeling Center (CCMC) and their use for space weather predictions at the National Weather Service Space Weather Prediction Center (*e.g.,* Arge and Pizzo, 1998). Guided by my comparison study of the WSA/ENLIL and MAS/ENLIL models at the CCMC, the numerical modelers can make improvements to their solar wind models.

If we are to anticipate upcoming major solar disturbances and their subsequent impacts on the near-Earth environment, one improvement that is important to make is getting the models to accurately predict the southward IMF (better known as southward B_z) field strength. It is the southward B_z that plays an important role in controlling the impact of solar disturbances impact the geospace environment.

Often, a southward B_z together with the passage of a coronal mass ejection (CME) would lead to large aurorae due to an injection of energy into Earth's magnetosphere. From my comparison study, I found that the model-generated values for the magnetic components of the total field were often underestimated by a factor of 2. It is possible that the boundary conditions, such as the source surface height of $2.5R_{\odot}$, used to drive the coronal component (WSA, MAS) of the coupled corona-solar wind model could contribute to the underestimation of the magnetic field values. This will need to be tested in the near future by the model developers, possibly by using the smaller source surface heights that I calculated in their model calculations and comparing the southward B_z values that are generated.

6.4 Future work

Through the course of this dissertation work, I have acquired an overall and deeper knowledge of the solar wind structure at 1 AU for quiet solar conditions, and have developed some important skills in using and essentially validating numerical solar wind models. To build upon this knowledge and set of skills, some of the obvious steps that I can take in my scientific career are studying the solar wind conditions during active solar periods and/or studying the solar wind conditions at other planetary locations. Below I describe my near-term scientific research plans that I hope to carry out:

6.4.1 CME "Cone" Modeling

In the inner heliosphere in general, the evolution and the propagation of a CME disturbance is not an entirely well understood process. As a result, it is a challenge to accurately simulate CMEs and their effects on the geomagnetic environment. CMEs are thought to occur when the magnetic fields in the corona evolve into an unstable configuration. The corona releases the excess energy and magnetic field by expelling both material and magnetic fields in a "cloud" of magnetized plasma. If the CME ejecta travel faster than the speed of the background corona and solar wind, it makes a leading shock wave that accelerates some of the ambient particles. Thus far, there are models that are designed to calculate the arrival times of CMEs directed toward Earth (i.e. halo CMEs). In the so-called "cone model", Zhao, Plunkett, and Liu (2002) cone shapes are fitted to white light coronagraph images of CMEs (see Figure 6.1a for an example) in order to estimate their geometric (angular width, central position) and kinematic (radial velocity) properties. The use of a cone shape for modeling the injection and propagation of an enhanced

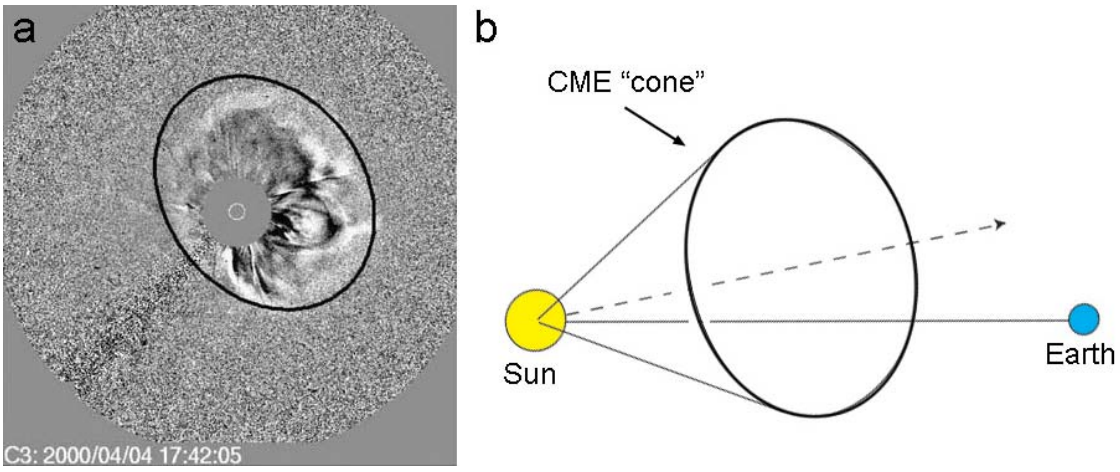

Figure 6.1: (a) Example of a modeled halo CME (black ellipse) superposed on a white light CME image from the LASCO instrument onboard the SOHO spacecraft. Figure from Xie, Ofman, and Lawrence (2004). (b) Illustration of cone orientation and angular width for an Earth-directed CME.

solar wind "gust" is ideal since CMEs radially expand outward in a self-similar way (see Figure 6.1b for an illustration). However, a limitation of the cone model is the lack of a detailed description of the CME ejecta, especially the magnetic field. This aspect remains a challenge for model developers. However, the cone model can be used with solar corona-solar wind models as a simple, approximate method for simulating the propagation of observed CMEs from the Sun out to Earth.

With encouraging results, Taktakishvili *et al.* (2009) recently used the coupled WSA coronal model (Arge *et al.*, 2004) and the 3D ENLIL MHD solar wind model (Odstrcil, 2003) together with the cone model (Zhao, Plunkett, and Liu, 2002) to simulate the effects of 14 fast halo CME events. They obtained cone model parameters for the CME events using a non-quantitative, fit-by-eye method, in which one unique fit was used for each simulated CME event. Based on these fits, their estimated arrival prediction times were superior to those obtained using other empirical methods. In using this relatively imprecise method, the cone model parameters, arrival prediction times, and other forecast parameters will naturally vary with the individual making the fits, but it is unclear to what degree.

I propose to conduct a more comprehensive assessment of the uncertainties in using the coupled WSA/ENLIL + cone set of models for forecasting. A larger sample of observed events would be selected and several sets of slightly different cone model fits could be used for each CME event. Given the ambiguities of fitting cones

to coronagraph images, by making multiple, yet slightly different cone model fits to the data for each event, a set of varying predictions would be obtained that reveal the uncertainties in the model forecast. In addition, I would vary the cone model CME densities in order to obtain better agreements between the calculated and observed values of the CME-related ram pressure arriving at Earth. These pressure values are important for determining the impact CMEs have in the deformation of the terrestrial magnetosphere and on associated magnetic storms. In the study by Taktakishvili *et al.* (2009), the model number density of the arriving CME was often overestimated. As part of the evaluation of the WSA/ENLIL/Cone model, I would also compare a selection of modeled events with near-Earth, in-situ spacecraft observations to determine how well the model predicts CME properties, including shock strength and post-shock interplanetary field orientation.

6.4.2 Multi-point study of a CME

As stated earlier, the evolution and propagation of a CME in the inner heliosphere is not an entirely well understood process. Until recently, observations of such events were limited since they predominantly came from single-point spacecraft measurements. Although there are now multi-perspective spacecraft observations that can provide a few additional vantage points of a CME as it evolves and propagates, the observations still do not provide enough of a global view of the event. Thus, it would be advantageous to simulate an event using a numerical model, such as the WSA/ENLIL/Cone model, to effectively provide many vantage points where no spacecraft observations are available for comparison. Such a study can provide important insights and a deeper understanding of the evolution and propagation of CMEs. Figure 6.2 shows an example of a WSA/ENLIL/Cone model simulation of an idealized CME event with "observers" at different longitudinal locations along the 1-AU orbit. The simulation and results were generated by Lee *et al.* (2008) in a preliminary study of the WSA/ENLIL/Cone model.

It would also be a unique study to compare the multi-vantage point model results for a CME event with multi-perspective spacecraft observations. Such a comparison is interesting and important since the results would reveal how accurately and realistically the cone model can capture the global properties of a CME event. If a CME event occurs by the time a model such as the WSA/ENLIL/Cone model is developed and if multi-perspective observations of the event are available, a detailed comparison could be made between the calculated and observed CME properties for each vantage point. An older event could also be selected for such a study based on whether it was observed by more than one spacecraft at different

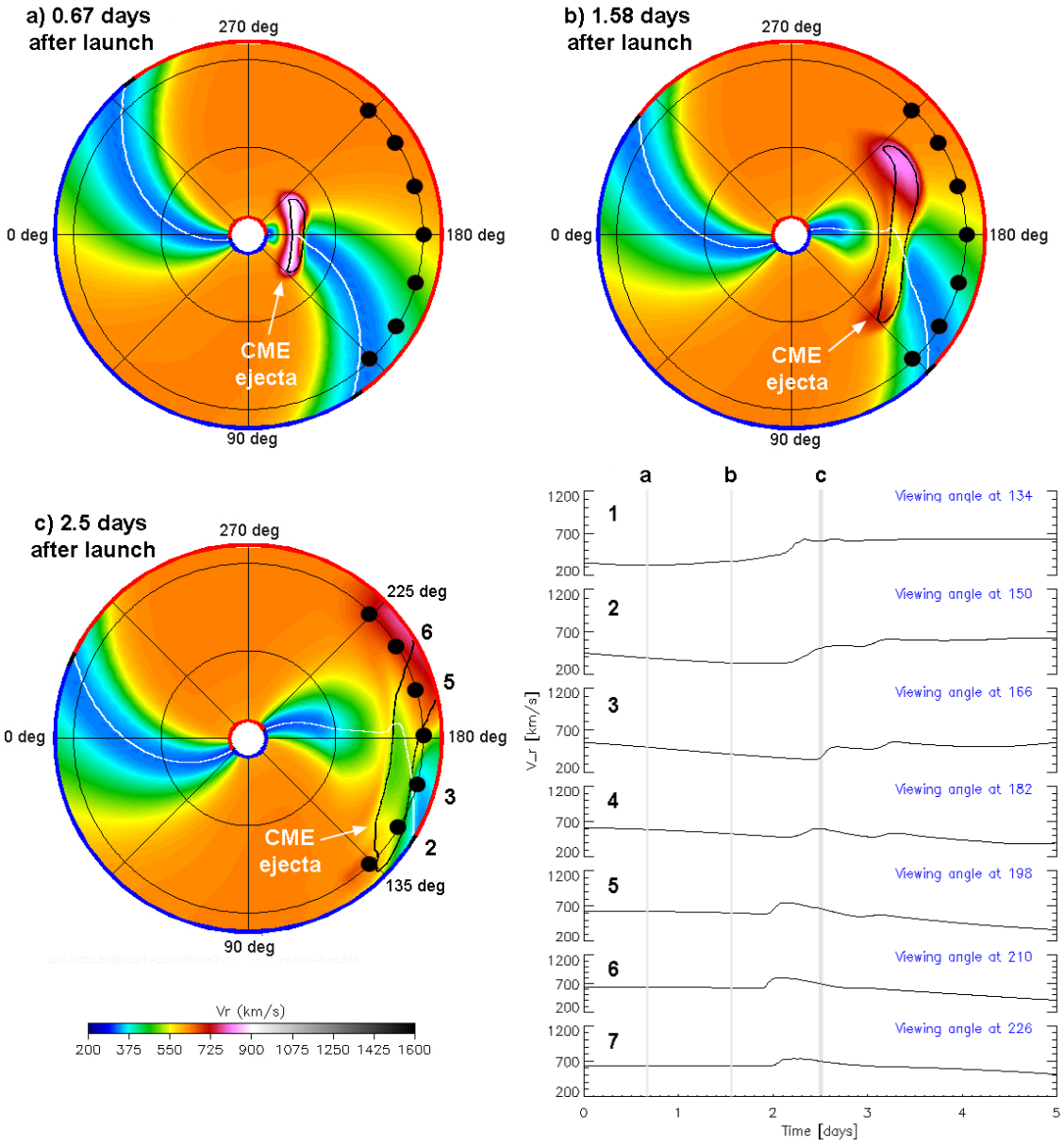

Figure 6.2: "Multipoint observations" at 1 AU of a CME. Shown is the ecliptic view of the evolution of a CME 0.67, 1.58, and 2.5 days after launch. The Sun-to-Earth line is located at 180° longitude. The bottom right shows the model-derived solar wind velocity time profiles at the different longitudinal vantage points (135° to 225°) along the 1 AU orbit. The numbers 1 to 7 coincide with the 1 AU vantage points shown on the bottom left. The gray vertical bars mark the times of the snapshots (a through c) shown throughout. Figure from Lee *et al.* (2008).

locations (*e.g.,* ACE together with STEREO or Ulysses; IMP-8 with Helios 1/2). The resulting analysis may show that the model predicts the CME properties better for one vantage point compared to another.

6.4.3 Space weather modeling at Mars

Space weather effects at Mars are currently not fully understood. Because Mars lacks a global magnetic field like Earth's (*e.g.,* Figure 1.13), the solar wind

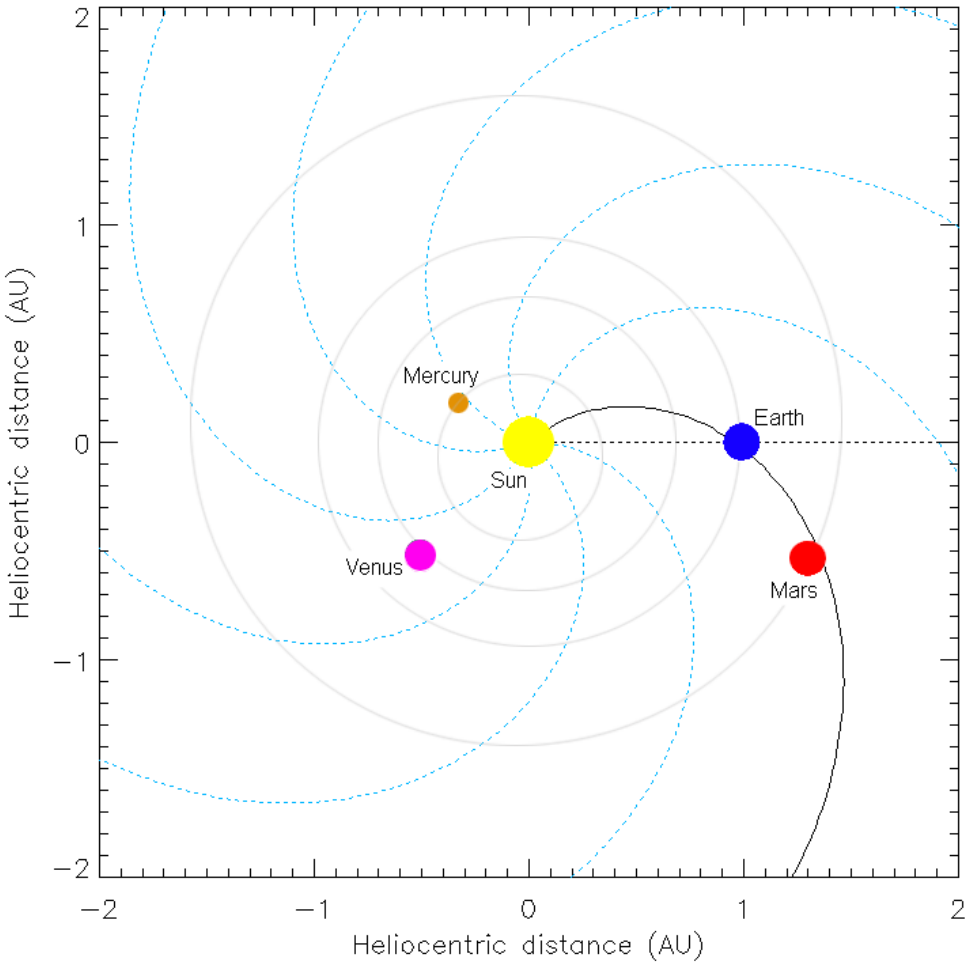

Figure 6.3: The IMF spiral configuration in the inner heliosphere during the Halloween storm. The planetary locations are generated from ephemeris data for 31 October 2003.

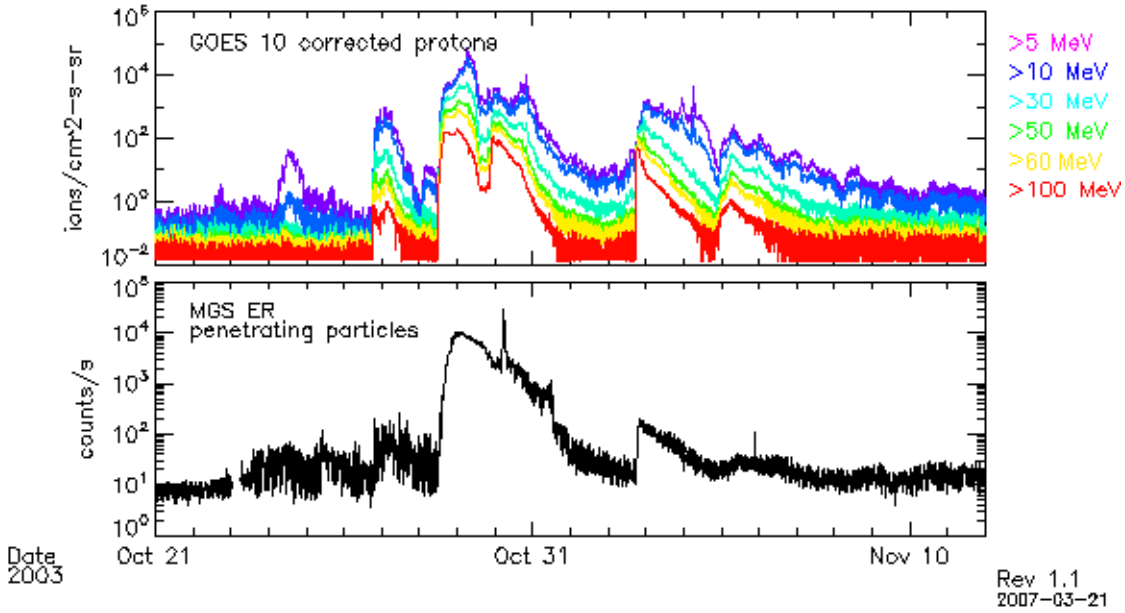

Figure 6.4: Time series of the 2003 Halloween solar storm shown for (top panel) protons (>15 MeV) detected by the GOES spacecraft near Earth and (bottom panel) penetrating counts measured by the MGS spacecraft at Mars. Adapted figure courtesy of G. Delory (personal communication).

interacts with the ionosphere directly, providing an obstacle to stand off the solar wind as it flows by. Although it is not certain whether solar wind stream interactions are important for the Mars plasma environment during quiet solar periods, observations from the Mars Global Surveyor (MGS) spacecraft during the 2003 Halloween solar storm revealed a response of the solar wind-ionosphere interaction region to a passage of a CME (Crider *et al.*, 2005). During this solar storm, Earth and Mars were aligned on the same spiral interplanetary field line (Figure 6.3) and thus were magnetically connected to the same set of solar storm events on the Sun and in interplanetary space. Figure 6.4 shows an example of a set of energetic particle events observed at Earth (top panel) and Mars (bottom panel) during the aforementioned Halloween storm. The Electron Reflectometer instrument on board the MGS spacecraft recorded impacts of energetic particles (>30 MeV) that were capable of penetrating the housing of the detector.

Currently there is no upstream solar wind monitor at Mars. As such, I would like to extend the terrestrial application of a numerical solar wind model (*e.g.*, WSA/ENLIL) to the distance of Mars at 1.5 AU. Such a model could serve as a

routine characterization tool or data substitute for the unmeasured solar wind conditions at Mars. In general, the development of such an inner heliospheric model would be essential for understanding the evolution of the solar wind structure and determining the differences in the space weather effects at various radial distances under both quiet and active solar periods. During quiet solar periods, dynamic pressure disturbances and energetic particles from corotating solar wind streams would behave differently and produce a different set of solar wind conditions at Mars compared to those at Earth. For active periods, as CMEs and solar energetic particles (SEPs) propagate to Mars' orbit their intensities diminish to some unknown extent. In addition, depending on their relative locations in the solar system, Earth and Mars would be impacted differently if they are connected to the same solar event on different magnetic field lines.

6.4.4 Space weather at Mercury and Venus

It would be straightforward to also investigate the space weather conditions at Mercury and Venus using an existing solar wind model since their radial distances (0.3 AU and 0.7 AU, respectively) are already included in the model description. I would compare the model results of the interplanetary conditions at each planetary location using archived in-situ observations from historical spacecraft missions such as Helios 1/2 (Figure 6.5), which observed the interplanetary medium between Earth and 0.3 AU, and Pioneer Venus Orbiter. Also, as new observations from the Mercury MESSENGER and Venus Express spacecraft become available, I would use them in conjunction with STEREO and ACE data to compare with the model results. As a test, one such comparison of model and observations of the Mercury magnetic field environment has been made by Baker *et al.* (2009). They simulated the space environment of Mercury using the WSA/ENLIL corona-solar wind model and compared the results with the (limited) magnetometer measurements obtained during the first MESSENGER flyby of the planet in January 2008. Their comparison showed the the WSA/ENLIL model performed well in reproducing the total field strengths that were observed.

One interesting problem related to Mercury is the total sodium concentration in the Mercurian exosphere. Mercury has an intrinsic magnetosphere generated by its weak dynamo field. However, because the magnetosphere only partially protects the surface from SEPs, a significant flux of energetic particles will reach and change Mercury's exosphere (see, for example Leblanc *et al.*, 2003). Ground-based observations have revealed an increase of the total sodium concentration inside the exosphere that may be caused either by CME events (Potter, Killen, and

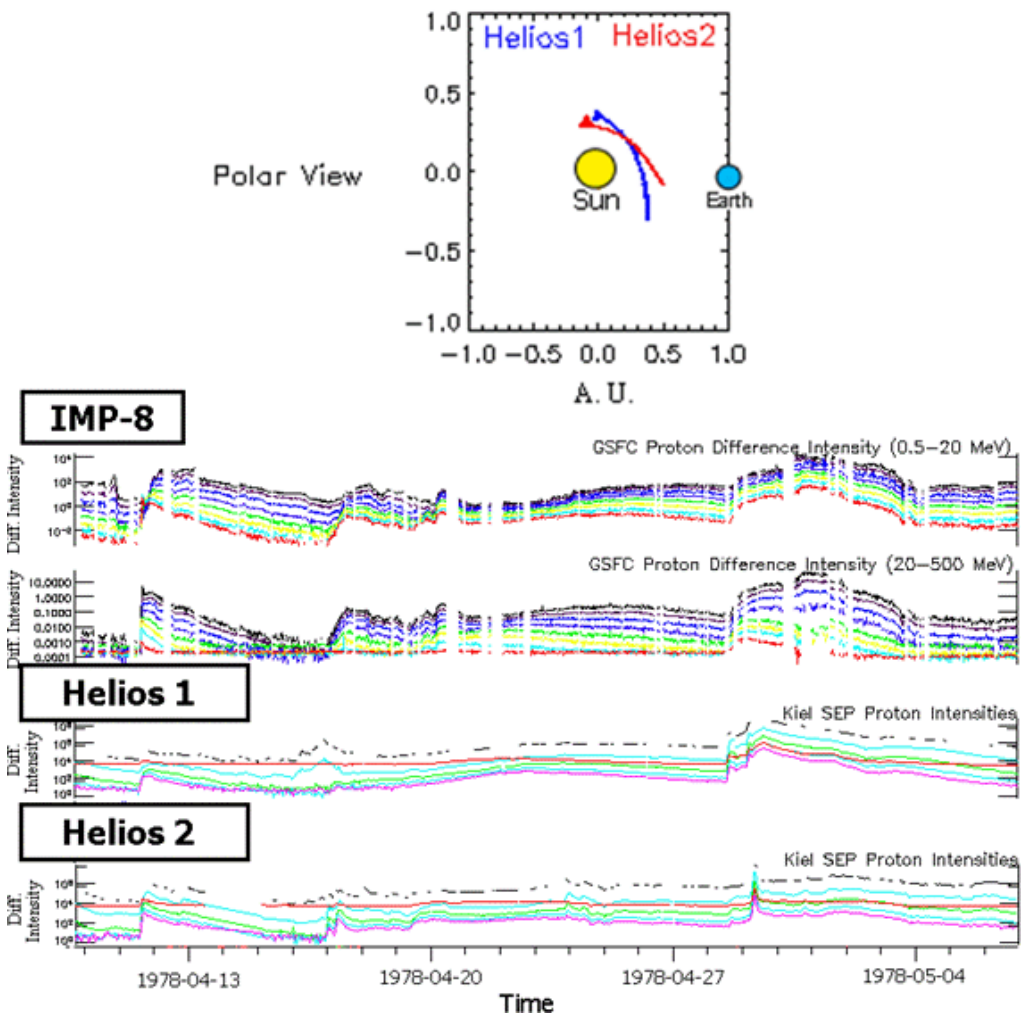

Figure 6.5: Time series of SEP events that occurred during April to May of 1978. (top) Trajectory of the Helios 1 and 2 spacecrafts. (bottom) Near-earth IMP-8 observations in the upper two panels and Helios data in the lower two panels, as labeled.

Morgan, 1999) or by strong variations in the solar wind flux or IMF orientation (Killen *et al.*, 2001). A comparison of results for the solar wind conditions at 0.3 AU with observations from Helios and/or Mercury MESSENGER would characterize the space weather environment for Mercury and help discern how important CMEs and SEPs are for the source production of sodium its the exosphere.

6.5 Final remarks

Today, we have a great opportunity to deeply understand the interplanetary medium on a more global context, thanks to the wide availability of ground-based and spacecraft observations as well as state-of-the-art solar corona and solar wind numerical models.

As the next solar maximum approaches around 2013, the models will for the first time be available for use as space weather forecasting and scientific research tools. Since the multi-spacecraft observations of events are now widely available, it will be possible to examine the performances of these models in capturing the global properties of a CME event by comparing the results with observations made at different locations (Mercury MESSENGER at 0.3 AU, Venus Express at 0.7 AU, STEREO and ACE at 1 AU). There is an exciting opportunity ahead to observe a CME event in unprecedented detail and to better understand the evolution and propagation of CMEs as they travel outward from the Sun.

Bibliography

Abramenko, V., Yurchyshyn, V., Linker, J., Mikic, Z, Luhmann, J.G., Lee, C.O.: 2009, Low-latitude coronal holes at the minimum of the 23rd solar cycle, *Astrophys. J.*, accepted.

Acuña, M.H., Curtis, D., Scheifele, J.L., Russell, C.T., Schroeder, P., Szabo, A., Luhmann, J. G.: 2008, The STEREO/IMPACT Magnetic Field Experiment, *Space Sci. Rev.*, **136**, 203–226.

Altschuler, M.D., Newkirk, G.: 1969, Magnetic fields and the structure of the solar corona, *Solar Phys.*, **9**, 131–149

Arge, C.N., Pizzo, V.J.: 1998, Space weather forecasting at NOAA/SEC using the Wang-Sheeley Model, In: Balasubramaniam, K.S. et al. (eds.) *Synoptic Solar Physics*, ASP Conf. Ser. 140, 423-430.

Arge, C.N., Pizzo, V.J.: 2000, Improvement in the prediction of solar wind conditions using near-real time solar magnetic field updates, *J. Geophys. Res.*, **105**, A10, doi:10.1029/2001JA000503.

Arge, C.N., Hildner, E., Pizzo, V.J., Harvey, J.W.: 2002, Two solar cycles of non-increasing magnetic flux, *J. Geophys. Res.*, **107**, A15, 10465–10480.

Arge, C.N., Luhmann, J.G., Odstrcil, D., Schrijver, C.J., Li, Y.: 2004, Stream structure and coronal sources of the solar wind during the May 12th, 1997 CME, *J. Atm Solar Terr. Phys.*, **66**, 1295–1309.

Aschwanden, M.J.: 1994, Irradiance observations of the 1–8 A solar soft X–ray flux from GOES, *Solar Phys.* **152**, 53–59.

Baker, D.N.: 2000, Effects of the Sun on the Earth's environment, *J. Atmos. Solar Terr. Phys.* **62**, 1669–1681.

Baker, D.N., Odstrcil, D., Anderson, B.J., Arge, C.N., Benna, M., Gloeckler, G., Raines, J.M., Schriver, D., Slavin, J.A., *et al.*: 2009, Space environment of Mercury at the time of the first MESSENGER flyby: Solar wind and interplanetary magnetic field modeling of upstream conditions, *J. Geophys. Res.*, **114**, A10101, doi:10.1029/2009JA014287.

Balogh, A., Beek, T.J., Forsyth, R.J., Hedgecock, P.C., Marquedant, R.J., Smith, E.J., Southwood, D.J., Tsurutani, B.T.: 1992, The magnetic field investigation on the Ulysses mission: Instrumentation and preliminary scientific results, *Astron. Astrophys. Supple. Ser.*, **92**, 221–236.

Balogh, A., Smith, E.J., Tsurutani, B.T., Southwood, D.J., Beek, Forsyth, R.J., Horbury, T.S.: 1995, The heliospheric magnetic field over the south polar region of the Sun, *Science*, **268**, 1007–1010.

Bame, S.J., McComas, D.J., Barraclough, B.L., Phillips, J.L., Sofaly, K.J., Chavez, J.C., Goldstein, B.E., Sakurai, R.K.: 1992, The Ulysses solar wind plasma experiment, *Astron. Astrophys. Supple. Ser.*, **92**, 237–265.

Barnes, C.W., Simpson, J.A.: 1976, Evidence for interplanetary acceleration of nucleons in corotating interaction regions, *Astrophys. J.* **210**, L91–L96.

Bucik, R., Mall, U., Gomez-Herrero, R., Korth, A., Mason, G.M.: 2009, STEREO observations of energetic ions in corotating interaction regions during the May 2007 solar events, *Solar Phys.* **259**, 361–380.

Burlaga, L.F., Ness, N.F., Mariani, F., Bavassano, B., Villante, U., Rosenbauer, H., Schwenn, R., Harvey. J.: 1978, Magnetic fields and flows between 1 and 0.3 AU during the primary mission of HELIOS 1, *J. Geophys. Res.*, **83**, 5167–5174.

Cane, H.V., Reames, D.V., von Rosenvinge, T.T.: 1988, The role of interplanetary shocks in the longitude distribution of solar energetic particles, *J. Geophys. Res.* **93**, 9555–9567.

Cane, H.V., Richardson, I.G.: 2003, Interplanetary coronal mass ejections in the near-Earth solar wind during 1996-2002, *J. Geophys. Res.*, **108**, Cite ID 1156, doi:10.1029/2002JA009817.

Cane, H.V., Lario, D.: 2006, An introduction to CMEs and energetic particles, *Space Sci. Rev.*, **123**, 45–56.

Cane, H.V., Mewaldt, R.A., Cohen, C.M.S., von Rosenvinge, T.T.: 2006, Role of flares and shocks in determining solar energetic particle abundances , *J. Geophys. Res.* **111**, doi:10.1029/2005JA011071.

Cohen, O., Sokolov, I.V., Roussev, I.I., et al.: 2007, A semiempirical magnetohydrodynamical model of the solar wind, *Astrophys. J.*, **654**, L163–L166.

Cohen, O., Sokolov, I.V., Roussev, I.I., and Gombosi, T.: 2008, Validation of a synoptic solar wind model, *J. Geophys. Res.*, **113**, A03104, doi:10.1029/2007JA012797.

Colin, L.: 1980, The Pioneer Venus Program, *J. Geophys. Res.*, **85**, 7575–7598.

Crider, D.H., Espley, J., Brain, D.A., Mitchell, D.L., Connerney, J.E.P., Acuna, M.H.: 2005, Mars Global Surveyor observations of the October 2003 solar super-storm's encounter with Mars, *J. Geophys. Res.*, **110**, A09S21, doi:10.1029/2004JA010881.

Crooker, N.U., Gosling, J.T., Bothmer, V., Forsyth, R.J., Gazis, P.R., Hewish, A., Horbury, T.S., Intriligator, D.S., Jokipii, J.R., Kota, J., *et al.*: 1999, CIR morphology, turbulence, discontinuities, and energetic particles, *Space Sci. Rev.*, **89**, 179–220.

Delaboudiniere, J.P., Artzner, G.E., Brunaud, J., Gabriel, A.H., Hochedez, J.F., Millier, F., Song, X.Y., Au, B., Dere, K.P., Howard, R.A., *et al.*, 1995, EIT: Extreme-Ultraviolet Imaging Telescope for the SOHO Mission, *Solar Phys.*, **162**, 291–312.

Desai, M.I., Mason, G.M., Mazur, J.E., Dwyer, J.R.: 2006a, Solar cycle variations in the composition of the suprathermal heavy-ion population near 1 AU, *Astrophys. J.* **645**, L81–L84.

Desai, M.I., Mason, G.M., Gold, R.E., Krimigis, S.M., Cohen, C.M.S., Mewaldt, R.A. , Mazur, J.E., Dwyer, J.R.: 2006b, Heavy-ion elemental abundances in large solar energetic particle events and their implications for the seed population, *Astrophys. J.* **649**, 470–489.

Forsyth R.J., Marsch, E.: 1999, Solar origin and interplanetary evolution of stream interfaces, *Space Sci. Rev.* **89**, 7–20.

Gold, R.E., Krimigis, S.M., Hawkins, S.E., III, Haggerty, D.K., Lohr, D.A., Fiore, E., Armstrong, T.P., Holland, G., Lanzerotti, L. J.: 1998, Electron, Proton, and Alpha Monitor on the Advanced Composition Explorer spacecraft, *Space Sci. Rev.* **86**, 541–562.

Gosling, J.T., Asbridge, J.R., Bame, S.J., Feldman, W.C.: 1978, Solar wind stream interfaces, *J. Geophys. Res.* **83**, 1401–1412.

Gosling, J.T., Pizzo, V.J.: 1999, Formation and Evolution of Corotating Interaction Regions and Their Three Dimensional Structure, *Space Sci. Rev.*, **89**, 21–52.

Haggerty, D.K., Roelof, E.C.: 2002, Impulsive near–relativistic solar electron events: Delayed injection with respect to solar electromagnetic emission, *Astrophys. J.* **579**, 841–853.

Haggerty, D.K., Roelof, E.C.: 2009, Probing SEP acceleration processes with near–relativistic electrons, In:*American Institute of Physics Conference Proceedings*, 3–10.

Henney, C.J., Keller, C.U., Harvey, J.W.: 2006, SOLIS-VSM Solar Vector Magnetograms. In: Casini, R., Lites, B. W. (eds.) *Solar Polarization 4*, CS358, Astron. Soc. Pac., San Francisco, 92–95.

Hiltula, T., Mursula, K.: 2006, Long dance of the bashful ballerina, *Geophys. Res. Lett.*, **33**, doi:10.1029/2005GL025198.

Hoeksema, J.T., Wilcox, J.M., Scherrer, P.H.: 1982, Structure of the heliospheric current sheet in the early portion of Sunspot Cycle 21, *J. Geophys. Res.*, **87**, 10331–10338.

Hoeksema, J.T., Wilcox, J.M., Scherrer, P.H.: 1983, The structure of the heliospheric current sheet: 1978, *J. Geophys. Res.*, **88**, 9910–9918.

Hoeksema, J.T.: 1984, Ph.D. Thesis, Stanford University.

Hoeksema, J.T., Scherrer, P.H.: 1985, An atlas of photospheric magnetic field observations and computed heliospheric magnetic fields from the John M. Wilcox Solar Observatory at Standford 1976-1984, *Rep. CSSA-ASTRO-85-11*, Stanford University, Stanford, California.

Hoeksema, J.T., Scherrer, P.H.: 1986, An atlas of photospheric magnetic field observations and computed coronal magnetic fields: 1976–1985, *Solar Phys.*, **105**, 205–211.

Hoeksema, J.T.: 2010, Evolution of the large-scale magnetic field over three solar cycles. In: Kosovichev, A.G., Andrei, A.H., and Rozelot J.-P. (eds.) *Solar and Stellar Variability: Impact on Earth and Planets*, Proceedings IAU Symposium, 222–228.

Howard, R.: 1976, The Mount Wilson solar magnetograph - Scanning and data system, *Solar Phys.*, **48**, 411–416.

Howard, R.A., Moses, J.D., Socker, D.G., Dere, K.P., Cook, J.W.: 2002, Sun Earth Connection Coronal and Heliospheric Investigation (SECCHI), *Adv. Space Res.*, **29**, 2017–2026.

Hundhausen, A.J.: 1995, The Solar Wind, In: Kivelson, M.G., Russell, C.T. (eds.) *Introduction to Space Physics*, Cambridge University Press, 91–128.

Issautier, K., Le Chat, G., Meyer-Vernet, N., Moncuquet, M., Hoang, S., MacDowell, R.J., McComas, D.J.: 2008, Electron properties of high–speed solar wind from polar coronal holes obtained by Ulysses thermal noise spectroscopy: Not so dense, not so hot, *Geophys. Res. Lett.*, **35**, doi:10.1029/2008GL034912.

Jian, L., Russell, C.T., Luhmann, J.G., Skoug, R.M.: 2006a, Properties of stream interactions at one AU during 1995–2004, *Solar Phys.* **239**, 337–392.

Jian, L., Russell, C.T., Luhmann, J.G., Skoug, R.M.: 2006b, Properties of interplanetary coronal mass ejections at one AU during 1995–2004, *Solar Phys.* **239**, 393–436.

Jian, L. 2008, Radial variation of large-scale solar wind structures, Ph.D. dissertation, Univ. California, Los Angeles.

Kaiser, M.: 2005, The STEREO Mission: an overview, *Adv. Space Res.*, **36**, 1483–1488.

Kallenrode, M.B.: 2001, Sun and solar wind: Plasmas in the heliosphere, In: Kallenrode, M.B. (eds.) *Space Physics: An introduction to plasmas and particles in the heiosphere and magnetospheres*, Springer-Verlag, Berlin, Second Edition, 103–158.

Killen, R. M., et al., 2001, Evidence for space weather at Mercury, *J. Geophys. Res.*, **106**, 20509.

Kirk, M.S., Pesnell, W.D., Young, C.A., Hess Weber, S.A.: 2009, Automated detection of EUV Polar Coronal Holes during Solar Cycle 23, *Solar Phys.*, **257**, 99–112.

Kunow, H., Witte, M., Wibberenz, G., Hempe, H., Mueller-Mellin, R., Green, G., Iwers, B., Fuckner, J.: 1977, Cosmic ray measurements on board HELIOS 1 from December 1974 to September 1975 Quiet time spectra, radial gradients, and solar events, *J. Geophys.*, **42**, 615–631.

Lang, K.R.: 1995, Sun, Earth, and Sky, *Earth, Moon, and Planets* **70**, 1–20.

Leblanc, F., Luhmann, J.G., Johnson, R.E., Liu, M.: 2003, Solar energetic particle event at Mercury, *Planet Space Sci.*, **51**, 339.

Lee, C.O., Odstrcil, D., Luhmann, J.G., de Pater, I.: 2008, A Sensitivity Study Using ENLIL Solar Wind And Cone CME Model, In: *Fall Meet. Suppl.*, *Abstract SA51A-1541*, *EOS Trans. AGU*, **89**(53).

Lee, C.O., Luhmann, J.G., Odstrcil, D, MacNeice, P.J., de Pater, I., Riley, P., Arge, C.N.: 2009a, The Solar Wind at 1 AU During the Declining Phase of Solar Cycle 23: Comparison of 3D Numerical Model Results with Observations, *Solar Phys.*, **254**, 155–183.

Lee, C.O., Luhmann, J.G., Zhao, X.P. Liu, Y., Riley, P., Arge, C.N., Russell, C.T., de Pater, I.: 2009b, Effects of the weak polar fields of Solar Cycle 23: Investigation using OMNI for the STEREO Mission Period, *Solar Phys.*, **256**, 345–363.

Lee, C.O., Luhmann, J.G., de Pater, I., Mason, G.M., Haggerty, D., Richardson, I.G., Cane, H.V., Jian, L.K., Russell, C.T., Desai, M.I.: 2010, Organization of Energetic Particles by the Solar Wind Structure During the Declining to Minimum Phase of Solar Cycle 23, *Solar Phys.*, **263**, 239–261.

Levine, R.H., Altschuler, M.D., Harvey J.W.: 1977, Solar sources of the interplanetary magnetic field and solar wind, *J. Geophys. Res.*, **82**, 1061–1065.

Levine, R.H., Altschuler, M.D., Harvey, J.W., Jackson, B.V.: 1977, Open magnetic structures of the Sun, *Astrophys. J.*, **215**, 636–651.

Levine, R.H.: 1977, Open magnetic fields and the solar cycle: I. Photospheric sources of open magnetic flux, *Solar Phys.*, **79**, 203–230.

Linker, J.A., Mikic, Z.: 1997, Extending coronal models to Earth orbit. In: Crooker, N., Joselyn, J., and Feynmann, J. (eds.) *Coronal Mass Ejections*, Geophys. Monogr. Ser., vol. 99, American Geophysical Union, Washington, D.C, 269-277.

Luhmann, J.G., Li, Y., Arge, C.N., Gazis, P.R., Ulrich, R.: 2002, Solar cycle changes in coronal holes and space weather cycles, *J. Geophys. Res.*, **107**, doi:10.1029/2001JA007550.

Luhmann, J.G., Solomon, S.C., Linker, J.A., Lyon, J.G., Mikic, Z., Odstrcil, D., Wang, W., Wiltberger, M.: 2004, Coupled model simulation of a Sun-to-Earth space weather event, *J. Atm Solar Terr. Phys.*, **66**, 1243–1256.

Luhmann, J.G., Curtis, D.W., Schroeder, P., McCauley, J., Lin, R.P., Larson, D.E., Bale, S.D., Sauvaud, J.A., Aoustin, C., Mewaldt, R.A., *et al.*: 2008, STEREO IMPACT Investigation Goals, Measurements, and Data Products Overview, *Space Sci. Rev.*, **136**, 117–184.

Luhmann, J.G., Lee, C.O., Li, Y., Arge, C.N., Galvin, A.B., Simunac, K., Russell, C.T., Howard, R.A., Petrie, G.: 2009, Solar wind sources in the late declining phase of Cycle 23: Effects of the weak solar polar field on high speed streams, *Solar Phys.*, **256**, 285–305.

Mariani, F., Ness, N.F., Burlaga, L.F., Bavassano, B., Villante, U.: 1978, The large-scale structure of the interplanetary magnetic field between 1 and 0.3 AU during the primary mission of HELIOS 1, *J. Geophys. Res.*, **83**, 5161–5166.

Mason, G.M., Gold, R.E., Krimigis, S.M., Mazur, J.E., Andrews, G.B., Daley, K.A., Dwyer, J.R., Heuerman, K.F., James, T.L., Kennedy, M.J., *et al.*: 1998, The Ultra-Low-Energy Isotope Spectrometer (ULEIS) for the ACE spacecraft, *Space Sci. Rev.* **86**, 409–448.

Mason, G.M., Sanderson, T.R.: 1999, CIR associated energetic particles in the inner and middle heliosphere, *Space Sci. Rev.* **89**, 77–90.

Mason, G.M., Leske, R.A., Desai, M.I., Cohen, C.M.S., Dwyer, J.R., Mazur, J.E., Mewaldt, R.A., Gold, R.E., Krimigis, S.M.: 2008, Abundances and energy spectra of corotating interaction region heavy ions observed during Solar Cycle 23, *Astrophys. J.* **678**, 1458–1470.

Mason, G.M., Desai, M.I., Mall, U., Korth, A., Bucik, R., von Rosenvinge, T.T., Simunac, K.D.: 2009, In–situ observations of CIRs on STEREO, Wind, and ACE during 2007–2008, *Solar Phys.*, **256**, 393–408.

Mason, G.M., Nitta, N.V., Cohen, C.M.S., Wiedenbeck, M.E.: 2009, Solar energetic particle ^{3}He-rich events from the nearly quiet sun in 2007-2008, *Astrophys. J.* **700**, L56–L59.

McComas, D.J., Bame, S.J., Barker, P., Feldman, W.C., Phillips, J.L., Riley, P., Griffee, J.W.: 1998, Solar Wind Electron Proton Alpha Monitor (SWEPAM) for the Advanced Composition Explorer, *Space Sci. Rev.*, **86**, 563–612.

McComas, D.J., Elliott, H.A., Schwadron, N.A., Gosling, J.T., Skoug, R.M., Goldstein, B.E.: 2003, The three-dimensional solar wind around solar maximum, *Geophys. Res. Lett.*, **30**, doi:10.1029/2003GL017136.

McComas, D.J., Ebert, R.W., Elliott, H.A., Goldstein, B.E., Gosling, J.T., Schwadron, N.A., Skoug, R.M.: 2008, Weaker solar wind from the polar coronal holes and the whole Sun, *Geophys. Res. Lett.*, **35**, doi:10.1029/2008GL034896.

McGregor, S.L., Hughes, W., Arge, C.N., Odstrcil, D.: 2006, Predicting Solar Wind Structures in the Inner Heliosphere, *Eos Trans. AGU*, **87**(52), Fall Meet. Suppl., Abstract SH21B-02.

Mewaldt, R.A., Cohen, C.M.S., Mason, G.M., Cummings, A.C., Desai, M.I., Leske, R.A., Raines, J., Stone, E.C., Wiedenbeck, M.E., von Rosenvinge, T.T., Zurbuchen, T.H.: 2007, On the differences in composition between solar energetic particles and solar wind, *Space Sci. Rev.* **130**, 207–219.

Mikic, Z., Linker, J.A.: 1995, The large-scale structure of the solar corona and inner heliosphere. In: Winterhalter D. et al. (eds.) *Solar Wind Eight*, *AIP Conf. Proc.*, **382**, 104.

Neugebauer, M., Goldstein, M., Goldstein, B.E.: 1997, Features observed in the trailing regions of interplanetary clouds from coronal mass ejections, *J. Geophys. Res.*, **102**, 19743–19751.

Odstrcil, D.: 2003, Modeling 3D solar wind structure, *Adv. Space Res.*, **32**, 497–506.

Odstrcil, D., Riley, P., Zhao, X.P.: 2004, Numerical simulation of the 12 May 1997 interplanetary CME event, *J. Geophys. Res.*, **109**, doi:10.1029/2003JA010135.

Odstrcil, D., Pizzo, V.J., Arge, C.N.: 2005, Propagation of the 12 May 1997 interplanetary CME in evolving solar wind structures, *J. Geophys. Res.*, **110**, doi:10.1029/2004JA010745.

Odstrcil, D., Linker, J.A., Lionello, R., Mikic, Z., Riley, P., Pizzo, V.J., Luhmann, J.G.: 2002, Merging of coronal and heliospheric numerical two-dimensional MHD models, *J. Geophys. Res.*, **107**, doi:10.1029/2002JA009334.

Ogilvie, K.W., Desch, M.D.: 1997, The Wind spacecraft and its early scientific results, *Adv. Space Res.* **20**, 559–568.

Owens, M.J., Spence, H.E., McGregor, S., Hughes, W.J., Quinn, J.M., Arge, C.N., Riley, P., Linker, J., Odstrcil, D.: 2007, Metric for solar wind prediction models: Comparison of empirical, hybrid, and physics-based schemes with 8-years of L1 observations, *Space Weather*, **6**, S08001, doi:10.1029/2007SW000380.

Parker, E.N.: 1958, Dynamics of the Interplanetary Gas and Magnetic Fields., *Astrophys. J.*, **128**, 664–676.

Pizzo, V.: 1978, A three-dimensional model of corotating streams in the solar wind: 1. Theoretical foundations, *J. Geophys. Res.* **83**, 5563–5572.

Pizzo, V.J.: 1982, A three-dimensional model of corotating streams in the solar wind: Magnetohydrodynamic streams, *J. Geophys. Res.*, **87**, 4374–4394.

Pizzo, V.J.: 1991, The evolution of corotating stream fronts near the ecliptic plane in the inner solar system. II - Three-dimensional tilted-dipole fronts, *J. Geophys. Res.*, **96**, 5405–5420.

Pizzo, V.J.: 1994, Global, quasi-steady dynamics of the distant solar wind 2: Deformation of the heliospheric current sheet, *J. Geophys. Res.*, **99**, 4185–4191.

Potter, A.E., Killen, R.M., Morgan, T.H.: 1999, Rapid changes in the sodium exosphere of Mercury, *Planet. Space Sci.*, **47**, 1441.

Pneumann, G.W. and Kopp, R.A.: 1971, Gas-magnetic field interactions in the solar corona, *Solar Phys.*, **18**, 258–270.

Reames, D.V.: 1999, Particle acceleration at the Sun and in the heliosphere, *Space Sci. Rev.* **90**, 413–491.

Richardson, I.G.: 2004, Energetic particles and corotating interaction regions in the solar wind, *Space Sci. Rev.* **111**, 267–376.

Riley, P., Linker, J.A., Mikic, Z.: 2001, An empirically-driven global MHD model of the solar corona and inner heliosphere, *J. Geophys. Res.*, **106**, 15889–15901.

Riley, P., Linker, J.A., Mikic, Z., Lionello, R., Ledvina, S.A., Luhmann, J.G.: 2006, A Comparison between Global Solar Magnetohydrodynamic and Potential Field Source Surface Model Results, *Astrophys. J.*, **653**, 1510–1516.

Riley, P., Gosling, J.T.: 2007, On the origin of near-radial fields in the heliosphere: Numerical simulations, *J. Geophys. Res.*, **112**, doi:10.1029/2006JA012210.

Roussev, I.I., Forbes, T.G., Gombosi, T.I., Sokolov, I.V., DeZeeuw, D.L., Birn, J.: 2003, A Three-dimensional Flux Rope Model for Coronal Mass Ejections Based on a Loss of Equilibrium, *Astrophys. J.*, **588**, L45–L48.

Sanderson, T.R., Lin, R.P., Larson, D.E., McCarthy, M.P., Parks, G.K., Bosqued, J.M., Lormant, N., Ogilvie, K., Lepping, R.P., Szabo, A., *et al.*: 1998, Wind observations of the influence of the Sun's magnetic field on the interplanetary medium at 1 AU, *J. Geophys. Res.* **103**, 17235–17247.

Schatten, K.H., Wilcox, J.M., Ness, N.F.: 1969, A model of interplanetary and coronal magnetic fields, *Solar Phys.*, **6**, 442–455.

Schatten, K.H.: 1971, Current sheet magnetic model for the solar corona, *Cosmic Electrodyn.*, **2**, 232–245.

Scholer, M., Hovestadt, D., Klecker, B., Gloeckler, G.: 1979, The composition of energetic particles in corotating events, *Astrophys. J.* **227**, 323–328.

Schwenn, R.: 1978, Large-scale structure of the interplanetary medium,. In: Schwenn, R. and Marsch, E. (eds.) *Physics of the Inner Heliosphere I*, Springer-Verlag, Berlin, 99–181.

Smith, E.J., Tsurutani, B.T., Rosenberg, R.L.: 1978, Observations of the interplanetary sector structure up to heliographic latitude of 16°: Pioneer 11, *J. Geophys. Res.*, **83**, 717–724.

Smith, C.W., L'Heureux, J., Ness, N.F., Acuña, M.H., Burlaga, L.F., Scheifele, J.: 1998, The ACE Magnetic Fields Experiment, *Space Sci. Rev.*, **86**, 613–632.

Smith, E.J. and Balogh, A.: 2008, Decrease in heliospheric magnetic flux in this solar minimum: recent Ulysses magnetic field observations, *Geophys. Res. Lett.*, **35**, Cite ID L22103, doi:10.1029/2008GL035345.

Solomon, S.C., McNutt, Jr., R.L., Gold, R.E., et al.: 2001, The MESSENGER mission to Mercury: scientific objectives and implementation, *Planet. Space Sci.*, **49**, 1445–1465.

Steinolfson, R.S., Suess, S.T., Wu, S.T.: 1982, The steady global corona, *Astrophys. J.*, **255**, 730–742.

Svalgaard, L., Duvall, Jr., T.L., Scherrer, P.H.: 1978, The strength of the Sun's polar fields, *Solar Phys.*, **58**, 225–240.

Svalgaard, L., Cliver, E.W.: 2007, A floor in the solar wind magnetic field, *Astrophys. J.*, **661**, L203–L206.

Taktakishvili, A., Kuznetsova, M., MacNeice, P., Hesse, M., Rastatter, L., Pulkkinen, A., Chulaki, A., Odstrcil, D.: 2009, Validation of the coronal mass ejection predictions at the Earth orbit estimated by ENLIL heliosphere cone model, *Space Weather*, **7**, doi:10.1029/2008SW000448.

Ulrich, R.K., Evans, S., Boyden, J.E., Webster, L.: 2002, Mount Wilson Synoptic Magnetic Fields: Improved Instrumentation, Calibration, and Analysis Applied to the 2000 July 14 Flare and to the Evolution of the Dipole Field, *Astrophys. J. Supp.*, **139**, 259–279.

Usmanov, A.V.: 1993a, Interplanetary magnetic field structure and solar wind parameters as inferred from solar magnetic field observations and by using a numerical 2D MHD model, *Solar Phys.*, **143**, 345–363.

Usmanov, A.V.: 1993b, A global numerical 3D MHD model of the solar wind, *Solar Phys.*, **146**, 377–396.

Usmanov, A.V., Goldstein, M.L., Besser, B.P., Fritzer, J.M.: 2000, A global MHD solar wind model with WKB Alfvén waves: Comparison with Ulysses data, *J. Geophys. Res.*, **105**, 12675–12696.

Usmanov, A.V., Goldstein, M.L.: 2003, A tilted-dipole MHD model of the solar corona and solar wind, *J. Geophys. Res.*, **108**, doi:10.1029/2002JA009777.

van Hollebeke, M.A.I., McDonald, F.B., Trainor, J.H., von Rosenvinge, T.T.: 1978, The radial variation of coroating energetic particle streams in the inner and outer solar system, *J. Geophys. Res.*, **83**, 4723–4731.

Wang, Y.M., Sheeley, N.R.: 1990a, Solar wind speed and coronal flux-tube expansion, *Astrophys. J.*, **355**, 726–732.

Wang, Y.M., Sheeley, N.R.: 1990b, Magnetic flux transport and the sunspot-cycle evolution of coronal holes and their wind streams, *Astrophys. J.*, **365**, 372–386.

Wang, Y.M., Sheeley, N.R.: 1992, On potential field models of the solar corona, *Astrophys. J.*, **392**, 310–319.

Wang, Y.M., Robbrecht, E., Sheeley, N.R.: 2009, On the weakening of the polar magnetic fields during Solar Cycle 23, *Astrophys. J.*, **707**, 1372–1386.

Webb, D. F., Allen, J.: 2004, Spacecraft and ground anomalies related to the October-November 2003 solar activity, *Space Weather*, **2**, S03008, doi:1029/2994SW000075.

Wimmer-Schweingruber, R.F., Crooker, N.U. Balogh, A., Bothmer, V., Forsyth, R.J., Gazis, P., Gosling, J.T., Horbury, T., Kilchenmann, A., Richardson, I.G., *et al.*: 2006, Understanding coronal mass ejection signatures, *Space Sci. Rev.*, **123**, 177–216.

Xie, H., Ofman, L., Lawrence, G.: 2004, Cone model for halo CMEs: Application to space weather forecasting, *J. Geophys. Res.*, **109**, doi:10.1029/2003JA010226.

Zhao, X.P. and Hoeksema, J.T.: 1995, Prediction of the interplanetary magnetic field strength, *J. Geophys. Res.*, **100**, 19–33.

Zhao, X.P., Plunkett, S.P., Liu, W.: 2002, Determination of geometrical and kinematical properties of halo coronal mass ejections using the cone model, *J. Geophys. Res.*, **107**, doi:10.1029/2001JA009143, SSH 13-1.

Zhao, X.P., Webb, D.F.: 2003, Source regions and storm effectiveness of frontside full halo coronal mass ejections, *J. Geophys. Res.*, **108**, doi:10.1029/2002JA009606.

Appendix: Commonly Used Abbreviations and Acronyms

ACE - Advanced Composition Explorer
AU - Astronomical Unit
CCMC - Community Coordinated Modeling Center
CH - Coronal Hole
CIR - Corotating Interaction Region
CME - Coronal Mass Ejection
CR - Carrington Rotation
ENLIL - Sumerian name for God of the Sun
EPAM - Electron, Proton, and Alpha Monitor
EUV - Extreme Ultraviolet
HCS - Heliospheric Current Sheet
ICME - Interplanetary CME
IMF - Interplanetary Magnetic Field
MAS - MHD Around a Sphere
MHD - Magnetohydrodynamics
MWO - Mount Wilson Observatory
NSO - National Solar Observatory
OMNI - Multi-source solar wind data
PCH - Polar Coronal Hole
PFSS - Potential Field Source Surface
SC - Solar Cycle
SEP - Solar Energetic Particle
SIR - Stream Interaction Region
SOHO - Solar and Heliospheric Observatory
STEREO - Solar TERrestrial Observatory
ULEIS - Ultra-Low Energy Isotope Spectrometer
WSA - Wang-Sheeley-Arge
WSO - Wilcox Solar Observatory